TRACK FINDING IN e^+e^- INTERACTIONS

ALAN J. CAMPBELL, IMPERIAL COLLEGE , LONDON

A thesis submitted for the degree of Doctor of Philosophy
at the University of London.

September 1983

TO MY PARENTS

ABSTRACT

This thesis describes the TASSO experiment at the e^+e^- storage ring PETRA at DESY in Hamburg. New methods for the reconstruction of charged particle tracks from the digitisings of the central detectors are presented. The performance of the cylindrical proportional chamber and its use is described. A fast track recognition program for the proportional chamber which uses the depth first search algorithm is presented and its use as a filter for low multiplicity events discussed. The pulse height readout from cathode strips is described together with the resulting improvement in track resolution. Hardware track recognition by purpose built processors for the cylindrical proportional chamber anode wires and cathode strips is described. The design and construction of a small high resolution drift chamber for the detection of charged track vertices is described and its performance in test with cosmic rays and PETRA data evaluated. The determination of the space-drift time relation and the alignment of the vertex chamber are given. A general track finding program utilising the back track

algorithm and capable of using the data of all three central detectors:the large cylindrical drift chamber,the cylindrical proportional chamber and the vertex drift chamber is presented. The performance of the track finding program is evaluated using a Monte-Carlo event and detector simulation. It is shown how charged tracks are reconstructed in three dimensions using the small angle stereo wires, helical cathode strips and charge division wires. Improved reconstruction for charged tracks at small angles to the beam direction which deposit energy in liquid argon endcap shower counters is obtained. The production of strange baryons in single photon annihilation at centre-of-mass energies above 30GeV is discussed and results presented on the cross-sections for Ξ^- and Σ^* production.

ACKNOWLEDGEMENTS

I would first like to thank my parents for their constant love and kindness.

I am indebted to my supervisor, Dr. Peter Dornan, for his encouragement and advice.

I thank Professor Ian Butterworth for the opportunity to work with the High Energy Physics Group and the DESY directorate for their hospitality during my stay in Hamburg.

I have enjoyed working with the TASSO collaboration and thank everyone for their work in building and running the experiment (A complete list of the members is given in Appendix B). In particular I would like to thank Drs Steven Lloyd and Ray Beuselinck for all their help, Brian Foster for his advice and reading of this thesis and Julia Sedgbeer for providing the basis for the analysis presented in Chapter 9.

I especially thank Jenny Thomas for her friendship during the long and odd hours of the postgraduate high energy physics student.

Acknowledgement should also go to the Science and Engineering Research Council for financial support.

CONTENTS

LIST OF FIGURES

LIST OF TABLES

1.1 INTRODUCTION: E^+E^- COLLISIONS

For the last ten years investigation of e^+e^- annihilation processes has been the principal source of information on the basic interactions of leptons and quarks.

In 1γ annihilation (Fig 1.1) the system has the quantum numbers of the virtual photon:spin 1,negative parity, negative charge conjugation parity and zero values of the additive quantum numbers,baryon number,electric charge, lepton number and so forth.

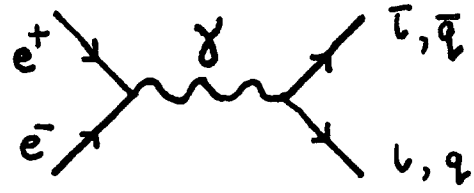

Figure 1.1:1γ annihilation

The differential cross-section for pair production of point-like spin 1/2 fermions,for an unpolarised beam is:

$$\frac{d\sigma(\vartheta)}{d\Omega} = \frac{\alpha^2.q^2.(1+\cos^2\vartheta).(3\beta-\beta^3)}{4s \qquad\qquad 2}$$

where:

q is the charge of the particle

βc its velocity

s the square of the centre of mass (CM) energy

α the fine structure constant

ϑ the angle between the incoming e^+ and outgoing $\bar{l}$ or $\bar{q}$ in the CM frame.

By integrating over ϑ the total cross-section is:

$$\sigma_t = \frac{4\pi q^2\alpha^2}{3s}.\ \frac{(3\beta-\beta^3)}{2} \qquad (1.1)$$

The β-factor, $(3\beta-\beta^3)/2$ represents the threshold behaviour associated with the pair production of spin 1/2 particles in an s-wave. By appropriate choice of charge q this formula can be applied to lepton,l, and quark,q,pair production.

The interference of the weak interaction quantum,the Z^0 boson can contribute to the cross-section (Fig 1.2),but at PETRA energies there is only a small effect because of the large mass of the Z^0.

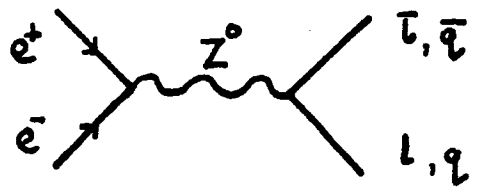

Figure 1.2:Z^0 Interference

The above formula does not apply to Bhabha scattering $e^+e^- \rightarrow e^+e^-$ where the space-like diagram (Fig 1.3) also contributes to the cross-section. Since this cross-section has a very large peak in the forward direction it is usually used as a luminosity monitor in e^+e^- annihilation.

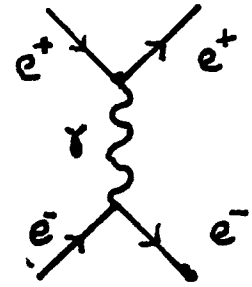

Figure 1.3:Bhabha Scattering

The energy of the produced pair is reduced by the 'radiative correction' diagram (Fig 1.4) which has a cross-section $\sim\alpha^3$.

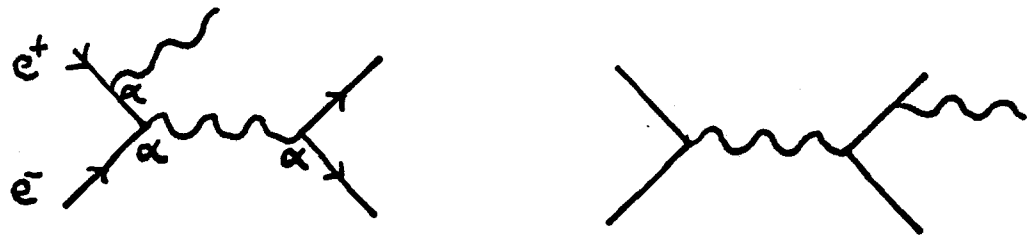

Figure 1.4:Radiative Corrections

The 2γ process $\sim\alpha^4$ (Fig 1.5) produces events with a small total energy in the produced system X and therefore leads to only a small background to the 1γ process.

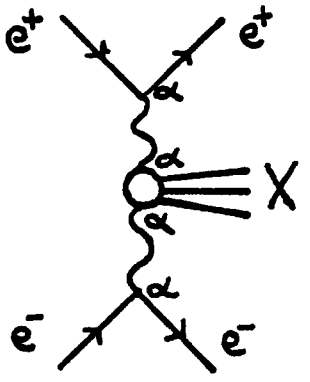

Figure 1.5:$\gamma\gamma$ Process

1.2 HADRONIC FINAL STATES-ONE PHOTON MECHANISM

Quark-antiquark pairs can be produced through the time-like diagram (Fig 1.1). From Equation 1.1 it can be seen that the ratio R of the total hadronic cross-section,σ_{tot},to the pair production cross-section $\sigma_{\mu\mu}$ is given by:

$$R = \sigma_{tot}/\sigma_{\mu\mu}$$

$$R = 3\sum e^2_q \quad ; \quad q=u,d,s,c,b$$

$$R = 3(4/9 + 1/9 + 1/9 + 4/9 + 1/9) = 11/3$$

provided the centre of mass energy is well above the threshold for the production of the bottom quark. The factor of 3 comes from the three colours of quarks required by Quantum Chromodynamics (QCD).

The production of hadrons in e^+e^- annihilation can be pictured as the production of $q\bar{q}$ pairs from the QCD vacuum in the colour field of the separating quark and antiquark. The hadrons cluster around the primary quark direction so that one observes two opposite jets of hadrons with a $(1+\cos^2\vartheta)$ distribution of the jet axis[1].

The candidate theory of hadron interactions,QCD,describes the binding of quarks by the exchange of gluons. At high energies (W~30GeV) the radiation of hard gluons can form an additional jet (Fig 1.6). Such three jet events have been observed[2]. The diagrams of Fig 1.6 lead to a correction to the total hadronic cross-section:

$$\sigma_{tot} = \sigma_{qq} + \sigma_{qqg} = \sigma_{qq}(1+\alpha_s/\pi)$$

where α_s is the strong coupling constant. The differential cross-section for hard vector gluon bremßtrahlung is given by:

$$\frac{d\sigma_{qqg}}{dx_1 dx_2} = \sigma_{qq} \cdot \frac{\alpha_s}{\pi} \cdot \frac{2}{3} \frac{(x^2_1+x^2_2)}{(1-x_1)(1-x_2)}$$

where $x_i=2E_i/E_{cm}$, the normalised energy of q and $\bar{q}$. This has been verified experimentally and demonstrates that the gluon has spin 1.

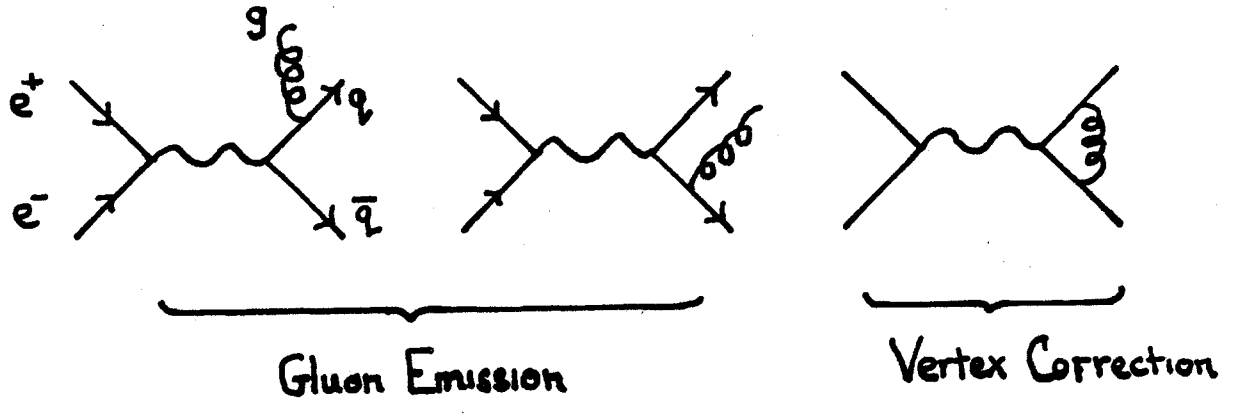

Figure 1.6:Hard Gluon Bremßtrahlung

1.3 GENERAL PROPERTIES OF HADRON PRODUCTION

Fig 1.7 shows the fraction of charged pions,kaons and nucleons in the final state at 34GeV[3]. At low momenta most of the charged hadrons produced are pions (>90% at p=0.4GeV/c). At higher momenta,kaon and $p,\bar{p}$ production become increasingly important:the pion fraction decreases smoothly to about 50% at 10GeV/c,while the $K^{\pm}$ and $p,\bar{p}$ fractions increase to about 30% and 20% respectively.

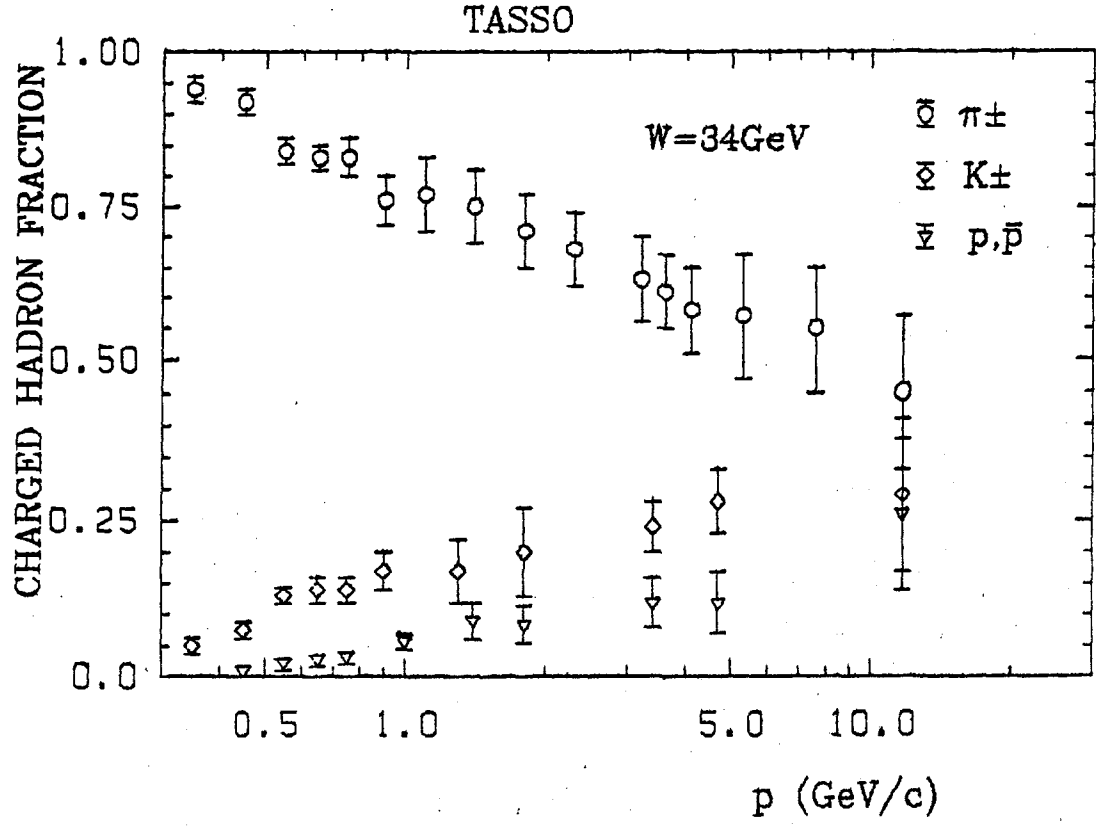

Figure 1.7

An event at W=34GeV contains on average:

10.3±0.4 $\pi^{\pm}$

2.0±0.2 $K^{\pm}$

1.6±0.1±0.2 $K^0,\bar{K}^0$

0.8±0.1 $p,\bar{p}$ (including $p,\bar{p}$ from $\Lambda,\bar{\Lambda}$ decay)

0.31±0.03±0.03 $\Lambda,\bar{\Lambda}$.

The majority of final state hadrons presumably result from the decay of heavier mass particles. From a measurement of inclusive ρ^0 production [4],assuming equal numbers of ρ^0,ρ^+, ρ^- one finds that roughly 30% of all charged pions result from ρ decay. About 25% of p,$\bar{p}$ result from Λ,$\bar{\Lambda}$ decay.

1.4 HADRON PRODUCTION MODELS

The process by which the quarks and gluons fragment into the observed hadrons are thought to be in principle describable by QCD. However the usual perturbative method of calculation, although it may be applicable to the initial quark fragmentation, cannot be used to calculate the complete process. In the absence of a calculable theory various phenomenological models have been constructed which simulate hadronic events. These computer models generate $q\bar{q}$ and $q\bar{q}g$ events, including initial and final state radiation,according to the above cross-sections. The various quarks are produced in the ratio of their charges (u:d:c:s:b as 4:1:4:1:1). The models differ in the algorithms used to fragment the quarks, antiquarks and gluons into further q,$\bar{q}$ and g particles and

recombine them to form the final state hadrons conserving energy-momentum,colour and flavour.

1.5 BARYON PRODUCTION

Baryon production in high energy e^+e^- annihilations is of interest because of the extra information it gives about the fragmentation process. The abundance of baryons,in particular at large momenta,is somewhat surprising. None of the most favoured models explain the large baryon yield in quark fragmentation nor the observation that gluons may produce more baryons[5].

1.5.1 Hoyer et al Monte Carlo

The Hoyer et al Monte Carlo program[6], describes hadron production by the chain decay model of Feynman and Field. The extension due to Meyer[6] includes baryon production by assuming that a quark cannot only pull a $q\bar{q}$ but also a diquark-antidiquark $(qq,\bar{q}\bar{q})$ out of the vacuum. The diquarks cannot be pointlike or they would give an extra contribution to σ_{tot} in disagreement with

observation. The important parameters (typical values are given in brakets) are:

1. α_s (=0.19) the strong coupling constant
2. The fragmentation function f(z) determines the fraction of the quark energy kept by the formed hadron (Fig 1.8):

$$f(z) = 1 - a_f + 3.a_f(1-z)^2$$

where $z = (p\|+E)_h \;/\; (p\|+E)_q$

and $p\|$ = momentum parallel to the jet axis.

a_f (=0.56) is assumed to be identical for u,d and s quarks. For the heavy quarks (c,b) either $a_f(c,b)=a_f$ or $a_f(c,b)=0$ may be used.

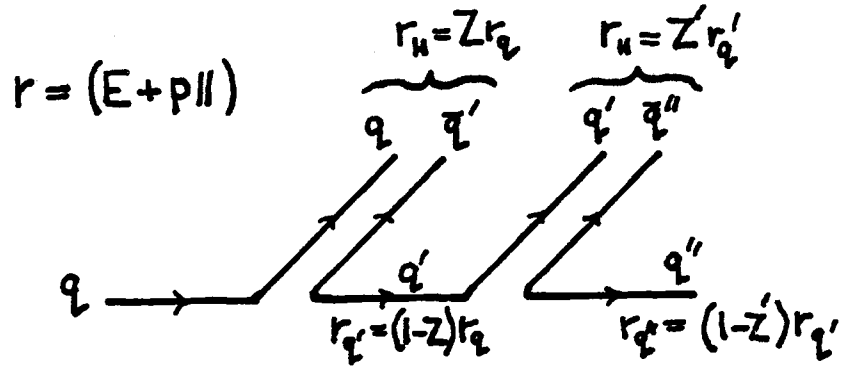

Figure 1.8

3. The quarks in the cascade are given a momentum component transverse to the direction of the primary quark according to a Gaussian probability function of width σ_q(=0.32GeV/c).
4. The formed hadrons are taken to be pseudoscalar mesons (P) or vector mesons (V) in the ratio P/(P+V) (=0.56).
5. Diquark-anti diquark pairs are formed rather than quark-antiquark pairs with probability FPAR (=0.075).

1.5.2 Lund Monte Carlo

In the Lund Monte Carlo jets are fragmented according to a string model. The Lund model also uses the diquark concept. The parameters in this model which are important for baryon production are:

1. p(qq)/p(q) (=0.075) diquark suppression
2. p(s)/p(u) (=0.3) strange quark suppression
3. {p(us)/p(ud)}/{p(s)/p(d)} (=0.2) extra suppression of strange diquark production compared to u or d pair production
4. 1/3 . $p(ud_1)/p(ud_0)$ (=0.05) suppression of spin 1 diquarks cf spin 0

5. (=1.0) extra suppression factor multiplying the ordinary SU(6) weight for spin 3/2 baryons and hence means to break SU(6) in addition to the dynamical breaking implied by (2),(3) and (4).

Chapter 9 presents a measurement of the inclusive production of $\Xi^-,\bar{\Xi}^-$ particles. These are S=-2,J=1/2 baryons with valence quark content ssd, $\bar{s}\bar{s}\bar{d}$. An upper limit is set on the production of $\Sigma^*(1385)$ particles. These are S=-1,J=3/2 baryons.

2.0 EXPERIMENTAL SETUP

2.1 INTRODUCTION

This chapter describes briefly the operation of the PETRA e^+e^- storage ring. A slanted description of the TASSO experiment is given-those components relevant to the subsequent chapters on track finding (Chapters 4,5,7,8) or to the physics analysis (Chapter 9) are described in depth while the other components are mentioned only briefly. Special chapters are devoted to descriptions of the cylindrical proportional chambers (Chapter 3) and the vertex detector (Chapter 6).

2.2 PETRA

The PETRA storage ring (Fig 2.1) consists of 8 bending magnet arrays ,4 long straight sections and 4 short straight sections encompassed by a 2.3km long pipe evacuated to 5.10^{-9} Torr.

Radio frequency accelerating cavities occupy the North and South long straight sections. Until 1983,64 cavities driven at 500kHz by 8 Klystrons of total power 4.5MW accelerated bunches of

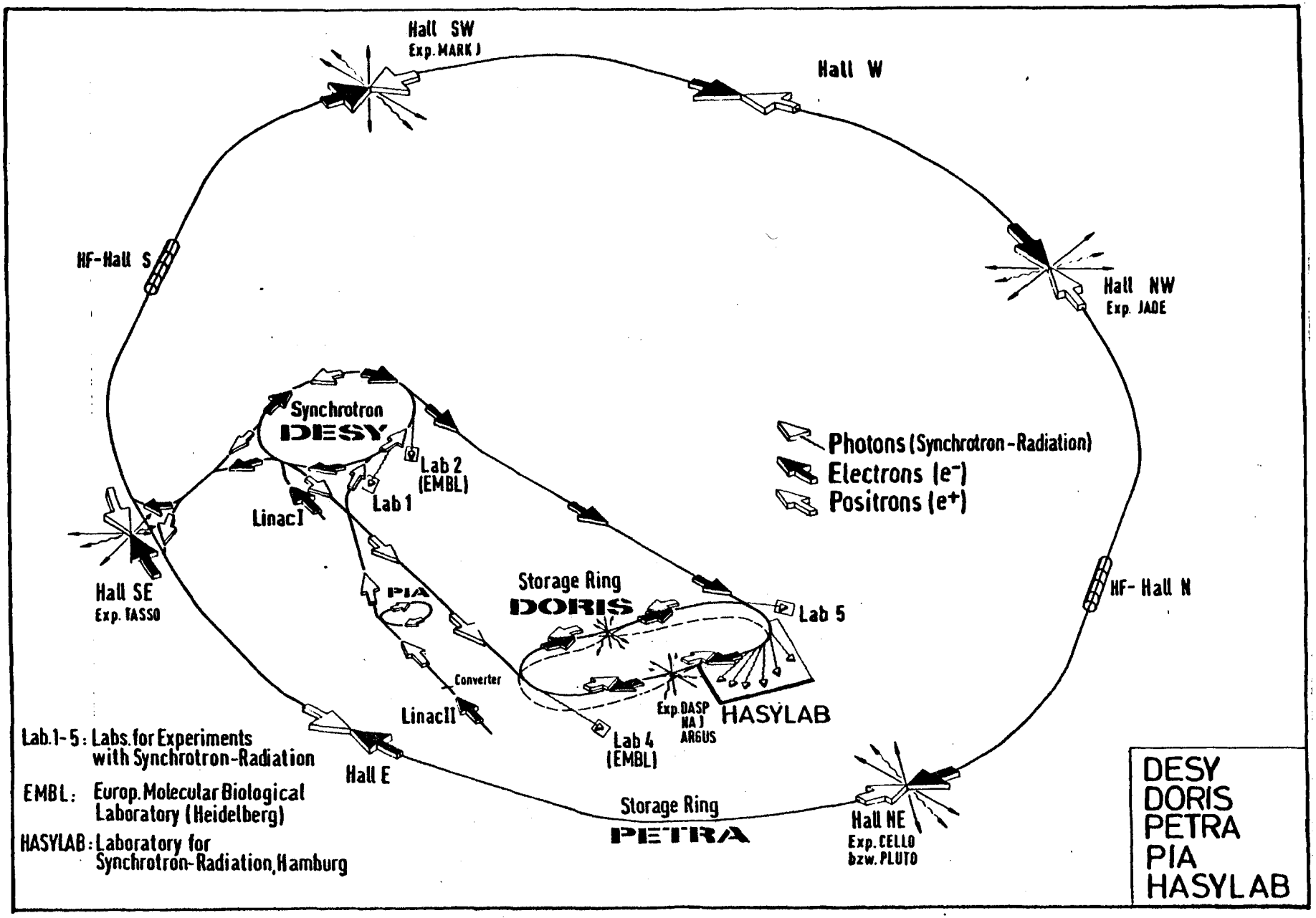
Hall SW
Exp. MARK J
Hall W
HF-Hall S
Hall NW
Exp. JADE
Synchrotron
DESY
Lab 2
(EMBL)
Lab 1
LinacI
Photons (Synchrotron-Radiation)
Electrons (e⁻)
Positrons (e⁺)
Hall SE
Exp. TASSO
PIA
Storage Ring
DORIS
Lab 5
HF- Hall N
Converter
LinacII
Exp. DASP
MARK J
ARGUS
HASYLAB
Lab 4
(EMBL)
Hall E
Storage Ring
PETRA
Hall NE
Exp. CELLO
bzw. PLUTO
Lab.1-5: Labs. for Experiments with Synchrotron-Radiation
EMBL: Europ. Molecular Biological Laboratory (Heidelberg)
HASYLAB: Laboratory for Synchrotron-Radiation, Hamburg
DESY
DORIS
PETRA
PIA
HASYLAB

Figure 2.1

electrons and positrons from 6.5GeV to a maximum energy of 18.3GeV. Electrons are injected from a linear accelerator into the storage ring DESY. Positrons are produced by directing electrons from the linear accelerator onto a target and are accumulated in the small storage ring PIA (Positron Intensity Accumulator) before transfer to DESY. DESY accelerates the bunches to 6.5GeV when they are transferred to PETRA. PETRA accelerates 2 bunches of positrons and 2 bunches of electrons and then maintains them at a constant energy against the energy loss due to synchrotron radiation. The e^+ and e^- bunches are made to collide nearly head-on at the 4 short straight sections where the resulting e^+e^- interactions are detected by the experiments. The bunches were typically 1.0cm in length,0.1cm in the plane of the ring and 0.01cm in the vertical. The momentum spread of the particles within a bunch due to synchrotron radiation emission was ~10MeV/c. At the start of a fill each bunch consisted of about $2.4.10^{11}$ particles giving a current of 5mA per bunch. In September 1982 extra accelerating cavities were installed so that by July 1983 a peak beam energy of 21.05 GeV was achieved.

2.3 MACHINE PERFORMANCE

The luminosity L gives the event rate N for a reaction of cross-section σ by: $N = L.\sigma$. The luminosity is related to the machine parameters by: $L = n^+.n^-.b.f/A$ where $n^+(n^-)$ are the numbers of positrons (electrons) per bunch,b is the number of bunches,f the rotation frequency,and A is the common geometrical cross-section of the bunches. A peak luminosity of $9.10^{-31}cm^{-2}s^{-1}$ was regularly achieved with a beam energy of 17GeV. This resulted in an integrated luminosity of $\sim 300nb^{-1}$ per day giving more than 100 events of the type $e^+e^- \rightarrow$ hadrons per day.

Fig 2.2 shows the observed luminosity at the TASSO interaction region from the beginning of operation in 1979 until the end of 1982.

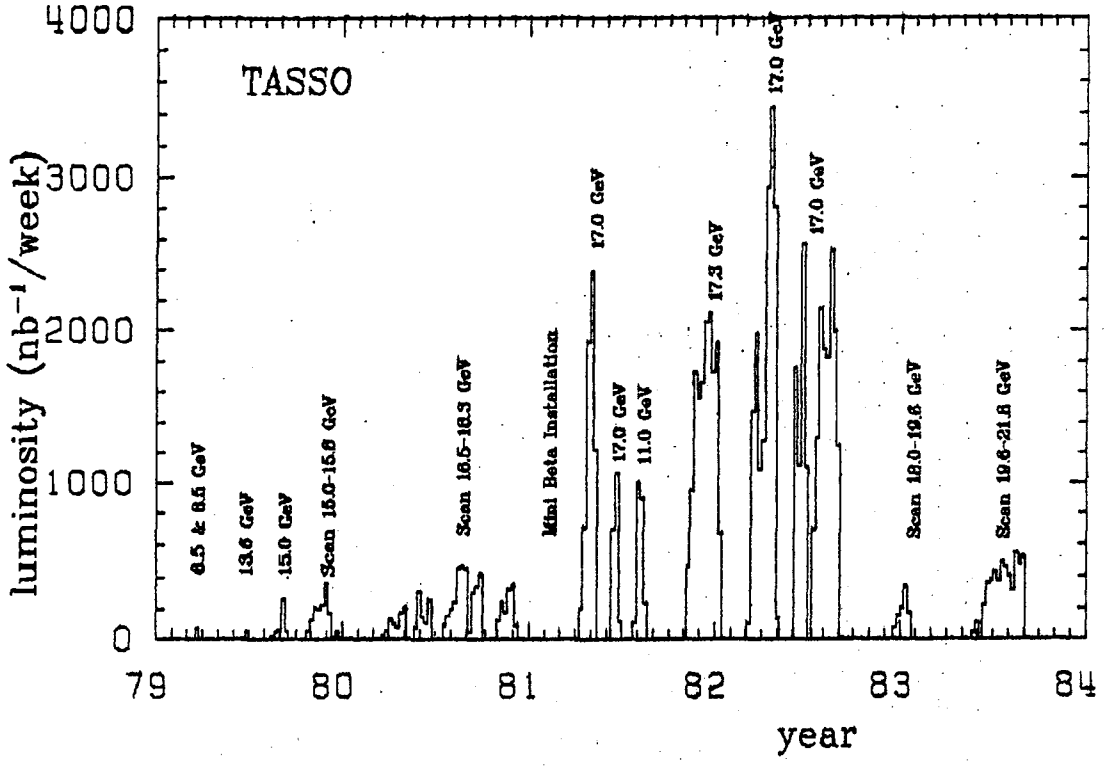

Figure 2.2

2.4 THE TASSO SPECTROMETER

In this section the components of the TASSO detector are described. Three views of the detector are shown in Fig 2.3.

A Cartesian coordinate system was defined:the momentum vector of the positron beam was taken as the z-axis,the x-axis was chosen to lie in the horizontal plane pointing towards the centre of the storage ring,the y-axis points vertically upwards (see Appendix A).

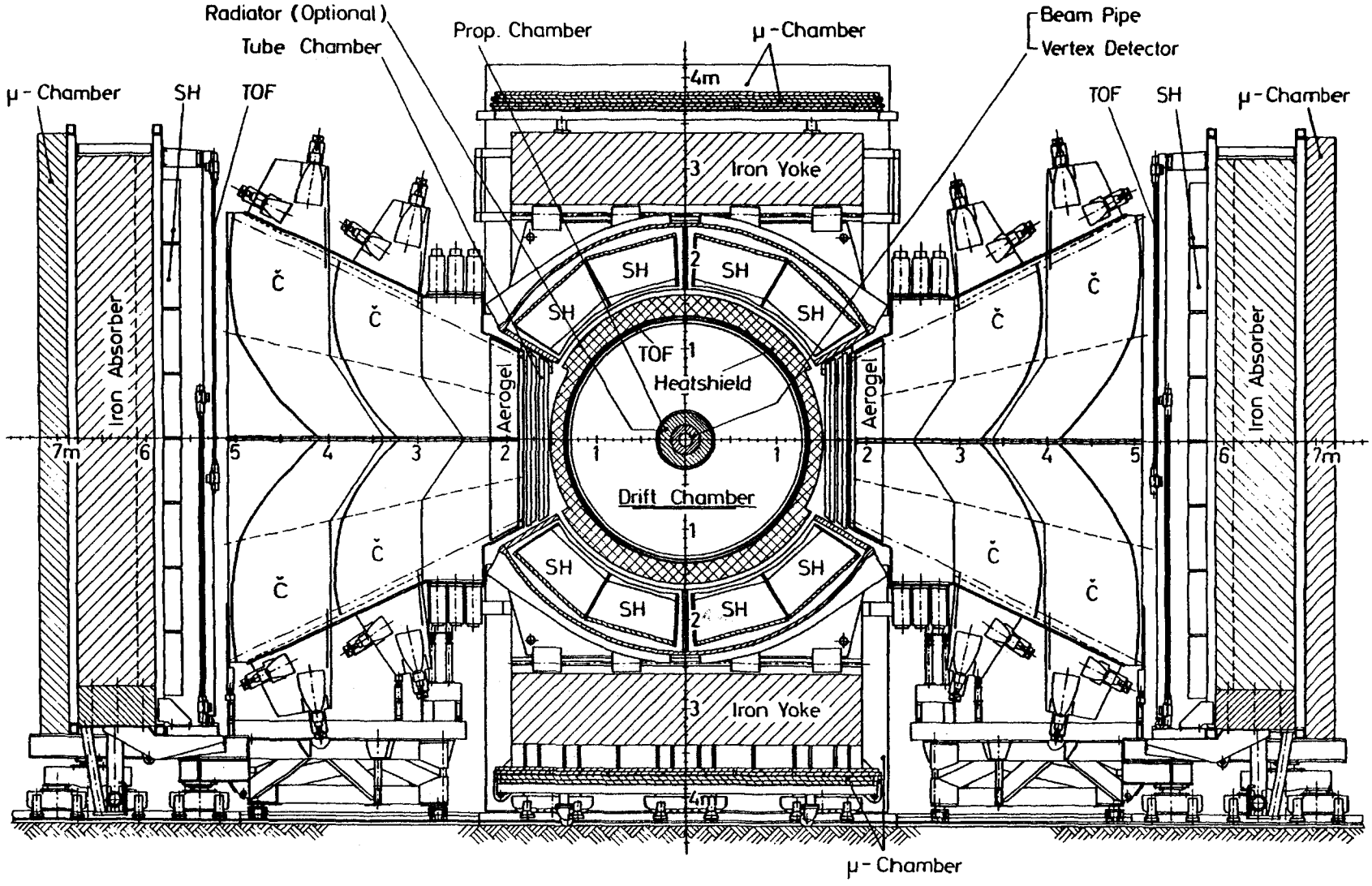
Radiator (Optional)
Tube Chamber
Prop. Chamber
μ-Chamber
Beam Pipe
Vertex Detector
μ-Chamber
SH
TOF
4m
Iron Yoke
TOF
SH
μ-Chamber
Iron Absorber
Č
SH
TOF
Heatshield
Aerogel
Drift Chamber
7m
6
5
4
3
2
1
Iron Yoke
4m
μ-Chamber
34953
TASSO

Figure 2.3a

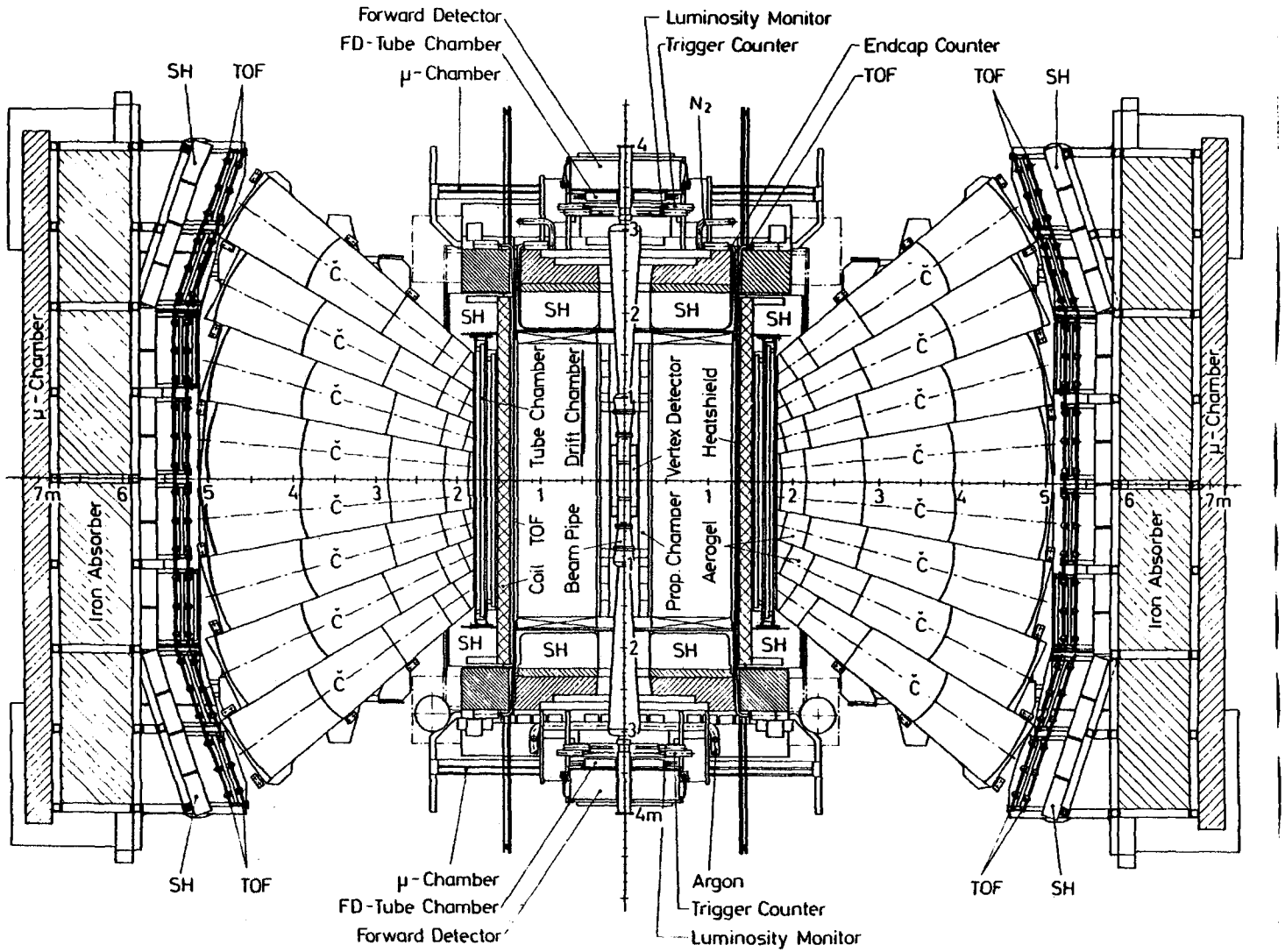
Forward Detector
FD-Tube Chamber
μ-Chamber
Luminosity Monitor
Trigger Counter
Endcap Counter
TOF
SH
N2
Tube Chamber
Drift Chamber
Vertex Detector
Heatshield
Coil
TOF
Beam Pipe
Prop. Chamber
Aerogel
Iron Absorber
Argon
TASSO
34980

Figure 2.3b

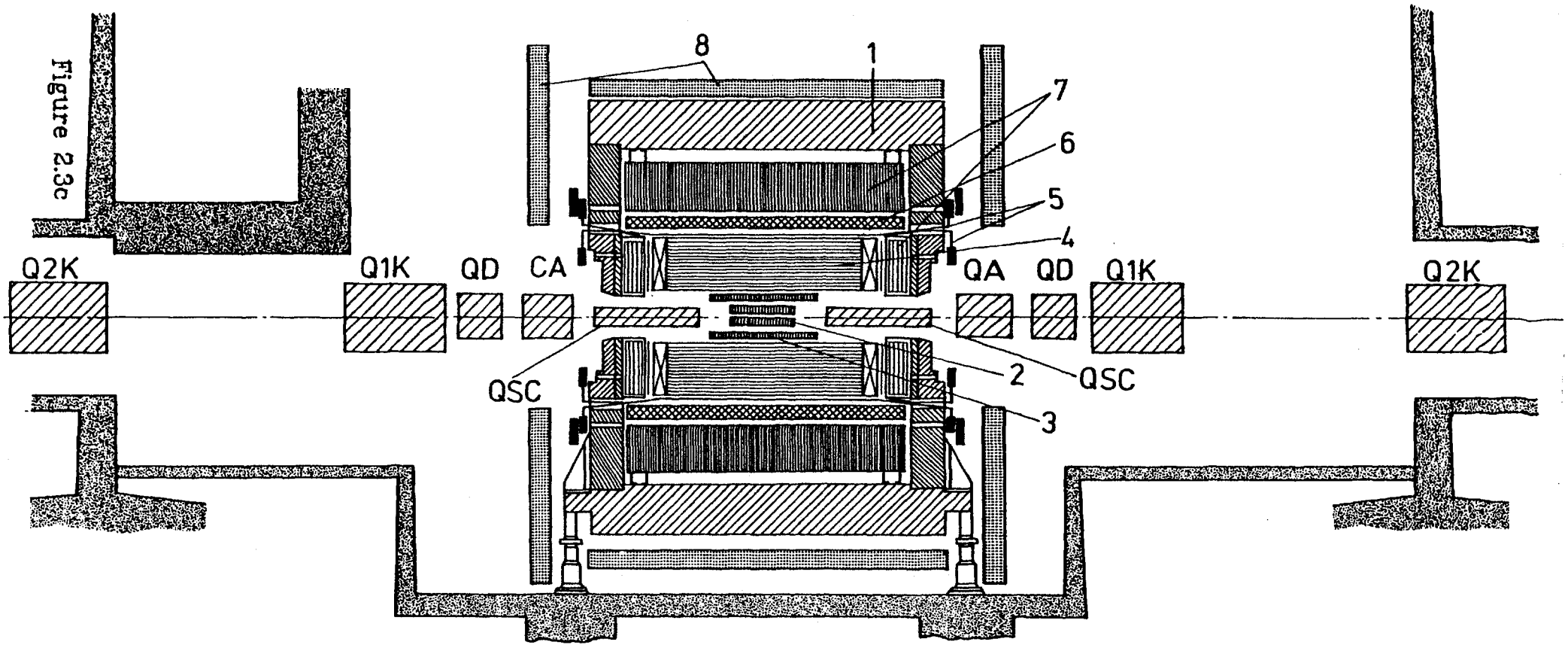

Figure 2.3c

TASSO
(Two Arm Spectrometer Solenoid)

Cut along beam

1 Magnet yoke
2 Vertexdetector
3 Proportional chamber
4 Drift chamber
5 TOF counter
6 Coil
7 LA calorimeter
8 Muon chamber

2.4.1 The Magnetic Solenoid

The momentum analyser of the detector was a thin walled, approximately one radiation length thick, conventional magnetic solenoid with an inner radius of 1.35m and a length of 4.4m. The magnet produced an axial magnetic field in the positive z direction with a maximum field of 4.93kG. The return yoke did not cover the whole azimuthal angle but consisted of iron plates 0.6cm thick at the top and bottom of the solenoid only. This permitted the introduction of large Čerenkov counters on each side. The uniformity of the solenoid field was sufficient that the path of charged particles could be described by simple helices.

2.4.2 The Large Volume Cylindrical Drift Chamber

The large cylindrical drift chamber[7] provides charged track detection and momentum measurement inside the coil. The chamber has 15 layers of drift cells between 36.7cm and 122.2cm from the interaction region,9 with sense wires parallel to the beam line (0°-wires) and 6 with wires at ~±4° (α-wires). The former allows

track reconstruction in the r-φ (x-y) plane and the latter allows track reconstruction in z (see Chapters 5 & 7).

The number of drift cells increases from 72 in the innermost plane to 240 in the outermost. All cells consist of one sense wire and six field wires and have the same dimensions:1.2cm in radial extent,3.2cm in azimuth (giving a maximum drift length of 1.6cm) and 320cm in length. The sense wires are 30μm gold plated tungsten wires and the potential wires 120μm gold plated molybdenum. A gas mixture of 50%Ar and 50%C_2H_6 resulted in operating voltages of +1.85kV for the sense wires and -0.62kV on the field wires. Since all cells are identical the voltages are common.

A wire efficiency of 96% including electronic failures was measured. The spatial resolution of 195μm gave a momentum resolution $\delta p_t/p_t=1.5\%p_t$.

In $\mu^+\mu^-$ pair events from the whole period an average of 0.61 noise hits per layer were observed. The crosstalk probability was 2.2% and the useful hit efficiency for track reconstruction 92.3%.

2.4.3 The Inner Time-of-Flight Counters

Inside the magnetic solenoid at a radius of 1.32m are 48 scintillation counters[8]. Each counter has dimensions 390*17*2cm and an attenuation length of 2m and is viewed by a photomultiplier tube at each end. The average counter efficiency was 98.7% per tube. The resolution varied from 270ps at each end to 450ps at the centre of the counter. This allowed the identification of electrons for momenta below 250MeV/c and, on a statistical basis, π/K separation up to 1.0GeV/c and (π-K)/p separation up to 1.4GeV/c.

2.4.4 Luminosity Monitor

The luminosity at the TASSO interaction region was measured by a system of counters designed to detect Bhabha scattering events at small forward angles, $25<\theta<115$mrad. These angles correspond to small momentum transfer by the virtual photon for which the validity of QED is well established. The luminosity monitor consists of 8 lead glass blocks in front of which are mounted scintillation acceptance counters with accurately surveyed positions.

2.4.5 Shower Counters

Outside the coil lead-liquid argon shower counters,LABC,cover the angular region $42°<\vartheta<138°$;φ:30°-150°, 210°-330°. These consist of 14 radiation lengths (14 X_0) of 0.2cm Pb plates separated by 0.5cm of argon. There are in total 5088 front towers,1248 back towers and 4592 strips for z,φ,and dE/dx measurement. The resolution achieved was:

$$\sigma_E/E = (0.11+0.02/(E-0.5))/\sqrt{E} \quad ,. \quad E>1.GeV$$

$$\sigma_\vartheta=\sigma_\varphi=2.mrad$$

At the ends of the large drift chamber are two endcap lead-liquid argon shower counters (LAEC). These cover $12°<\vartheta<30°$,$150°<\vartheta<168°$; φ:0-360° and consist of $12.6X_0$ of 0.2cm Pb with 0.3cm Ar filled gaps. There are 1444 front towers,872 back towers and 840 strips to localise energy deposits in r and φ.

2.4.6 Hadron Arms

For particle identification up to high momenta following the coil in the angular ranges $50°<\vartheta<130°$;$-26°<\varphi<26°$, $154°<\varphi 206°$ are 8 layers of planar drift chambers, 3 Čerenkov counters,followed by time-of-flight counters and lead-scintillator shower counters. The innermost Čerenkov counters consist of 32 cells of aerogel of refractive index n=1.024. They are followed by 64 cells of Freon 114 (n=1.0014,1atm.) and 64 cells of CO_2 (n=1.00043,1atm.) giving the threshold momenta (GeV/c):

	π	K	p
Aerogel	0.6	2.2	4.2
Freon 114	2.6	9.3	17.8
CO_2	4.8	16.8	32.0

2.4.7 Muon Detection

Muons were identified by 4 layers of proportional tube chambers $4*4cm^2$ positioned behind the magnet yoke (50-80cm Fe) and behind the hadron wall (87cm Fe).

2.5 EXPERIMENTAL TRIGGER

The experiment was designed to investigate the wide range of final states cited in Chapter 1. This required a complex trigger consisting of several independent trigger components OR'd together. Only the trigger designed to select beam crossings in which single photon annihilation to hadrons occurred will be described. This was used to enable the readout of all the detector components for the events analysed in Chapter 9.

2.5.1 Trigger Hardware

The proportional chamber processors (CPC processors) are described in Chapter 3.

The drift chamber processor (DC PREPRO) is the major trigger element. The CPC 48-bits from the CPC anode processor (see §3.10.1) indicate coincidences between the hits on the 4 proportional chambers in 48 φ sectors. The CPC 48-bits, the 48 ITOF mean timer bits and information from 6 of the 9 0° layers of the drift chamber are input. The drift chamber hits are OR'd into sectors

for each layer; a sector being one cell wide for the innermost layer. Track elements are defined as having hits in at least 5 out of the 6 layers and satisfying 1 of 15 curvature masks which correspond to different transverse momenta,p_T. A DC Prepro track requires one track element, the corresponding CPC 48-bit and ITOF mean timer bit (to within ±1 bit of the track extrapolation). The event multiplicity is defined by the number of mean timers set with consistent tracks.

2.6 DATA ACQUISITION SYSTEM.

A detailed description is given in [9]. Here only a brief review will be given of the data acquisition system and the online checks it performs.

The data acquisition and experiment monitoring are performed by a Norsk Data NORD 10/S computer. On receiving a valid trigger, data from the experiment's components are read in via a CAMAC system and reformatted for transfer to the main DESY IBM computer. Approximately 5 events can be stored in the NORD memory (an event is typically 2500 words long). The data are first output to a

local buffer disc and then transferred to a 100 Mbyte disc on the IBM via a microprocessor link. When the disc is full its contents are dumped to a 6250 bpi tape (called a dumptape).

The input rate to the NORD is typically 2-3 Hz and the deadtime is ~8%. Data taking is divided into runs; each run usually corresponding to a PETRA filling and lasting ~2-4 hours. At the start and end of each run there are also calibration runs for several devices. During data taking the experiment is monitored in several different ways:

- for each component several quantities are histogrammed (e.g. wire hits, TDC and ADC distributions) for ≈10% of all events,
- events can be displayed on a colour display,
- most components have monitors of high voltage and gas flows which either give an audible alarm or interrupt the experiment when there is a fault,
- several components also have checking programs that monitor the data taken by them,
- at the end of each run a run summary is output showing trigger rates and a selection of the histograms.

All components are also checked offline at different stages of the analysis. The performance of PETRA is monitored by measuring the luminosity online and also by the background rate in the ITOF.

2.7 HADRONIC FINAL STATE SELECTION

The fast track recognition program FOREST (see Chapter 5) is applied to all triggers (PASS 1). Certain triggers are selected and written to PASS 2 tapes. The selection of hadronic final states proceeds in two further stages called PASS 3 and PASS 4. Events satisfying the selection criteria for PASS 3 are run through the MILL program (see Chapter 5) to provide the final track reconstruction and written to a PASS 3 tape. The final hadronic sample is then selected from these events and is written to the PASS 4 dataset.

2.7.1 PASS 3

The triggered events are input and the following selection criteria are applied :

- $\geq$ 3 tracks reconstructed in the (r-φ) plane with $|d_0| < 2.5$ cm,
- $\geq$ 2 tracks reconstructed in 3-dimensions with $|d_0| < 2.5$ cm and $|z_0| < 15.0$ cm.

Where d_0 is the distance of closest approach of the track to the origin in the r-φ plane and z_0 is the distance of the track from the origin along the z-axis.

2.7.2 PASS 4

In order to separate one photon induced hadronic final states from the remaining background of beam-gas scattering, beam-pipe interactions, tau pair events ($e^+e^- \rightarrow \tau^+\tau^-$), Bhabha scattering events where one or both of the final state leptons has interacted, and two photon scattering events tighter selection criteria must be applied. Good tracks are first selected as follows:

1. The track must be reconstructed in 3-dimensions,

2. $\chi^2 \leq 10$ per d.o.f. for (r-φ) fit,

   $\chi^2 \leq 20$ per d.o.f. for (s-z) fit,

3. $|d_0| < 5.0$ cm,

4. $p_T > 0.1$ GeV/c,

5. $|\cos\vartheta| < 0.87$,

6. $|z_0 - \langle z_0 \rangle| < 20.0$ cm, where $\langle z_0 \rangle$ is the average value of z_0 for those tracks satisfying tests (1)-(5).

These cuts remove spurious tracks, very low momentum tracks and tracks which did not cross the sixth 0° layer of the drift chamber. (In order to be reconstructed a track must have at least five drift chamber hits associated with it).

Using these good tracks the following selection criteria are applied to the whole event:

1. ≥ 4 tracks if $W \leq 13$ GeV,

   ≥ 5 tracks if $W > 13$ GeV.

---

[1] The sphericity axis is defined as the axis which minimises $\sum_{ij} p_T^i \cdot p_T^j$ where the sum is over all the "good" tracks in the event.

2. The event is divided into two hemispheres by the plane perpendicular to the sphericity axis.[1]

   If $W \leq 16$ GeV and there are three tracks in one hemisphere and one in the other,

   or $W > 16$ GeV and there are three tracks in each hemisphere, the mass of the three prong system must be ≥ 1.78 GeV (the mass of the tau).

3. $\langle z_0 \rangle \leq 6$ cm where $\langle z_0 \rangle$ is the average value of z_0 for all the good tracks.

4. If $W < 16$ GeV the total charge of the tracks must be less than four and there must be at least one track in each hemisphere defined by the (r-φ) plane.

5. $\sum_i |p_t| \geq 0.265 \cdot W$ where p_t is the momentum of each track and the sum is over all good tracks.

Criterion (1) removes low multiplicity background, (2) removes tau pair events, (3) and (4) remove most of the remaining beam-gas and beam-pipe interactions and (5) removes high multiplicity two photon scattering events. The final data sample is then scanned to remove interacting Bhabha events and the remaining background from all sources is estimated to be $(3.0 \pm 1.7)\%$ [10].

3.0 THE CPC :CYLINDRICAL PROPORTIONAL CHAMBER

3.1 INTRODUCTION

This chapter describes the cylindrical multiwire proportional chamber (CPC) developed and built by Imperial College and the Rutherford Laboratory,and its hardware track recognition processors used as part of the experimental trigger. The author was involved in the day to day checking and maintenance of this hardware. New results on the performance of the cathode strips is presented. The hardware track recognition processors have been described in more detail previously[12].

3.2 DESIGN REQUIREMENTS

The CPC was designed principally for use in the experimental trigger. A multiwire proportional chamber was chosen because the background close to the interaction region was expected to be high. A proportional chamber would be able to withstand these conditions and would allow a fast estimate of the z vertex of events using cathode strips. A dedicated hardware processor for the anode wires could recognise tracks originating from the beam axis

within 900ns of the beam pickup strobe,and could therefore be used in the pretrigger as the time between bunch crossings,with 4 bunch operation of PETRA would be 1.92μs and a 1μs time is required to reset all components. Low mass construction was required to minimise the number of photons converting within the material of the chamber, multiple scattering and the absorption of particles.

3.3 PRINCIPLE OF OPERATION

The proportional chamber detects the passage of charged particles by collecting the ionisation they produce in the chamber gas. An electric field obtained by grounding the anode wires and applying a negative potential,typically -4kV to the cathode strips, produces secondary ionisation through the collision of accelerated electrons with atoms of the chamber gas. The avalanche in the high field near the anode wires produces amplification ,and the measured current on the anode wires is proportional to the number of primary ionisation electrons. The remaining positive ion cloud induces a charge on the adjacent cathode strips.

3.4 GENERAL DESCRIPTION

The important dimensions of the 4 proportional chambers are listed in Table 3.1.

		Radius (cm)	# chan-nels	Orient-ation (°)	Strip Width (mm)	Separ-ation (mm)
1	I.C	18.02	120	-36.5	6.30	1.26
	A	18.72	480	0.0	-	2.5
	O.C	19.42	120	+36.5	6.97	1.36
2	I.C	21.07	120	-36.5	7.37	1.47
	A	21.77	480	0.0	-	2.8
	O.C	22.97	120	+36.5	7.86	1.57
3	I.C	24.13	120	-36.5	8.44	1.70
	A	24.83	480	0.0	-	3.3
	O.C	25.53	120	+36.5	8.93	1.79
4	I.C	27.18	120	-36.5	9.51	1.90
	A	27.88	480	0.0	-	3.7
	O.C	28.58	120	+36.5	10.00	2.00

I.C ≡ Inner Cathode; A ≡ Anode; O.C ≡ Outer Cathode

TABLE 3.1 Principal Dimensions of CPC

The chambers are concentric with one another and with the beam axis. Each chamber consists of 480 equally spaced wires running parallel to the beam axis and 120 inner and 120 outer cathode strips which form helices about the beam axis with a rake angle of 36.5°,the inner and outer layers having opposite sense of rotation. The anode wires from layer to layer are approximately aligned in azimuthal angle. This aids greatly the pattern recognition task as tracks of high momentum originating from the interaction region fire corresponding wires on each chamber. The wires are 20μm diameter,gold plated tungsten strung at a tension of 50g/cm^2 and glued to nonconducting supports at both ends of the chamber. The wire separation was maintained against electrostatic instability by two plastic support rings of 5mm thickness glued to the inner cathode cylinder and extending to the anode radius. These supports were positioned at z=±30cm from the centre of the chamber. Their presence produced a local distortion in the electric field which was corrected by applying an appropriate voltage to an insulated conducting wire attached to each support.

The 4 closed chamber volumes were defined by 5 cylindrical shells of expanded styrafoam sealed with rubber 'o' rings to the

aluminium endrings. The copper cathode strips were formed on 1.9mm thick Kapton sheets by a photographic process. These sheets were then formed into cylinders and bonded to the styrafoam shells.

3.5 GAS SUPPLY

The gas rig supplied ~15l/hour of 'magic' gas mixture to the chamber,resulting in a complete change of gas every 8 hours. The gas was composed of 75% Ar as the basic ionisable medium,25% isobutane,to limit the ultraviolet transmittance which could enable a large spatial spread of the ionisation,0.25% Freon to quench the ionisation by absorbing electrons and a small amount of methyal to prevent polymerisation of the isobutane.

3.6 CHAMBER ELECTRONICS

A schematic diagram of the anode and cathode readout electronics is given in Fig 3.1.

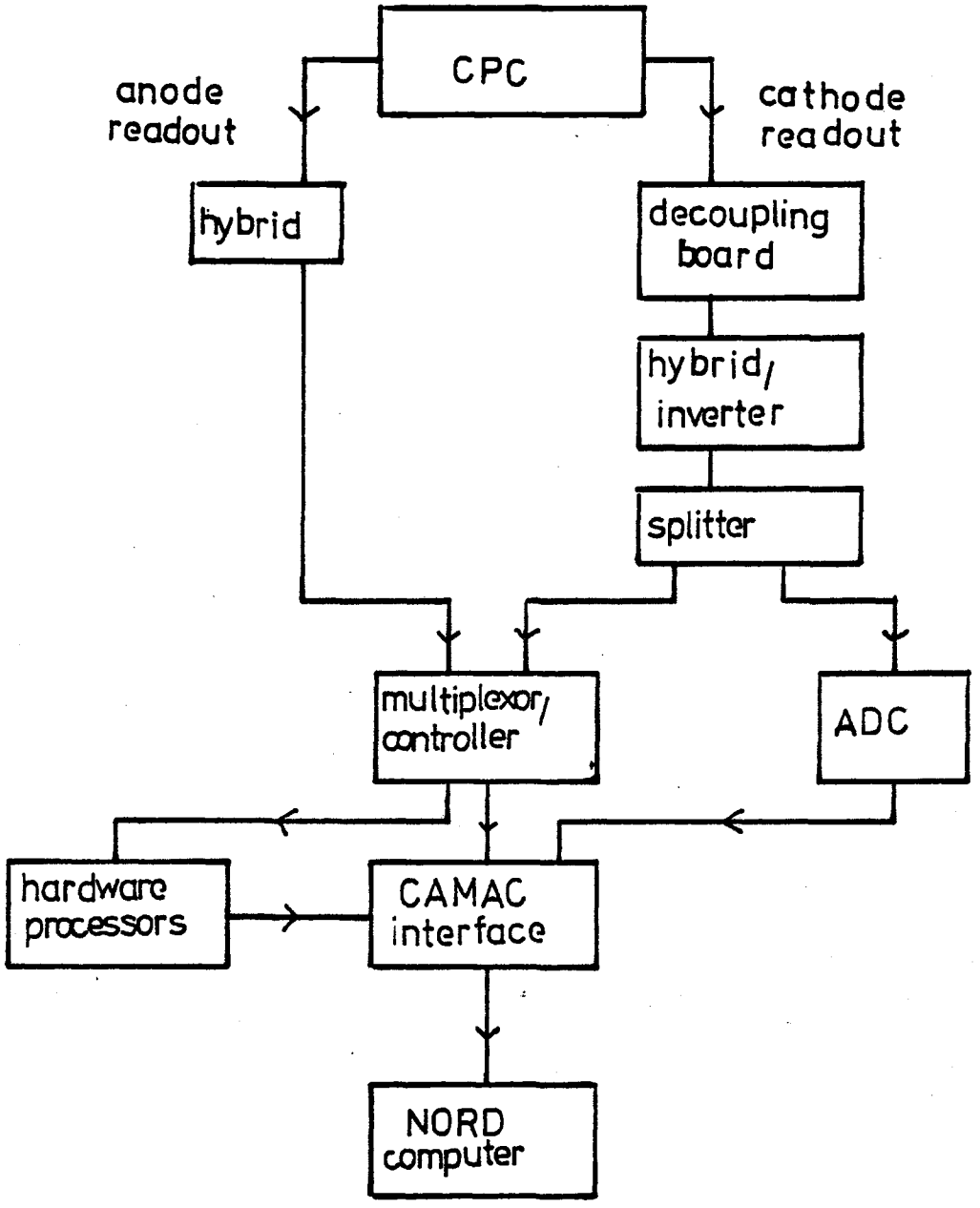

Figure 3.1 Anode and Cathode Readout

Chamber signals travel along some 3m of 50Ω coaxial cable to hybrid thick film discriminators. To allow anode and cathode electronics to be as similar as possible the cathode signals were first amplified and inverted before proceeding to the discriminators. These discriminators produced 50ns output pulses for input signals above the externally set thresholds (500μV for the anodes and 100μV for the cathodes). These pulses were passed along twisted pair cables to the multiplexor modules,which set latches when input pulses were received in coincidence with a gate signal derived from the beam pickup strobe. The multiplexor controllers provided the online computer with a list of addresses of the hit wires. This method of data transfer is very efficient for low multiplicity events,in that only the addresses of hit wires are readout. However for high multiplicity events it is disadvantageous. To reduce the demand on the online computer it is planned to read the multiplexors using a microprocessor and to output a list of wire clusters. The data will be output as a list of first hit wire in cluster and number of consecutive hit wires. This format requires considerably fewer words for high multiplicity events and so facilitates data transfer and reduces data storage requirements. The cathode signals were in addition split before their input to the multiplexors and supplied to analogue-to-digital converters (ADCs). These ADCs

provided digital pulse heights for all channels above threshold. Cadas CPU modules corrected these pulse heights for individual channel variations in the ADCs before supplying pulse height,wire address combinations to the online computer.

3.7 THE ALIGNMENT OF THE CPC

The alignment of the CPC within the large drift chamber was determined by studying two-prong and cosmic ray events. This was necessary due to the difficulty of surveying the CPC when installed in situ within the large drift chamber.

To find the displacement in the x-y plane of the centre of the CPC the difference $\Delta\varphi$ between φ_{DC},the φ of the projected track from the drift chamber and φ_{CPC} the φ of the hit anode wire was plotted as a function of φ_{DC}. The displacement x,y required to correct φ_{CPC} so that $\Delta\varphi=\varphi_{CPC}-\varphi_{DC}$ showed no dependence on φ_{DC} gives the true chamber displacement. This was found to be:

POSITION OF CPC

x_{centre} = -2.4±0.1mm

y_{centre} = -0.0±0.1mm

To avoid systematic errors when the z position of a track was computed from the cathode strip clusters two corrections were necessary because of the non-zero displacement of the x-y centre of the CPC (see Fig 3.2).

1. The arc length s along the track from its point of closest approach to the origin of coordinates to its intersection with the anode cylinder is given by

$$s = RO.\left[\cos^{-1}\left\{LO^2+RO^2-R^2/(2.LO.RO)\right\}\right.$$
$$\left.+SIG.\sin^{-1}\left\{(DX\vec{O}\times X\vec{R})_3/(RO-DO)\right\}\right]$$

where $DX\vec{O} = X\vec{R}-DXPR\vec{P}$

$X\vec{R}$ = centre of track circle
$DXPR\vec{P}$=centre of CPC
RO = track circle radius
R = anode cylinder radius
SIG = geometrical sign of track
DO = DO of track

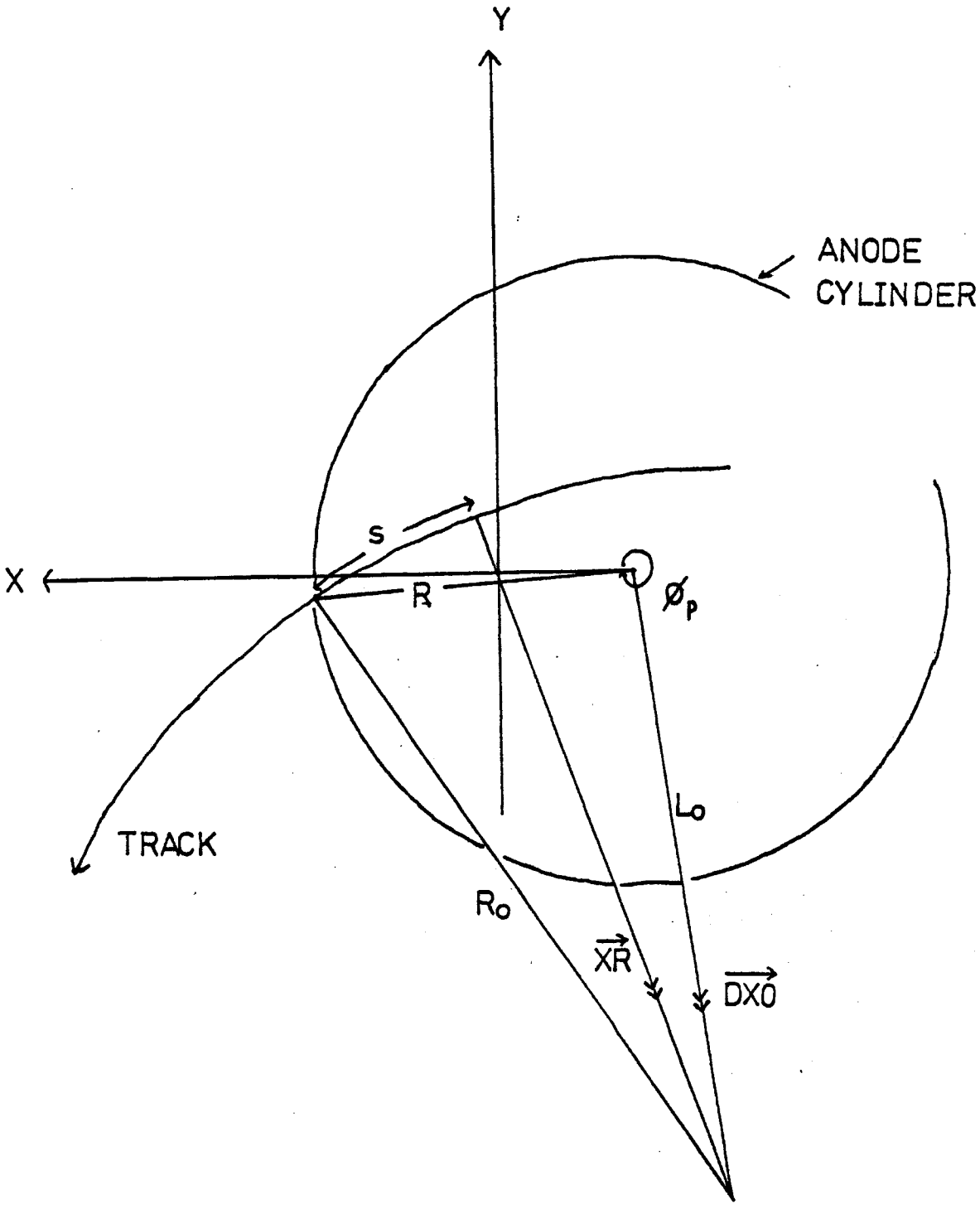
Y
ANODE
CYLINDER
X
s
R
ϕ_p
L_o
TRACK
R_o
$\overrightarrow{XR}$
$\overrightarrow{DXO}$

Figure 3.2

2. φ_p the φ angle of the track at the corresponding anode cylinder radius must be computed with respect to the centre of the CPC rather than with respect to the centre of the drift chamber:

$$\varphi_p=\varphi_0-SIG.\sin^{-1}\left\{(R^2+LO^2+RO^2)/(2.R.LO)\right\}$$
$$-SIG.\sin^{-1}\left\{(DX\vec{O}\times X\vec{R})_3/(RO-DO)\right\}$$

where LO is the separation of the origin of CPC and centre of the track circle

The effect of this correction is shown (Fig 3.3) in the variation of the mean of $\tan\lambda_1+\tan\lambda_2$ with φ_1 where λ_1, λ_2 are the reconstructed dip angles of the tracks from Bhabha events when the CPC cathodes are included with the drift chamber α-wires in the fit (subscript 1 refers to the track of more positive $\tan\lambda$).

Fig 3.3 shows the variation before before correction. To understand this consider a 2-prong in the x-z plane,then s≡ x (Fig 3.4).

Since the CPC is shifted in the negative x direction,the track sloping to positive x is assigned cathode s values which are too small,and the other track s values which are too large. This results in z values being shifted towards the centre of the CPC,

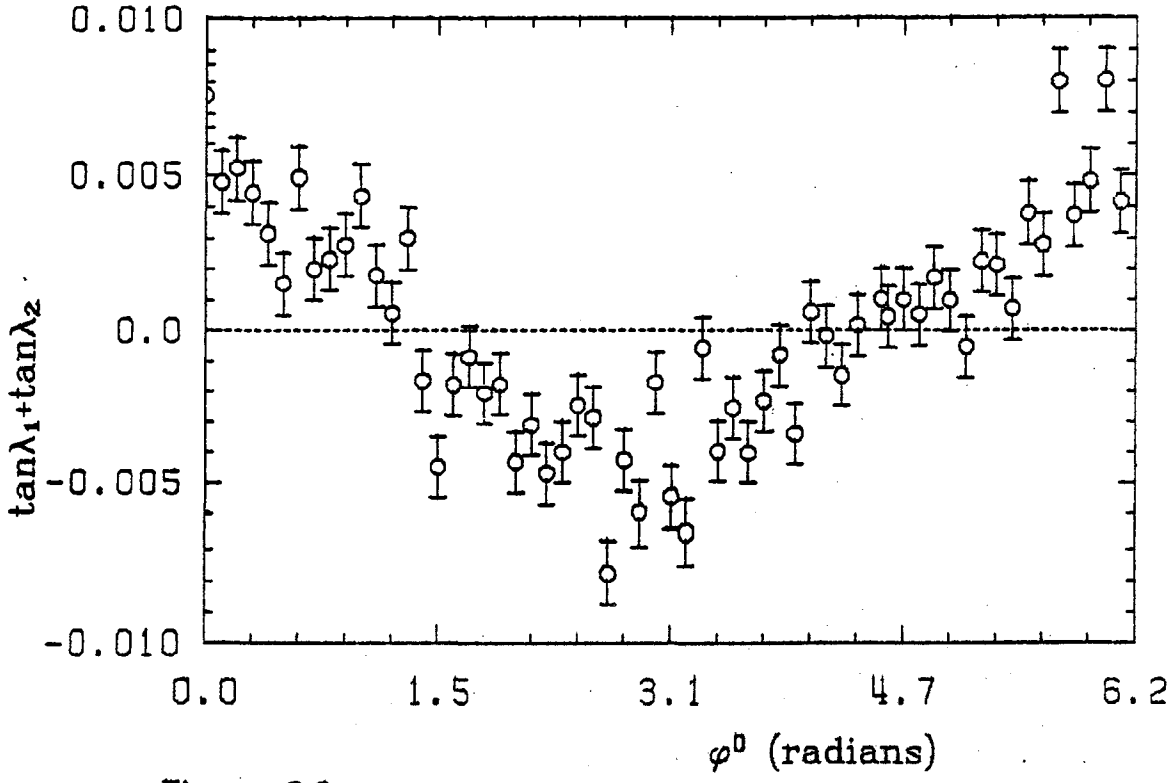

Figure 3.3

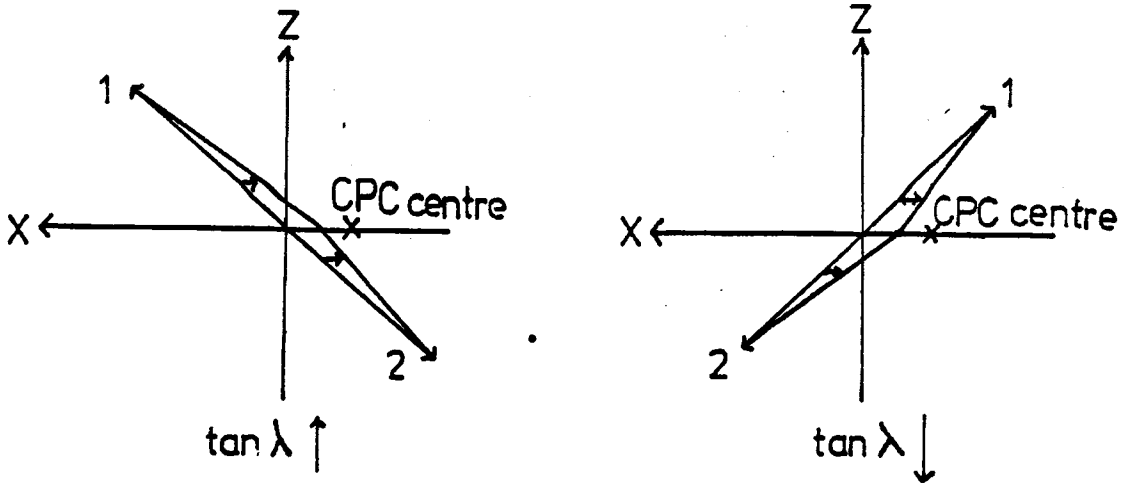

Figure 3.4

causing an increase (decrease) in $\tan\lambda_1$ and $\tan\lambda_2$ if track 1 is in the positve (negative) x direction.

3.8 ALIGNMENT IN Z AND DETERMINATION OF Z FROM CATHODE HITS

For a given track circle in r-φ and a given cathode cluster centre the z position of the track at the anode cylinder is given by:

$$z=\left[120.N_i/(2\pi)-\varphi_p+f_i-\left\{152.\tan(36.5°)/2/R_i + 16.5\pi/180\right\}.\alpha_i/|\alpha_i|\right].$$
$$R_i/\tan\alpha_i$$

where N_i is cathode cluster centre in terms of hardware strip number $0 \leq N_i < 120$.

φ_p φ of track at anode cylinder wrt centre of CPC

f_i constant to be determined for each cathode plane i

R_i radius of cathode cylinder i

α_i rake angle of the cathode strip

The alignment and geometry of the chamber was checked as follows. The cathode cluster peaks were used in a straight line fit in the s-z plane together with the drift chamber α-wire hits for tracks from Bhabha events. The offset f_i for each cathode plane

was determined by adjustment so that the mean residual ($z_{reconstructed}-z_{measured}$) for each plane was zero,and the mean sum of the tangent of the track dip angles of the two tracks in an event was zero. The offsets f_i correct for the true z position of the CPC and for the rotations of the cathode cylinders. If the f_i resulted from just a z-shift and a rotation of the CPC as a whole then they would be related by

$$f_i.\alpha_i/|\alpha_i| = \varphi_{rot}-z_{shift}|\tan(\alpha)|/R_i$$

Fig 3.5 shows a plot of $f_i\alpha/|\alpha_i|$ against $1/R_i$. This suggest that planes 1,2,4,5,8 obey the above relation with φ_{rot}=0.025 radians and z_{shift}=-1.30cm. This would put the z position of the cathode read-out at -(74.825+1.30) =-76.1cm,and the start of the cathode readout at φ=±15.1°, or about half a strip width from the nominal value ±16.5°. Planes 3,6,7 appear to be rotated by about 5.10^{-3} radians with respect to the others. During the installation of the vertex detector the CPC position was accidentally changed to -75.1cm.

The rake angle α of the cathode strips was determined by observing the variation of the mean ($z_0.\tan\lambda/|\tan\lambda|$) with $\tan\lambda$,where z_0 is the z of the closest point of approach to the origin

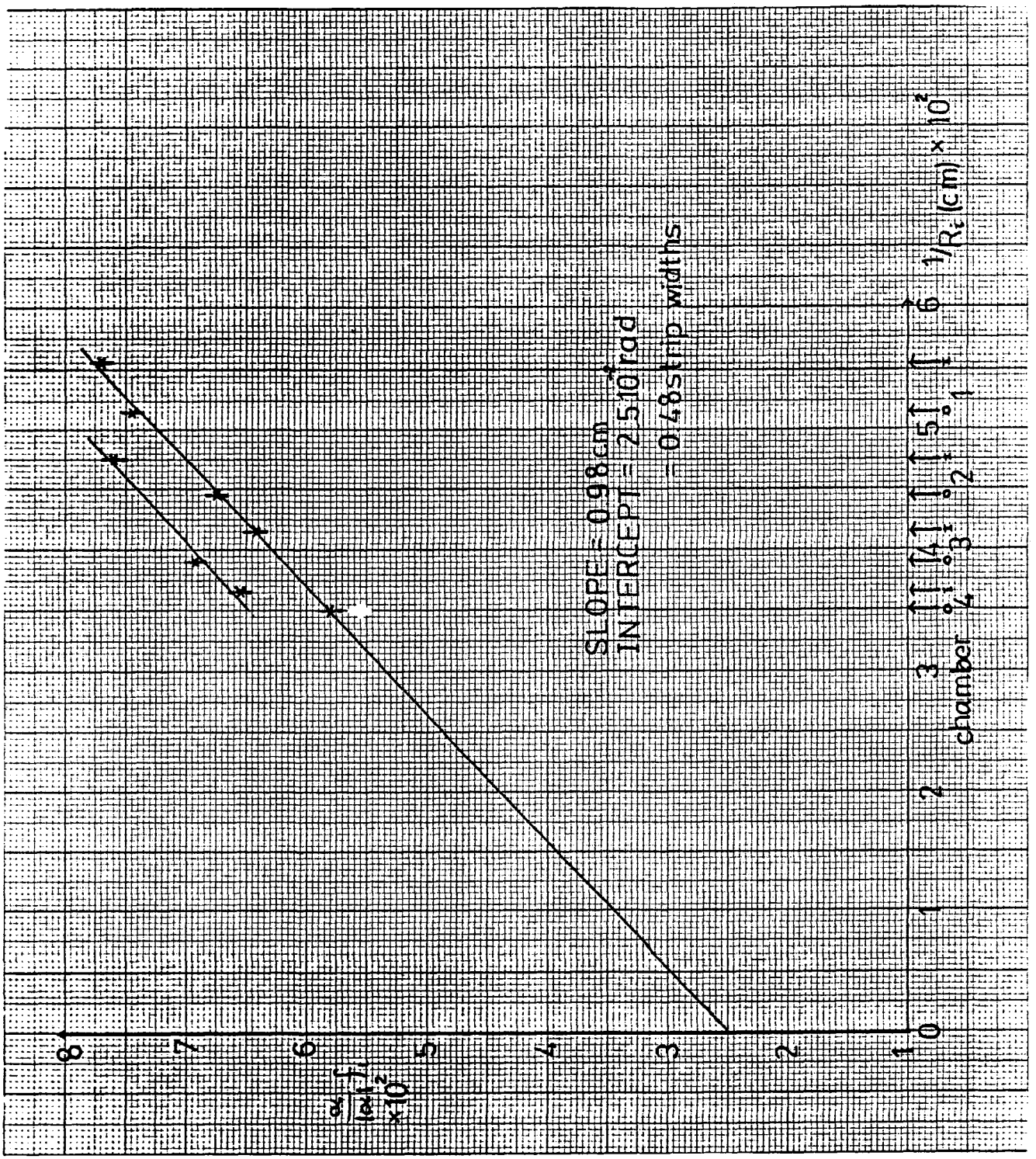
SLOPE = 0.98 cm
INTERCEPT = 2.5 10⁻³ rad
= 0.48 strip widths
chamber
1/R_i (cm) x 10²
d_i |d_i - f_i|
x10²

Figure 3.5

in x-y and λ the dip angle. If α is set incorrectly low cathode z points are shifted away from z=0 so that tracks with a positive (negative) dip angle will result in a z_0 shifted to positive (negative) z. Fig 3.6 shows the variation of the mean of the difference $z0_1$-$z0_2$ (1 refers to the track of more positive tanλ) with α. It is seen that the mean $z0_1$-$z0_2$ = 0 for α = 36.55±.05° in agreement with the design value α = 36.5°.

3.9 CPC EFFICIENCY AND RESOLUTION

3.9.1 Anodes

The efficiency of the anode wires was typically 98%. This was measured by extrapolation of tracks reconstructed in the large drift chamber and was carefully monitored during datataking.

The resolution of the anode hits is determined by the spatial separation of the wires and the cluster size. The inclusion of the anode wire hits in the track fit improved the resolution $\delta p_t/p_t$ from 1.5%p_t measured with the drift chamber to 1.4%p_t for $\mu^+\mu^-$ pairs.

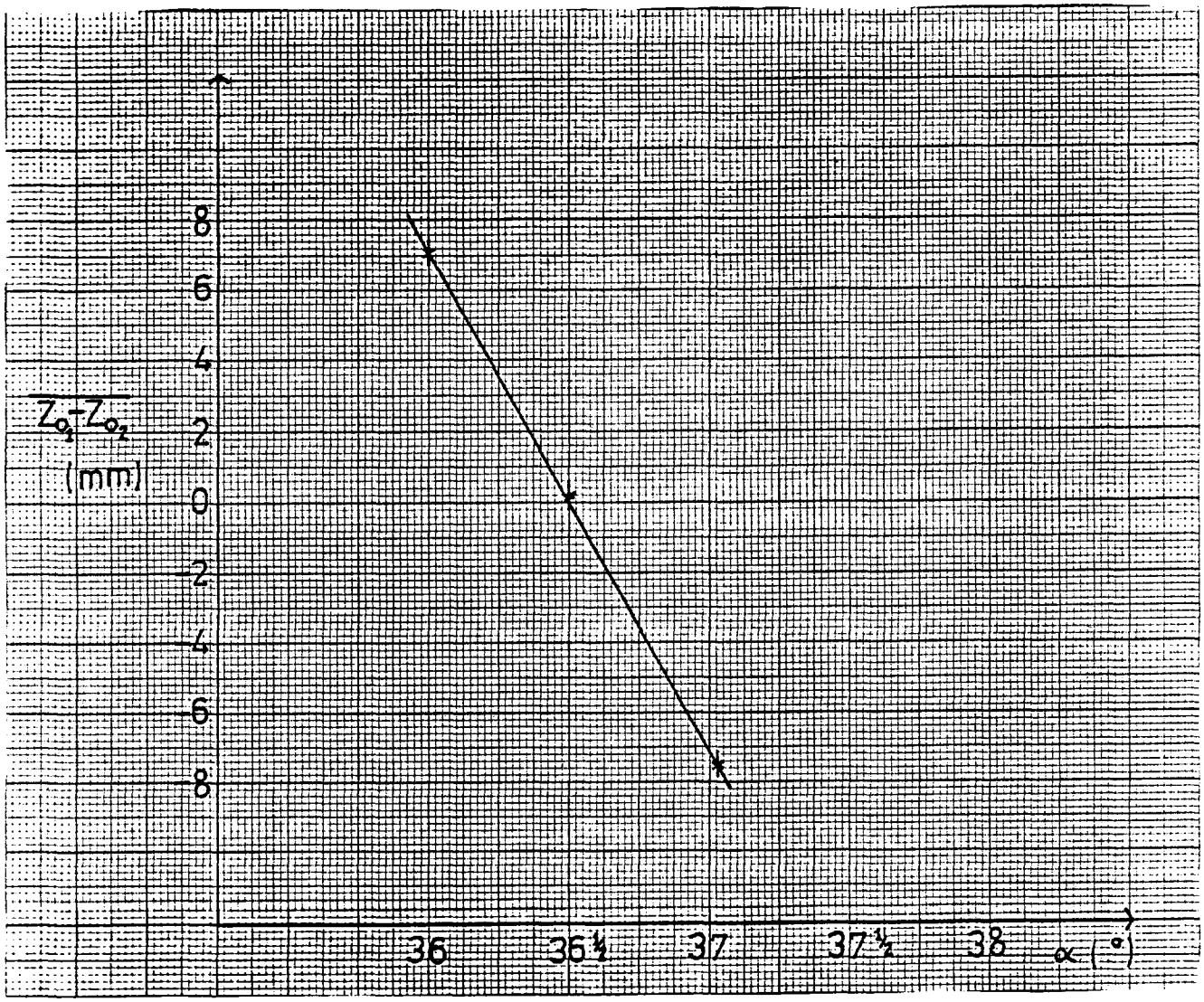

Figure 3.6

		Voltage (kV)	Effic-iency	Multip-licity
1	Inner Cathode		81.4±1.4	2.34
	Anode	4.5	98.2±0.5	1.46
	Outer Cathode		89.8±1.1	2.62
2	Inner Cathode		89.8±1.1	2.87
	Anode	4.2	98.5±0.4	1.34
	Outer Cathode		93.3±0.9	2.92
3	Inner Cathode		93.3±0.9	2.92
	Anode	3.9	98.8±0.4	1.33
	Outer Cathode		95.4±0.7	3.80
4	Inner Cathode		97.1±0.6	5.61
	Anode	3.8	99.4±0.3	1.33
	Outer Cathode		97.6±0.5	4.60

TABLE 3.2

3.9.2 Cathodes

For tracks reconstructed in 3 dimensions using the drift chamber 0° and α-wires the expected positions of hits on the cathode strips can be computed using the equation of section 3.7.2. Typical efficiencies found in this way for two prong events are given in Table 3.2. The amplitude of the induced pulse on the cathode strips increases with the track length in the chamber. This is seen clearly in Fig 3.7a where the sum of all ADCs in a cluster is plotted against the cosine of the angle of the associated track with the beam axis. Pulses from tracks travelling perpendicular to the anode wires can be very small and result in a reduced efficiency for such tracks. There is a strong correlation between the measured charge of the clusters caused by a single track on the inner and outer cathode planes (Fig 3.7b).

The cathode ADC pulses are conveniently displayed together with the anode wire hits by drawing the cylinders unfolded into straight lines. Fig 3.8 shows a 2-prong event in this manner. The anode wire hits and associated inner and outer cathode pulses are easily identified. The ADC cluster centres are indicated by vertical lines

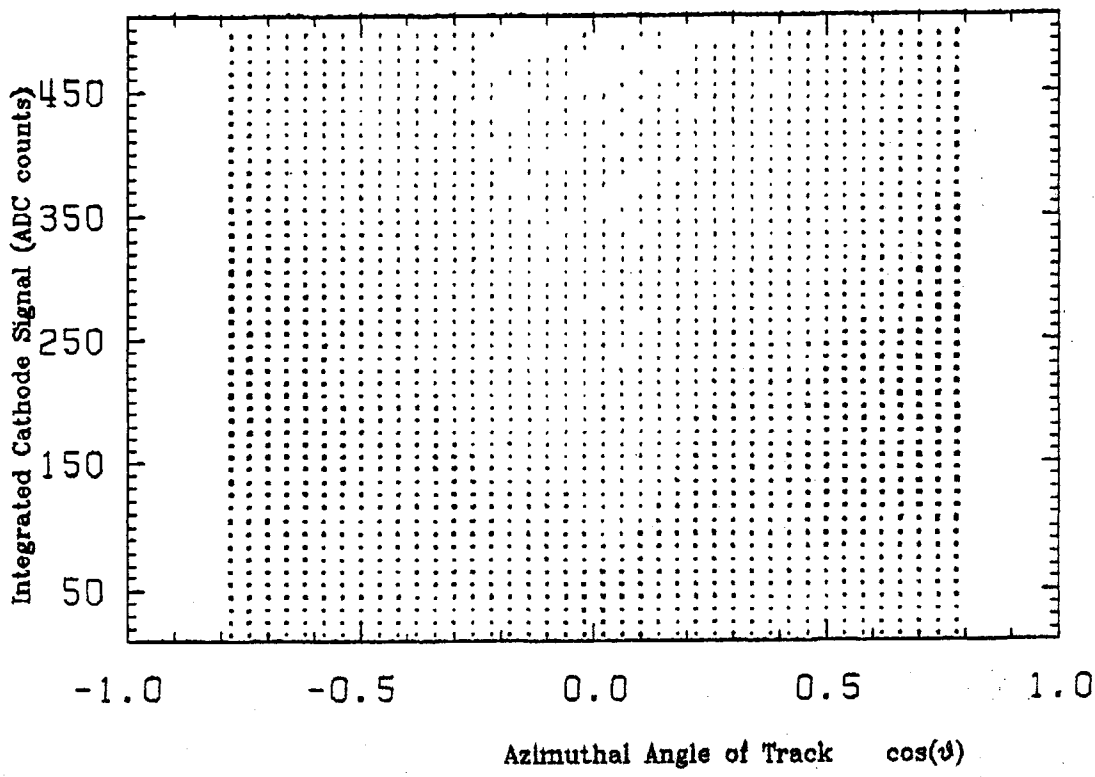

Figure 3.7a

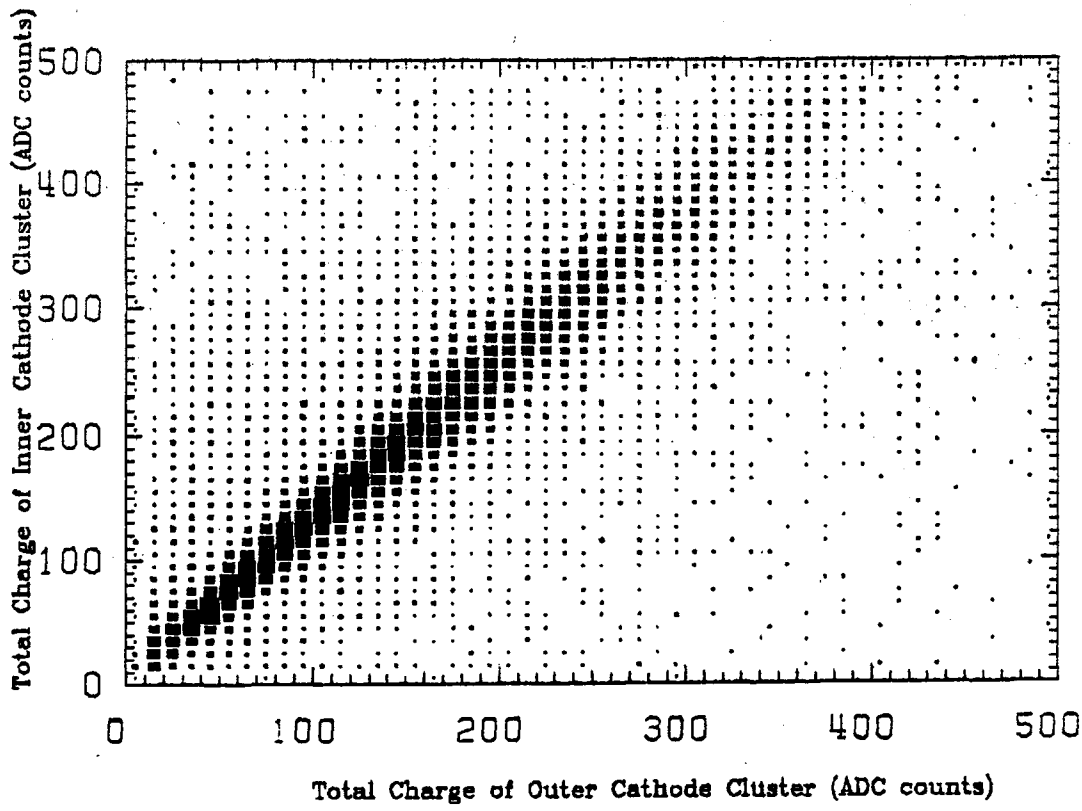

Figure 3.7b

and those associated to tracks are marked by a small triangle at their base.

The procedure used to improve the z reconstruction of tracks is now described.

First clusters are identified in the ADC pulses and their centre computed as follows. Peak channels are selected as those which have a pulse height greater than the neighbouring channels on each side by at least a factor 20/17. For each peak channel a cluster is defined. The centre of the cluster is computed (Figure 3.9) by searching for the channel on each side of the peak which straddles the value of 2/3rds the height of the peak channel. The edge positions are defined by linear interpolation between these channels to the 2/3rds peak height position. The cluster centre is taken as the mid-point between the edge positions on either side of the peak. If the pulse heights on neighbouring channels do not decrease as low as 2/3rds peak before increasing again,or if the 2/3rds peak value is not passed before one is 5 channels distant from the peak,the centre of the peak channel is taken as the cluster centre. To reduce the effect of dead and hot channels on this cluster search procedure such channels were

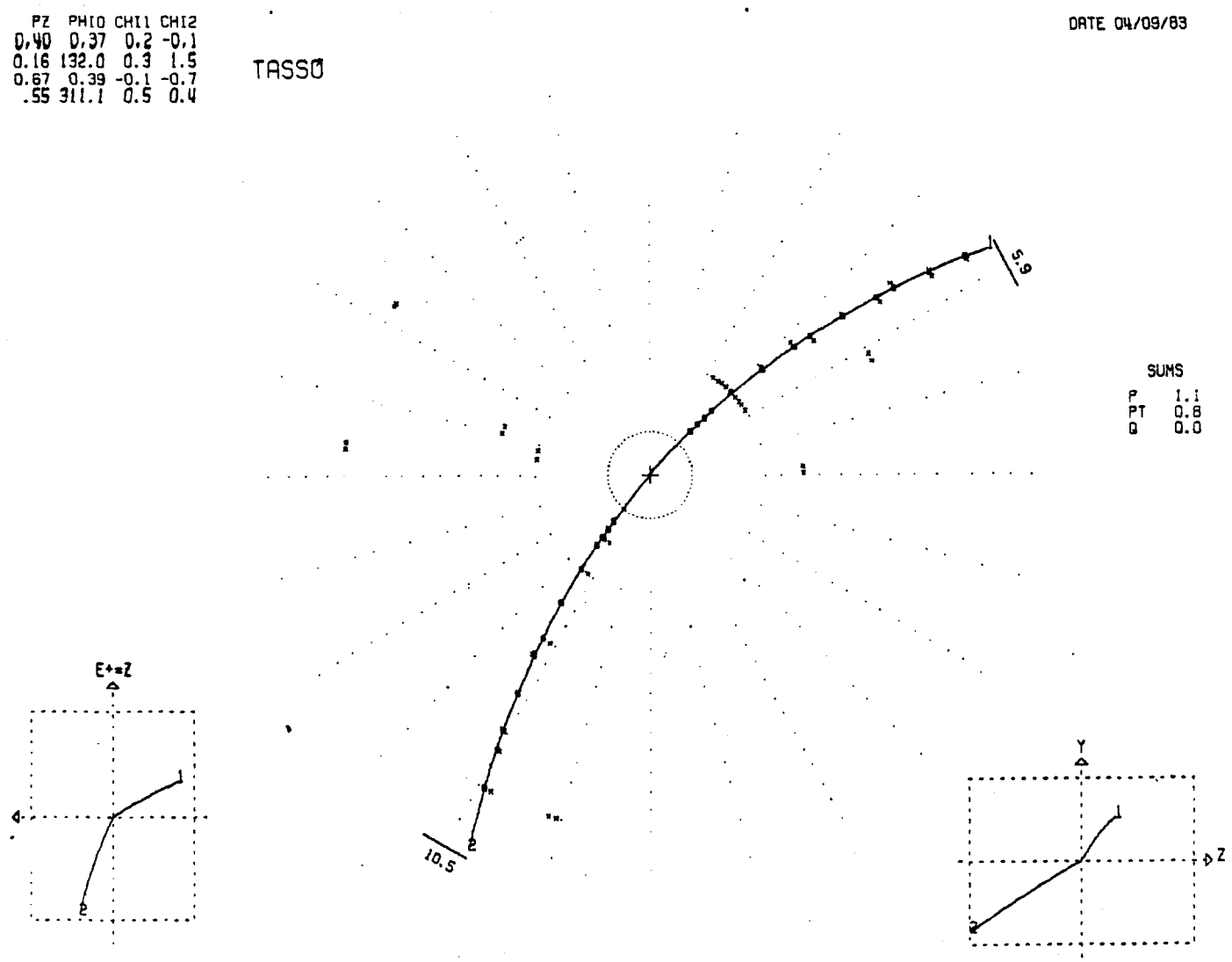
PZ PHIO CHI1 CHI2
0.40 0.37 0.2 -0.1
0.16 132.0 0.3 1.5
0.67 0.39 -0.1 -0.7
.55 311.1 0.5 0.4
TASSO
DATE 04/09/83
SUMS
P 1.1
PT 0.8
Q 0.0
5.9
10.5
E+=Z
Y
Z

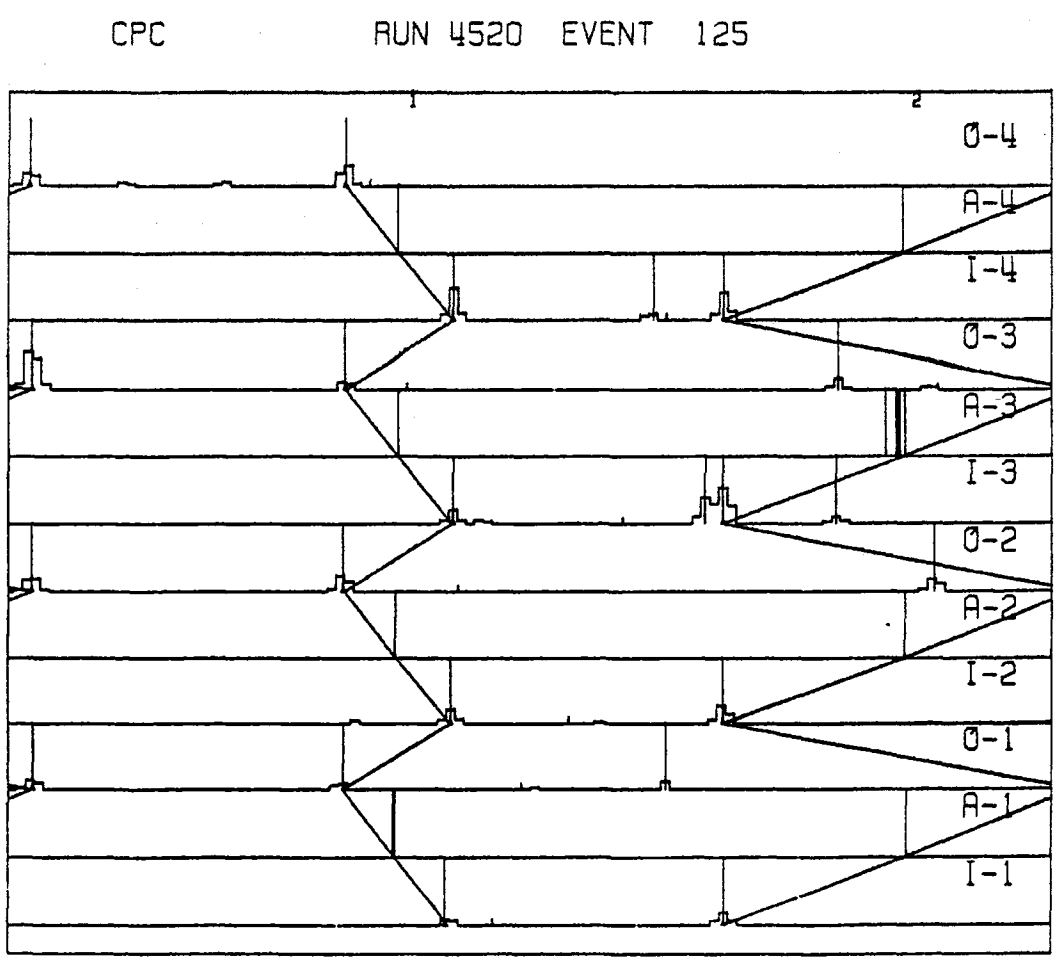
CPC RUN 4520 EVENT 125
0-4
A-4
I-4
0-3
A-3
I-3
0-2
A-2
I-2
0-1
A-1
I-1

Figure 3.8

identified and their contents replaced by the mean of the signals in adjacent channels,provided the adjacent channels were not themselves faulty. This algorithm provided a quick and simple way of identifying clusters ,independent of cluster size and which was not too sensitive to individual channel variations. Further computations used only the cluster centre positions.

All tracks reconstructed in three dimensions by MILL (see Chaper 5) using the CPC anode hits and the large drift chamber hits were considered in turn. For each associated anode wire hit the z values were computed for all cathode clusters on the corre-

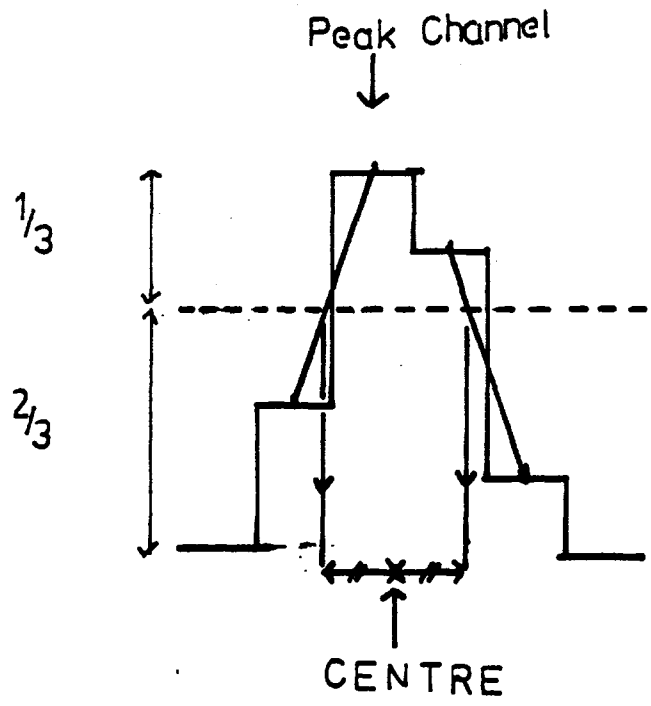

Figure 3.9

sponding inner and outer cathode planes by the equation of §3.7.2. The corresponding arc length along the track circle from its closest point of approach to the origin to its intersection with the anode cylinder was computed by the equation of §3.7.1b. All hits lying within a road of width 10 strips from the previous reconstruction of the track in the drift chamber were accepted. All combinations of accepted hits were then subjected to a common fit to a straight line in s-z with the drift chamber α-wire hits and the best fit chosen as that with the most hits which minimised the sum of squared residuals. Any hit which contributed excessively to the χ^2 was removed from the fit. An example of such a fit for the tracks seen in Fig 3.8 is given in Fig 3.10.

The mean cluster efficiency for use in this manner was 73% for 2-prong events and the z resolution of the cluster centres judged by the weight required in the fit was 0.35cm or about 1/4 of a strip width. The comparable numbers for the drift chamber stereo wires are a useful hit efficiency of 83% and a resolution of 0.66cm in z.

The resulting improvement in the resolution in the z position of a track at its point of closest approach to the beam spot in r-φ (z_0) is shown by Fig 3.11 where the difference in z_0 of tracks in 2-prong

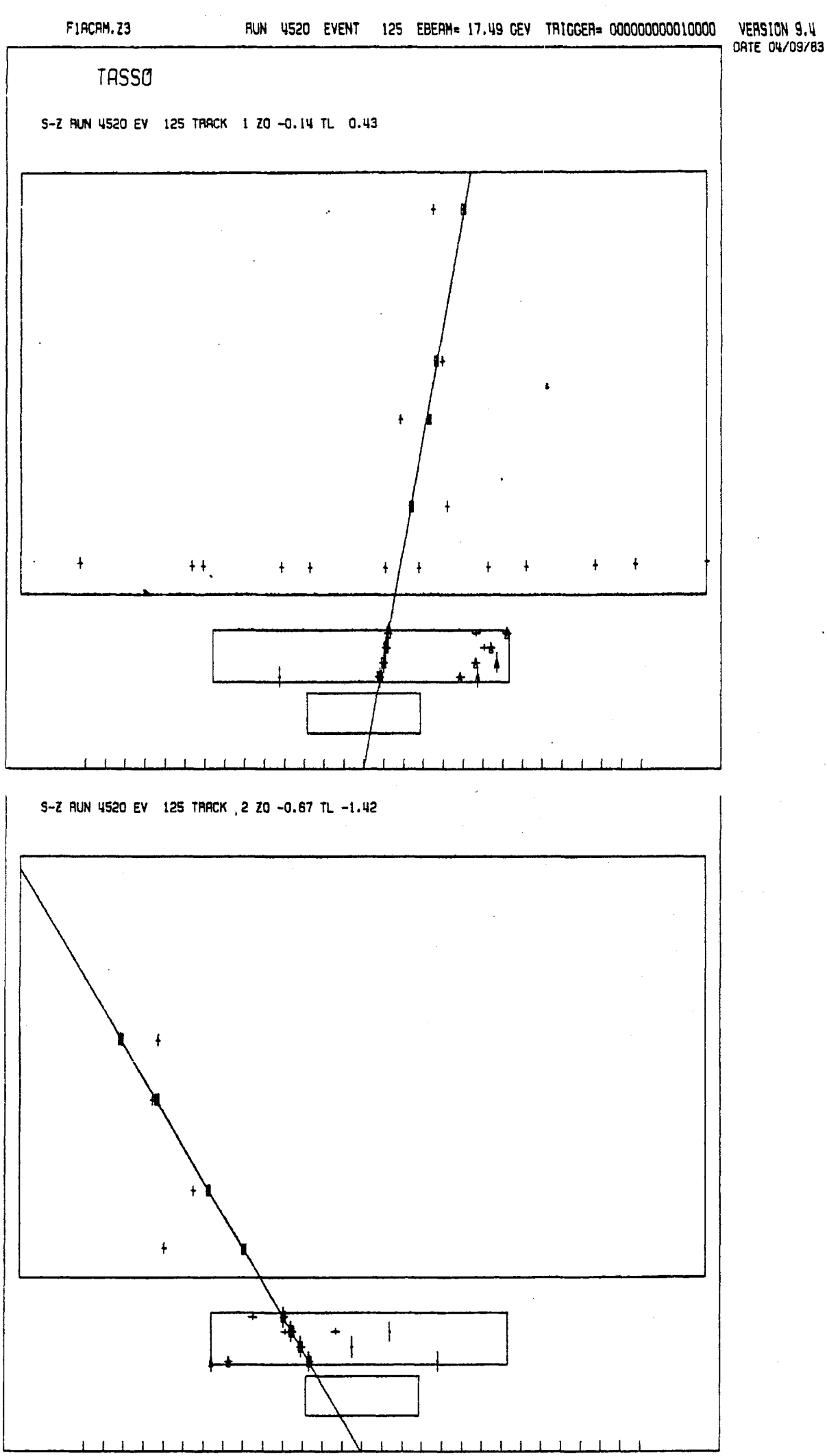
FIACAM.23 RUN 4520 EVENT 125 EBEAM= 17.49 GEV TRIGGER= 0000000000010000 VERSION 9.4
DATE 04/09/83
TASSØ
S-Z RUN 4520 EV 125 TRACK 1 ZO -0.14 TL 0.43
S-Z RUN 4520 EV 125 TRACK 2 ZO -0.67 TL -1.42

Figure 3.10

events (mainly Bhabhas) is plotted before and after inclusion of the cathode hits in the z-fit. An improvement in z_0 resolution by a factor of 3 is observed. Fig 3.12 shows that there is also an improvement in the resolution of the angle of tracks with the beam direction by plotting the sum of the tangents of the tracks with a perpendicular to the beam axis.

In multi-hadronic events with many tracks in narrow jets the ADC clusters from different tracks often overlap and so there usefulness is degraded. However well separated tracks are still clearly resolved (see Fig 3.13, as a guide the projected hit positions are indicated by the zig-zag lines).

Application of the fitting procedure described above to multihadron events resulted in a mean used cluster efficiency of 77%. However if all clusters which may be associated to more than one track are removed then the mean cluster efficiency drops to 36%. The improvement in z_0 resolution is evident from Fig 3.14 which plots the difference between the z_0 of each track and the mean z_0 of all the tracks in the event before and after the refit.

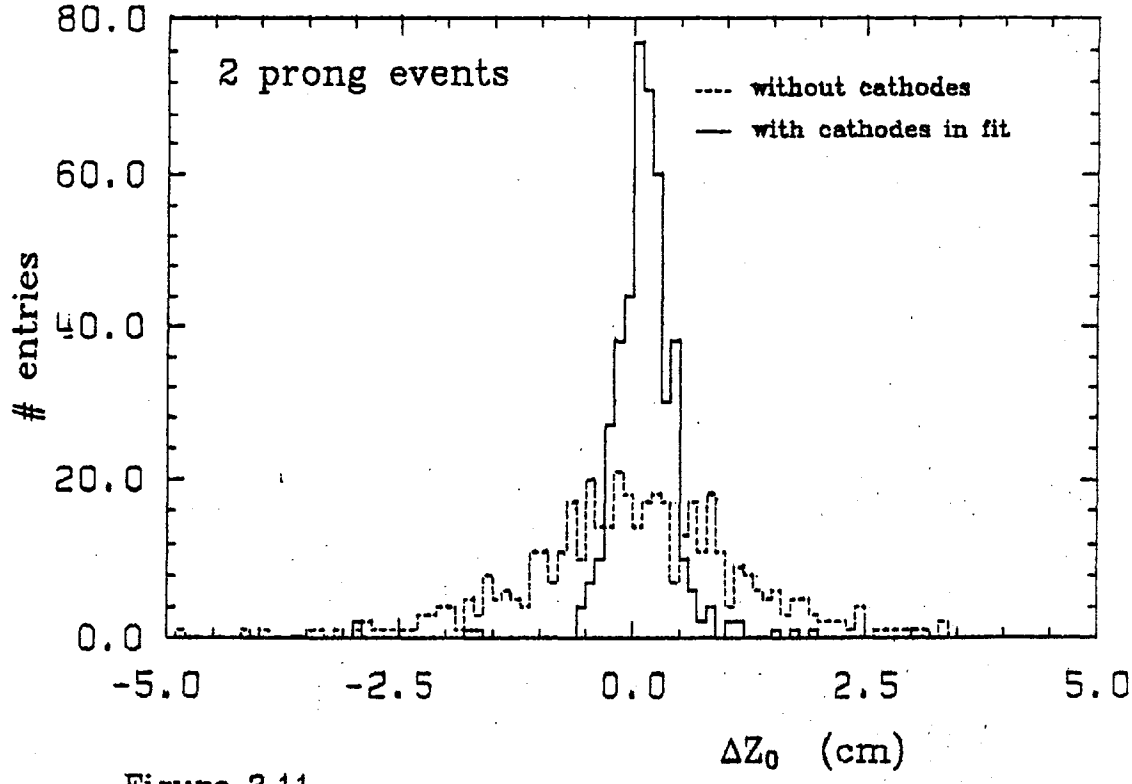

Figure 3.11

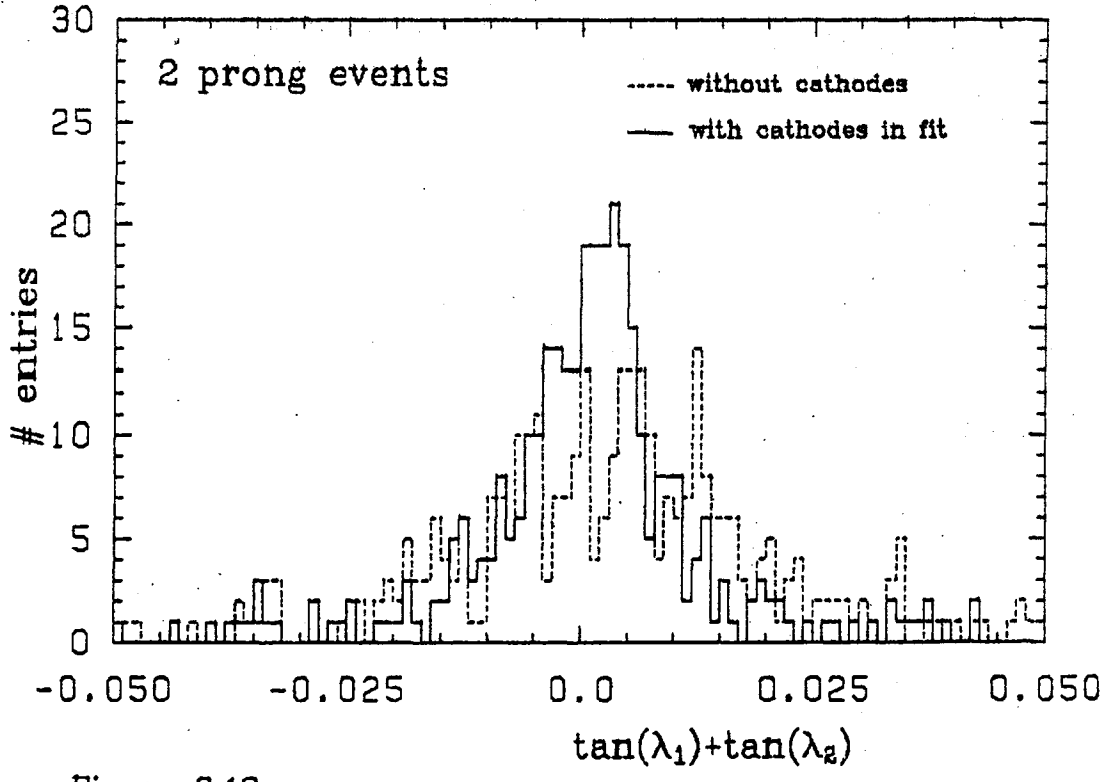

Figure 3.12

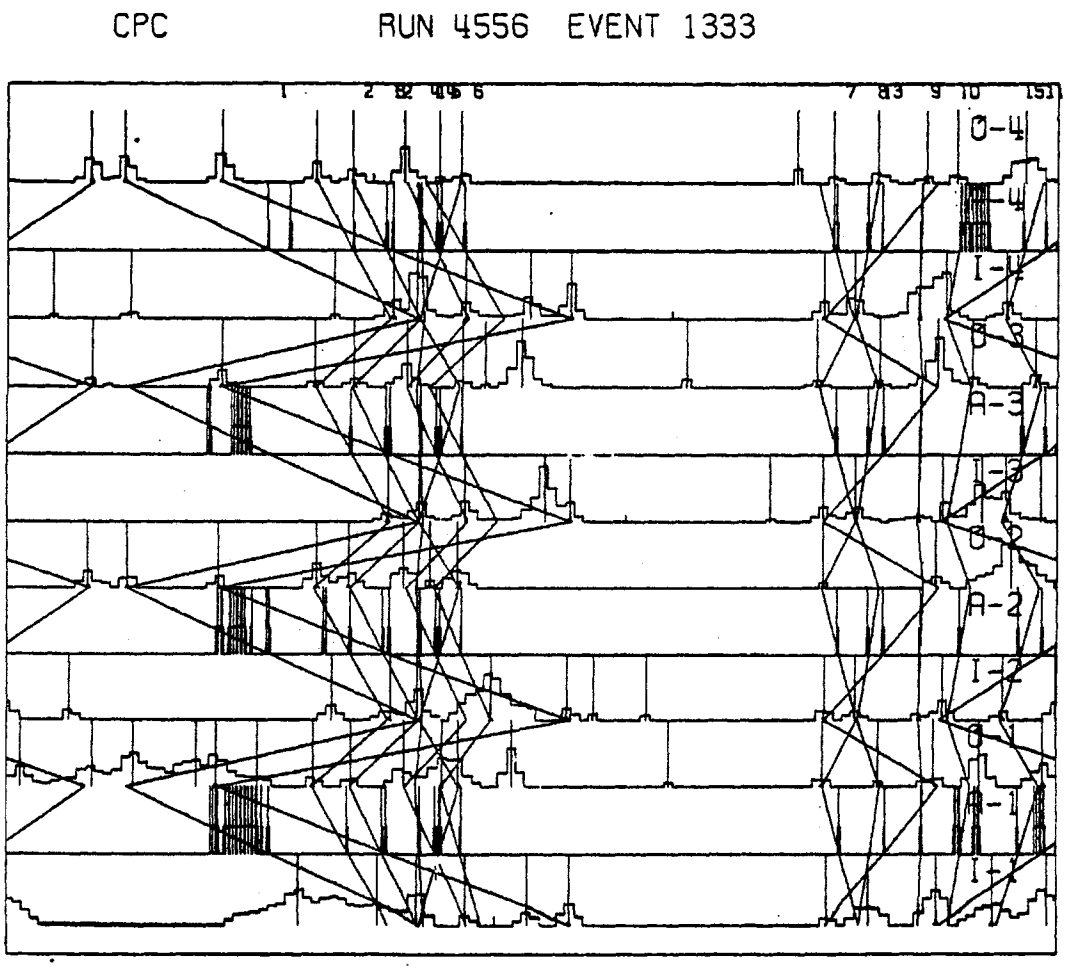

Figure 3.13

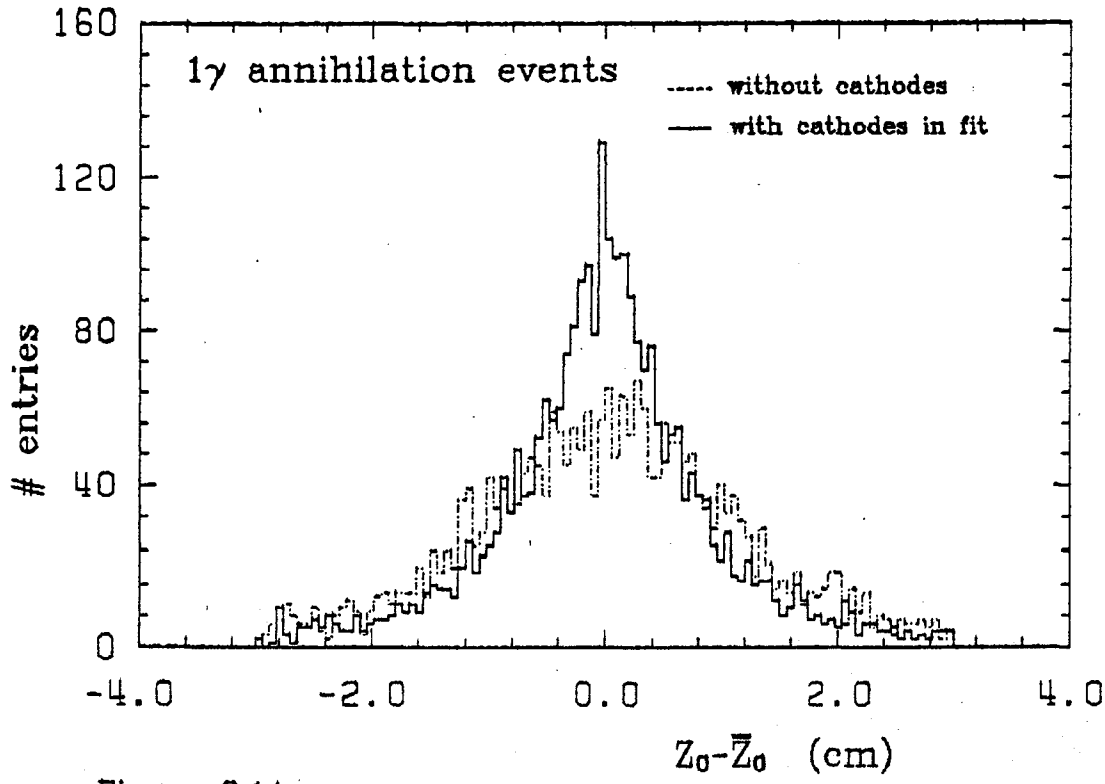

Figure 3.14

3.10 THE PROPORTIONAL CHAMBER PROCESSORS

The proportional chamber hardware processors attempt to recognise wire hit patterns which can result from real tracks originating in the interaction region,and thus provide fast logic triggers capable of rejecting unwanted events.

3.10.1 The CPC anode wire processor

Coincidence logic recognises selected classes of track patterns through the 4 proportional chambers a,b,c,d by simultaneously examining coincidences between designated anodes in chambers a-b,b-c,c-d and a-d (see Fig 3.15).

The coincidence logic array is implemented in a flexible way using the special random access device type C10115 from Synertek. This is basically a 1×256 RAM with 16X and 16Y address lines. The output is the NOR function of the contents of all addressed locations. The X and Y address inputs are connected to the chamber wire outputs, or computer/manually controlled sets of lines and a coincidence between any two wires is selected by storing a logic 1 or a logic 0 in the corresponding locations. Possible contents of a 16×16 array is illustrated in Fig 3.16.

The inner detector is divided into 96 equal sectors based on 5 wires in the innermost chamber 'a'. Each sector forms its own threefold ((ab+cd)*(bc+ad)) and fourfold (ab*bc*cd*ad) outputs by combining the RAM outputs representing the ab,bc,cd and ad pairs. The threefold ouput allows for inefficiencies and broken channels

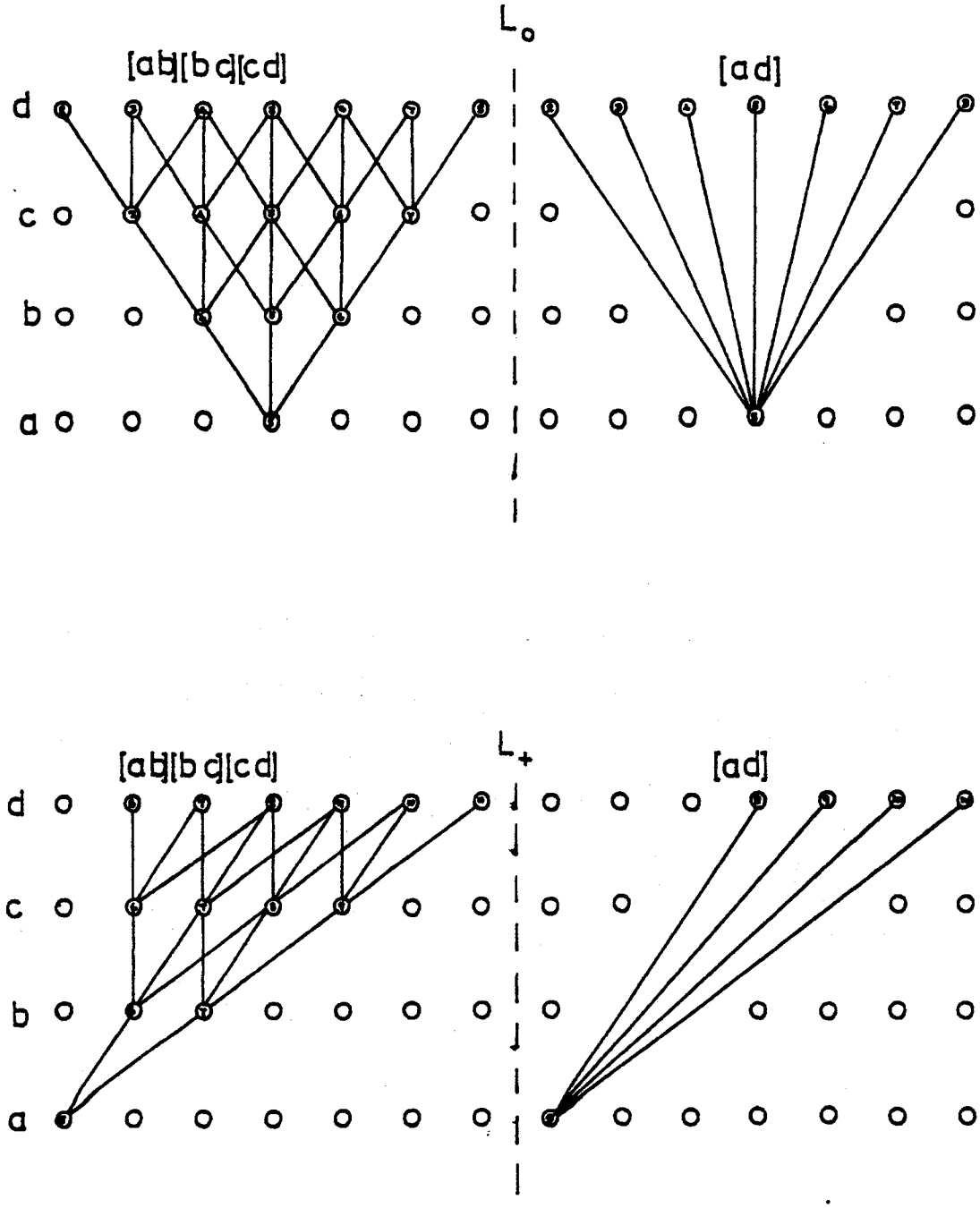

Figure 3.15

or wires in the chambers. These outputs are then used in the generation of the topology information and multiplicity decisions.

To provide more flexibility the wires are connected to three sets of RAMs,finding negative (L^-),positive(L^+) and high momentum (L^0) tracks. L^0 tracks have momenta of ±220MeV/c or more transverse to the beam axis,whilst L^+ and L^- tracks span the 100-200MeV/c momentum range (Fig 3.17).

During normal datataking the processor outputs were used in both the pretrigger and postriggers. The pretrigger stopped the

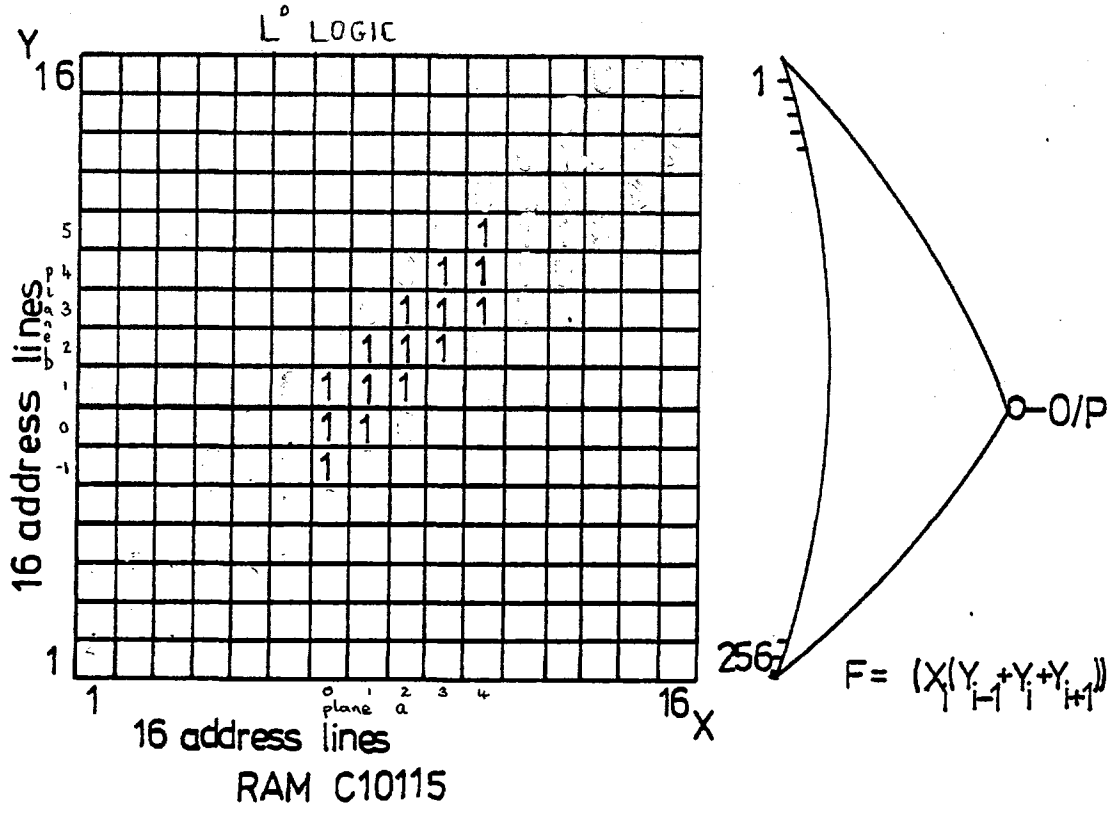

Figure 3.16

experiment for 1 or 2 beam crossings while the slower postrigger made its decision. The processor was set to accept only L^0 tracks,and the threefold signals from adjacent sectors were ORed together to form 48 signals for the drift chamber processor (PREPRO). The pretrigger included the requirement of at least one threefold coincidence. This reduced the pretrigger rate by a factor of two and hence the deadtime by ~10kHz.3.8μs=7.6%. Furthermore,the addition of the 48 sector signals to the PREPRO reduced the trigger rate by a factor of two.

3.10.2 The CPC cathode processor

Any tracks originating from r=0,z=0 hit,after a defined shift of the strip addresses,the same strip number on each of the four outer sets of 120 cathode strips. By counting straight up coincidences as different sets of shifts appropriate to tracks originating from z=-60,-30,0,30,60cm are applied,it becomes possible to determine the origin of any event along the z-axis. No attempt is made to recognise individual tracks. Figure 3.17 shows a cosmic ray event and the hits produced in the CPC cathodes by the incoming (1) and outgoing (2) sections of the track, which passed close to the beam

line at a z of 14.5cm. The peaks in the 4 outer sets of cathode strips do not align in φ whereas those caused by tracks from z=0 (Figure 3.10) are aligned and so cause coincidences in the z=0 shift. As in the anode processor both threefold and fourfold coincidences are counted. The number of channels was reduced to 60 per plane by ORing adjacent cathode signals.

The shifts were performed by the shifter element type Am25S10 supplemented with a read/write memory and AND gates. This device can shift 4 bits by 0,1,2, or 3 places. By combining several layers of such shifters shifts by 0-15 channels for planes b and c and 0-31 channels for plane d are made possible.

An event is accepted if the number of coincidences at a shift corresponding to z=0 is greater than the numbers at other z values in some sense. The numbers of threefold N_3 and fourfold N_4 coincidences are counted and weighted according to $N = N_3 + 3*N_4$. This number is calculated for each of the five shifts and outputs indicating $N \geq 16, N \geq 32$ and $N \geq 64$ for the first shift (z=0) generated. Table 3.3 summarises the special and programmable output algorithms. These are designed to find a peak in the distribution of tracks in z. For the 'cathode' trigger special output 3 was anded

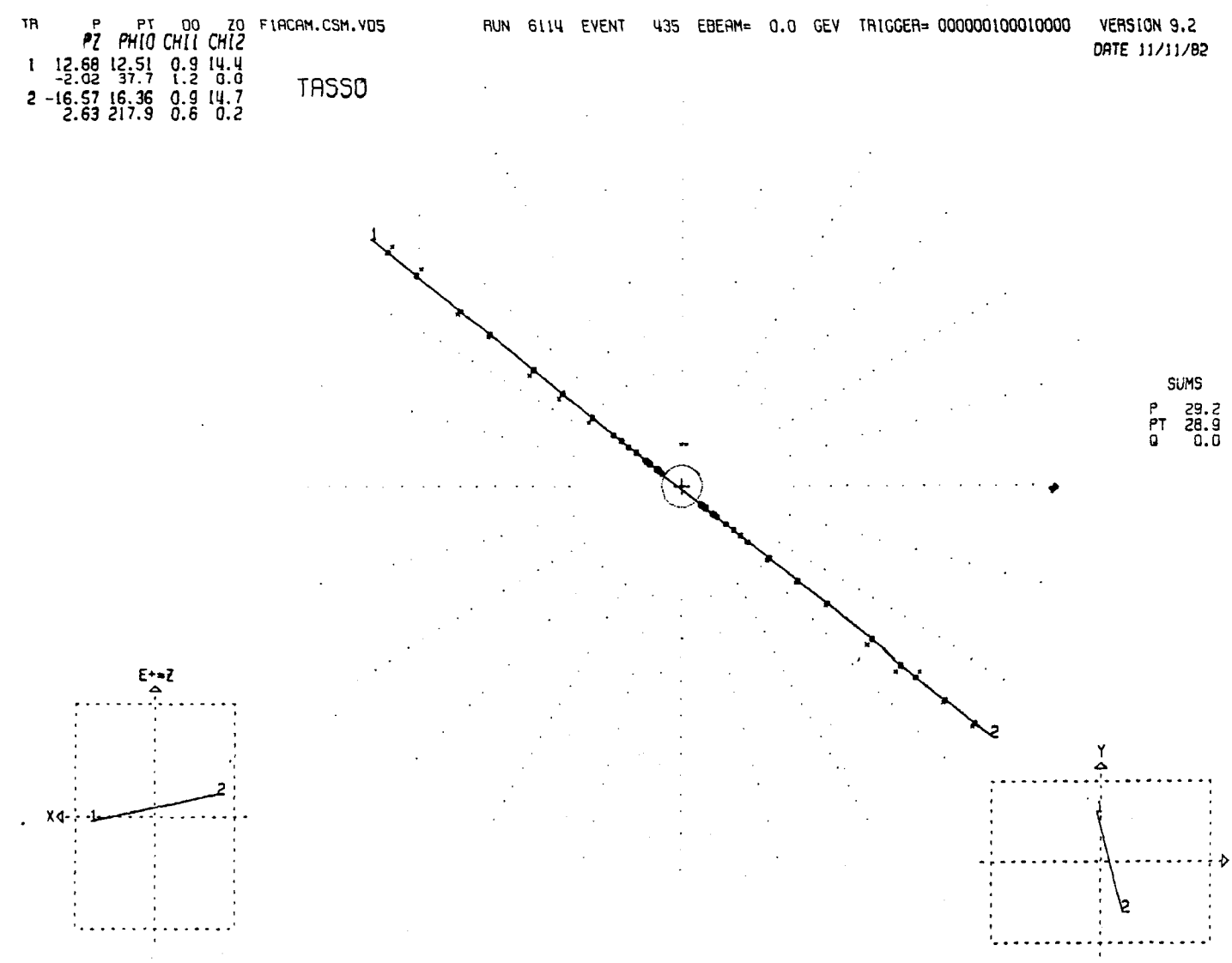
TR P PT QQ ZQ FIACAM.CSM.V05 RUN 6114 EVENT 435 EBEAM= 0.0 GEV TRIGGER= 0000001000010000 VERSION 9.2
PZ PHIQ CHI1 CHI2
DATE 11/11/82
1 12.68 12.51 0.9 14.4
-2.02 37.7 1.2 0.0
2 -16.57 16.36 0.9 14.7
2.63 217.9 0.6 0.2
TASSO
SUMS
P 29.2
PT 28.9
Q 0.0
E+=Z
X
Y
Z

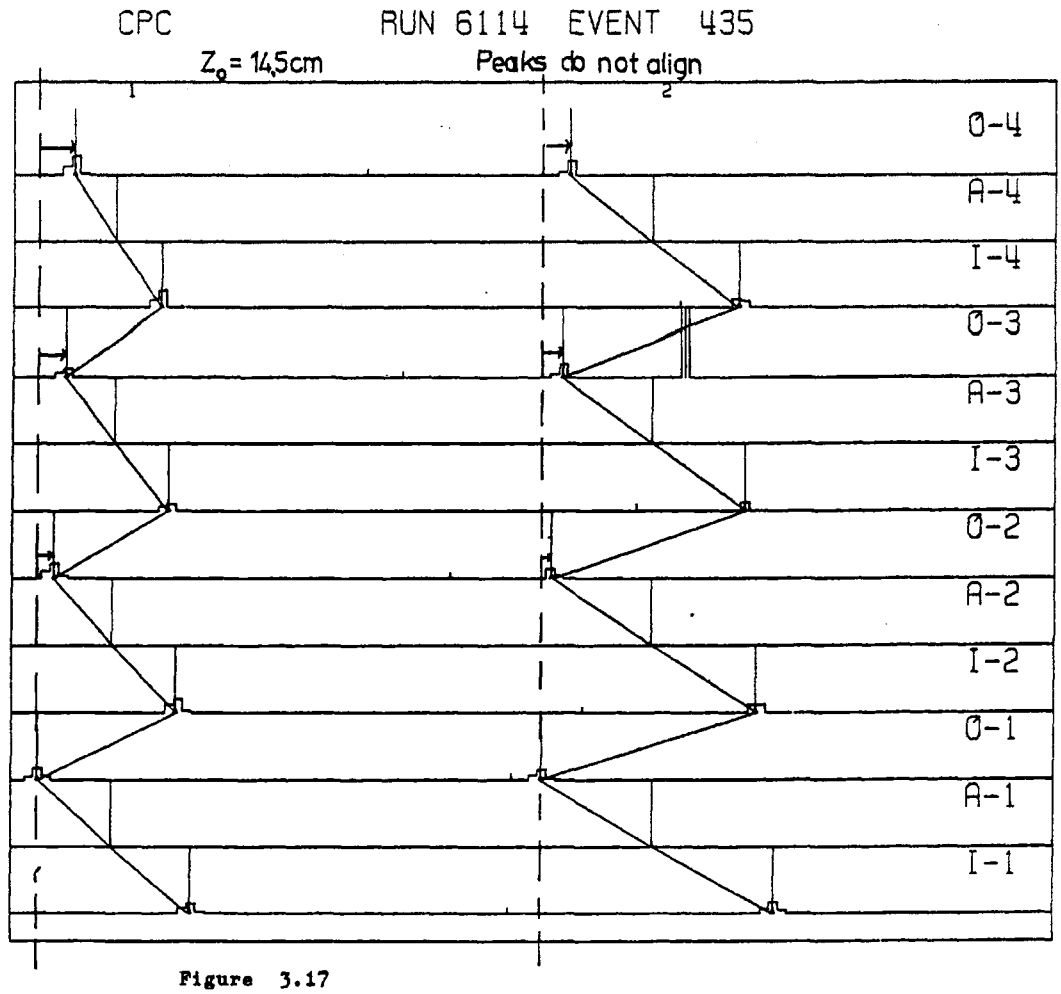
CPC
RUN 6114 EVENT 435
Z_0 = 14.5cm
Peaks do not align
0-4
A-4
I-4
0-3
A-3
I-3
0-2
A-2
I-2
0-1
A-1
I-1

Figure 3.17

with the requirement of ≧2 sectors from the PREPRO to form a general low multiplicity trigger. Special output 3 required $2N_1-N_2-N_3-2\geq 0$ and $2N_1-N_4-N_5-2\geq 0$ where $N_1,N_2,,,N_5$ denotes the value of N defined above for the five shifts.

Special 1 $\quad 2N_1-N_2-N_3 > \gamma_2$

Special 2 $\quad 2N_1-N_4-N_5 > \gamma_2$

Special 3 (Special 1 .and. Special 2)

Special 4 $\quad N_2+N_3+N_4+N_5 = 0$

Programmable $N_1-\beta_1N_2-\beta_2N_3-\beta_3N_4-\beta_4N_5 > \gamma_1$

where β_{1-4},γ_{1-2} are integer constants, in the range 0 - 15.

N_1 is the number of coincidences at the z=0 shift.

TABLE 3.3 Special and Programmable Cathode Triggers

The 6 cycles of operation of the processor took 1.7μs to perform, although the first special output was ready in about 900ns. The 'cathode' trigger requirement results in a limit to the vertex position of events of about ±15cm in z from the interaction point. The measured efficiency was 96.5±0.5%. An increase in acceptance for 4-prong events by almost a factor of 3 was obtained. This greatly

improved the ability to study the reactions $\gamma\gamma \to \rho^0\rho^0, \gamma\gamma \to f'$, $\gamma\gamma \to K\bar{K}$. The track trigger efficiency improved from 50% at p_t=0.2GeV/c; 95% at $p_t \geq$0.37GeV/c to 50% at p_t=0.17GeV/c; 95% at $p_t \geq$0.29GeV/c.

4.0 TRACK FINDING IN THE CPC

4.1 INTRODUCTION

This chapter describes in detail the motivation for and operation of a computer program for the recognition of tracks in the CPC.

4.2 MOTIVATION

The TASSO data reduction chain (see Chapter 2) selects events of interest from background triggers by making cuts on the number of tracks reconstructed in the drift chamber using the fast track reconstruction program FOREST [17][19]. Since 1981 ≥2 tracks reconstructed in r-φ with $|d_0|<2.5$cm and ≥1 track reconstructed in r-φ-z with $|d_0|<2.5$cm and $|z_0|<15$cm have been required. By comparision[18] with the much slower but more efficient track reconstruction program MILL it was estimated that this procedure resulted in a loss of ~25% of non-coplanar 2-prong events,primarily because of the inefficiency of FOREST for low p_t tracks.

A fast,efficient program for the recognition of tracks using only the information from the CPC would be independent of FOREST which uses only the central drift chamber and so could serve both as a method of improving the efficiency of finding non-coplanar 2-prong events and as a monitor of the event selection efficiency.

The need for speed is essential as some 10^6 triggers per day are taken during normal operation of PETRA.

4.3 TRACK RECOGNITION IN CPC ANODES

4.3.1 General Considerations

Track recognition in the CPC anodes is facilitated by the fact that there are the same number of anode wires in each chamber (see Chapter 3). High p_t tracks originating at the beam spot will fire the same channel number on each chamber,while allowing for an offset of two channels between chambers will accept tracks with $p_t \geq 120 MeV/c$.

The poor spatial resolution (essentially the anode wire spacing/$\sqrt{2}$) ,the non-Gaussian error of such a spatial measurement and the small track length spanned by the proportional chambers mean that it is unreasonable to select track candidates by fitting a circle or straight line to the 4 hits (3 if we allow for one inefficiency). Instead a choice of track candidates can be made based on the number of hits,the number of hits shared with previously found track candidates and a system of costs based on the difference in channel numbers on adjacent chambers. This system of costs replaces the smaller χ^2 criterion used when a fitting procedure is adopted.

The proportional chambers do not have the problem of drift time ambiguities which produce incorrect space points close to the track (see Chapter 5). The two-track resolution of the proportional chambers can at best be one wire spacing. In practice however a single track often fires two and sometimes three adjacent wires. In addition background induced by the beam occasionally causes many wires on all chambers to fire and large bands of hits on neighbouring wires in a single chamber are often observed. The physical origin of these bands is not clear:they may be caused by low energy δ electrons or by electronic pickup between channels.

The presence of such noise hits can result in many coincidences between wires and would severely affect the speed of the tracking program. This problem is ameliorated ,before the operation of the track recognition routines,by the removal of bands of adjacent hits and the replacement of pairs of hits by a single fake hit positioned mid-way between the two wires.

Unwanted triggers caused by cosmic rays can usefully be reduced if the origin in z of the tracks found in the anodes is reconstructed using the cathode strip information (see Chapter 3.8.2).

The algorithms developed to perform the track reconstruction are now described in detail.

4.3.2 Track recognition algorithm:the depth-first search

The track recogntion in the CPC anodes utilises the depth-first-search algorithm [18]. This algorithm was first applied to track recognition problems in high-energy physics by H.Kowalski

[17] in the reconstruction program for tracks in the TASSO drift chamber (FOREST/MILL). This will be reviewed in Chapter 5.

In our applications the depth-first search is used as a simple method of finding all the paths from a given vertex of a directed graph.

A directed graph consists of a set of vertices and a set of edges;the edges are ordered pairs (ν,ω) of these vertices as illustrated in Fig 4.1.

ν is known as the tail and ω the head of the edge. A path is a sequence of edges of the form (ν_1,ν_2), (ν_2,ν_3), ... ,(ν_{n-1},ν_n). Such a path can also be represented by the sequence $\nu_1,\nu_2,...,\nu_n$ of vertices on the path.

The complete track recognition task uses the depth-first search twice, with different associations between the mathematical notions of vertices and edges and the physical quantities of the track recognition. (see Table 4.1). The following description of the depth-first search algorithm will be kept general by couching it in the graph theoretical terms described above.

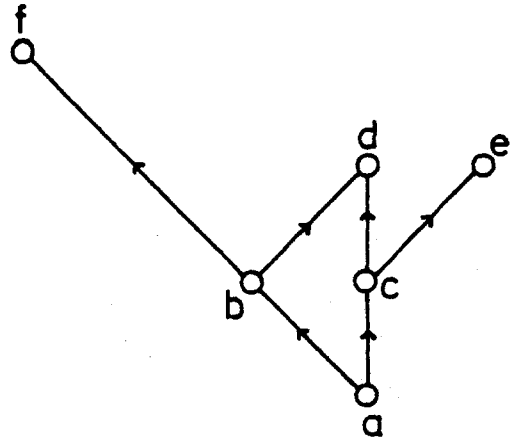

Verticies : a, b, c, d, e, f

Edges : (a,b), (a,c), (b,f), (b,d), (c,d), (c,e)

Paths : abf, abd, acd, ace

Fig. 4.1 A Directed graph.

To make a depth-first search we select and 'visit' a starting vertex ν. Then we select an edge (ν,ω) incident upon ν and directed towards ω,and visit ω. In general,suppose x is the most recently visited vertex. The search is continued by selecting some unexplored edge (x,y) directed out of x. Then we visit y and begin the search anew starting at vertex y. After completing the search

Vertex	Hit anode wire
Edge	Association between hits on different chambers
Direction	From innermost to outermost chamber
Path	Possible track candidate
(a)	
Vertex	Link between hits on different chambers
Edge	Association between links sharing a common hit
Direction	From innermost to outermost chamber
Path	Track candidate
(b)	

TABLE 4.1 theoretical->physical concepts

through all paths beginning at y,the search returns to x,the vertex from which y was first reached. The process of selecting unexplored edges incident upon x is continued until the list of these edges is exhausted. This method of visiting the edges of a graph is called a depth-first search since we continue searching in the forward (deeper) direction as long as possible.

Whenever,during the depth-first traversal,a vertex is encountered which has no edges directed out of it,the end of the path has been reached. On completion of the process all paths starting from vertex ν will have been formed. As an example the paths from vertex a of Fig 4.1 would be enumerated as abf,abd,acd,ace.

4.3.3 The track recognition procedure

Fig 4.2 gives a possible pattern of wire hits in a section of the CPC. Suppose we wish to decide whether there is a track including the hit on the innermost chamber. We proceed as follows:

1. First we replace the pair of adjacent hits on chamber 2 by a single hit between them as shown in Fig 4.3. This is accom-

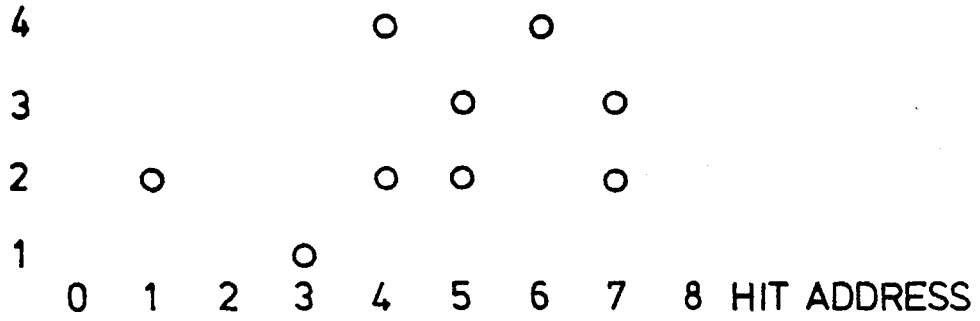

Fig. 4.2 Example wire hit pattern.

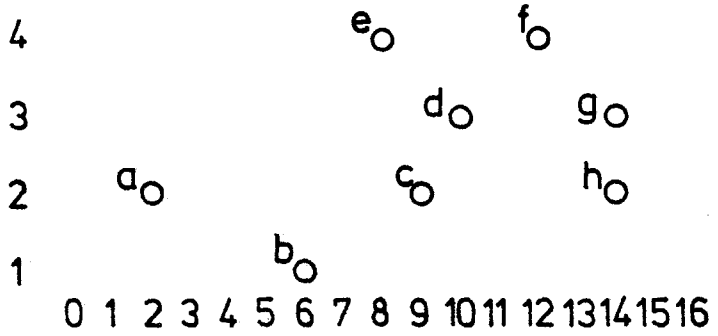

Fig. 4.3 Replacement of adjacent hits.

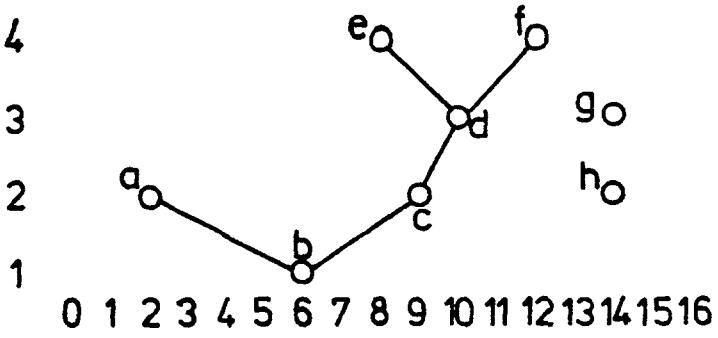

Fig. 4.4 Formed edges.

plished by doubling all hit addresses,deleting the two adjacent hits and inserting a hit at the odd numbered address between them. The following refers only to these new hit addresses.

2. Next we make the associations:

vertex≡ "hit" of Fig 4.3

edge ≡ permissable associations between these "hits"

and start a depth-first search from the hit on the innermost chamber. Whenever we visit a new hit we search for hits on the next outermost chamber and form edges to all hits found in a region ±2 wires (±4 hit addresses) from the new hit. If no hit is found then we try a search in a region ±4 wires on the next chamber but one. If we have previously visited a hit we do not search for edges from it again,but return to the hit from which we came. At the end of this excercise we will have formed the edges shown in Fig 4.4.

The rationale for this step is that we have formed all edges which may be required to identify a track which includes our initial hit. This could have been accomplished by searching from all hits on all chambers and forming all the edges which

satisfy the local cut of a maximum of ±2 wires between chambers. However a maximum of 240*3*3=2160 edges instead of just 27 edges could then be formed. More storage space would be required for the edges and time would be needed to select these edges of interest.

3. We now make the associations:

   vertex≡ link between chambers

   edge ≡ permissable associations between these links.

Here link is used to describe the edges of the previous step. All these links are assigned a cost c=2*Δ where Δ= |difference in the hit addresses| and a sign s=sign of difference in the hit addresses. Edges are formed between links provided

a. the head of one link is the tail of the other
b. the absolute difference in the cost of the links is not more than 8 for links of the same sign or the sum of the cost of the links is not more than 11 for links of opposite sign.

These criteria were chosen to select hit patterns possible for physical tracks. For example the hit patterns of Fig 4.5a,b

would be accepted while no edge would be formed between the links of Fig 4.5c.

The edges are formed in this step by examining all links found in 2. The depth-first search algorithm is not used as the total number of links from the previous step is small and the total number of edges which can be formed is also small.

Fig 4.6 shows the graph which could be prepared from the links of Fig 4.4.

4. This final step enumerates all possible track candidates which satisfy the local cuts of steps 2 and 3. This is accomplished by making a depth-first traversal from each of the vertices at the base of the graph prepared by the previous step. In our example we would make two searches:the first from vertex ba would not find any paths,the second from vertex bc would identify the paths bcde and bcdf.

It was thought that a reasonable measure of track multiplicity may be useful. To improve this not every track was retained as a candidate. Instead whenever a path was found it was compared with these paths already constructed. Paths containing 4 hits were

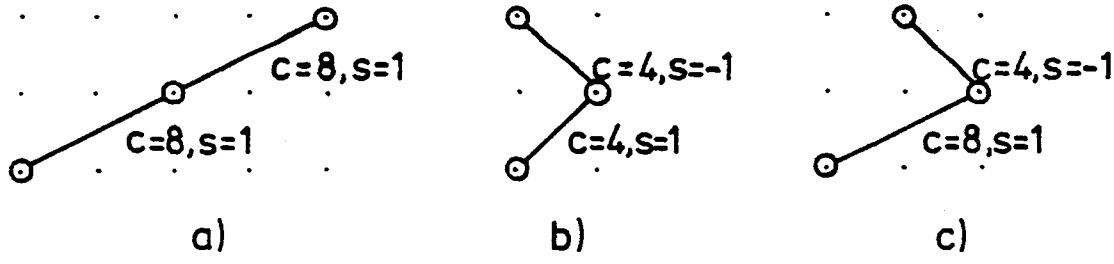

Fig. 4.5 Link costs.

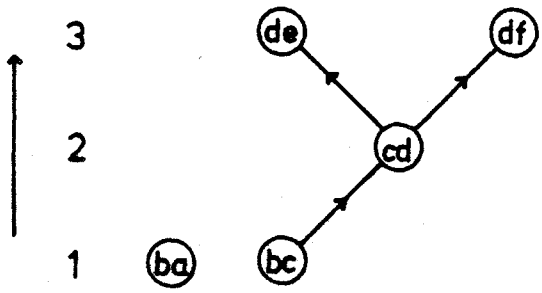

Fig. 4.6 Graph of links.

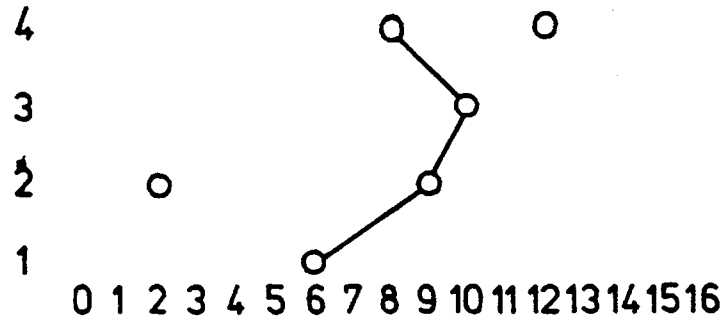

Fig. 4.7 Identified track.

only allowed to share 2 hits and a path with 3 hits only 1 hit with another path. In cases of conflict the 'best' path was retained where 'best' was defined by the following tests:

1. the path with the greater number of hits
2. the path whose highest cost link was of lower cost
3. the smaller absolute difference in wire address between the innermost and outermost hits for 3 hit paths or the smaller difference between the mean of the wire addresses of the hits on chambers 1 and 3 and that of chambers 2 and 4.

The complete track recognition procedure consisted of repeating steps 2,3 and 4 above starting from hits on chambers 1 and 2. A single pass was made round chambers 1 and 2 starting the search from all hits on chamber 1 and those hits on chamber 2 for which there were no hits on chamber 1 within ±2 wire spacings.

The final tracks identified for the example of Fig 4.2 are shown in Fig. 4.7.

Some examples of the tracks identified in real events are given in Fig 4.8. The accepted tracks are indicated by the lines joining

hits of different chambers. The circumferential lines indicated the 3 and 4-fold coincidence sectors identified by the hardware processor (see Chapter 3). The extrapolation of the tracks identified by the MILL program (Chapter 5) are drawn as circle segments.

4.3.4 Computer implementation

This section describes how the algorithms described in the previous section are realised in a computer program.

4.3.4.1 The removal of bands of consecutive hits

The addresses of hit wires in the 4 proportional chambers are stored as singly linked lists in the arrays ICPC and NXCPC. This data structure is illustrated in Fig 4.9.

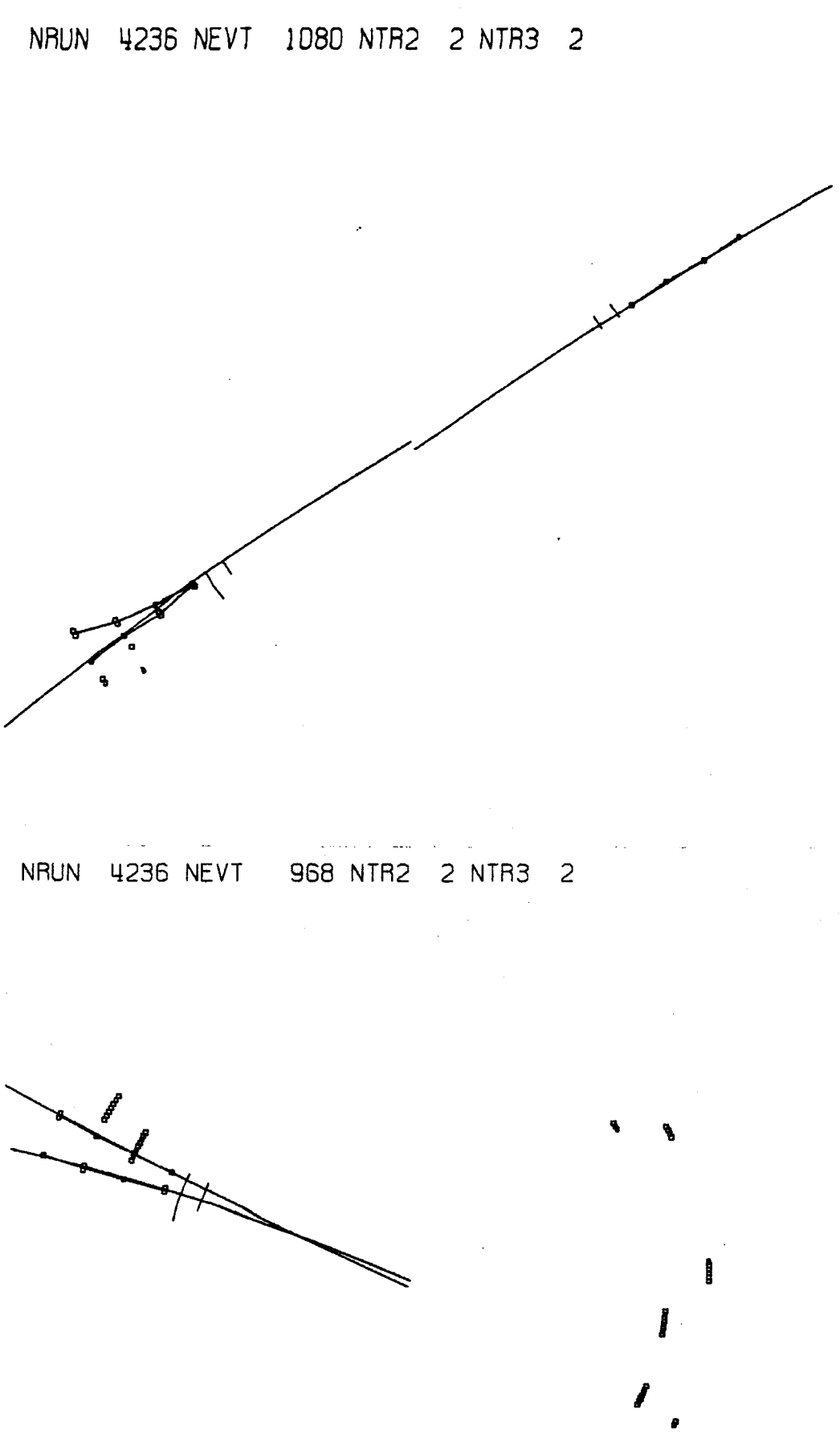
NRUN 4236 NEVT 1080 NTR2 2 NTR3 2
NRUN 4236 NEVT 968 NTR2 2 NTR3 2

Figure 4.8

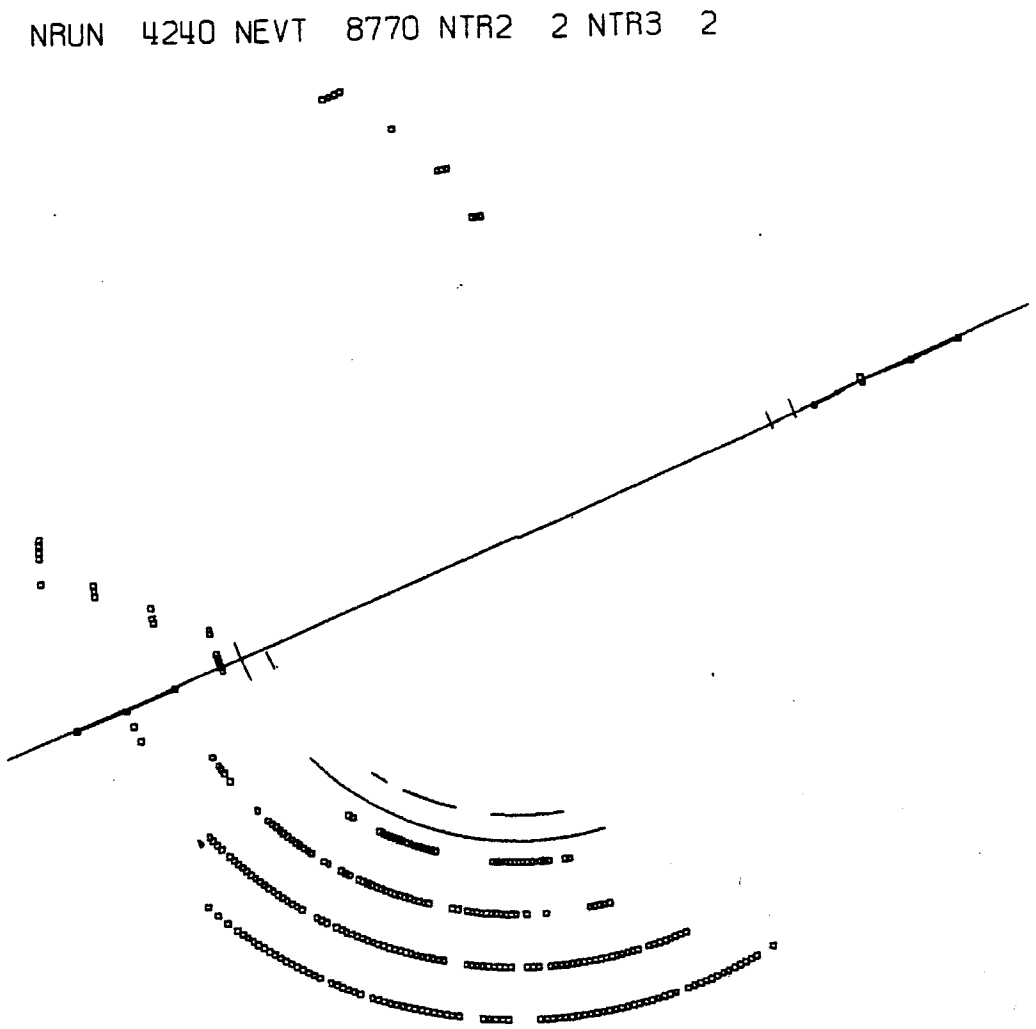

Figure 4.8

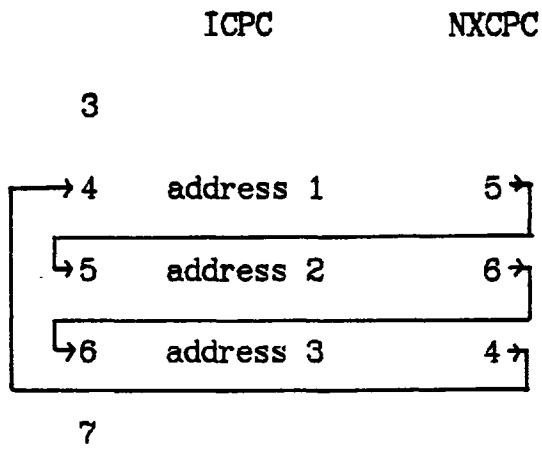

FIG (4.9) A Linked List For A Chamber With 3 Hits

There are pointers, NCPCP, which point to the addresses in ICPC where the first hit on each chamber is stored. The array NXCPC points from each location in ICPC to the location where the next hit on the same chamber is stored. The cyclical symmetry of the proportional chambers is maintained by setting the next pointer from the hit of highest wire address to point to that of lowest wire address. This data structure facilitates the deletion of hits:all that is required is the overwriting of the next pointer of the previous hit by the next pointer of the hit which is to be deleted.

The removal of bands of more than 3 adjacent hits is achieved as follows. First we step through the linked list until the hit address of the previous hit is different from that of the current hit by more than one. We maintain a pointer LK to the hit before the gap and a second pointer NRBEG to the first hit of the new cluster. We make a complete circuit of the chamber. On each step we first check whether the current hit is adjacent to the previous hit. If it is NSEQ is incremented and we continue to the next hit. Otherwise we have come across a new gap between clusters. In this case if NSEQ is less than 3 we set the last hit of a retained cluster LK to point to NRBEG,the first hit of the present cluster,so retaining the present cluster. LK is then reset to point to the last hit of the present cluster. Whether NSEQ was greater than 3 or not we zero NSEQ and set NRBEG to point to the current hit. If NSEQ was greater than 3 this step has effectively deleted the current cluster as the last hit of the last kept cluster can no longer be set to point to the first hit in the present cluster but may be set to point to the first hit of the new cluster at a later stage.

The algorithm is illustrated in Fig 4.10.

```
        LK     <- NC
       NRBEG <- NXCPC(NC)
        NC     <- NX
        NX     <- NXCPC(NC)
        NSEQ   <- 0
Do for I=1,NCPC(ICHAMB)
If MOD(ICPC(NX)-ICPC(NC),480).EQ.1
       then  NSEQ <- NSEQ+1
       else  If  NSEQ.LT.3
             then NXCPC(LK) <- NRBEG
                  LK        <- NC
             NSEQ  <- 0
             NRBEG <- NX
NC  <- NX
NX  <- NXCPC(NX)
```

FIG (4.10) Algorithm for Removal of Bands of Consecutive Hits

4.3.4.2 Replacing pairs of adjacent hits

A single pass is made through the linked list of each chamber. The wire addresses are doubled and copied into a new arrray ICPR which stores the hits sequentially. If two adjacent wires are found a single entry is made in ICPR of the odd numbered address between the doubled addresses of the two hits.

4.3.4.3 The hit search procedure

We often require to search for a hit on a specific chamber within a region ±4 in wire address about a specific wire address. Such a search may be repeated several times as we repeat the track reconstruction procedure from each initial hit as described in §4.3.2. To enable the search to be made rapidly an array LNPRO is constructed which points from every wire address on each chamber to the address of the nearest hit in a clockwise sense on the same chamber ie LNPRO('wire address','chamber')=address in ICPR of the nearest hit in a clockwise direction to 'wire address' on 'chamber'. This array is formed by a single loop over all wire addresses and hits in ICPR for each chamber as follows:

We fill the locations of LNPRO in descending order with the address of the first hit on the chamber. When we reach the location in LNPRO corresponding to the last hit on the chamber we fill LNPRO with this address and continue,filling LNPRO with this address until we reach the second last hit when we start to fill with this new address and so on until we have filled all 960 locations in LNPRO.

The search procedure using LNPRO is illustrated in Fig 4.11 for a search about wire number IWIRE on chamber CHAMBER.

```
      ISTART = IWIRE-4
->    IF(ICPR(LNPRO(ISTART),CHAMBER)>IWIRE+4) STOP
|     LNPRO(ISTART) is found hit
|     ISTART = ICPR(LNPRO(ISTART),CHAMBER)
-<--CONTINUE
```

FIG (4.11) Hit Search Procedure

We wish to find all hits on a specific chamber within ±4 of the wire address IWIRE. We examine LNPRO(IWIRE-4,'chamber') to find the

location INEAR in ICPR of the nearest hit in a clockwise direction. If ICPR(INEAR)>IWIRE+4 we know immediately that there are no hits within the search region. This single operation is much faster than the 9 operations which would be required if we had used a simple pointer from wire address to hit address. If ICPR(INEAR)<IWIRE+4 then INEAR is the address of a hit within our range and we must continue by examining LNPRO(ICPR(INEAR), 'chamber') to find further hits.

4.3.4.4 The depth-first search for links

The depth-first search for links described in §4.3.3 is implemented in the following way. The three arrays NEXT,IVERT,NOLD allow the recursive search on hits. NEXT consists of two parts. The first 999 elements are addressed as the basic hit list and store a pointer from the hit to a location in the second half of next,whenever a link has been made from the hit to some other hit. If further hits are associated to this hit then the element in the second half of NEXT is filled to point to the next element again and so on. The array IVERT is addressed as NEXT and the elements are

filled with the addresses of the hits at the head of the links. Fig 4.12 shows how hit 10 might point to hits 20 & 21.

ARRAY ELEMENT	10	1000	1001	1002
NEXT	1000	1001	1002	0
IVERT		20	21	
NOLD	5			

FIG (4.12)

The array NOLD enables the recursion to unwind by pointing back to the hit at the tail of the link. Fig 4.12 shows that we came to hit 10 by associating it with hit 5. A logical array MPHIX,addressed as the hits (as is ICPC), is used to indicate when a hit has been previously visited and so prevent multiple searches from the same hit.

The complete algorithm is given in Fig 4.13.

```
      NOLD(NSTERT) = 0
      IH = NSTART
    1 CONTINUE
      search from hit IH
      NEXT(IH)=0
      IF(MPHIX(IH)) GO TO 102
       go on to next chamber
       search for hits
       NEDGE=NEDGE+1
       IF(NEXT(IH).EQ.0) NEXT(IH)=NEDGE
       IF(NEXT(IH).NE.0) NEXT(NEDGE)=NEDGE+1
       IVERT(NEDGE)=IX
        store link IH—IX
      have collected all links from IH
      IF(NEXT(IH).NE.0) NEXT(NEDGE) = 0
  102 CONTINUE
      advance to new IH
      NX=NEXT(IH)
      IF(NX.eq.0) GO TO 2
      NEXT(IH) = NEXT(NX)
      IHNEW    = IVERT(NX)
      NOLD(IHNEW)=IH
      IH=IHNEW
      search from new hit
      GO TO 1
    2 CONTINUE
      backstep
      IF(NOLD(IH).EQ.0) GO TO 107
      IH = NOLD(IH)
      GO TO 102
  107 STOP
```

FIG (4.13) Depth First Search For Links

The setting up of NEXT and IVERT when links are formed has just been described. To advance to a search from a new hit we set the current hit IH to that pointed to by NEXT(IH),reset NEXT(IH) to point to the next hit associated to IH if any,and set NOLD to point from

the new current hit to the old IH. For the example of Fig 4.12,hit 20 would be selected,NEXT(10) would be set to 1001 and NOLD(20) set to 10. If there are no further hits to consider ie if NEXT(IH)=0 then we backstep to the previously considered hit NOLD(IH) and attempt to advance to further hits associated to this hit. The algorithm ends on return to the initial root hit NSTART.

4.3.4.5 The depth-first climb on links

This final step makes a depth-first traversal of the graph defined by the links constructed by the algorithm of the previous section. This traversal enumerates all possible paths. The best path is chosen and retained as a possible track candidate.

4.4 Z RECONSTRUCTION WITH THE CPC CATHODE STRIP READOUT

For each track of three or four associated anode hits we can attempt to reconstruct the position of the origin of the track along the beam axis using the information from the cathode strips. The intersection of the cathode strip helices with peak pulse heights

and the anode wire of the track in each proportional chamber provides a list of possible z coordinates of the track at the radius of the anode wire. The trajectory of the track in the coordinates r,z is approximately a straight line for tracks with no significant curve in the CPC. The pattern recognition problem is to recognise the straight line associating the (r,z) points from the 8 layers of cathode strips. A simple road algorithm was used. A point from the innermost and a point from the outermost chamber defined one possible solution. All hits within a road five times wider than the resolution were collected and a fit was made to each permutation,if there were hits on at least as many chambers as the best solution found. All points on the innermost and outermost chambers were allowed to form roads and if no solution was found hits on the other chambers were also used to define roads. The true solution was taken as that with the least χ^2 for the most hits.

4.5 SELECTION OF 2-PRONG EVENTS

This section describes how the CPC trackfinder can be used to select 2-prong events of interest from all triggered events. The

specific task was to select 2-prong events not chosen by the standard procedure.

Events were selected by requiring that exactly 2 tracks were identified by the CPC anode track finder and that at least one of these tracks was reconstructed in z using the cathode strips to have a z_0 of less than 4cm.

Table 4.2 shows the result of an examination of 4 PASS1 tapes.

TAPE	T2442	T2448	T2212	T2198
#triggers	15,243	13,086	12,676	13,147
EXCLUDE because				
LAEC trigger	1052	781	349	485
FOREST $\geq$2r-φ,$\geq$1r-φ-z	5538	4236	4281	5474
$\geq$3r-φ	290	225	252	275
2r-φ,same charge	437	333	419	434
therefore consider				
#events	9,456	12,727	7,589	7,584
CUTS				
2 anode tracks	1020	893	917	872
|z0|<4cm,$\geq$1 track	186	151	82	89
MILL				
BHASEL	62	48	10	8
COPLANAR 2-prong	13	7	2	4
DC PREPRO setting	220	220	324	324

TABLE 4.2 2-PRONG SELECTION

Triggers which passed the standard selection cuts and events with 2 tracks of the same charge reconstructed by FOREST were excluded. Triggers with a liquid-argon endcap trigger were also not considered as these contain tracks at small angles to the beam direction which do not traverse the large drift chamber and so are not reconstructed by FOREST. Such events would however be

unnecessarily selected by the CPC track finder. The remaining events,~9000 per tape were analysed by the CPC track finder. This required ~4 minutes CPU time for each tape. Some 900 events had 2 reconstructed tracks but only ~100 events satisfied the z requirement in addition. These events were processed by the MILL program to reconstruct tracks using both the drift chamber and CPC information and the standard cuts applied to the events thus reconstructed. From the 4 tapes,26 additional coplanar 2-prong events had been selected. The MILL program used an additional 4 minutes CPC time per tape.

The efficiency of the CPC track finder was estimated by processing 6000 MILLed 2-prongs selected for $\gamma\gamma$ physics analysis. Two anode tracks were identified with an efficiency of 93±1.0%. The z requirement was found to have an efficiency of 97.9±1.0%. The combined efficiency was 91.1±1.2%. Thus this method can select 2-prong events with an efficiency of ~91%. The FOREST selection procedure is estimated to have inefficiencies of 5% (25%) for coplanar (noncoplanar) 2-prong events[16]. The selection method presented is essentially independent so the inefficiency of the combined procedures is 2% (8%) for coplanar (noncoplanar) 2-prong events.

The single track efficiency is shown in Fig 4.14 as a function of the momentum of the track transverse to the beam direction. It is greater than that of FOREST and extends to lower momenta.

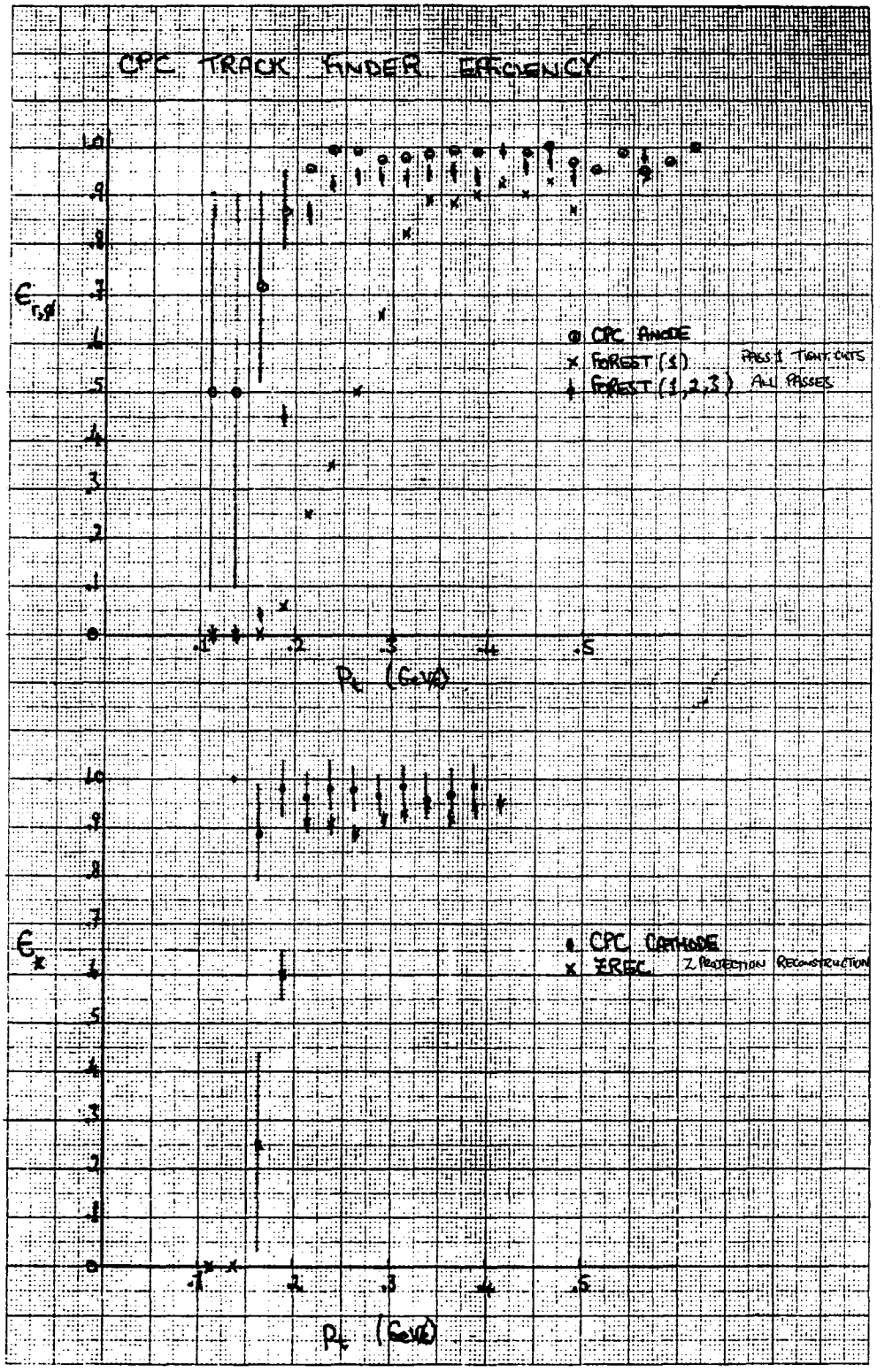

Figure 4.14

5.0 THE FOREST AND MILL TRACK RECONSTRUCTION PROGRAMS

5.1 INTRODUCTION

This chapter briefly summerises the operation of the standard TASSO track reconstruction programs FOREST and MILL. These were written by H.Kowalski[19] and D.G.Cassel[17] and are described in more detail in the references.

Both programs search for tracks in the large drift chamber using a tree algorithm. FOREST is used as a fast filter to select events which contain charged tracks coming from the interaction region. MILL is used to provide track reconstruction for physics analysis. It uses the same tree algorithm but with looser requirements on the links. This provides a first reconstruction and defines roads. It then uses a road algorithm to make the final reconstruction and include the CPC anode hits. The CPC cathode hits are not used.

Tracks are reconstructed in 3-dimensions by first reconstructing the circular projection of the track helix in the plane perpendicular to the magnetic field (r-φ plane) using the hits on the 9 layers of wires which run parallel to the field (the 0° wires). Given

the track circle in r-φ hits on the 6 layers of drift cells which are inclined at a small angle to the field (α-wires) provide possible z positions along the track (see Chapter 7). In the coordinates s,the arc length round the track circle from its closest point of approach to the origin in the r-φ plane, and z, the coordinate along the beam axis, the track helix projection is a straight line. Thus the z reconstruction reduces to the recognition of the straight line amongst the (s,z) coordinates computed from the α-wire hits.

The search for track circles and the straight line reconstruction are both accomplished by the depth-first-search algorithm (see Chapter 4).

5.2 R-φ RECONSTRUCTION

The search for circles among the hits on the 0° layers is carried out in a similar way to that described in Chapter 4 for the reconstruction of tracks from the hits on the CPC anode wires. First hit wires on nearby layers with similar φ angles are associated. Next links are formed between hits;the left-right ambiguity gives two hits for every wire so that 2 neighbouring wires give 4 links. The

curvature, κ, of a link is defined as the curvature of the circle joining the two hits of the link and the origin. It is given by:

$$\kappa = 1/(2R) = (\varphi_1-\varphi_2)/(r_1-r_2)$$

where φ_1,φ_2 are the φ positions of the hits, r_1,r_2 are the radii of the hit cells, and R is the circle radius. All links with a curvature less than a maximum value κ_{max} are stored. The link list is then ordered according to increasing κ. This biases the search towards finding the high momentum tracks first. The ordering helps to optimize the speed of the search as the links for a real track are gathered together near the beginning of the list, and nearly all long chains including bad hits require links appearing later in the list.

The links are pulled out of the list one by one and associated to those links already removed from the list which share a hit and which do not differ greatly in curvature. These links and associations form the vertices and edges of a graph. The new link is used as the starting vertex for a depth-first traversal of the graph. By climbing in both directions the longest chain including the new link is found. If not all layers are crossed additional links are taken from the list. If the found chain is not extended by these links the

search is stopped. The hits on the found chains are fitted and the chain with the least χ^2 for the most hits selected as the best track.

The MILL program gathers all hits near the found track and fits all permutations to ensure that the best solution has been reconstructed. In addition the CPC anode hits near the found track are included in the fit.

After a track is found and accepted all hits from drift chamber wires used in the track are cancelled from the active hit list to prevent their reappearance in subsequent tracks.

5.3 S-Z RECONSTRUCTION

The s-z reconstruction using the 6 α-wire layers is performed by a highly systematic and exhaustive search for straight lines. First links are formed between hits on adjacent chambers provided the hits project within some maximum distance from the origin on the z-axis. A depth-first traversal is made from the links between the two innermost chambers and so all 6 hit chains are found and fitted. If a 6 hit track is found with an acceptable χ^2 and a small z_0

the search stops. Otherwise links which span one chamber are formed. All possible 5 hit tracks are then constructed by a) climbing outwards from all links between the 2nd and 3rd innermost chambers b) deleting hits on the outermost chamber from 6 hit tracks and c) climbing in both directions from links which span one chamber. If no acceptable 5 hit track is found, 4 and 3 hit tracks are constructed by considering also links spanning 2 and 3 chambers.

This z-reconstruction algorithm is used both by FOREST and by MILL.

6.0 HIGH PRECISION VERTEX DETECTOR

6.1 INTRODUCTION

In 1981 it was proposed[20] that the removal of the aluminium beampipe and its replacement by a thin-walled beryllium beampipe and high precision drift chamber mounted inside the CPC would significantly enhance TASSO's performance in several physics areas. This chapter describes the physics motivations for and the design of the vertex detector , and results of initial tests using cosmic rays and PETRA data.

The main aim of the vertex detector project is to greatly improve the precision with which charged tracks can be projected to their point of closest approach to the event vertex. The importance of this quantity (d_0) (see Fig 6.1) is that it determines the extent to which tracks originating from the primary interaction (primary tracks) can be separated from those due to secondary interactions and decays (secondary tracks).

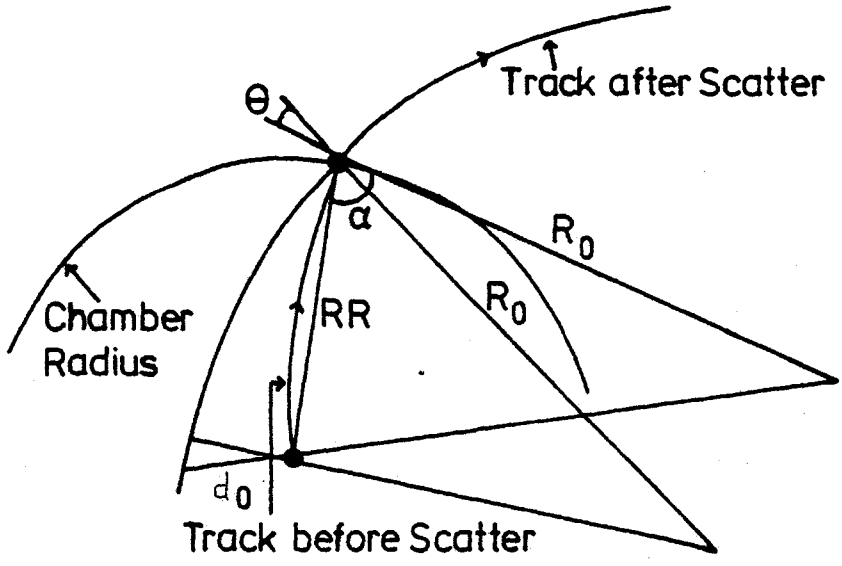

Fig. 6.1

Figure 6.1

6.2 ANTICIPATED PHYSICS BENEFITS

Based on Monte-Carlo studies the following physics benefits are expected if a spatial resolution of 50 μm can be achieved.

1. Charmed meson lifetimes. Greatly improved sensitivity for the measurement of the lifetime of short-lived particles, particularly the D^0 meson is expected (see section 6.3).
2. B meson lifetime. High energy leptons with large transverse momentum (p_t) with respect to the jet axis in two jet like annihilation events result primarily from the leptonic decay of heavy mesons. Thus measurement of the d_0 for high p_t muon tracks will allow a measurement of the lifetime of the $B^{\pm}$ mesons.
3. The study of the τ lepton. The major source of background in previous studies [24],Bhabhas with a converting photon,will be reduced by a factor of ten due to there being less material in the beampipe. The measurement of the τ lepton lifetime is an important check on e,μ,τ universality. It is measured by comparing reconstructed 3-prong decay vertices with the mean beam position,or by measuring the separation ot the vertices in 6-prong τ pair events. The predicted lifetime of $2.8\pm0.2*10^{-13}$

s leads to an expected decay length of ~1.5mm at E_{cm}=38GeV. We estimate that with the vertex detector we will be able to measure the τ lifetime with a statistical error of 6% with ~1000 τ pairs.

4. The detection efficiency for strange particles. The detection efficiency for $K^0_s \rightarrow \pi^+ \pi^-$ decays will improve from ~20% to ~55% and for $\Lambda \rightarrow p \pi^-$ by a factor of 3.

5. K^0_s mass resolution. The K^0_s mass resolution will become 17MeV rather than 21Mev.

6. The detection of Σ^- particles. Approximately 25% of Σ^- particles with momentum of at least 1GeV will decay beyond the first layer of the high precision detector so that the measurement of strange charged baryons may become feasible.

7. The study of hadronic resonances. Improved isolation of secondary tracks will reduce background in the study of hadronic resonances such as the vector meson ρ^0.

6.3 D MESON LIFETIME MEASUREMENT

Recent results suggest that the $D^{\pm}$ lifetime is 9.10^{-13} s and the D^0 lifetime is 4.10^{-13} s [25]. D^0 events can be isolated by observation of the decay of D^{*+} mesons. through the decay channel:

$$D^{*\pm} \rightarrow D^0 \pi^{\pm}$$

$$D^0 \rightarrow K^{\pm} \pi^{\pm}$$

using the fact that the D^* decay has a very low Q value. By reconstructing the primary vertex and the D^0 decay vertex we will be able to measure the lifetime of the D^0. This method is particularly appealing as the selection of the D^0 decay products,unlike previous measurements from emulsion experiments and hybrid bubble chamber experiments,does not require observation of a secondary vertex so that the lifetime measurement may be less sensitive to systematic error. The hard charm fragmentation in e^+e^- annihilations [26] provides D mesons of high momenta so that the expected decay lengths are of the order of 500 μm.

In addition it may be possible to directly tag charm events and measure the charged D lifetime but this problem,although eased by

the somewhat longer lifetime of the $D^{\pm}$ is considerably more difficult because events must be selected by the identification of secondary charged track vertices. Nevertheless preliminary Monte-Carlo studies indicate that with a $D^{\pm}$ lifetime of $\sim 9.10^{-13}$s a tagging efficiency of about 7% of all accepted $c\bar{c}$ events may be achievable with a signal to background ratio of ~2:1.

6.4 VERTEX CHAMBER DESIGN

6.4.1 General considerations

The above physics aims together with the environment within which the vertex detector must operate dictate the design of both the chamber and beampipe. The precision with which the impact parameter (d_0) of tracks can be measured is limited for low momentum tracks by multiple scattering in the material between the first tracking chambers and the interaction point. For tracks of large momenta the spatial precision of the measurements from the first tracking chambers and their distance from the interaction point are the limiting factors.

Small angle multiple scattering results in an RMS scattering angle projected onto a plane of $\Theta_{2D} \sim 0.015\ E\ \sqrt{xx}\ /\ p^2$ where xx is the thickness of the scatterer in radiation lengths and E and p are the particle energy and momentum. This leads to an RMS d_0 of (see Fig.6.1)

$$d_0 = RO - \sqrt{\{RO^2 + RR^2 - RO.RR.\cos(\alpha \pm \Theta_{2D})\}}$$

$$\sim RR.\Theta_{2D}$$

where RR=radius of scatterer

RO=radius of track circle

and $\alpha = \text{acos}(RR/2RO)$

and RO is given by $p_t = 3.10^{-4}|BFIELD|.RO$ where

p_t is the particle momentum component transverse to the magnetic field direction.

Table 6.1 gives the expected RMS Θ and d_0 for tracks at $\cos\vartheta = 0$ of various p_t, both for the old beampipe and the new beampipe. For the new beampipe the rms d_0 is smaller by a factor of ~ 7.

OLD BEAMPIPE	XX=0.0715	RR=13.85cm
pt (GeV/c)	ϑ(2d) (mrad)	DO (RMS) (μm)
0.1	68.7	9515
1.0	4.0	554
10.0	0.4	55
NEW BEAMPIPE	XX=0.0061	RR= 6.80cm
pt (GeV/c)	ϑ(2d) (mrad)	DO (RMS) (μm)
0.1	20.1	1367
1.0	1.2	82
10.0	0.12	8.2

TABLE 6.1 Effect of Multiple Coulomb Scattering

To obtain sufficient mechanical strength and stability (the beampipe must be leak-tight and must withstand the heating caused by the beam) and yet cause as little scattering as possible,the beampipe was constructed of 0.17cm thick beryllium.

The error in d_0 coming from the spatial resolution of the chamber can be estimated following Gluckstern [22]. For a straight line

fit to N points spanning a distance L ,being equally spaced and having equal error σ_{point}

$$\sigma_{gradient}=\sigma_{point}/L\sqrt{12(N-1)/N/(N+1)}$$

$$\sigma_{intercept}=\sigma_{point}\sqrt{2(2N+1)/N/(N+1)} \ .$$

To estimate the error on d_0 we extrapolate the fit by a distance ~L by

$$\sigma_{d0}^2 = \sigma_{intercept}^2+L^2\sigma_{gradient}^2$$

→ For N=8 $\sigma_{d0}\sim 1.33\sigma_{point}$

In our application we should consider a circle fit and unequal spacing and resolutions but this estimate shows that the error $\sigma_{d0} \sim \sigma_{point}$. Hence to achieve a σ_{d0} of ~100μm as required by the physics aims presented above we must achieve a point resolution σ_{point} in the range 50-100μm.

The device must function satisfactorily very close to the circulating beam,where the main backgrounds result from synchrotron radiation and off-momentum particles. Although solid-state detectors can achieve better resolutions than drift chambers practical

devices have not yet been developed which can withstand the backgrounds in storage rings and provide a sufficiently large area coverage [21]. This lead to the choice of a drift chamber. A typical resolution of the large drift chamber is ~200μm while the TASSO vertex detector design aims to achieve a resolution of ~50μm.

The overall design of the chamber was based on the observation that, very near to the interaction point,all tracks are approximately radial. The chamber is therfore radially symmetric from the interaction point. The outer radius of 15cm is fixed by the inner radius of the CPC (see Chapter 3). The inner radius of 8cm is fixed by the requirement to keep outside the cone of synchrotron radiation which floods down the beampipe from the upstream quadrupole and bending magnets.

To reduce the synchrotron radiation background a copper layer of ~15μm thickness was sputtered onto the inside of the beryllium beampipe. Synchrotron radiation photons of less than 40keV are absorbed by the K shell of the Cu nuclei. The resulting fluoresence reemits photons of 8.4keV. Provision was made for the inclusion of a layer of Xenon gas round the outside of the beampipe to absorb

these low energy photons. This has however not yet been required and so is filled with the normal chamber gas.

The granularity of the detector must be high to allow efficient measurement of the tracks within a jet. However the total number of sense wires is limited by the physical size of the chamber and the congestion of connections at the endplates. Monte-Carlo studies showed that a chamber of 8 layers of ~0.8cm cells (~1000 sense wires) equipped with single hit electronics should resolve >95% of all tracks at E_{cm}=30GeV.

6.4.2 Drift cell design

The design of the drift cell is based on the fact that,for good resolution,only the electrons produced near the point of the track closest to the sense wire are of interest. This leads to the design of the 'unit cell' as shown in Fig 6.2. The two field wires help to focus electrons towards the sense wire, thereby collecting electrons only from the track segment near to the sense wire,whereas a single field wire would collect electrons from a larger length of the track. The two field wires have the same potential. If the charge on the

sense wire is Q,the field wires will each have charge -Q/2 (not quite exact in the real chamber due to curvature). The repulsion of the field wires is balanced by the attraction of the the sense wires on either side when $d/l=1/\sqrt{7}$ (see Fig 6.3). This ratio seems quite suitable for focussing electrons and was therefore chosen in the design.

The high density of electrical connections required that the field wires be grounded and the sense wires raised to high voltage.

The cells at different radii can be made to operate similarly. Consider a system of parallel wires at positions $\vec{r}_i$ with charges per unit length Q_i , i=1,n. The field $\vec{E}$ at some point $\vec{r}$ is

$$\vec{E} \propto \sum_{i=1}^{n} Q_i(\vec{r}-\vec{r}_i)/\ |\vec{r}-\vec{r}_i|^2 \quad .$$

If we alter all distances and charges by the same factor,$\vec{E}$ remains invariant. Hence if we choose the wire potentials so that each charge scales with the radial position of the corresponding sense wire,electrons produced at corresponding points in cells of different radii all experience the same $\vec{E}$ and therefore move with the same drift speed. Furthermore,as the magnetic field B is constant

with r and the Lorentz angle depends on $\vec{v}\times\vec{B}/\vec{E}$,they all move in the same direction. However the reflection of this scaling in the measured drift times will be spoilt to some extent as diffusion,length of useful drift path and electronic thresholds do not scale.

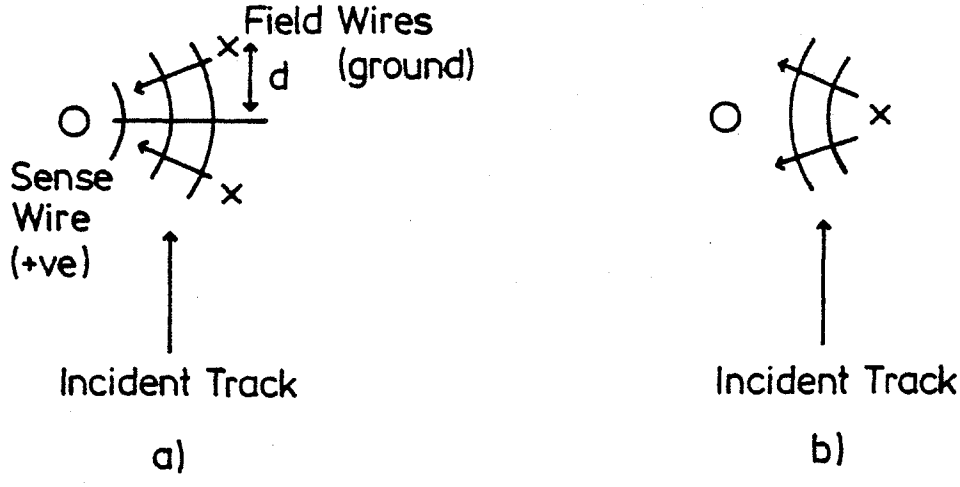

Figure 6.2

The chosen cell configuration is shown in Fig 6.4. There are 8 layers of cells arranged in two groups of 4. The inner four layers have 72 cells and the outer four 108 cells each. The cells on adjacent layers are offset by half a cell width so that the sense wires are aligned with the field wires of the adjacent layer. This means that tracks do not in general pass through the same relative position within the cell on each layer and that the incorrect drift-time ambiguities do not align and hence will not lead to spurious tracks.

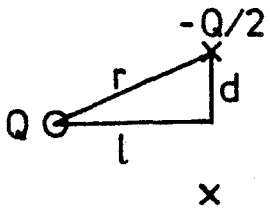

Force out $= \frac{Q}{2}\frac{Q}{2}\frac{1}{2d}$

Force in $= 2Q\frac{Q}{2}\frac{l}{r}\frac{d}{r}$

Balance $r^2 = 8d^2$ i.e. $l^2 = 7.d^2$

Figure 6.3

This feature also improves the 2 track resolution. Between the two groups is a layer of anode wires to collect low energy electrons.

The design was studied in some detail with a computer simulation. Given the positions and voltages of all the wires,the charge on each wire was calculated. From these charges the field at any point can be determined. The field and field gradients at each wire were calculated. It was found that the resulting deflecting forces are small and do not set a significant restraint on the minimum wire tension needed for stability.

The basic ionizable medium was Ar to which CO_2 was added in the ratio 90%Ar to 10%CO_2. The CO_2 quenches low energy photons produced by the avalanche near the anode wires. The chamber was designed to withstand a pressure of 3 atmospheres above atmospheric. Increasing the gas pressure increases the number of ions produced along the track and so reduces the fluctuations of ionisation statistics.

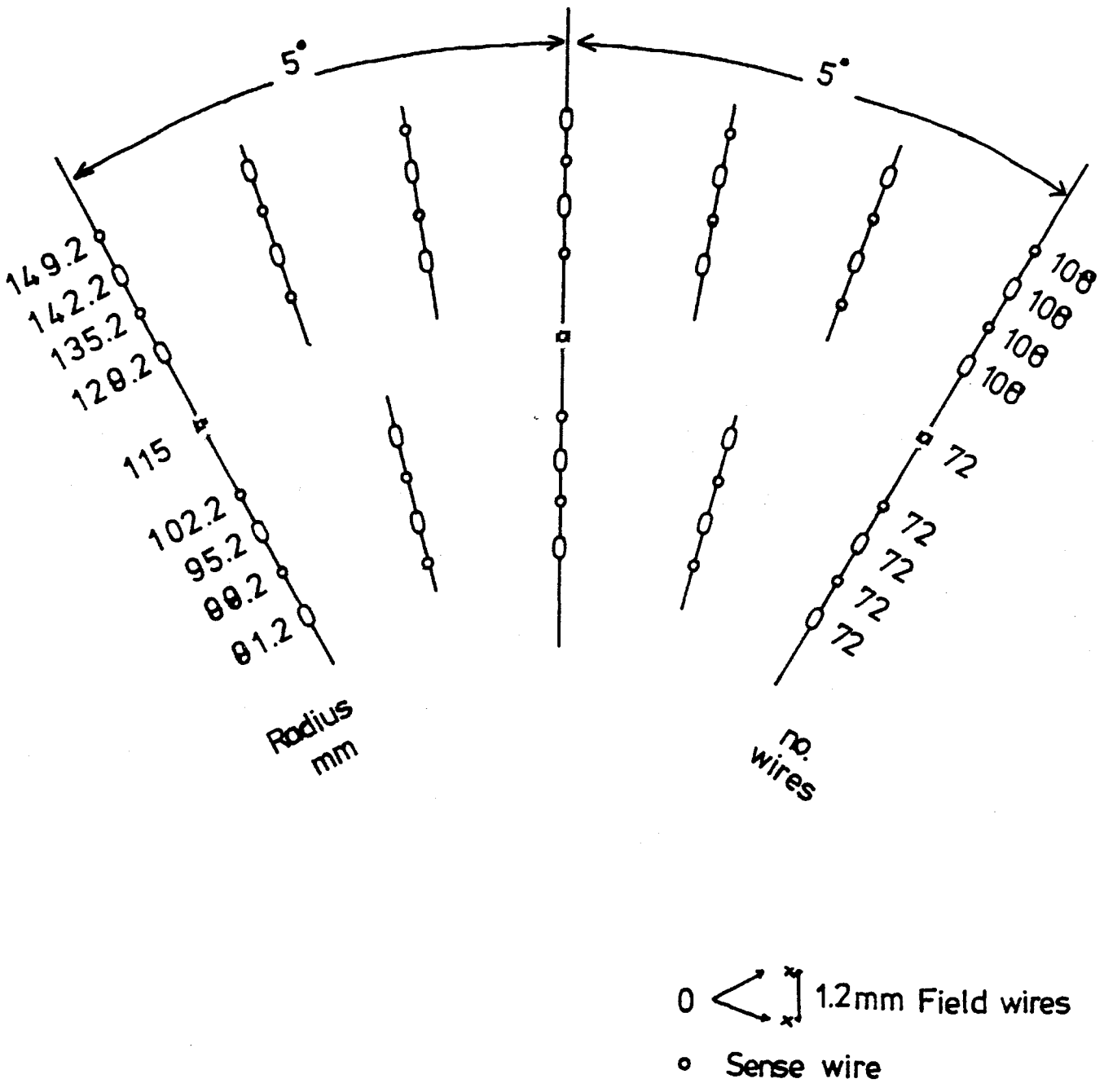
5°
5°
149.2
142.2
135.2
128.2
115
102.2
95.2
88.2
81.2
Radius mm
108
108
108
108
72
72
72
72
72
no. wires
0
1.2mm Field wires
Sense wire

Figure 6.4

6.4.3 Chamber electronics.

The design of the electronics is dominated by the requirement of detecting the arrival of the first few electrons at the sense wire. An amplifier is therefore required with excellent slewing characteristics and good stability. The amplifier/discriminator was designed by D.J.White of RAL and is based on observing the zero-cross from a constant fraction discriminator circuit. The results of tests made on this amplifier using simulated drift chamber pulses are shown in Fig 6.5. Performance is good for a range of attenuations between 5 and 45 dBs, with a time slew of less than 200 picoseconds in this range.

The output from the amplifier/discriminator is fed into a LeCroy 4291B TDC system with a least count of 500 ps. The analogue output is fed into an ADC system which allows a measurement of the z coordinate by charge division. Only sense wires on chambers 3,4,7 & 8 are equipped with ADCs.

For test purposes the TDC system was readout by an LSI11 minicomputer which wrote the data on magnetic tape for later analysis. During normal PETRA data taking the vertex detector TDC system

was readout by the NORD10 computer which performs also readout from the rest of the TASSO experiment and online monitoring tasks (see §2).

The TDC system employs self-calibration with an internal pulse generator. This sets both slope and offset corrections for every channel. Calibration was repeated before each data taking run. The resulting corrections did not drift by more than one count per day.

Fig 6.6 shows the electrical connections to the chamber.

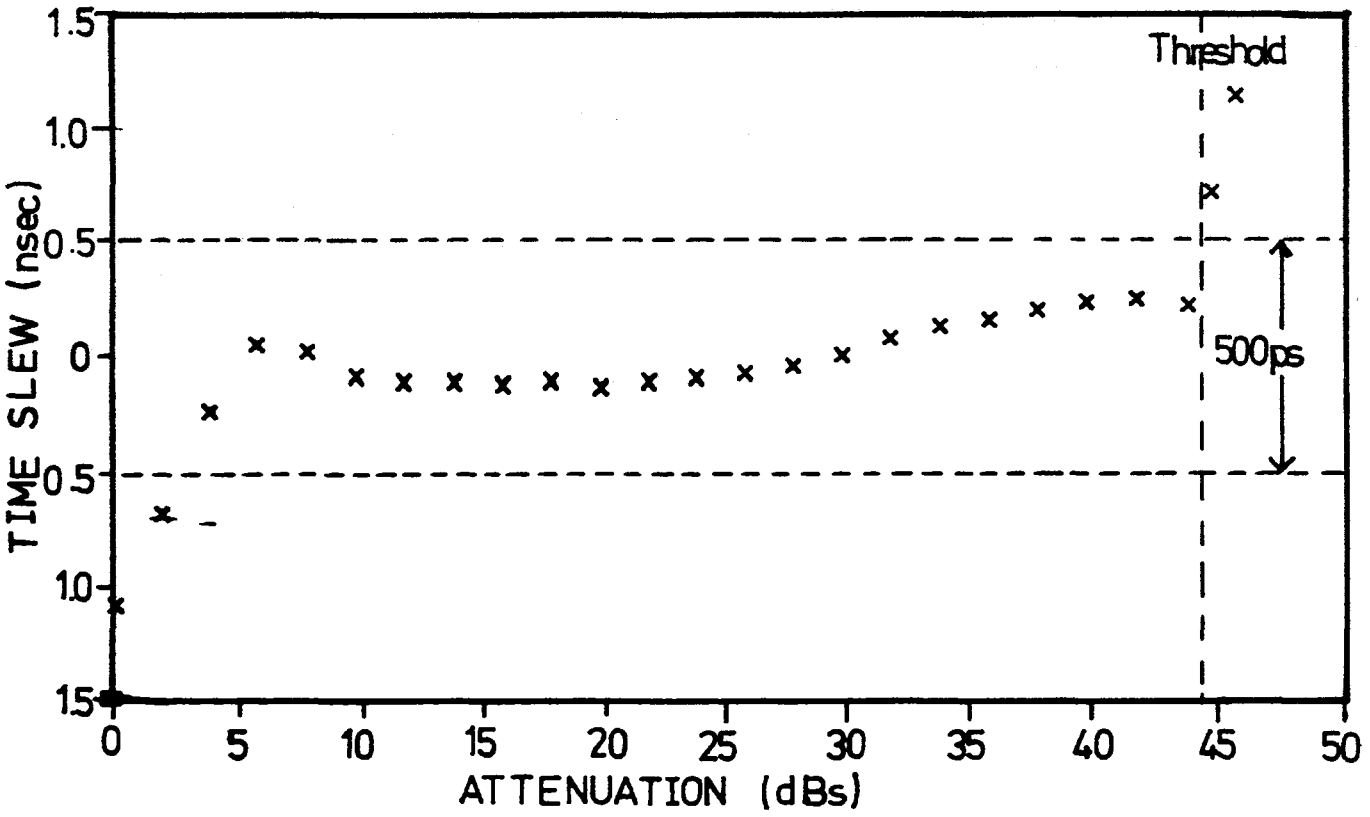

Figure 6.5 Time slew v attenuation

The vertex detector/beampipe assembly was installed within TASSO during the shutdown of PETRA in August 1982. The critical dimensions are summarised in Table 6.2.

Inner Radius (cm)	Material	Thick-ness (cm)	Radia-tion length (%)	Extreme position in z (cm)	what
6.6665	Cu	0.0015	0.10	19.75	Coating of Beampipe
6.668	Be	0.17	0.51	19.75	Beampipe
6.848	70% Ar/ 30% CO_2	0.644	0.0006	19.75	"Xenon" chamber
7.496	Kapton	0.0125	0.04	28.28	Equipot-ential
7.509	Al	0.005	0.06	28.28	Equipot-ential
~11.46	70% Ar/ 30% CO_2at 1.2atm.	7.89	0.07	29.37	Gas
15.40	Cu	0.0030	0.2	29.37	Equipot-ential
15.403	Kapton	0.0125	0.04	29.37	"
15.95	Al	0.15	1.69	40.6	Pressure vessel

TABLE 6.2a Specifications of the Vertex Detector.

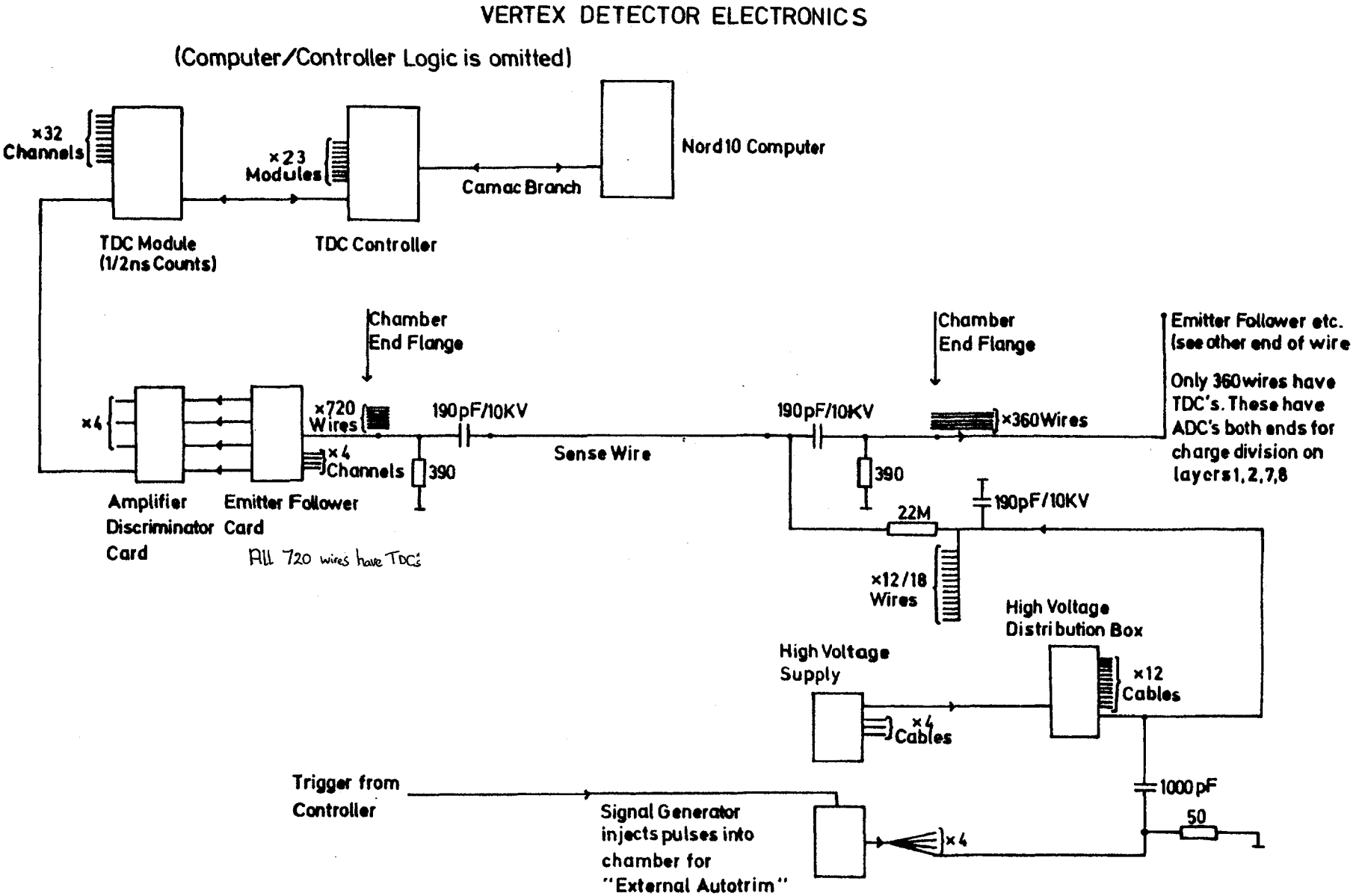
VERTEX DETECTOR ELECTRONICS
(Computer/Controller Logic is omitted)
×32 Channels
TDC Module (1/2ns Counts)
×23 Modules
TDC Controller
Camac Branch
Nord10 Computer
Chamber End Flange
Chamber End Flange
Emitter Follower etc. (see other end of wire
Only 360 wires have TDC's. These have ADC's both ends for charge division on layers 1, 2, 7, 8
×4
×720 Wires
190pF/10KV
Sense Wire
190pF/10KV
×360 Wires
×4 Channels
390
390
22M
190pF/10KV
Amplifier Discriminator Card
Emitter Follower Card
All 720 wires have TDCs
×12/18 Wires
High Voltage Distribution Box
High Voltage Supply
×12 Cables
×4 Cables
Trigger from Controller
Signal Generator injects pulses into chamber for "External Autotrim"
×4
1000pF
50

Figure 6.6

Total radiation length = 2.71%
Active length of chamber = 57.2cm
Sense wires: 720 * 20μm diameter, Tungsten-Rhenium
Field wires: 1440 * 100μm, Beryllium-copper,each pair is separated by 1.2mm.
Flanges: 1.2cm thick Al,inner face at z = ±29.4cm
2.0cm GFK ,inner face at z = ±40.6cm
Guard wires: 71 wires of 100μm diameter Be-Cu at a radius of 11.5cm

Radius of sense wire planes (cm)	# sense wires	Max. drift space (cm)
8.1	72	0.3534
8.8	72	0.3840
9.5	72	0.4145
10.2	72	0.4451
12.8	108	0.3723
13.5	108	0.3927
14.2	108	0.4131
14.9	108	0.4334

TABLE 6.2b More Specifications of the Vertex Detector

6.5 TESTS WITH COSMIC RAYS.

Cosmic ray muons provided clean single tracks invaluable for the study of the efficiency,resolution and positioning of the drift chambers the checking out of the associated electronics and read-

out system,free from the high trigger rates and backgrounds experienced during PETRA operation.

During cosmic ray tests the chamber was filled with a mixture of 90%Ar,10%CO_2 by volume at a pressure of 1 atmosphere. Argon is the basic ionisable medium and CO_2 provides quenching of the photons produced by the avalanche. Initially C_2H_6 was used instead of CO_2 but this was observed to form whiskers on the cathode wires.

The efficiency plateau curve (Fig 6.7) was measured by scanning events online and counting missing hits. The operating voltage is chosen to be slightly above the knee. The hit efficiency on the plateau was nearly 100%.

During cosmic ray data taking the TDCs were read out by the NORD and the data was sent to the IBM central computer. The events were reconstructed in the vertex detector using the program FELIX (see Chapter 7). A typical cosmic ray event is shown in Fig 6.8.

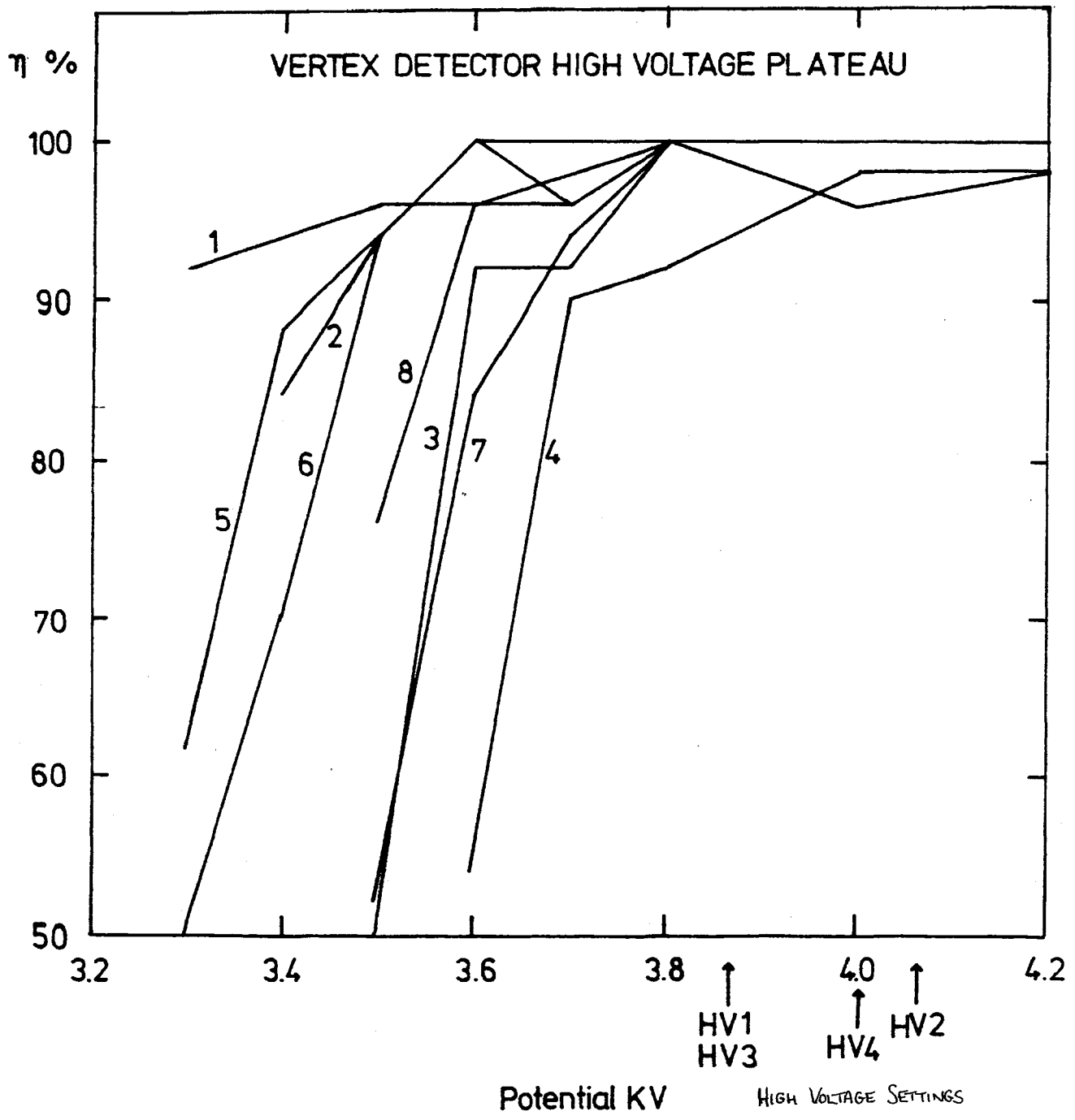
η %
VERTEX DETECTOR HIGH VOLTAGE PLATEAU
100
90
80
70
60
50
1
2
8
3
7
4
6
5
3.2
3.4
3.6
3.8
4.0
4.2
HV1
HV3
HV4
HV2
Potential KV
High Voltage Settings

Figure 6.7

6.6 DETERMINATION OF SPACE-DRIFT TIME RELATION.

The drift-distance drift-time relation was determined by an iterative procedure illustrated in Fig 6.9. The resulting relation is shown in Fig 6.10 for the 8 chambers. The corresponding distribution of the distance to the sense wire (Fig 6.11) is reasonably flat.

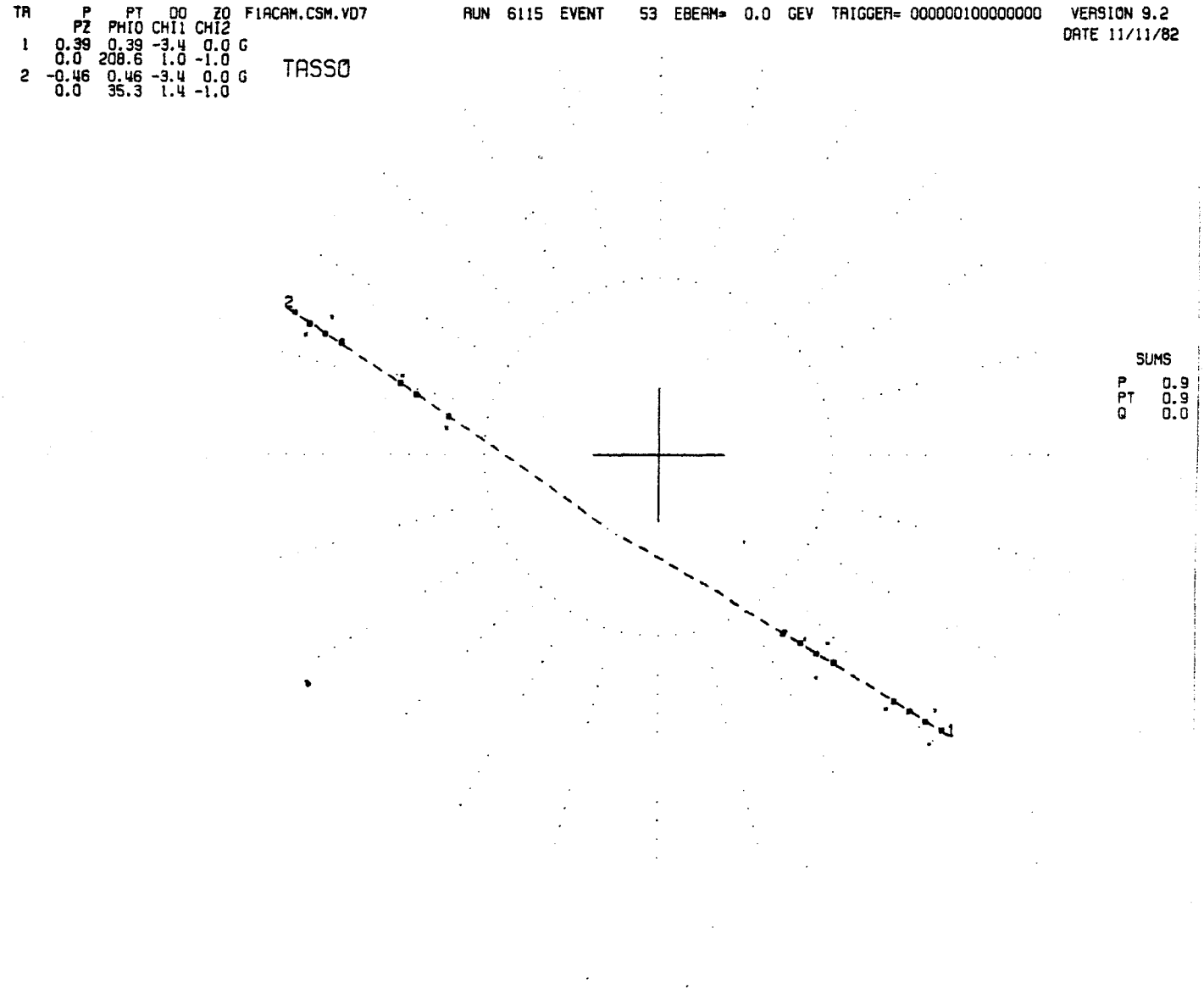

Figure 6.8 Cosmic ray event

1	Reconstruct tracks in VXD alone using FELIX	
2	Plot distance of track from sense wire v TDC count-Fit to quadratic over first 90% of cell-This is new drift-time drift-distance relation	
3	Has mean squared residual decreased significantly?	
YES		NO
4	Use this new relation to yield improved estimate of hit positions-return to 1.	Convergence-take current relation as best obtainable

FIG (6.9) Procedure for the Determination of the Space-Drift time Relation

A typical drift velocity near the centre of the cell was 0.0060cm/ns.

The residuals of the hits from the fitted tracks after drift time corrections showed no dependence on drift distance,the entrance angle of the track with the cell or the z position of the track in the chamber. The z position was found by reconstructing the track in the large drift chamber and CPC. A fit of a Gaussian to the distrib-

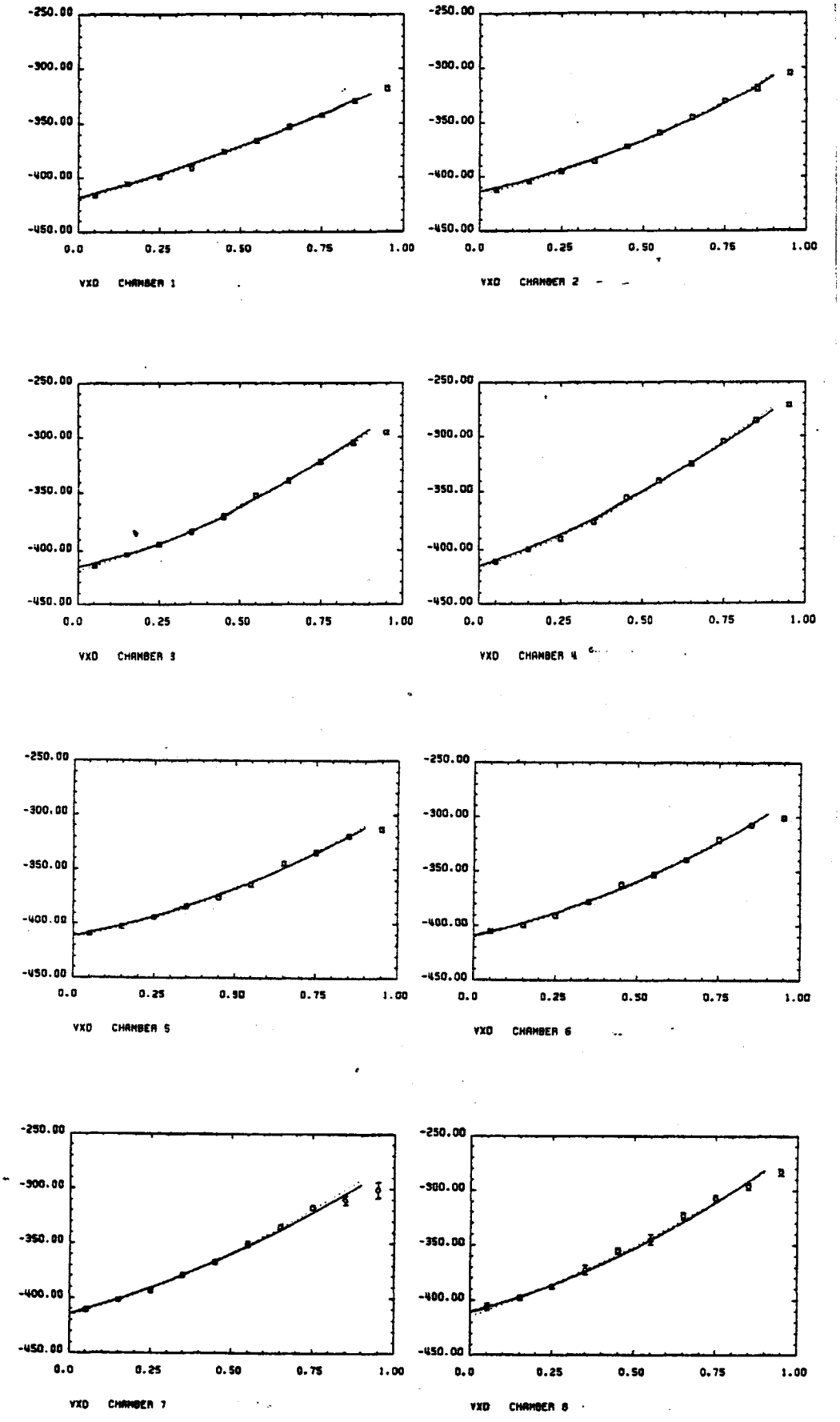

Figure 6.10 Space drift-time relation

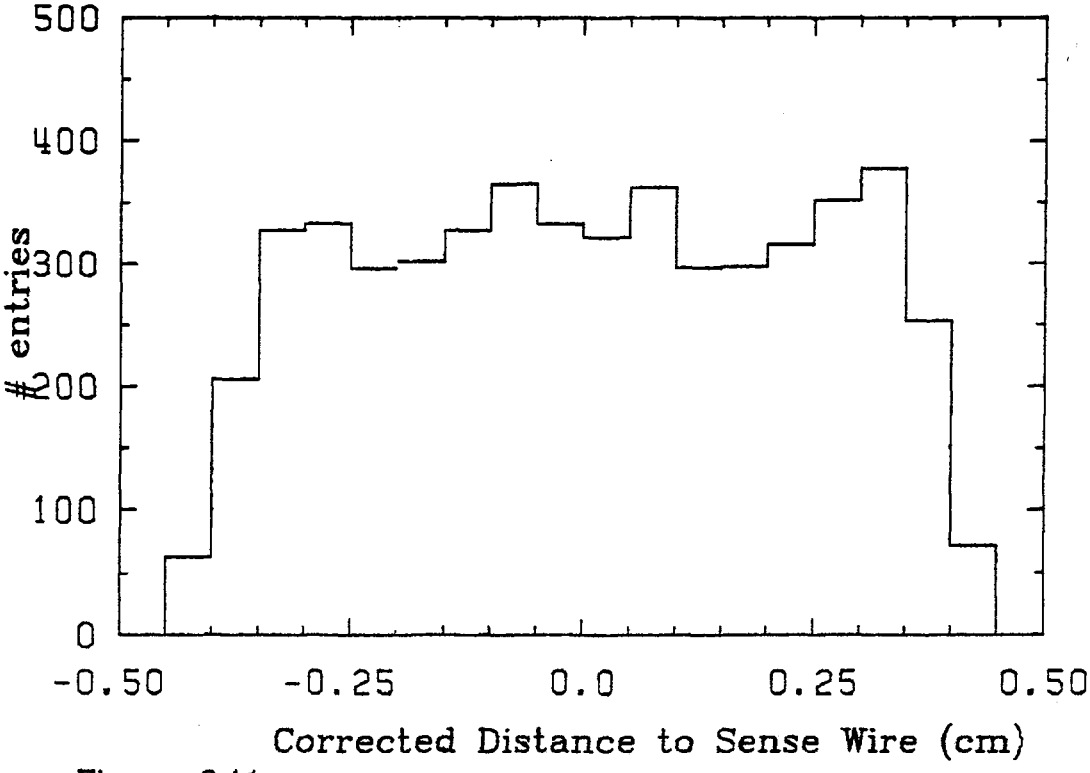

Figure 6.11

ution of residuals yielded resolutions ranging from 140μm for chamber 1 to 260μm for chamber 6. The average resolution was ~200μm. There were several reasons for this poor resolution. Firstly these results come from the first data taken after the installation of the detector within TASSO. The gas pressure was atmospheric rather than the design pressure of 4 bars. In addition there were many problems with the electronics which have since been detected and corrected. Latest results show resolutions of ~80 micron., despite the change in the chamber gas to avoid whisker formation. The parameters of the space-drift time relation,efficiencies and resolutions are given in Table 6.3.

Results from Cosmic Runs 6114 to 6117					
			$T=A+Bx+Cx^2$		
CHAMBER	$\varepsilon(\%)$	$\sigma(\mu m)$	A	B	C
1	98.2	142	-419.3	76.9	34.8
2	94.9	171	-416.3	72.4	54.8
3	96.7	186	-419.0	85.4	58.0
4	98.5	181	-417.3	100.1	66.2
5	97.5	213	-412.2	55.9	64.3
6	94.6	260	-409.8	68.5	63.0
7	95.3	252	-415.4	80.9	63.5
8	96.3	190	-414.5	103.0	47.8

T=-TDC counts x=drift distance(cm)

TABLE 6.3

6.7 DETERMINATION OF THE ALIGNMENT OF THE CHAMBER.

The cosmic ray data were also used to determine the geometrical position of the vertex detector with respect to the large cylindrical drift chamber. To avoid introducing systematic errors in track fits one needs to know this position to the same order as the resolution

of the chamber hits. The inaccessibility of the vertex detector when installed in situ within the CPC prevented the determination of its position by survey. Cosmic ray tracks were fitted to a single circle using the 0° chambers of the large drift chamber. The angular separation $\Delta\varphi$ between this circle and each hit vertex detector wire was plotted against the absolute φ value of the wire. Later drift time corrected hit positions rather than the hit wire positions were used (Fig 6.12). A sine-wave like curve is seen to result. The mean level,amplitude and phase give,respectively,the overall rotation of the chamber,the separation of the centre of the chamber from that of the big drift chamber and the direction of this separation. The result was:

POSITION OF VERTEX DETECTOR

x_{centre} = -0.33±0.01cm

y_{centre} = -0.18±0.01cm

$\varphi_{wire\ 0}$ = -0.0254±0.0002radians

The same distribution is shown in Fig 6.13 after correction for the found position and split into 3 regions in z along the chamber axis. There is no evidence for a tilt of the chamber axis with respect to

the axis of the large drift chamber. More data will allow the accuracy of the position measurement to be improved.

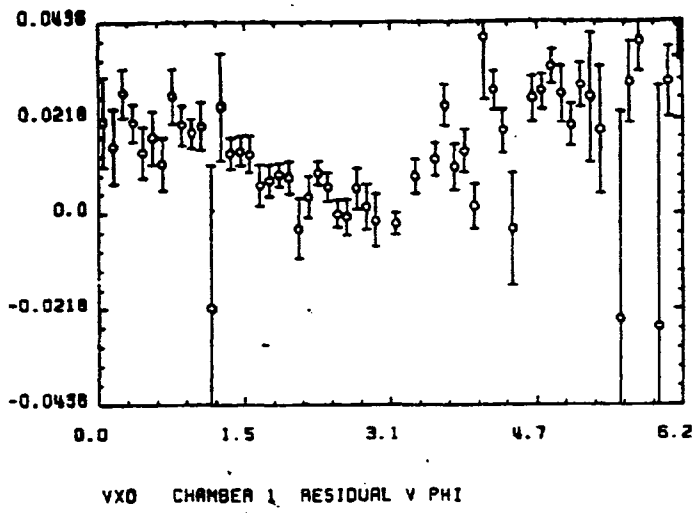

Figure 6.12

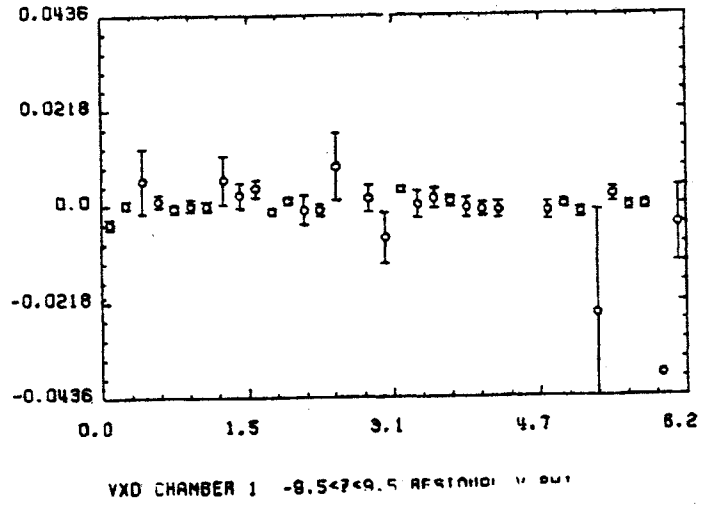

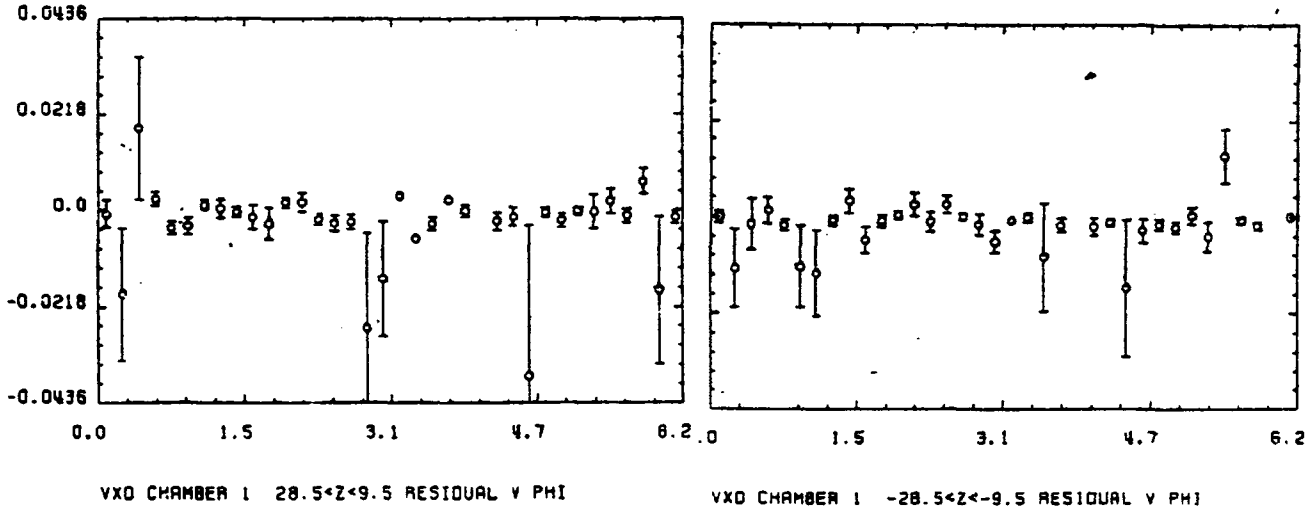

Figure 6.13

7.0 FELIX-CENTRAL DETECTOR TRACK RECONSTRUCTION PROGRAM

7.1 MOTIVATION

A new track recognition program developed by the author is presented in this chapter. Several problems needed to be tackled.

1. The track recognition program MILL does not make use of the CPC anode hits in the track recognition stage although these hits are added to the final fit;the CPC cathode information is not used at all. The use of these hits for track recognition,together with the CPC cathode hits for z reconstruction would allow increased track reconstruction efficiency for tracks at small angles to the beam axis.
2. The additional hits from the vertex detector posed the problem of how to enable further improvement to be made to the track reconstruction and fitting.
3. The development and testing of the vertex detector required the ability to reconstruct tracks of cosmic rays when only the vertex detector information was available.

To meet these requirements a flexible track reconstruction program was written which allows the user to specify the detector con-

figuration: the number of tracking chambers,their radii,granularity,type- drift chamber,proportional chamber,charge division,cathode strip etc. The track fit consists of a circle fit in the r-φ projection and a straight line fit to the s-z projection. A kink can be allowed for in the circle fit.

The following section describes the basic algorithm and the reason for its use. Section 7.3 presents its application to the r-φ recognition problem while section 7.4 describes its use to provide the z-reconstruction. The performance of the program is presented and compared to that of the MILL program in chapter 8.

7.2 THE BACKTRACK METHOD

FELIX employs as its basic driving algorithm not the depth first search algorithm used by FOREST (see chapters 4&5) but the backtrack method [27]. Nijenhuis and Wilf proposed the backtrack method as a reasonable approach to use on problems of exhaustive search when all possibilities must be enumerated or processed.

The method may be formulated mathematically as follows:We are required to find all the vectors $(a_1,a_2, \ldots a_n)$ of a given length n, whose entries $a_1,a_2,\ldots a_n$ satisfy a certain condition C. In the most naïve approach,we might first make a list of all possible vectors whose entries a_i lie within the range of the problem;then,from this list we could strike out all vectors which do not satisfy our condition C.

In the backtrack procedure,we grow the vector from left to right,and we test at each stage to see if our partially constructed vector has any chance to be extended to a vector which satisfies C. If not,we immediately reject the partial vector and go to the next one, thereby saving the effort of constructing the descendants of a clearly unsuitable partial vector.

Thus,at the kth stage (k=1,n),we have before us a partial vector

$$(a_1,a_2, \ldots ,a_{k-1})$$

which is not inconsistent with C. We construct from it the list of candidates for the kth position in our vector. To say that a partic-

ular element x is a candidate is just to say that the new partial vector

$$(a_1,a_2, \ldots ,a_{k-1},x)$$

does not yet show any irretrievable inconsistency with our condition C.

If there are no candidates for the kth position,ie,if for every x,the extended vector $(a_1,a_2, \ldots ,a_{k-1},x)$ is inconsistent with C, we "backtrack" by reducing k by 1,deleting a_{k-1} from the list of candidates for position k-1,and choosing the new occupant of the (k-1)th position from the reduced list of candidates.

If and when we reach k=n,we exit with $a_1,\ldots,a_n$. Upon reentry,we delete a_n from the list of candidates for position n and proceed as before.

The application of the backtrack method to track recognition is straightforward. A track is described by the vector $(a_1,a_2,\ldots,a_n)$ of the n hits assigned to it. The condition C that a partial vector

$(a_1,a_2,\ldots,a_n)$ be admissable is that its χ^2 probability for the partial vector to be a partial track is greater than some minimum value.

7.2.1 Computer Implementation

The computer implementation of this algorithm is performed by the routine BACKTR. The current vector or partial vector is stored in the array IOUT(I);I=1,KLEN. The list of possible candidates for each position up to the KLENth position in the partial vetor is kept in the first LSTK elements of the array ISTK in the form of a stack (see Fig 7.1).

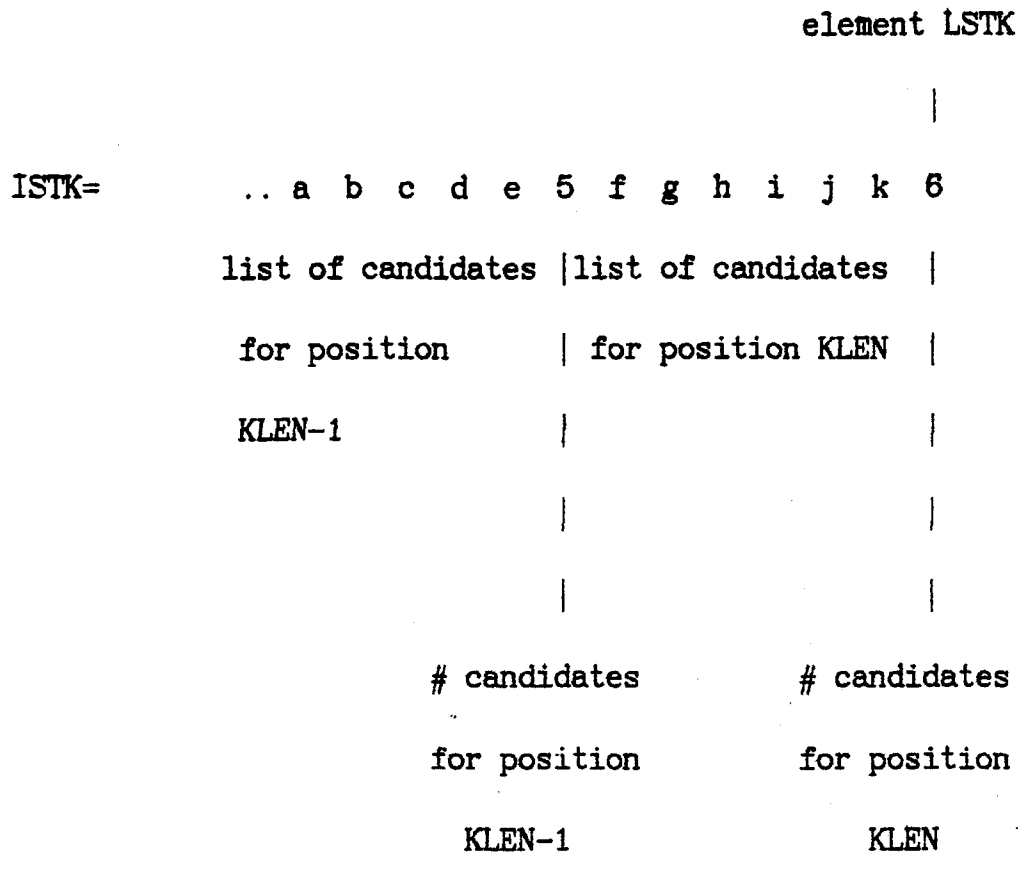

FIG (7.1) Layout of stack

A flow diagram of the procedure BACKTR is given in Fig 7.2.

The procedure is initiated by placing the N candidates for position 1 of the vector into the first N elements of the stack and setting LSTK=N+1;ISTK(LSTK)=N;KLEN=1.

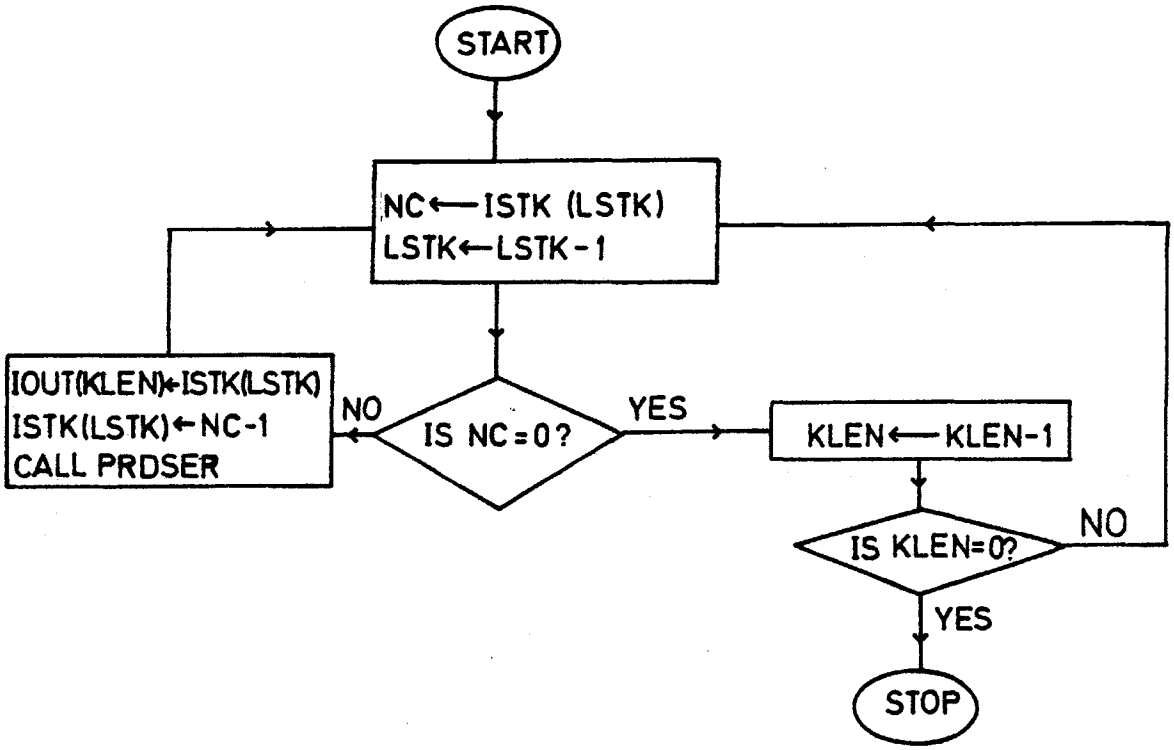

Fig. 7.2 The backtrack algorithm.

Routine BACKTR provides the next partial vector to the routine PRDSER (the predict and search algorithm,see §7.2.3). It does this by examining position LSTK of ISTK. If this is zero then there are no more candidates for position KLEN so we decrement LSTK and KLEN and return to examine the next element of ISTK unless KLEN should become zero,when the search is completed. If ISTK(LSTK) is non-zero then there are candidates still to be considered;we decrement LSTK and copy the first of these candidates, ISTK(LSTK) into IOUT(KLEN) and write the new number of remaining candidates into the end of the stack ISTK(LSTK).

We can now appreciate the advantages of the backtrack method for track recognition. The algorithm requires only two one-dimensional arrays:IOUT to contain the current vector and ISTK,the stack of hits. The depth first search algorithm used by FOREST (see Chapters 4&5) requires on the other hand large two-dimensional arrays to define links and associations between them. The backtrack procedure itself is simple and therefore fast. The inherent disadvantage of this method is that whenever we backtrack we have to search again for candidates for the next position;all information about the earlier candidates in this position is

lost. A second disadvantage is that we must fit many partial tracks rather than a few complete track candidates.

7.2.2 Routine PRDSER

Routine PRDSER tests whether the current partial vector is acceptable as a partial track. If it is not PRDSER returns control to BACKTR so that a new partial vector may be provided. If the current partial vector is acceptable then PRDSER , the PReDict and SEaRch algorithm,predicts from the current partial track the range within which possible candidates for the (KLEN+1)th position of the partial vector must lie and searches for hits within this range. If hits are found they are added to the stack and KLEN is incremented ,before returning to BACKTR which will add one of the found hits to the current vector and call PRDSER again.

PRDSER retains the best acceptable track candidate provided to it. On completion of the backtrack algorithm all permissible permutations have been considered and the best acceptable track candidate,if one exists,is accepted as the reconstructed track.

Up to now our discussion has been quite general in that we have not specified what we mean by a track,except that it is defined by a discrete list of elements. These may ,for example,be a set of (x,y) coordinates which lie approximately on a circle or a set of (s,z) points which form a straight line. PRDSER,therefore,by its method of prediction and its definition of an acceptable track candidate,can be used to reconstruct any desired trajectory. In the following sections descriptions of the operation of PRDSER for both the above examples are presented.

7.3 CHARGED TRACK RECONSTRUCTION IN THE CENTRAL DETECTOR

As in MILL the track reconstruction is carried out in two stages: a search in the r-φ plane for the circular projection of the track helices and a search in s-z for the straight line projection corresponding to each track circle found in r-φ. (The r-φ plane is perpendicular to the z-axis which is also the axis of the magnetic field. s is the arc length along the track circle from its closest point to the origin of coordinates.) In FELIX both of these searches are carried out by the backtrack algorithm. They are now described in detail.

7.3.1 r-φ Reconstruction

This section describes how FELIX reconstructs track circles in the r-φ projection using the large drift chamber,CPC anode,and vertex detector hits. Figure 7.3 shows a typical multi-hadronic event before track recognition. Drift-cells measure only the drift-time to the sense wire leading to possible track positions both right and left of the sense wire. These must be resolved by pattern recognition and both are marked in Fig 7.3.

FELIX starts by reading the hits in the central detector and masking those hits which form bands of more than a preset number of consecutive hit wires. The physical origin of these bands is not clear. They may be due to low energy electrons or to electronic pick-up between channels. It is particularly important to mask bands in the proportional chambers as large bands of hits contain no useful information and would only waste time if included in the pattern recognition.

The search for circles is driven by a loop over all hit sense wires which have not been masked. Hits are masked either by the removal of consecutive hits or by their assignment to an accepta-

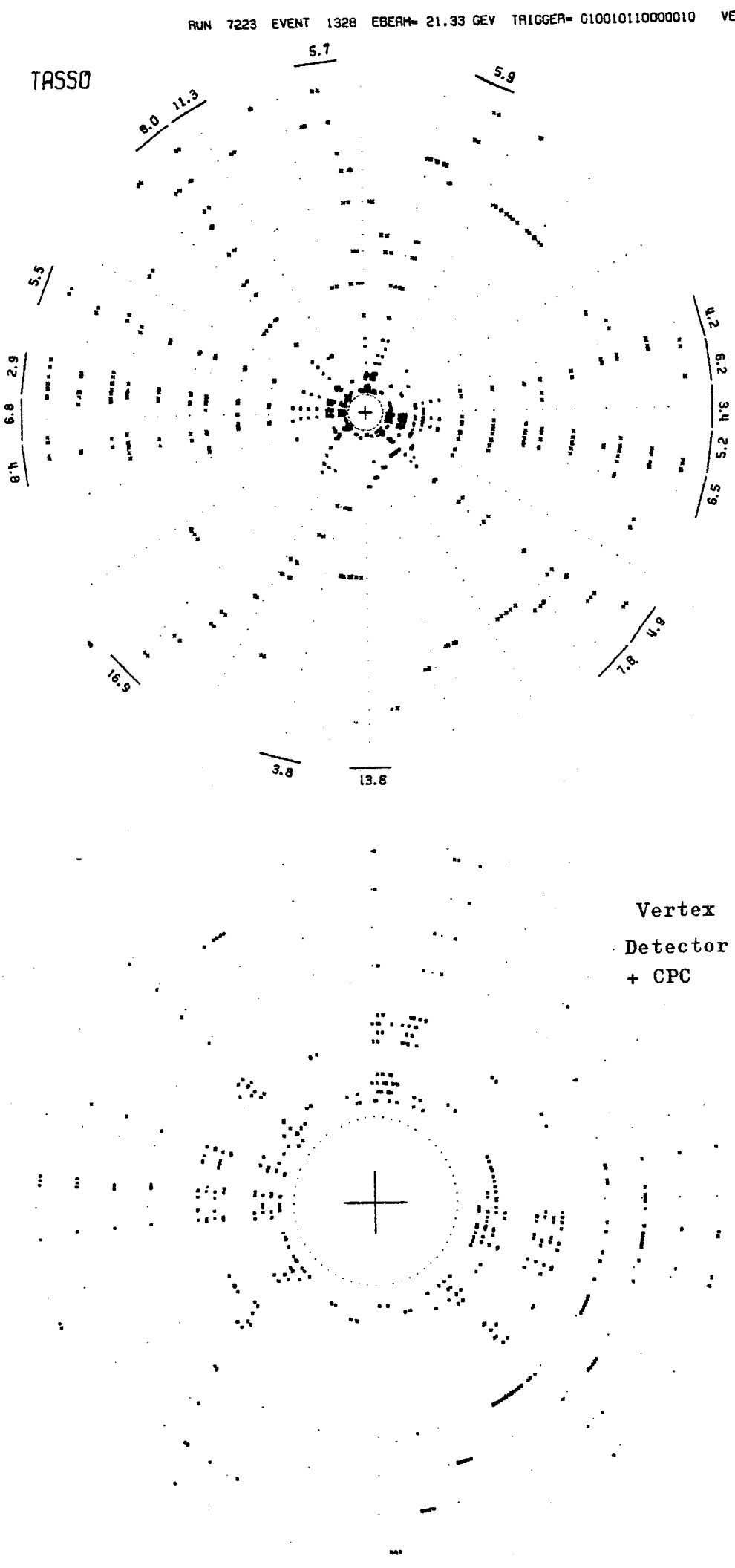

Figure 7.3 A Multihadronic Event

ble track. As each hit is considered we attempt to reconstruct the track which caused it. The hits are examined in a specified order,usually starting with those in the outermost chambers and working inwards to those closer to the interaction region. The final starting hits considered are those on the Nth chamber from the interaction region when a minimum of N hits are required for a track to be accepted.

The loop over unmasked hits is repeated several times,normally 5 times, each with a different definition of an acceptable track. First we accept tracks which have many hits,few missing hits,good χ^2 , z reconstruction,and which pass reasonably close to the interaction region. This organisation both helps to speed up the program by removing the hits of the more easily found tracks at an early stage and tends to prevent hits belonging to them from being assigned to accidental patterns which form poor tracks. Also it allows us to make use of the fact that most tracks pass close to the interaction region. As we try to grow a track from the initial hit a restriction on the impact parameter of the partial track can greatly reduce the number of combinations which need to be considered. If the track really does have a large impact parameter

our search will quickly fail and the hits are left unmasked so that the track can be found at a later stage.

Table 7.1 lists the various cuts and their values for the 5 passes. The meaning of each will be elucidated as they are encountered in the following description of the reconstruction of a track.

parameter	description	value				
	pass	1	2	3	4	5
DOMAX	maximum DO	10	20	20	8	30
ROMIN	minimum RO	67	67	34	675	33
FACT3	search width	60	60	60	60	60
IJMPR	max. #consecutive missing chambers	2	3	3	3	3
EXFAC	width defining bad hits	5	5	5	5	5
IBADSK	max. #consecutive bad hits	2	2	2	2	2
CHPMAX	max.pull of final hit in partial track	4	4	4	4	4
CHIDM	max.permissable χ^2/dof	12	12	12	12	12
IMSEND	max.#missing chambers at end of track	2	6	9	15	15
NHTMIN	min.#unshared hits	15	10	6	5	6

TABLE 7.1 r-φ reconstruction parameters

Consider the search in r-φ for the track which caused our initial hit. We start by placing the hit and if it is a drift cell hit,its drift

time ambiguity,into the stack to initiate the backtrack algorithm described in §7.2. This copies the hit into the first position of the current vector. A possible hit pattern is illustrated in Fig 7.4 together with the contents of the stack ISTK and the current vector IOUT at the first call to PRDSER and before the call to BACKTR. The ambiguity remains in the stack to be considered at a later stage.

PRDSER is called with the single hit,2, in the current vector IOUT. PRDSER determines the chamber and the region within which to search for hits which could qualify as the second hit on the track. The chamber to be searched is usually taken as the next innermost r-φ chamber to that of hit 2. We search for unmasked hits in the range $\varphi \pm \Delta\varphi$ where φ is the φ position of hit 2 and $\Delta\varphi$ is determined from the maximum d0 DOMAX,the minimum radius of curvature ROMIN,the road width FACT3 and the nominal resolution SIGICH of the chamber to be searched. The idea is that the region $\varphi\pm\Delta\varphi$ should be such that the hits which may belong to tracks satisfying the DOMAX,ROMIN cuts must lie within it. The solution for $\Delta\varphi$ depends on the relative magnitudes of DOMAX ,ROMIN and the larger chamber radius R1 and the smaller chamber radius R2 and is given in Fig 7.5.

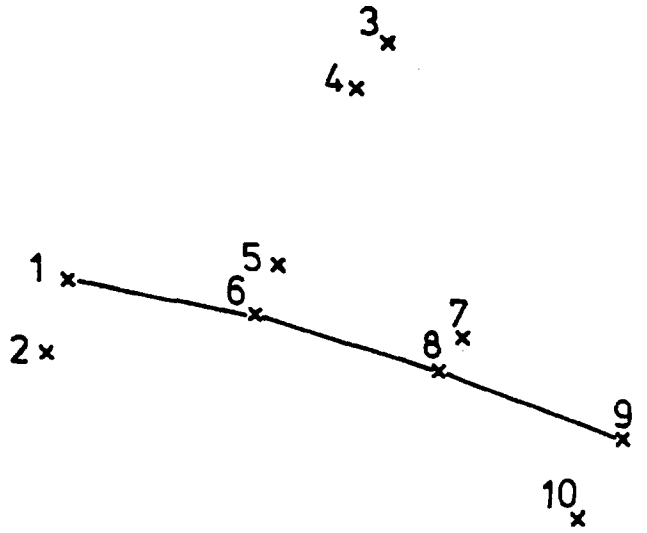

BEFORE BACKTR:

ISTK 1 2 2 LSTK 3

IOUT KLEN 1

BEFORE PRDSER:

ISTK 1 1 LSTK 2

IOUT 2 KLEN 1

AFTER FIRST RETURN FROM PRDSER:

ISTK 1 1 5 6 2 LSTK 5

IOUT 2 KLEN 2

Fig. 7.4

Figure 7.4 Example hit pattern and stack contents

Fig. 7.5 Determination of Δφ

Figure 7.5 Determination of $\Delta\varphi$ when single hit in current vector

In our example hits 3 & 4 may fall outside the search range and so only hits 5 & 6 will be found. The found hits are ordered according to their closeness to the position φ of the first hit and placed into the stack,those farthest from φ being inserted in the earlier positions in the stack. This ordering means that if the hits belong to a high momentum track coming from the interaction region then the corresponding pattern of hits will be one of the first considered. In our example the hits 5,6 are inserted into the stack as shown in Fig 7.4.

It may happen that the search does not find any hits. In this event,to allow for chamber inefficiences we continue to compute and search regions on farther chambers up to a maximum of IJMPR chambers without hits. If still no hits are found then PRDSER returns and the next call would start from the ambiguity of our original hit.

Returning to our example , PRDSER has returned after inserting hits 5 & 6 into the stack. BACKTR then adds hit 6 to IOUT and PRDSER is called with the two hits (2 & 6) in the current vector.

The new chamber to be searched for hits is taken as the next innermost to the chamber of hit 6. We search a region $\varphi \pm \Delta\varphi$ where φ is found by extrapolating by a straight line to the radius of the search chamber as illustrated in Fig 7.6. The width $\Delta\varphi$ is taken as the difference in φ between R2 and R plus FACT3*SIGICH. Again we search only for unmasked hits,are allowed to jump over up to IJMPR chambers without hits,and insert the found hits into the stack after ordering with respect to φ. For the example of Fig 7.4 hits 7 & 8 would be found and inserted into the stack,7 first,then 8. We return to BACKTR.

This time the third hit,hit 8 is added to the current vector and PRDSER called once more. The three hits define a circle. If this circle has R0<R0MIN or |d0|>d0MAX then it is not an acceptable partial track and PRDSER returns immediately. BACKTR will then supply a new current vector, such as in this case.

An acceptable partial track is projected to the new search chamber,the chamber inside that of the third hit,and a road of width ±FACT3*SIGICH searched for hits. Again the found hits are ordered and inserted into the stack,those hits farther from the projection first,so that the hit most likely to be the correct one will

be placed at the end of the stack. Masked hits are included in this search. If the best hit found on the ordering is a masked hit then only a special procedure is adopted:Only the masked hit is copied to the stack and only then if it is closer than EXFAC*SIGICH to the track. As masked hits are specifically excluded from track fits insertion of only the masked hit into the partial vector excludes

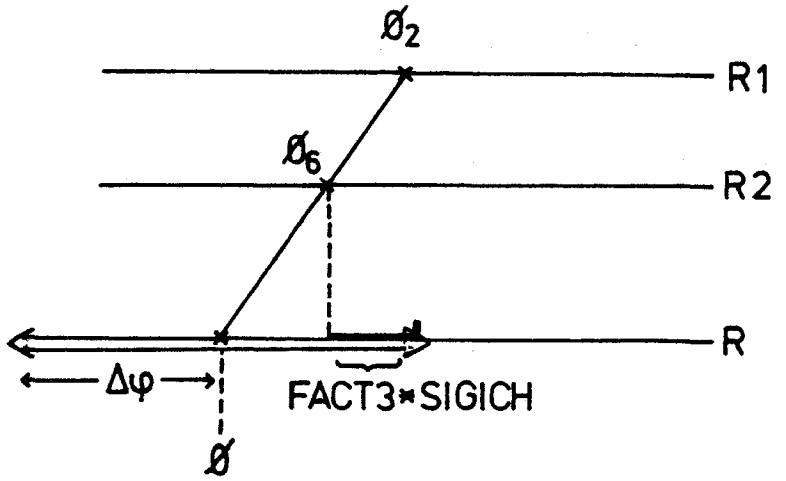

Figure 7.6 Determination of $\Delta\varphi$ when two hits in current vector

hits on this chamber from the track fits and so removes the influence of this chamber on the track finding and therfore ensures that track will not be pulled away from masked hits towards unmasked hits. This is desirable to prevent a track sharing cells with a previously found track from being pulled away to the next nearest hit and therefore being misfitted. Two tracks quite frequently pass through the same drift cell so that it would be unreasonable to assume that our track candidate did not share a cell with some other track.

The next stage allows for the reconstruction of tracks with missing hits due to hardware inefficiency in the chambers or poor hits due to noise. We decide whether to search on further chambers for more candidate hits for the next position in the current track. If we have not yet found any hits we continue to search on further chambers up to a maximum of IJMPR chambers. This allows for up to IJMPR consecutive chambers being inefficient. If we have found some hits but the best hit found is farther than EXFAC*SIGICH from the current track (but closer than FACT3*SIGICH) it is said to be 'bad' and we continue to search on further chambers up to a maximum of IBADSK chambers. Should further hits be found the hits already inserted into the stack are copied to the end and the newly

found hits inserted earlier in the stack. This means that we will try to form an acceptable track using the 'bad' hits before we consider ignoring the chamber with the 'bad' hits. If we can form an acceptable track by including them it will be reconstructed,otherwise we will try to build an acceptable track without 'bad' hits. This procedure means that the hits on the track which are candidates for the fourth or later positions in the current vector need not all belong to the same chamber.

An example may help to illuminate this procedure. Figure 7.7 shows a possible hit geometry. Hits 1,4,5 define the track circle. A search on chamber D finds hits 10,11 within the road of width FACT3*SIGICH and farther than EXFAC*SIGICH from the projection of the track circle onto chamber D. Our search is therefore continued to chamber E where hits 20,21 are found within the road. These hits are inserted into the stack in the order 20,21,11,10 so that they are considered as candidates for the fourth position of the current track in the sequence 10,11,21,20. If we fail to find an acceptable track with hits 10 or 11,hit 21 will be inserted into the fourth position and there will be no hit from chamber D in the current partial track.

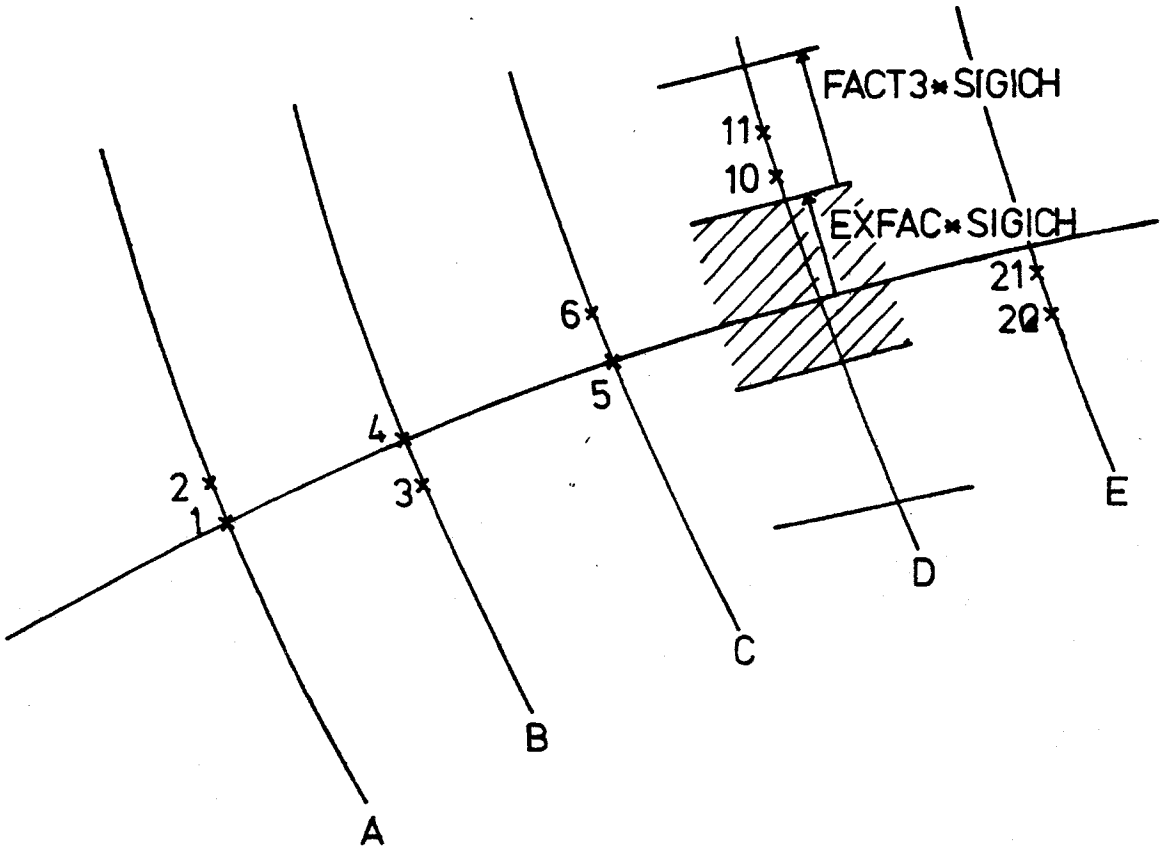

Fig. 7.7

Figure 7.7 Example of treatment of 'bad' hits

Consider again the example of Fig 7.4. The third call to PRDSER has placed hits 9,10 into the stack. BACKTR adds hit 9 to the current vector and PRDSER is called with the four hits 1,6,8,9 as the current vector. PRDSER operates as when called with only three hits in the current vector except that now a circle is fitted to the hits and the partial track is tested not only against ROMIN and DOMAX but also must satisfy χ^2/dof < CHIDM and pull of last hit < CHPMAX for it to be accepted.

The final task of routine PRDSER is to remember the best track or partial track so far considered. If the current partial track is acceptable and it has at least NHTMIN unshared hits,at least as many hits as the current best track and no more than IMSEND chambers missing after that of the last hit,it may become the new best track. A refit is made using corrected drift distances computed from the parameters of the initial fit. This refit[28] allows a kink in the track circle at a radius of 25cm, near the centre of the CPC,whenever the track has more than 6 hits in total at least 3 of which are in the vertex detector. The magnitude of the kink is constrained by the track momentum and compensates for the effect of multiple scattering in the material of the CPC. If the refit

gives a better χ^2/dof than the best track,the current partial track becomes the new best track.

Whether we have replaced the current best track or not,as long as the current partial track was acceptable,projection and searching is continued just as for the case of only 3 hits in the current vector, and the found hits added to the stack.

The procedure for more than four hits is precisely the same as for four hits in the current vector.

Continuing until BACKTR completes considers all admissable track candidates. The best track,if one exists,is the reconstructed track from our initial hit.

The process is speeded up by partially aborting the backtrack procedure when it is unlikely to lead to an improvement to the current best track. There may be difficulties in projecting tracks between the large drift chamber and the vertex detector. So,whenever the innermost chamber has just been searched and the current best track is acceptable,we check for a better solution using a different link to the vertex detector by destroying the cur-

rent vector and stack from the outermost vertex detector chamber with a hit on the current track. This causes a search with the same hits in the large drift chamber and CPC but linking to a different hit in the outermost vertex detector layer. If there were no vertex detector hits for the current track the stack is destroyed right back to the ambiguity of the initial hit if this still has to be considered. Otherwise backtracking is aborted,and the current best track becomes the final track candidate.

Our description of the search for a track from an initial hit and its ambiguity is complete. If this search did not yield a best track which had at least NHTMIN hits and a χ^2/dof<CHIDM then we have not found an acceptable track from the initial hit and we abandon this initial hit. A track may still be reconstructed from this hit when unmasked hits are reconsidered in a later pass with looser requirements.

When an acceptable track is found we make some checks to see if it can be improved. All the hits on the track are examined and if there is another hit closer to the track it is assigned to the track instead,irrespective of whether this new hit is masked or not. Hits farther than 1.25*CHPMAX*SIGICH from the track are removed.

Chambers on which a hit was missing are examined and the closest hit added to the track provided it is closer than 2*1.25*CHPMAX*SIGICH to the track and irrespective of masking. A new fit is made to the changed track and the above checks repeated with the new track parameters. A refit is made only if any of the assigned hits are altered.

We may now have on the current track hits or their ambiguities which are assigned to previously reconstructed tracks. In such cases we remove the hit from the track to which it fits least well. All tracks on which hits were altered are refitted. Finally we test our current track once more against the requirement for at least NHTMIN hits and χ^2/dof<CHIDM. When we have found a track circle acceptable in the current pass we attempt to reconstruct this track in the s-z projection(see §7.3.2). The requirements for an acceptable track have been set out in Table 7.1. If the fully reconstructed track is acceptable it is saved for output.

The values of the cuts used for each pass (Table 7.1) were chosen so that tracks with many hits and small d_0 would be reconstructed first. Then more missing hits are allowed and larger d_0 Pass 4 searches for hard tracks with small d_0 and finally pass 5 has

very loose track requirements. This organisation helps to make the pattern recognition fast by limiting the combinations considered in the early stages when there are many unmasked hits to those which may form good tracks. A good efficiency is obtained by reconstructing the poorer tracks in the later passes.

7.3.2 Reconstruction in s-z projection

7.3.2.1 Introduction

The projection of a track helix in the coordinates s,the arc length along the track circle in r-φ from its point of closest approach to the origin,and z,the coordinate along an axis parallel to the magnetic field,is a straight line. Given the track circle we can compute coordinates (s,z) for each hit on the DC α wires,the CPC cathode strips and the charge division chambers. As an example the reconstruction of the event of Fig 7.3 is shown in Fig 7.8,and Fig 7.9 shows the s,z projection for track number 1. The pattern recognition problem is to find the hits which lie on the best straight line, using at most one hit from each chamber.

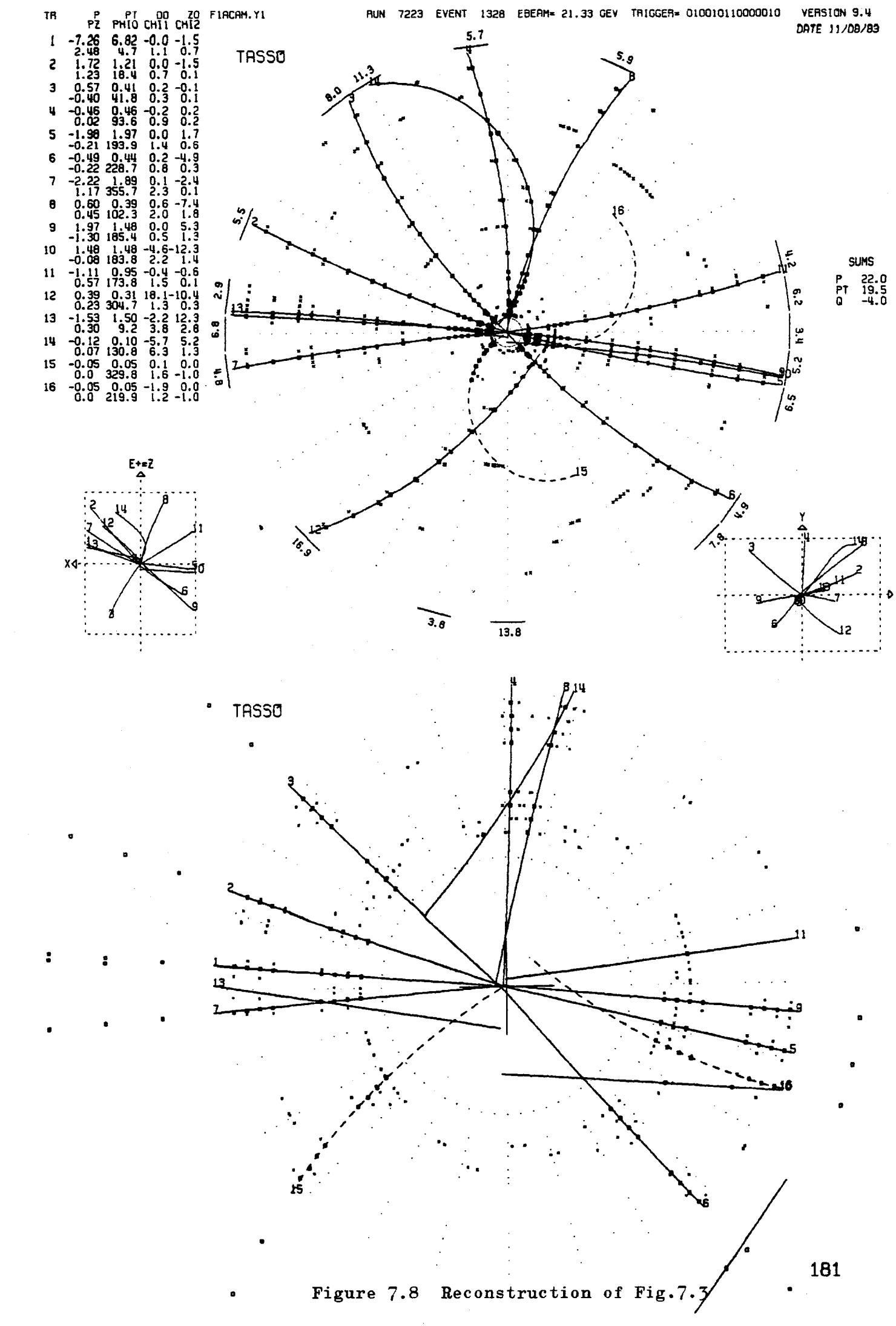

Figure 7.8 Reconstruction of Fig.7.3

FELIX employs once more the backtrack algorithm as the central driving mechanism for the generation of all permutations of hits which might be the solution to our problem. The layout is therefore similar to that adopted for the r-φ recognition. A master routine prepares the list of (s,z) coordinates for each chamber and initiates the backtrack algorithm for various sets of possible can-

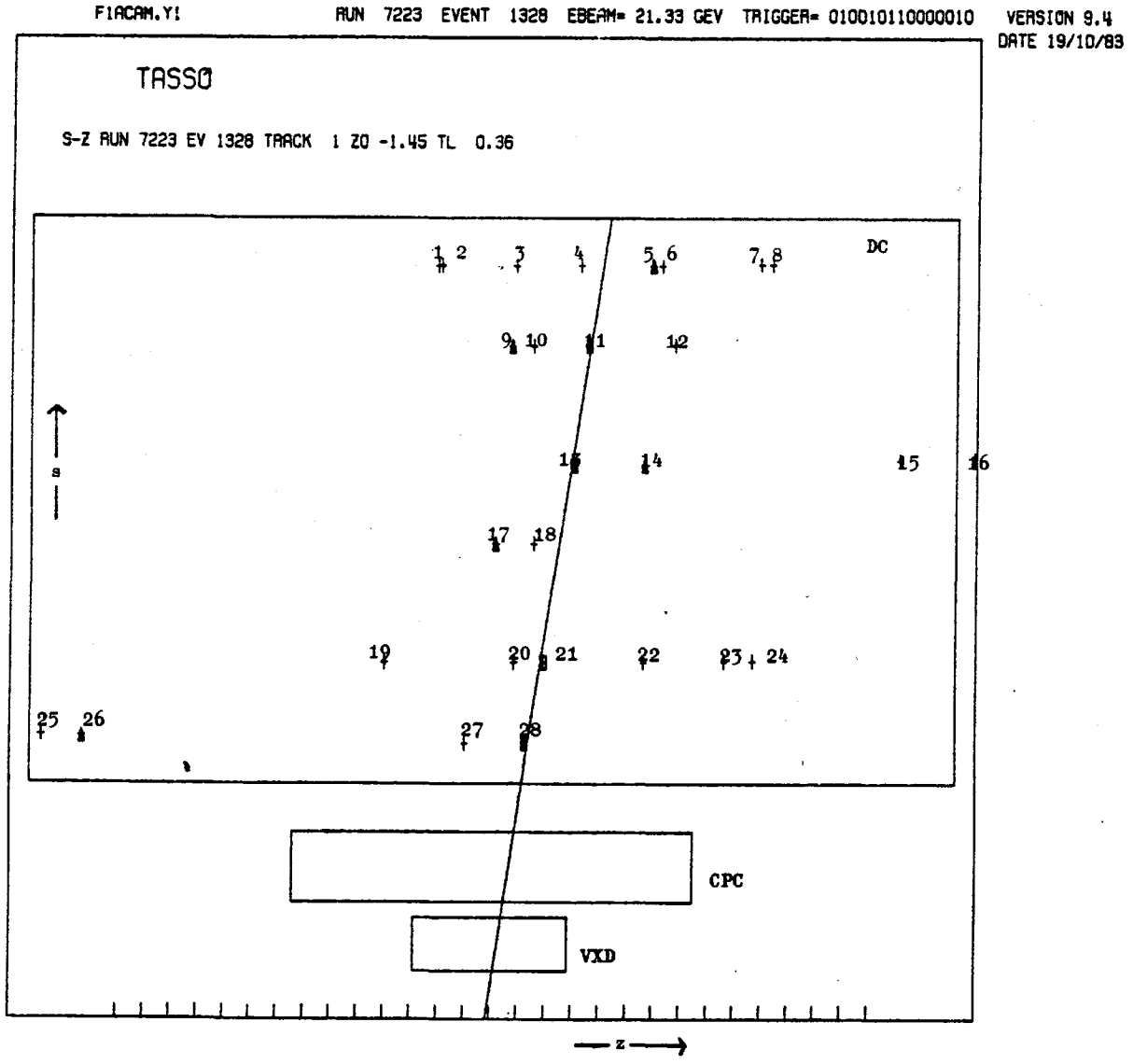

Figure 7.9 s,z projection of track 1 of Figure 7.8

didates for the first position. The backtrack algorithm itself is implemented precisely as described in §7.2 except that the predict and search routine PRDSER is replaced by a new predict and search routine PSSZ. PSSZ performs precisely the task of PRDSER as described in §7.2 except that it is set up to consider straight lines rather than circles.

The backtrack algorithm was chosen because it could accommodate a large number of chambers without great demands on storage requirements. It was desired to provide the ability to include in addition to the 6 stereo chambers of the large drift chamber,the 8 cathode strip layers of the CPC and the 4 layers of vertex detector cells equipped with charge division readout,an increase from 6 to 18 chambers in all. The depth first search based algorithm used by MILL is very thorough but would require prohibitively large arrays for this by a simple extension.

The adoption of the backtrack algorithm allows a convenient reduction in the labour of straight line fitting. The solution of the least squares fit to a straight line requires only knowledge of the sums $\sum^{n}_{i=1}s_i^2$, $\sum^{n}_{i=1}s_iz_i$, $\sum^{n}_{i=1}z_i^2$ over the n coordinates in the track (see Table 7.2).

$$z0 = (SY.SXX - SXY.SX)/D$$

$$\tan\lambda = (S.SXY - SX.SY)/D$$

where :

$$S = \sum 1/\sigma^2_i$$

$$SX = \sum s_i/\sigma^2_i$$

$$SY = \sum z_i/\sigma^2_i$$

$$SXX = \sum s_i^2/\sigma^2_i$$

$$SXY = \sum s_i z_i/\sigma^2_i$$

$$D = S.SXX - SX.SX$$

All sums over i=1,n the n hits on the track

Here σ_i is the error (cm) of hit i.

TABLE 7.2 Straight Line Fit

As hits are added or removed from the current vector these sums can be updated,replacing the task of forming the complete sums for each new fit. This considerably reduces the time spent in track fitting.

7.3.2.2 Detailed Description.

The s-z reconstruction begins with the calculation of all possible (s,z) coordinates from the hits on the α-wires,cathode strips and charge division layers. The formulae used are listed in Table 7.3. This list of hits is made starting with the outermost stereo chamber and continuing in the order of decreasing radius to the innermost charge division layer of the vertex detector. The hits on both the outer and inner cathode strips are ignored unless the r-φ track includes an anode wire hit from the same chamber. Similarly charge division information is only considered when the measured drift time was fitted to the track circle.

The hits from each chamber are ordered by increasing z coordinate. This can be accomplished easily as the hits are already stored in order of increasing φ so that we need only reverse this

$$z = z0 + s.\tan\lambda$$

α-wires

The φ of the track circle at a radius r is given by:

$$\varphi(r) = \varphi^0 + SIG.\sin^{-1}\left\{ (2.RO.DO - DO^2 - r^2) \;/\; (2.r.(RO-DO)) \right\}$$

where

RO = radius of track circle
φ^0 = φ direction of track near the origin
DO = impact parameter
(+ve if track circle encloses origin)
SIG = geometrical sign of track

The z position of the hit is calculated in 2 steps:

First $\varphi(R)$ is computed at the chamber radius R.

The radius of the wire at the z position of the hit is approximated by:

$$R_{wire} = R/\cos(\varphi(R) - \varphi_{hit})$$

Then the z position of the hit is computed from:

$$z = R/\tan(\alpha) \;.\; \tan(\varphi(R_{wire}) - \varphi_{hit})$$

The s coordinate is given by:

$$s = 2.RO.\sin^{-1}\sqrt{(R^2 - DO^2/(4.RO.(RO-DO)))}$$

Cathode Strips

See Chapter 3

TABLE 7.3 s,z Computation

order for negative stereo or dip angles. This ordering reduces the effort of searching for hits within a given range as we know as soon as we have considered a hit which has too large a z coordinate,that all further hits will also be out of range and so we can abort the search.

Some of the hits may already have been assigned to a reconstructed track or may be masked by the removal of bands of consecutive hits (see §7.3.1). The option exists to mask these hits from the z reconstruction of the current track. A full list of the parameters of the z-reconstruction is given in Table 7.4.

One further computation is made at this initialisation stage. It is helpful to require that our solution must be consistent with the r-φ hits on the track. We should not assign a z-trajectory which implies that the track did not enter a chamber on which its r-φ projection has been assigned a hit;and vice versa,if there are more hits than could reasonably be missing due to inefficiencies from the outer r-φ chambers,it is reasonable to assume that the track did not reach these chambers but passed through the endplates. We therefore compute the z coordinates of the endplates of the shortest chamber on which an r-φ hit was assigned and of the out-

ermost chamber with an r-φ hit. In addition the corresponding s coordinate at the outermost r-φ chamber is calculated and,if there are 3 or more r-φ chambers missing from the outer end of the track,the s coordinate at the third is calculated.

Consider the example of Fig 7.9. The (s,z) coordinates shown have been calculated and stored together with the products s^2 and sz for the fit and we are ready to perform the track recognition. For simplicity this example does not contain hits in the CPC cathodes or vertex detector charge division readout.

Unlike the search in r-φ where there was a reasonably high chance that there would be no track circle satisfying our criteria and we wished to recognise this as quickly as possible,we now want to make a very thorough search. It is not improbable that the correct solution contains only 3 α-wire hits.

The search is begun by placing all hits on the first chamber (the outermost stereo chamber) into the stack so that the backtrack algorithm will place each in turn into the first position of the current vector (see § 7.3). Masked hits are not copied to the stack if hit sharing is forbidden. In our example,the 8 outer hits are placed

in the stack,the first of these inserted in position 1 of the current vector,and PSSZ called.

PSSZ searches on the next innermost chamber for hits and adds them to the stack if the projection of the straight line joining the found hit and the hit in the current vector on the z axis is within 170cm of z=0. This is not a serious limitation as tracks of interest originate from within a few centimetres of the origin in z but it does greatly reduce the number of permutations which are considered. If hit sharing is not allowed,masked hits are not picked up by the search. In our example we search from hit 1 and find that hit 9 projects outside 170cm on the z axis,so the search is abandonned. If some acceptable hits were found we would return so that they would be considered in the second position of the current vector. We have failed to find any hits so we consider searching the next innermost chamber. This allows for chamber inefficiencies. We search the next chamber provided we have not already failed to find hits on IJMPZ chambers. In our example we find hit 13 projects just within the 170cm limit while hit 14 projects to a larger z. Hit 13 is added to the stack and PSSZ returns.

The backtrack algorithm adds hit 13 to the second position of the current vector and PSSZ is called with the two hits 1,13 in the current vector. The first chamber to search is taken as usual as the inner neighbour to that of the last hit,hit 13. The two hits define a straight line and we look for hits within a road of half-width 2*ZFACT*ZERR from the projection of this line. ZFACT is a parameter of the search (see Table 7.4) and ZERR is the nominal resolution of the chamber on which the search is made. In our example hits 17,18 lie outside the road so that we skip to the next chamber and find hit 23 is acceptable. This is added to the stack and PSSZ returns.

The 3 hits 1,13,23 are presented to PSSZ in the current vector. A straight line is fitted to these hits and we test whether it should be considered the best acceptable solution yet considered. An acceptable solution must satisfy the constraints from the r-φ hits as discussed above;must have at least NREQ hits;and a χ^2/dof < CHI2M. The current best acceptable solution is replaced by another acceptable solution if it has more hits or a smaller χ^2 and the same number of hits. In our example 1,13,23 becomes the best acceptable solution.

The fitted track is projected to the next chamber and we search for hits within ZFACT*ZERR cm. No hits lie in this range and as our example has not used the CPC cathodes or the charge division layers there are no further chambers to search and PSSZ returns.

The backtracking removes hits 23 and 13 and replaces hit 1 by hit 2 in the first position of the current vector. In turn we try to build an acceptable track from each of the hits on the outermost chamber and store the best solution found.

We must entertain the possibility that none of the hits on the outermost chamber belong to the track. So,once the backtrack algorithm has completed,we restart by inserting all the hits on the next chamber (hits 9,10,11,12 in the example) into the stack and searching as before for a better solution. This procedure is continued,starting from each chamber in turn,until either there are no longer enough chambers inside to form a track with NREQ hits or until the best acceptable solution already contains more hits than there are chambers inside the new initial chamber. In the example the final accepted solution with 4 hits is found when searching from the second outermost chamber. We attempt to find a better solution starting from hits on the third chamber as this

could also give a 4 hit track,but stop at this stage as starting from the fourth chamber could only give a 3 hit solution.

The reconstruction is complete and if an acceptable solution was found it is retained as the z reconstruction for the current track. In Fig 7.9 the hits assigned to the reconstruction are boxed. Those assigned to other tracks are marked by triangles.

parameter	description	value				
	pass	1	2	3	4	5
IJMPZ	maximum jump over missing chambers	4	4	4	4	4
ZFACT	search width	9	9	9	9	9
CHI2M	max.χ^2/dof	20	20	20	20	20
NREQ	minimum # hits	4	4	3	3	3
ZOMAX	maximum acceptable z0	20	20	50	150	150

TABLE 7.4 r-z reconstruction parameters

7.4 EXTENSIONS

The preceeding sections have described in detail the backtrack method and its implementation as the driving mechanism for both the recognition of track circles in the r-φ plane and the reconstruction of straight line projections in the s-z plane. These have been discussed in the context of the reconstruction of events in the TASSO central detector,including the vertex drift chamber. The track reconstruction efficiency will be discussed in chapter 8. The remainder of the present chapter briefly presents some extensions to and additional uses of the FELIX track recognition program.

7.4.1 Additions to the s-z search

7.4.1.1 CPC cathodes

The CPC cathodes can be added to the list of s-z chambers and the z-reconstruction algorithm used without alteration. This is particularly useful for the reconstruction of tracks at small angles to the beam axis which pass out of the endplate of the drift cham-

ber and hit insufficient chambers to allow reconstruction with the stereo wires alone. The s-z reconstruction of track 5 in Fig 7.10a is shown in Fig 7.10b. Fig 7.10c shows a display of the CPC for this event.

7.4.1.2 Vertex detector charge division

As of August 1983 the vertex detector charge division readout is not yet fully operational. Its inclusion in the track reconstruction has been implemented and the s-z reconstruction of a Monte-Carlo event with vertex detector hits is shown in Fig 7.11.

7.4.2 Additions to r-φ search

7.4.2.1 Track reconstruction from LAEC clusters

It is of interest to determine whether energy deposits in the liquid argon endcap shower counters (LAEC) result from a charged or neutral incident particle. Such particles pass through only the

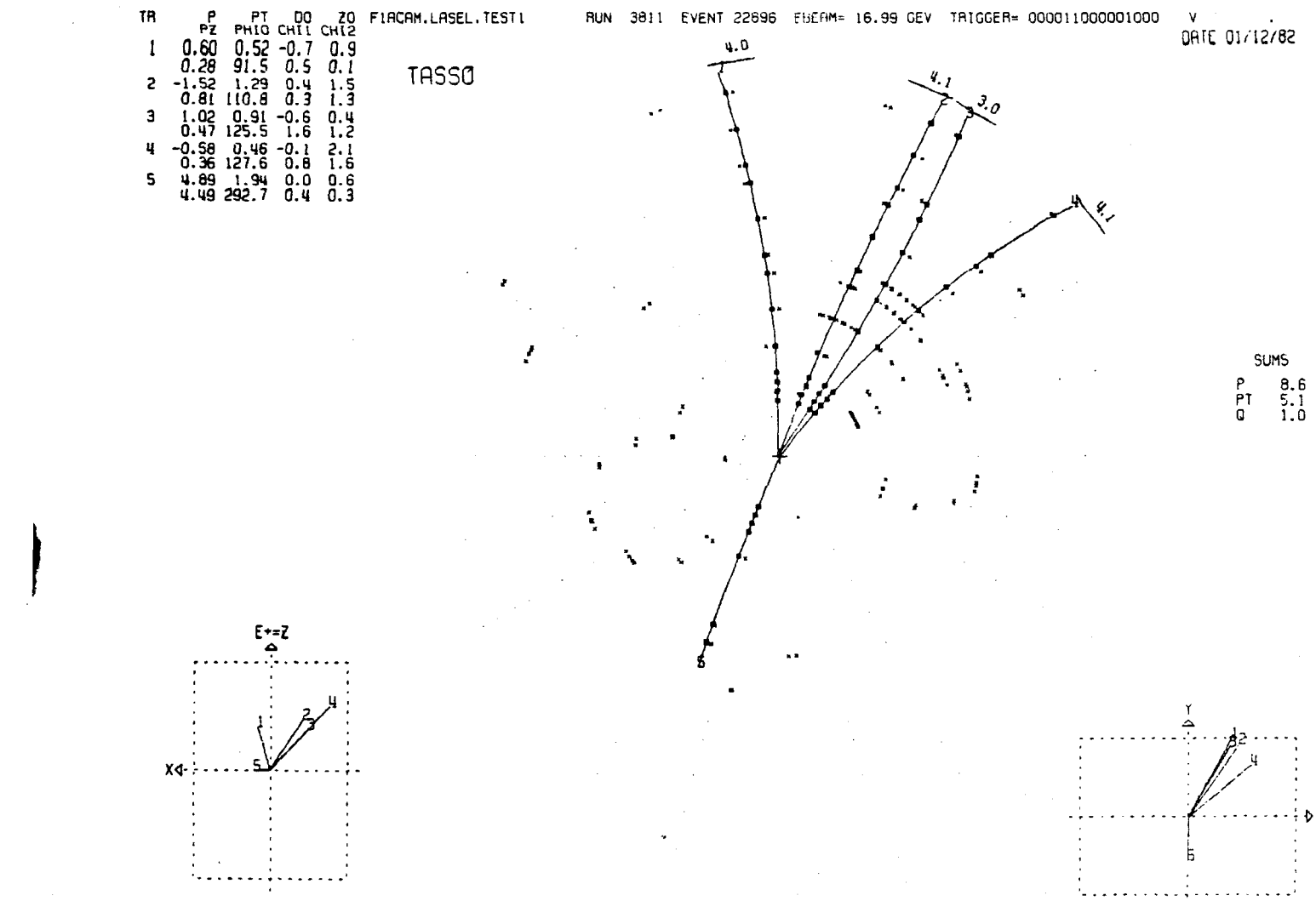

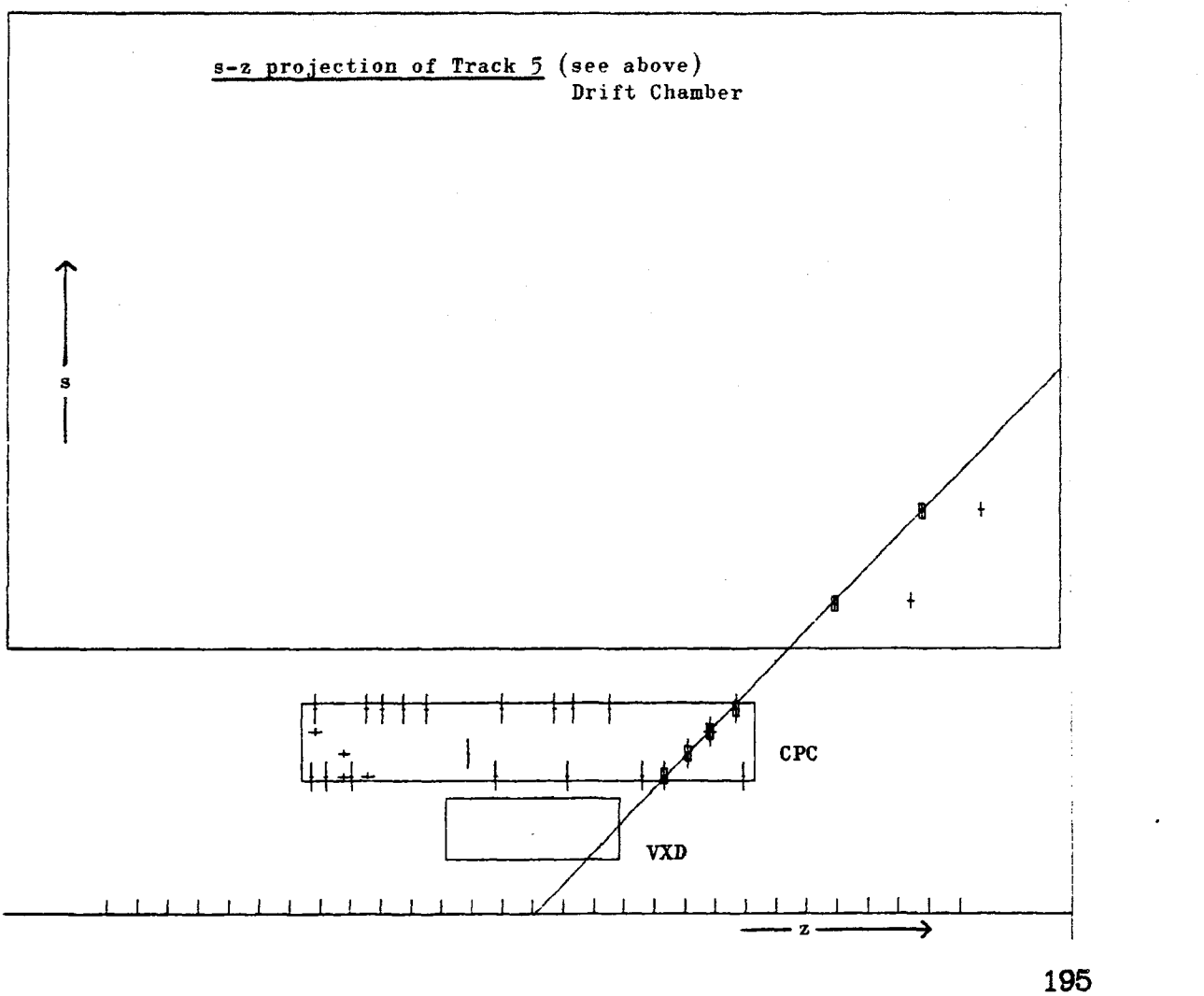

Figure 7.10a & 7.10b

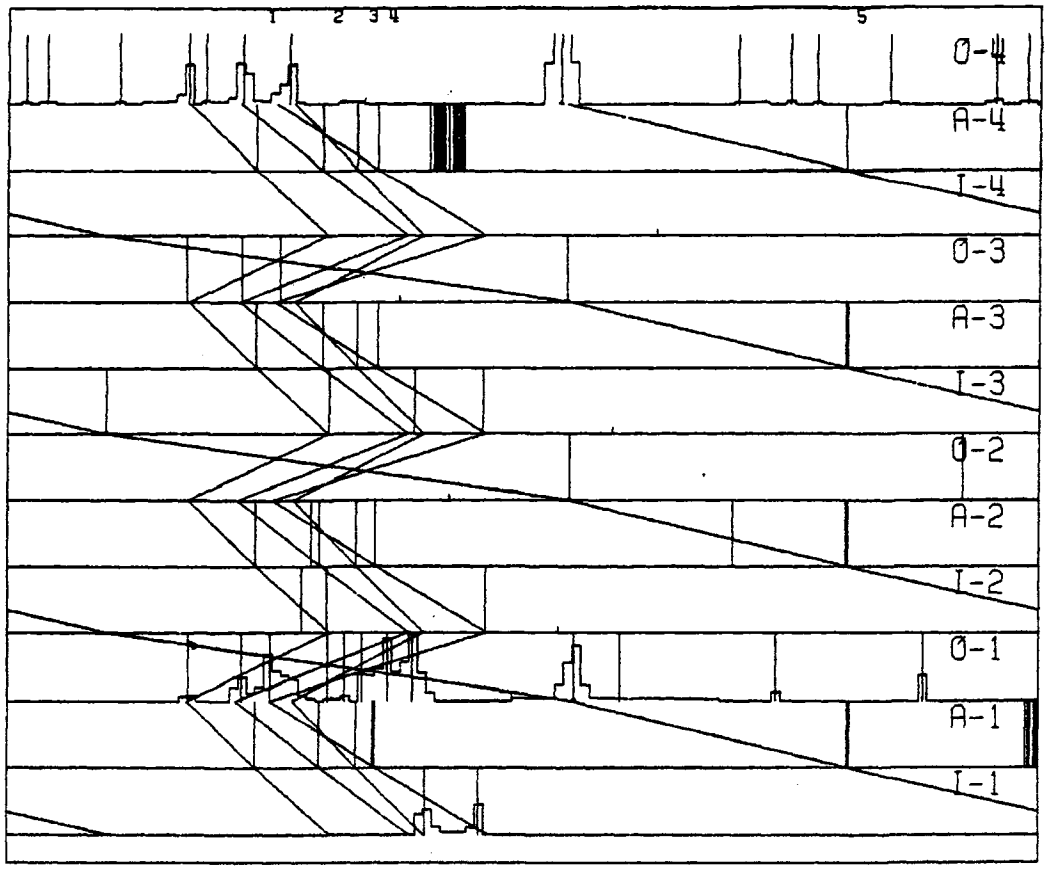

Figure 7.10c

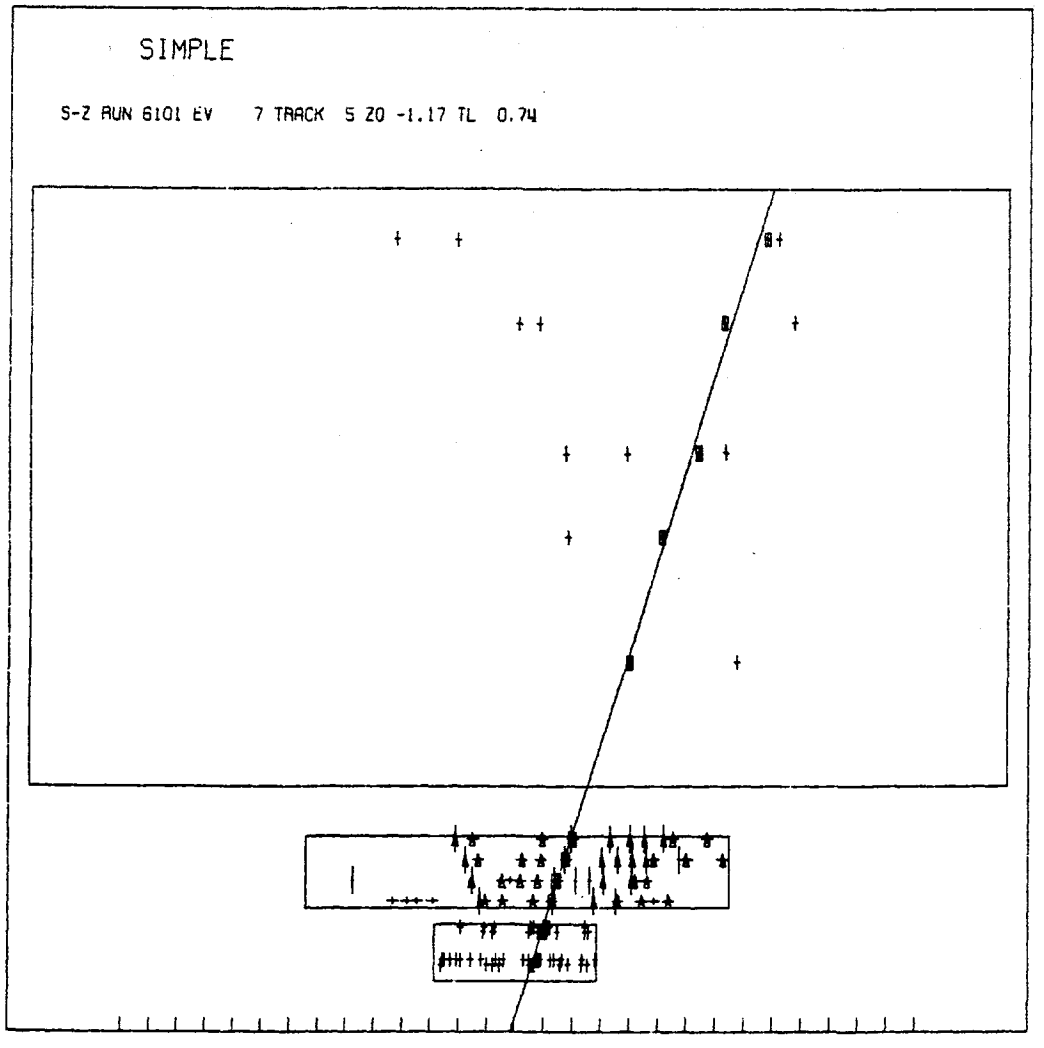

Figure 7.11

innermost chambers so that charged tracks fire insufficient cells for reconstruction by the MILL program. The facility has been added to FELIX to initiate the backtrack search from the cluster position and attempt to reconstruct a track using the drift chambers and proportional chambers at sufficiently small radii. Track 5 was added to the 4 MILL tracks of Fig 7.10a by this method. The r-φ position of the cluster is taken as the initial point on the track. If sufficient hits are found in the central detector the cluster position is removed from the track fit. Similarly the z reconstruction is initiated from the (s,z) coordinate of the energy cluster. This method is presently used by the standard LAEC analysis routines[29].

7.4.2.2 Adding to MILL tracks

To enable initial studies of the vertex detector during poor background conditions FELIX can copy tracks reconstructed by MILL into the current vector and initiate the backtrack search thus extending those tracks to include the vertex detector hits.

7.4.2.3 Reconstruction with only the vertex detector

The r-φ reconstruction of tracks with the vertex detector alone was useful for the reconstruction of cosmic ray events during tests before the installation of the detector within TASSO and later for the reconstruction of 2-prong events to study the space-drift time relationship (see Chapter 6).

Track circles can be reconstructed just as described above for the complete detector. Fig 6.8 showed the reconstruction of a cosmic ray event.

It is often sufficient to consider a cosmic ray track as a straight trajectory within the vertex detector. To improve their reconstruction we can treat the problem as the recognition of a straight line through 16 chambers rather than reconstructing the incoming and outgoing sections of the track separately. This has been achieved by a modified version of the s,z projection reconstruction program. Instead of s,z coordinates we supply x,y coordinates of the hits and their drift time ambiguities,treating the chamber as if made up of 16 sections by dividing the 8 chambers by the line 90° from a hit on the outermost chamber.

7.4.2.4 Reconstruction without the vertex detector

FELIX may be used on TASSO events before the installation of the vertex detector. Hits assigned to MILL tracks can be masked and additional tracks searched for with the remaining hits. The use of the CPC anode and cathode hits enables the reconstruction of additional tracks at small angles to the beam. The improved angular acceptance is particularly useful for the reconstruction of 4-prong two-photon annihilation events.

8.0 PERFORMANCE OF TRACKING PROGRAMS

8.1 INTRODUCTION

This chapter presents an evaluation of the performance of the track reconstruction program FELIX (see Chapter 7),and a comparision to the MILL program (see Chapter 5). Track reconstruction efficiencies are computed for charged tracks in single photon annihilation events at E_{cm}=34GeV in the TASSO central detector.

8.2 MONTE-CARLO SIMULATION

Monte-Carlo hadronic events were generated using the LUND program [31] and passed through the detector simulation program SIMPLE [32],which simulates the hardware information as it would be delivered from the TASSO detector during actual data taking. In particular hits in the central detector drift and proportional chambers and their drift time ambiguities were generated and the number of the Monte-Carlo track causing each hit noted. Single hit efficiences of 92%,97%,90%,100% were assumed for the large drift chamber,CPC anode wires,cathode strips and vertex drift chamber

respectively. Hits in the large drift chamber were smeared with a Gaussian of σ 300μm;the vertex detector cells were given a resolution of 150μm. Noise hits were added in the large drift chamber with a 0.8% probability per layer, and in the CPC with a 2.6% probability. Crosstalk hits were added with a 2% probability and bands of consecutive hits in the proportional chambers were simulated.

No attempt was made to ensure that the above efficiencies and resolutions were in excellent agreement with real data. This was not possible as no data had been taken with the vertex detector at the time of this study and was in any case not important as the purpose of this study was to check the performance of FELIX and the improvement which we might obtain with the vertex detector compared to the MILL program which uses only the drift chamber and CPC anodes.

In the following only events which would have triggered the experiment and passed the standard hadronic event selection (see Chapter 2) have been considered.

8.3 TRACK RECONSTRUCTION EFFICIENCY

To determine how efficiently tracks are reconstructed we consider Monte-Carlo (MC) tracks which fall within the central detector and check wether there is a corresponding reconstructed track. We define tracks as falling within the central detector by the following cuts on the parameters of the Monte-Carlo tracks:

(1)	radius of production vertex	$RP < 18.7cm$
	radius of final point on track	$RF > 49.0cm$
	z of final point on track	$\|ZF\| < 3m$
	Impact parameter	$\|d_0\| < 5.0cm$
	z at impact point	$\|z_0\| < 20.0cm$
	polar angle of track	$\|\cos\vartheta\| < 0.87$
	momentum component transverse to beam	$\|p_t\| > 100MeV/c$

The association between generated MC tracks and reconstructed tracks is made by comparing the hits caused by the MC track with those assigned to the reconstruc-ted track by the tracking program. A MC track is associated to the reconstructed track which has the most correct hits (incorrect drift-time ambiguities are not

considered) provided that the reconstructed track has at least 7 correct hits,otherwise no association is made.

A MC track is considered to have been reconstructed if such an association was made to a found track and in addition the found track had :

(2) $\chi^2_{r-\phi}/\mathrm{dof} < 12.0$

$\chi^2_{s-z}/\mathrm{dof} < 20.0$

and was reconstructed in 3-dimensions.

The resulting track reconstruction efficiencies for FELIX and MILL were :

	EFFICIENCY (%)
FELIX	95.3±0.3
MILL	90.6±0.4.

We can study how this efficiency depends on the track parameters by relaxing the requirements (1) in turn. Fig 8.1 shows the efficiency as a function of the track momentum component transverse

to the beam direction,p_t,and Fig 8.2 presents the efficiency against cosϑ,the polar angle of the track. The gain in efficiency of FELIX over MILL at large polar angles is mainly due to the use of the CPC cathodes for z-reconstruction. The reconstruction efficiency was found to be independent of d_0 for $|d_0| < 5$cm and of z_0 for $|z_0| <$ 20cm.

To show how efficiently all tracks are reconstructed and not merely those charge tracks which satisy (1) , and also to give a parametrisation of tracking efficiency less dependent on track overlap,Table 8.1 gives the track reconstruction efficiency as a function of the number of hits on the various detectors. The MC track was required to have caused at least 6 hits in total. The efficiency for MILL to reconstruct tracks which caused $\leq$2 hits in the large drift chamber is zero as MILL only uses the drift chamber for track recognition.

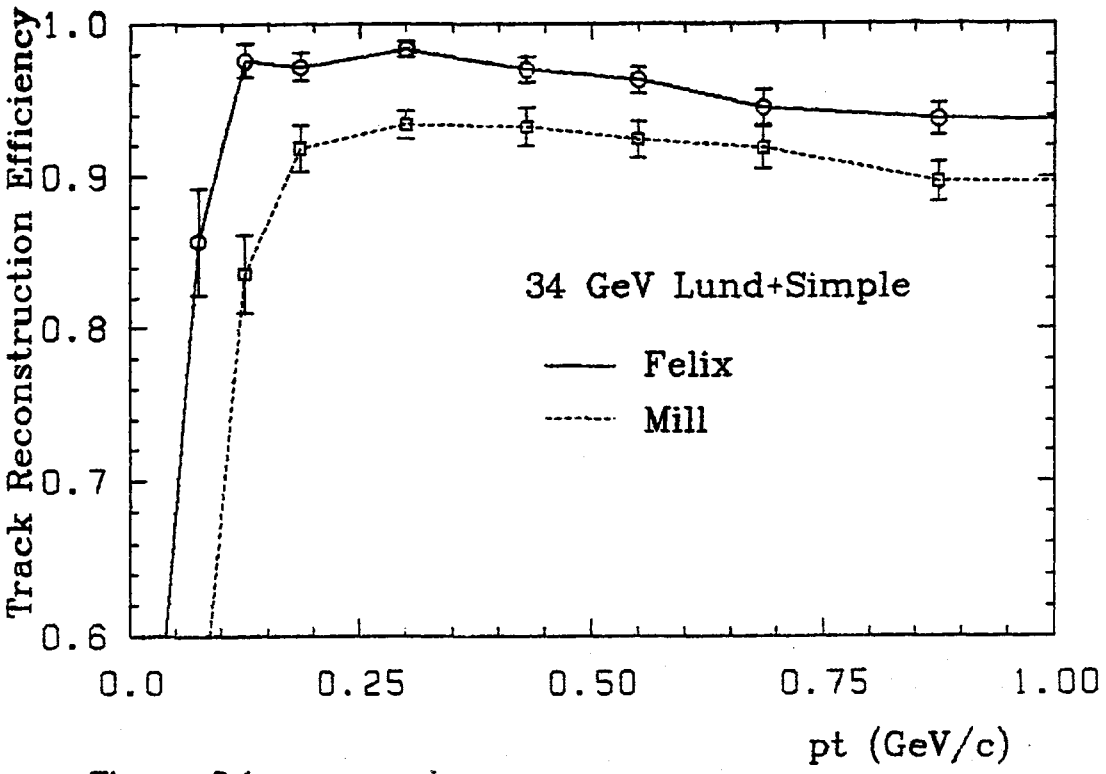

Figure 8.1

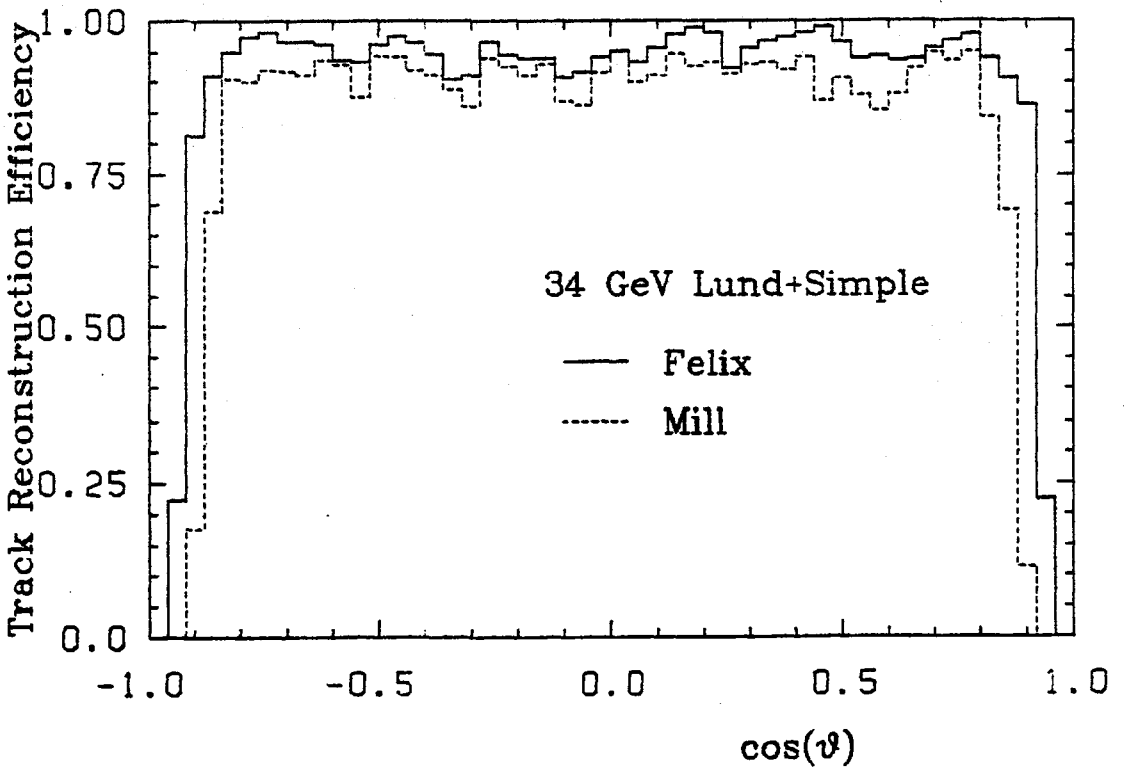

Figure 8.2

MILL TRACK RECONSTRUCTION EFFICIENCY					
# HITS	DC 0°	DC α	CPC anode	CPC cath.	VXD
0	0.0	0.7			
1	0.0	5.9			
2	0.0	24.3			
3	1.2	56.0			
4	9.4	82.5			
5	63.4	93.2			
6	87.1	96.8			
7	95.9				
8	98.3				
9	99.3				

TABLE 8.1a MILL Track Reconstruction Efficiency

FELIX TRACK RECONSTRUCTION EFFICIENCY					
# HITS	DC 0°	DC α	CPC anode	CPC cath.	VXD
0	31.9	29.5	40.2	57.1	49.3
1	13.9	37.6	48.6	80.1	42.9
2	25.8	55.4	56.8	82.6	52.0
3	47.9	72.8	86.0	87.6	69.9
4	57.6	86.5	94.5	90.4	76.9
5	73.7	94.2		93.5	88.2
6	87.4	96.9		95.3	91.2
7	94.1			95.3	97.5
8	98.1			95.9	98.1
9	98.6				

TABLE 8.1b FELIX Track Reconstruction Efficiency

8.3.1 Spurious tracks

A tracking program is also required not to produce spurious tracks. A reconstructed track is considered to be spurious if it was

not associated to a MC track (association was described above). We call a reconstructed track 'accepted' if it satisfies:

(3) $|d_0| < 5.0\text{cm}$

$|z_0| < 20.0\text{cm}$

$|\cos\vartheta| < 0.87$

$p_t > 100\text{MeV/c}$

$\chi^2_{r-\varphi}/\text{dof} < 12.0$

$\chi^2_{s-z}/\text{dof} < 20.0$

Reconstructed in 3-dimensions.

Table 8.2 shows the mean number of reconstructed tracks per event which fall in the classes correct/spurious and accepted/not-accepted for the tracking programs FELIX and MILL. FELIX finds more (correct,accepted) tracks but also more spurious tracks. No tracks were both spurious and accepted.

# tracks/event		
MILL	ACCEPTED	NOT ACCEPTED
CORRECT	11.3	0.7
SPURIOUS	0.0	0.8
FELIX	ACCEPTED	NOT ACCEPTED
CORRECT	11.5	1.5
SPURIOUS	0.0	1.3

TABLE 8.2 # Tracks Per Event

8.4 HIT ASSIGNMENT EFFICIENCY

We can define a 'hit assignment efficiency per chamber' C by

$$C = \frac{\#\text{hits on associated reconstructed tracks on the given chamber}}{\#\text{hits generated by MC tracks satisfying (1) on the chamber}}$$

The values found for C are listed in Table 8.3. The improvement in the efficiency of the CPC anode hits in FELIX is due to the extra constraint which the vertex detector provides and to the use of the

CPC anode hits in the track recognition stage rather than only at the final track fitting. The CPC cathode efficiency computed in this way is large as the same clusters may be used by several tracks.

CHAMBER	DC0°	DCα	CPC a	CPC c	VXD
MILL	88.8	89.4	72.7		
FELIX	90.5	88.8	91.6	139.5	99.4

TABLE 8.3 Hit Assignment Efficiencies (%)

8.4.1 Spurious hits

It is of interest to note how frequently incorrect hits are assigned to the reconstructed tracks. Hits on reconstructed tracks are assigned to the five classes : correct,ambiguity,missing,extra,wrong as defined in Table 8.4(a). The distribution of hits into these classes is shown in Table 8.4(b).

Definition of Hit Types	
TYPE	DESCRIPTION
CORRECT	Hit belongs to associated MC track or there was no hit generated and none assigned to the reconstructed track
WRONG	A noise hit or hit from some other track was assigned and the associated MC track did produce a hit
MISSING	No hit was assigned but a hit was generated by the MC track
AMBIGUITY	Assigned hit is associated ambiguity of the correct hit
EXTRA	No hit was generated by the MC track but a hit was assigned to the associated reconstructed track

TABLE 8.4a

MILL	Fraction in each class (%)				
CHAMBER	DC0°	DCα	CPC a	CPC c	VXD
CORRECT	94.4	92.2	75.3	53.2	23.4
WRONG	0.1	0.4	6.6	0.0	0.0
MISSING	2.0	1.7	14.3	46.9	76.6
AMBIGUITY	1.9	2.3	0.0	0.0	0.0
EXTRA	1.6	3.3	3.8	0.0	0.0
FELIX	Fraction in each class (%)				
CHAMBER	DC0°	DCα	CPC a	CPC c	VXD
CORRECT	91.0	82.3	90.7	62.1	82.9
WRONG	0.5	1.6	3.5	6.2	1.5
MISSING	3.6	7.1	2.7	3.1	3.9
AMBIGUITY	2.4	3.9	0.0	0.0	3.6
EXTRA	2.6	5.2	3.0	28.6	8.2

TABLE 8.4b Track Hit Confusion Statistics

8.5 RESOLUTION IN THE TRACK PARAMETERS

As well as reconstructing tracks as efficiently as possible we want to measure the parameters of the track helix and hence the

momenta and directions of the tracks accurately. We compare the resolutions found for FELIX and MILL tracks which satisfy (1) above.

Fig 8.3 shows the difference between the d_0 of the generated MC track and that of the associated reconstructed track. For FELIX the spread σ_{d0}=564±8μm while for MILL we find σ_{d0}=2722±33μm. This improvement is due to the use of the vertex detector by FELIX. As discussed in Chapter 6 the improvement lessens for tracks at low transverse momenta due to multiple Coulomb scattering in the material of the beampipe and tracking chambers. This can be seen in Fig 8.4 which shows how σ_{d0} varies with p_t.

Fig 8.5 shows the error in the direction of the track circle at the origin ,φ^0. We find $\sigma_{\varphi 0}$=5.20±0.07mrad and $\sigma_{\varphi 0}$=8.56±0.11 mrad for FELIX and MILL respectively. This improvement is also due to the vertex detector.

The difference between the generated and reconstructed position of the track along the beam direction is shown in Fig 8.6. From FELIX σ_{z0}=0.95±0.01cm and from MILL we find σ_{z0}=1.21±0.02cm. The improvement is due to the use of the CPC cathode hits by FELIX.

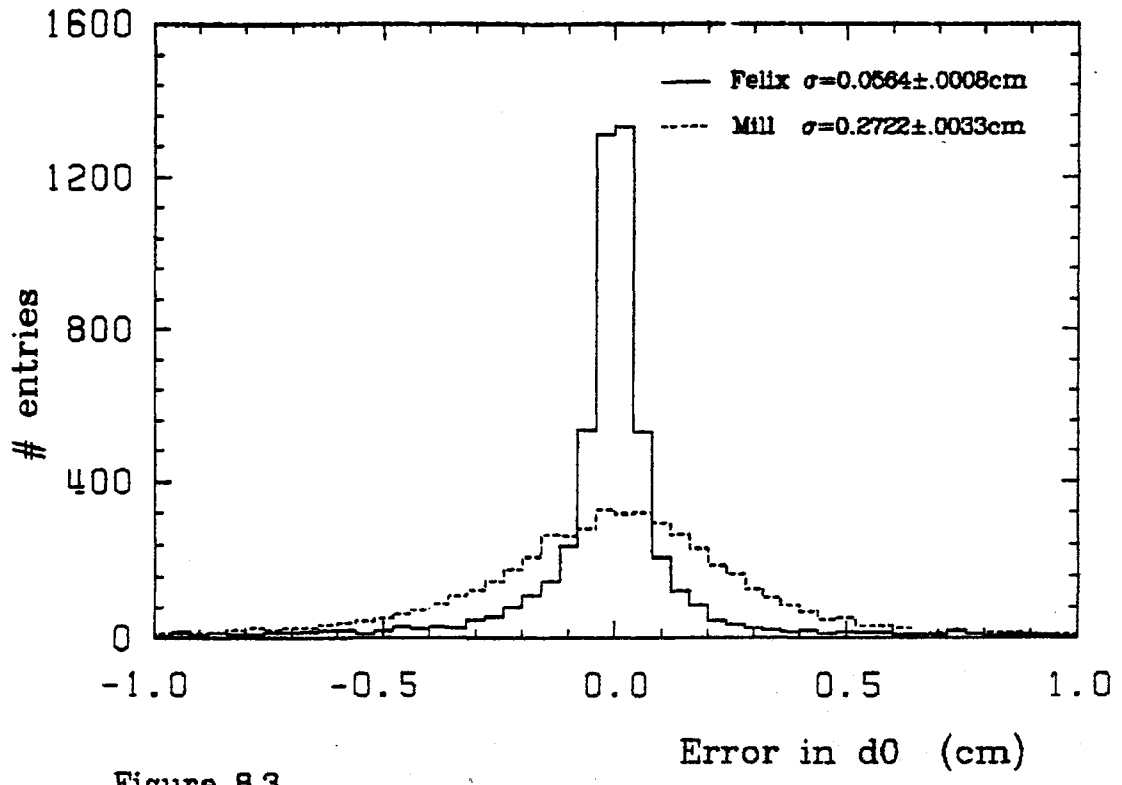

Figure 8.3

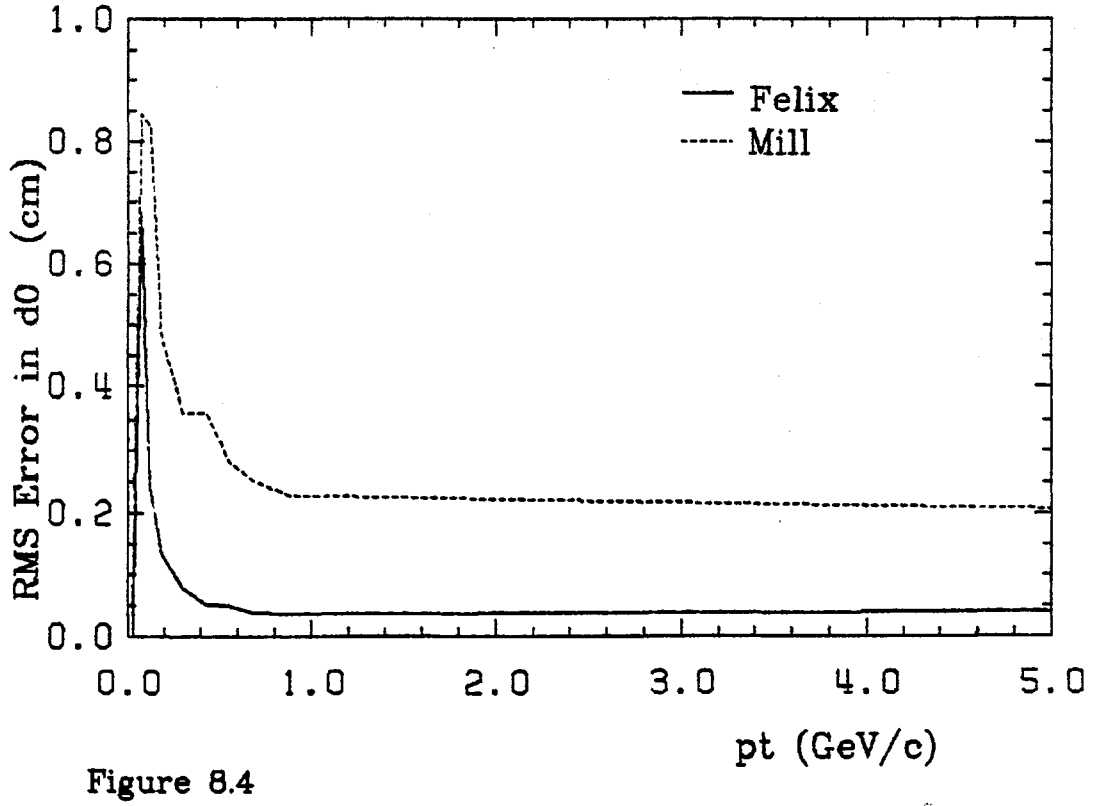

Figure 8.4

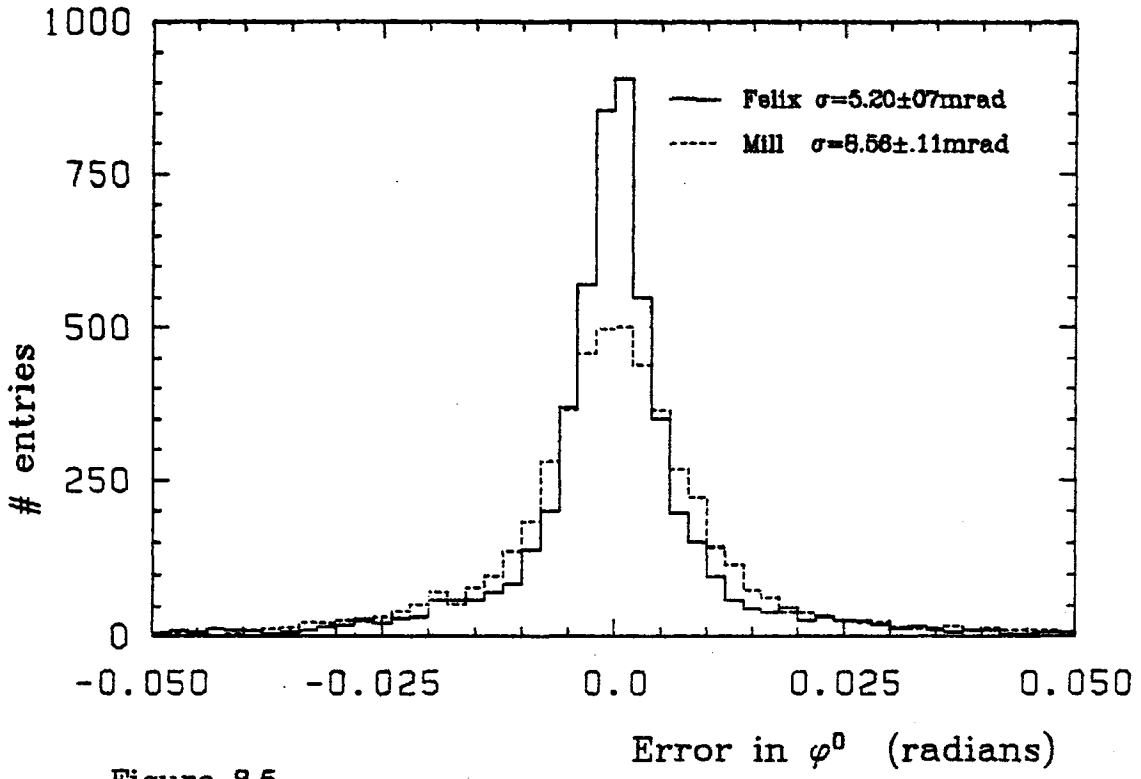

Figure 8.5

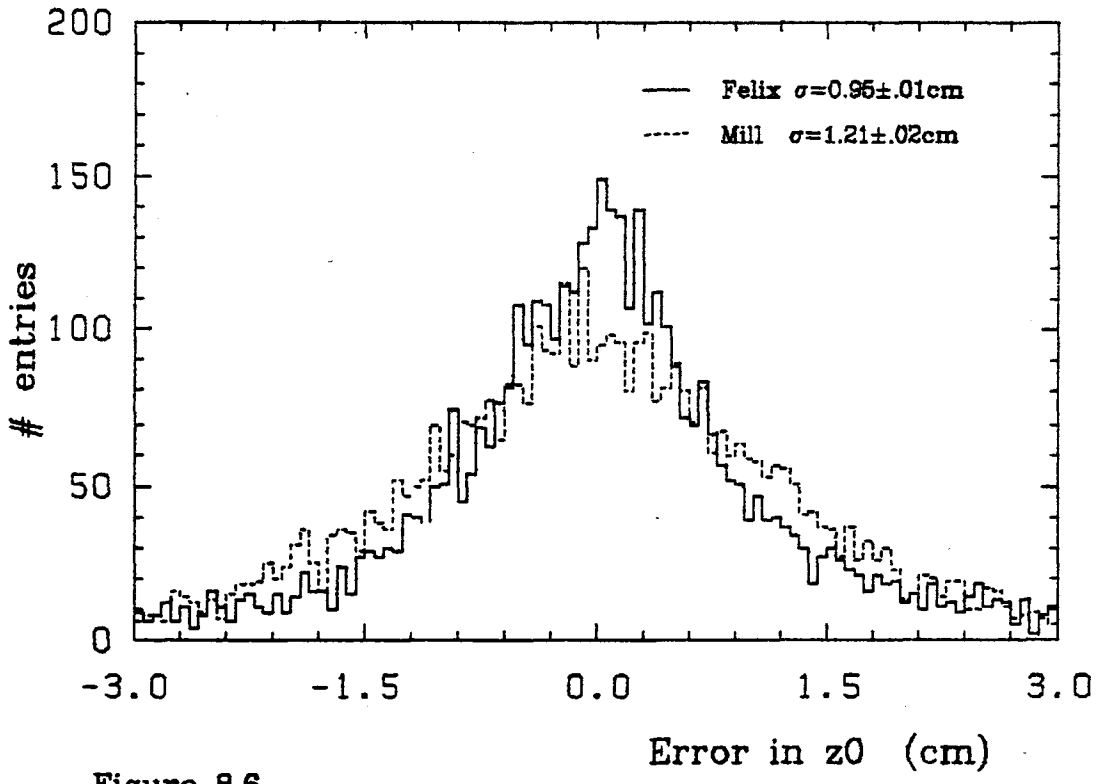

Figure 8.6

The error in $1/p_t$ (p_t in GeV/c) is shown in Fig 8.7 and its variation with p_t in Fig 8.8. The resolution $\sigma(1/p_t)$ (an average for all tracks) was 4.88±0.07% for FELIX and 5.60±0.07% for MILL. This improvement results from the use of the vertex detector by FELIX, as the fitted hits then cover a longer path length.

The resolutions quoted above correspond to the vertex detector resolution of 150 micron. used in the Monte-Carlo simulation. Further improvements would be expected for smaller point errors in the vertex detector.

8.6 EFFECT OF KINK FIT

The effect of allowing a kink in the track in the r-φ plane is shown in Figs 8.9 and 8.10. Fig 8.9 compares the error in d_0 when the measured d_0 is taken as that appropriate to the track circle before the kink with that found when the measured d_0 is taken as that appropriate to the track circle after the kink. For the inner d_0, σ_{d0}=534±7μm whereas for the outer σ_{d0}=2410±30μm. Fig 8.10 shows a similar plot for φ^0. The RMS angle of scatter from the fit for all tracks (1) was 11.1±0.2mrad.

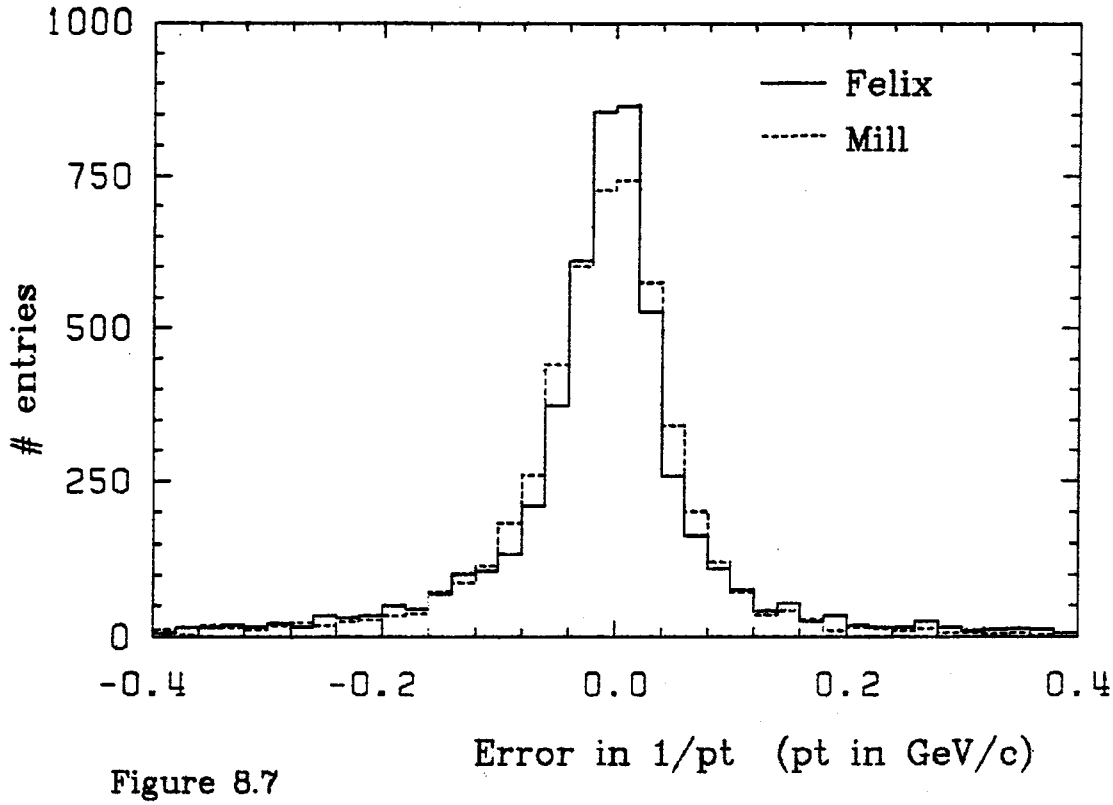

Figure 8.7

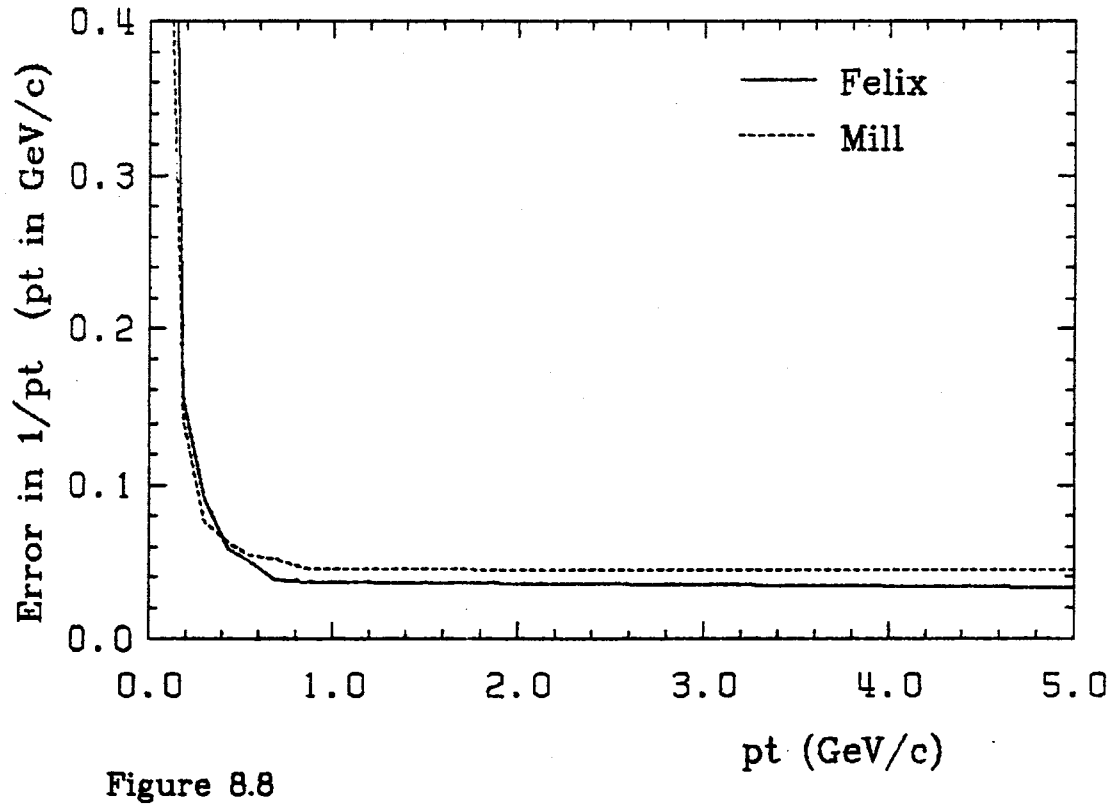

Figure 8.8

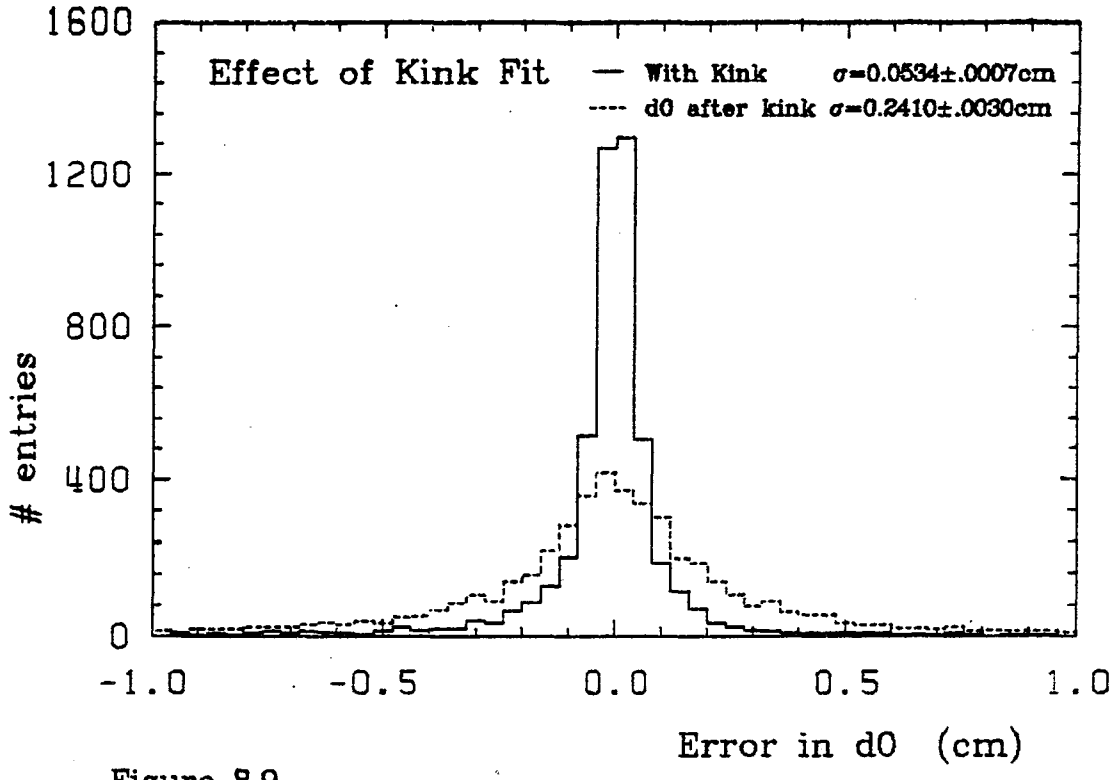

Figure 8.9

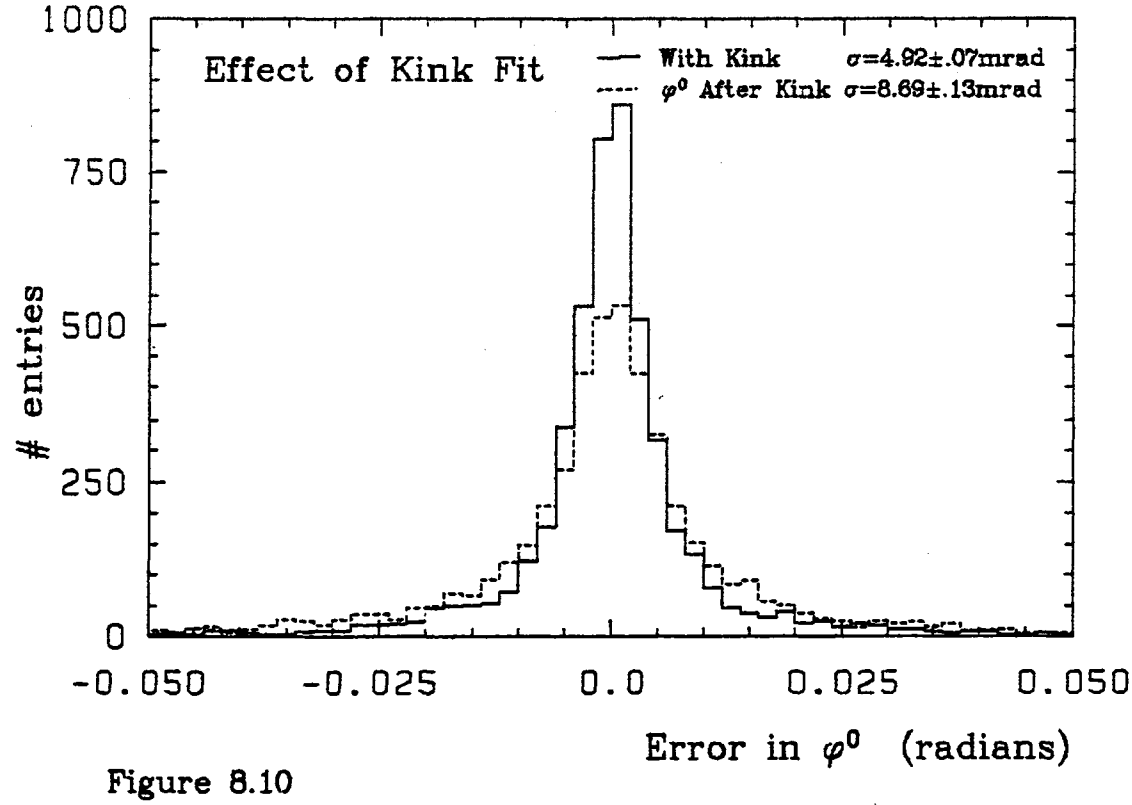

Figure 8.10

8.7 COMPARISON WITH PETRA DATA

Fig 8.11 compares the distribution in $\cos\vartheta$ of all tracks found by MILL and FELIX for the TASSO hadronic data collected in November 1982. The gain in tracks at large $|\cos\vartheta|$ by FELIX is evident.

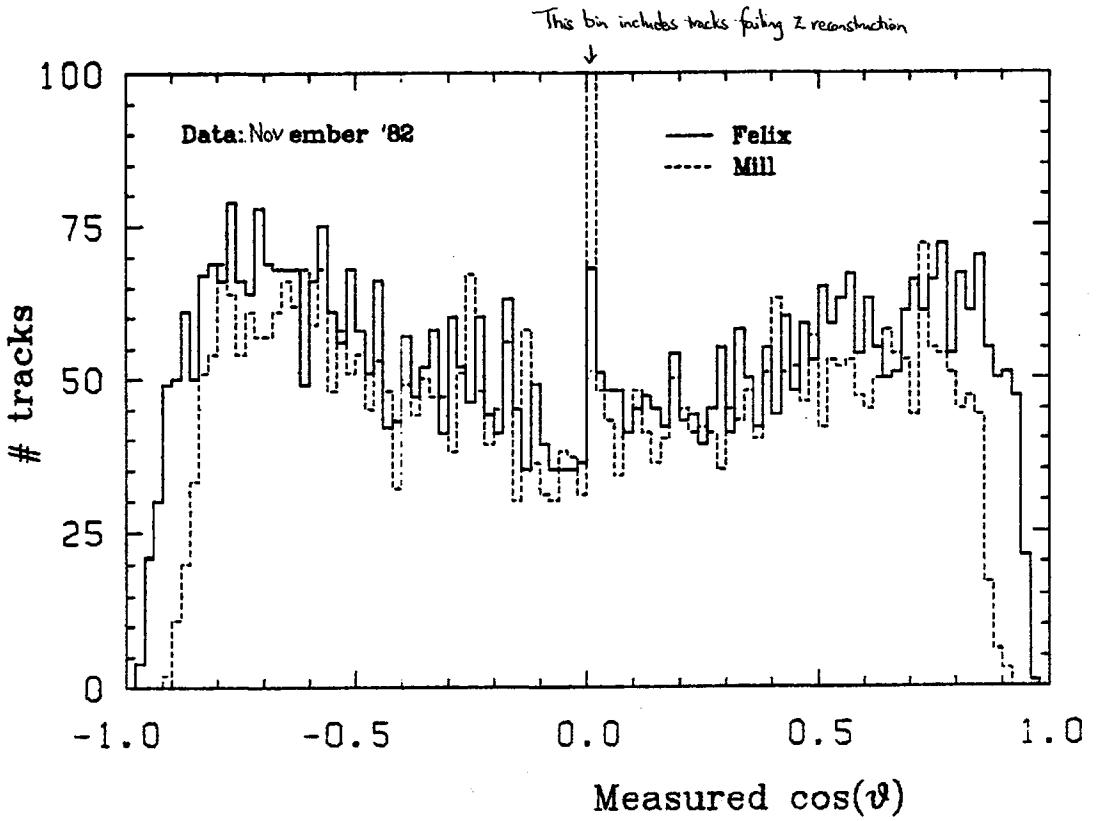
This bin includes tracks failing Z reconstruction
Data: November '82
Felix
Mill
tracks
100
75
50
25
0
-1.0
-0.5
0.0
0.5
1.0
Measured cos(ϑ)

Figure 8.11

9.0 PHYSICS ANALYSIS

9.1 INTRODUCTION

This chapter presents 3 measurements relating to the production of Λ particles in e^+e^- annihilation to hadrons and made possible by the large statistics (~20,000 events at W=34.4GeV) now available. Section 9.2 presents a measurement of the Λ inclusive cross-section in the momentum range from 0.6-1.5GeV using proton identification by time-of-flight. In section 9.3 the inclusive production cross-section of $\Xi^-,\bar{\Xi}^-$ is measured. Finally section 9.4 presents an upper limit on the production rate of the $\Sigma^*(1385)$ resonance.

For all of the following measurements a sample of 20,773 hadronic events at centre of mass energies $W \geq 30$GeV were selected as described in Chapter 2.

9.2 $e^+e^- \rightarrow \Lambda,\bar{\Lambda} + X$

The inclusive $\Lambda,\bar{\Lambda}$ production cross-section has been measured by TASSO[30] for $\Lambda,\bar{\Lambda}$ momenta above 1.0 GeV/c. Here we have extended the measurement to $\Lambda,\bar{\Lambda}$ momenta as low as 0.6GeV/c by

using the inner time-of-flight (ITOF) counter system to tag proton/antiproton particles.

9.2.1 Signal Isolation

For the reconstruction of the $\Lambda,\bar{\Lambda}$ we have used the charged decays:

$$\Lambda \rightarrow p\ \pi^-$$
$$\bar{\Lambda} \rightarrow \bar{p}\ \pi^+$$

which have a branching ratio of 64.2±0.5%.

Unless specifically stated we shall refer to $\Lambda,\bar{\Lambda}$ simply as Λ.

To select Λ candidates we calculated the invariant mass for each combination of two oppositely charged particles ,considering the higher momentum track the proton (antiproton). The momenta were measured after a fit requiring that the two track helices intersect. The Λ candidates were required to satisfy the following cuts:

1. each particle should have a transverse momentum p_t,with respect to the beam direction greater than 0.1GeV/c and a polar angle ϑ with $|\cos\vartheta| < 0.87$
2. each pair had to have a momentum greater than 0.6GeV/c
3. the invariant mass of the pair,considered as an e^+e^- pair had to be greater than $50MeV/c^2$ to reject converting photons
4. all pairs had to intersect in the plane transverse to the beam (r-φ plane) between 0.3 and 45.cm from the interaction point
5. the angle ψ between the line joining the average interaction point (as determined from Bhabha scettering events) and the decay point and the direction of the Λ momentum vector in the r-φ plane had to satisfy $\cos\psi < 0.988$
6. pairs consisting of tracks with more than 3 hits missing immediately following the decay point were rejected
7. The decay angle ϑ^* of the proton in the rest system of the Λ,measured with respect to the Λ direction of flight had to satisfy $|\cos\vartheta^*| < 0.9$

In addition for the present analysis:

- the proton track had to be identified by the time-of-flight. This was achieved by the requirements:

the momentum |p| of the track had to satisfy $0.4GeV/c \leq |p| \leq 1.2GeV/c$

- the closest distance of approach (d_0) of the track in r-φ to the interaction point in the r-φ projection had to be less than 10cm
- no other track should have extrapolated to the same ITOF counter
- the TOF measurement from both ends of the counter should agree within 3ns
- the TOF was defined as the weighted mean of the measurements from the two ends. The error from each end was measured to be

$$\sigma = 0.3\ (1+2.z_{frac})\ ns$$

where z_{frac} was the distance of the projected track from the phototube expressed as a fraction of the total length of the counter. The expected time-of-flight,t_{exp},was computed for the assumptions that the particle was a π,K and p by:

$$t_{exp} = l/c \sqrt{(1 + m/p^2)}\ ns$$

where l is the path length of the track between the interaction point and the counter in cm

c is the speed of light (=29.98)

m is the mass of the particle species in GeV/c^2

p is the particle momentum in GeV/c

The differences $\Delta t = |t_{measured} - t_{exp}|$ were required to satisfy:

$$\Delta t_\pi \geq \sigma$$

$$\Delta t_K \geq \tfrac{1}{2}\sigma$$

$$\Delta t_p \leq 3\sigma$$

for the three particle species.

The distributions of $\Delta t_\pi/\sigma$, $\Delta t_K/\sigma$ and $\Delta t_p/\sigma$ found for the tracks in the hadronic data are shown in Figure 9.2.1.

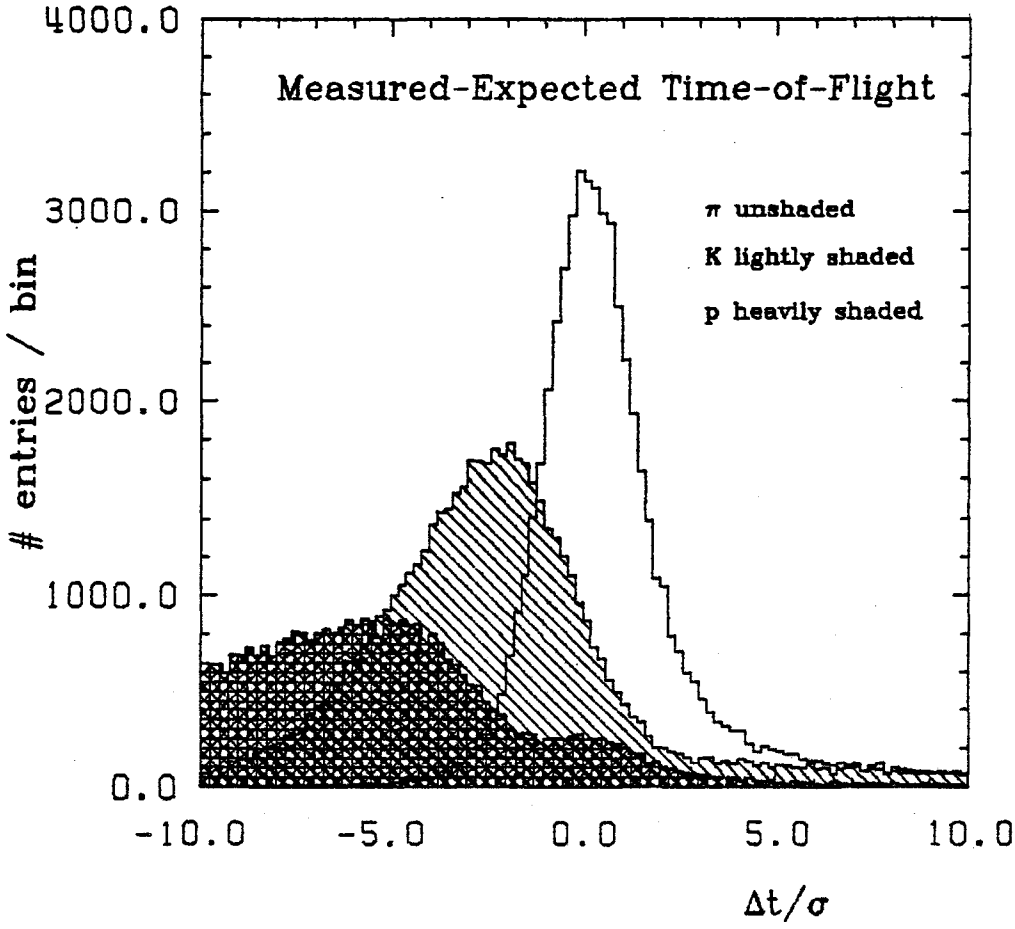

Figure 9.2.1

The resulting mass spectrum of $p\pi^-$ and $\bar{p}\pi^+$ combinations is shown in Fig 9.2.2,9.2.3 for the momentum intervals 0.6-1.0 GeV/c and 1.0-1.5GeV/c,and the separate $p\pi^-$ and $\bar{p}\pi^+$ mass spectra are given in Fig 9.2.4 - 9.2.7. A clear signal is seen in all spectra. Table 9.2.1 lists the estimated signals after subtraction of the background. The background was estimated by extrapolation from the side-bands.

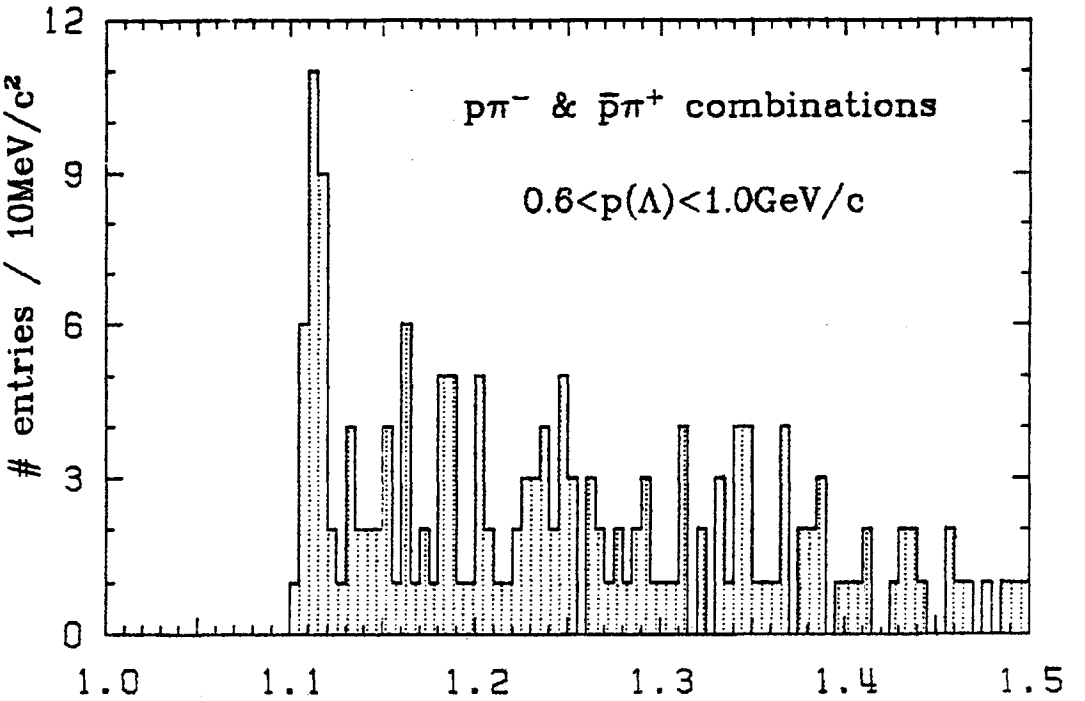

Figure 9.2.2

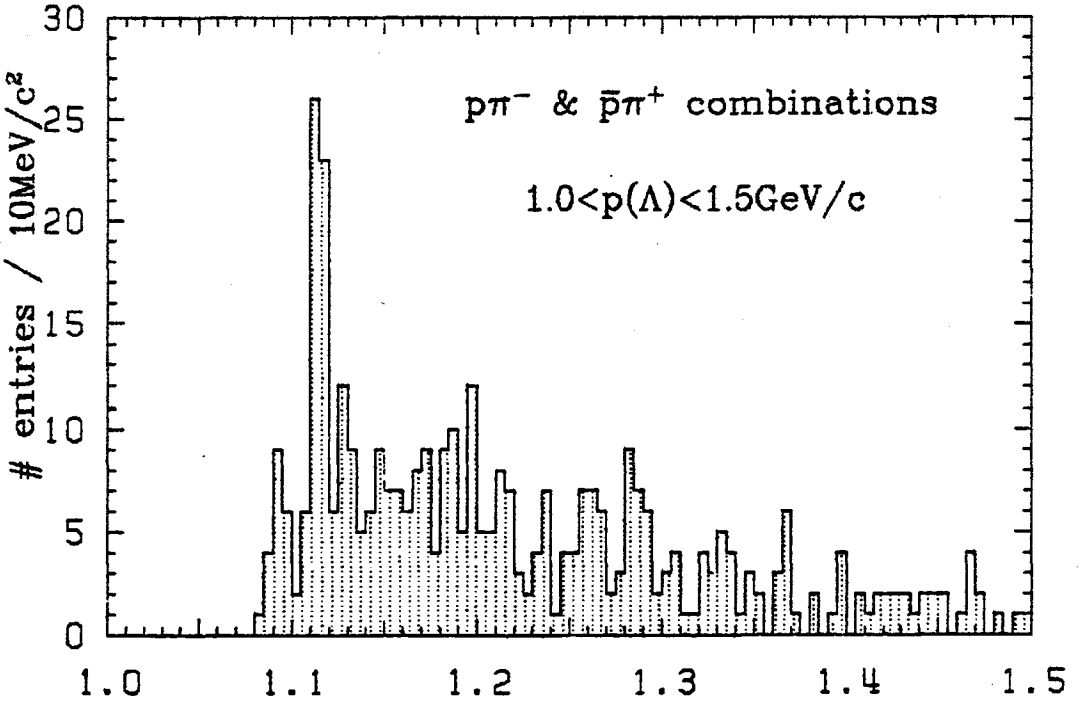

Figure 9.2.3

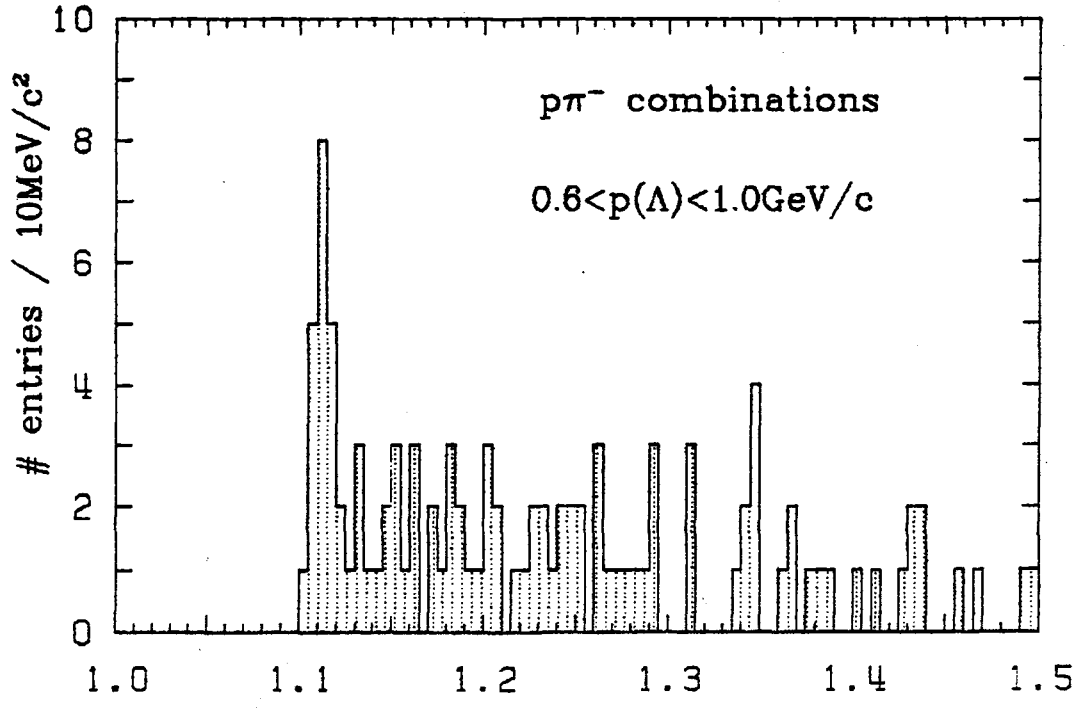

Figure 9.2.4

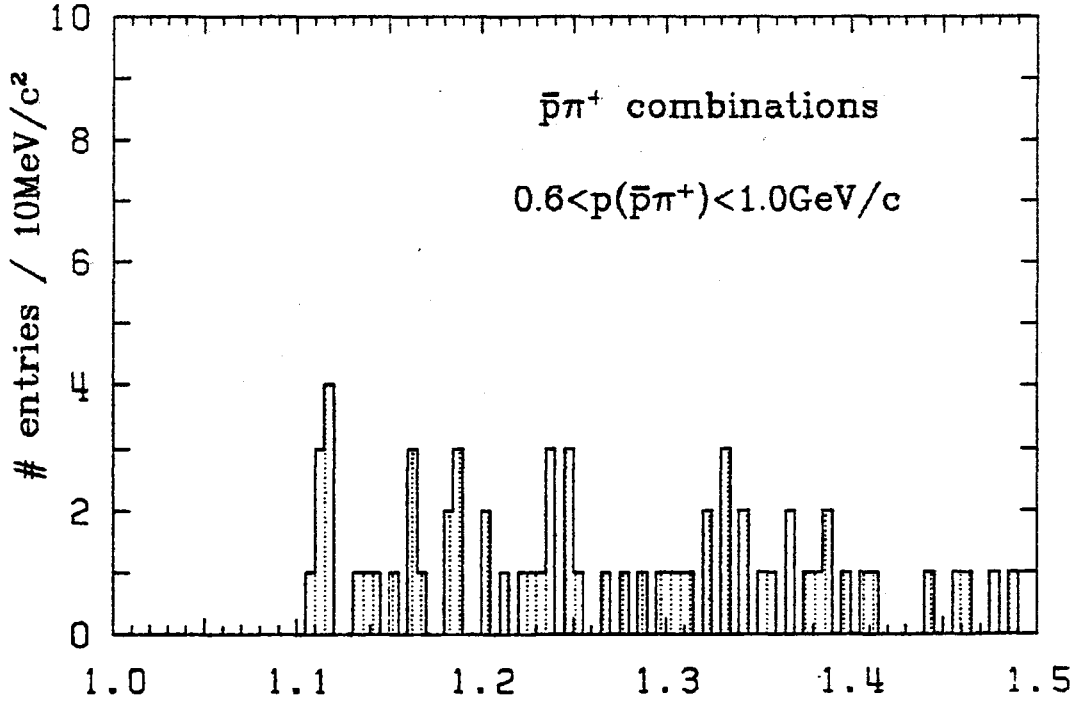

Figure 9.2.5

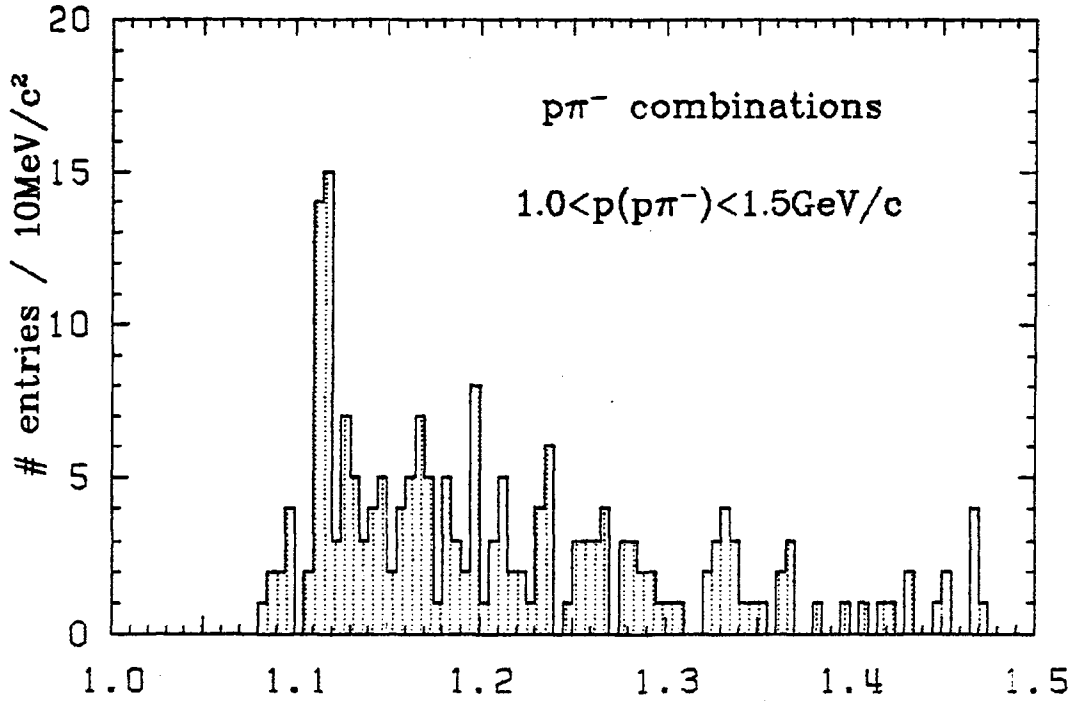

Figure 9.2.6

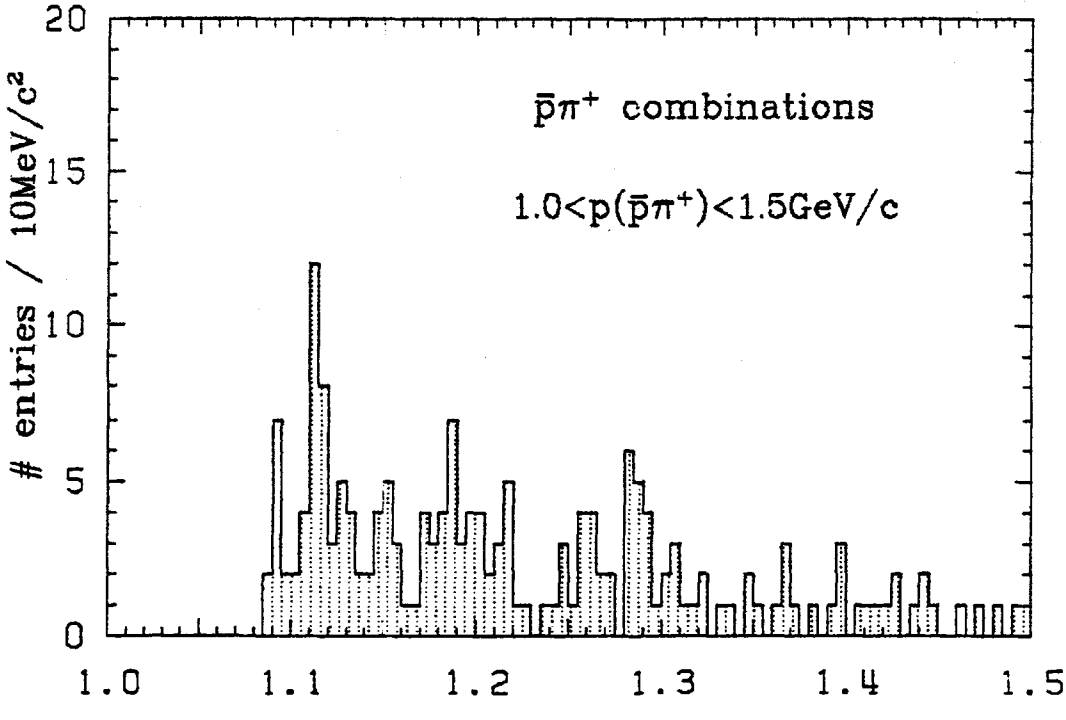

Figure 9.2.7

Λ	0.6-1.0 GeV/c	1.0-1.5 GeV/c
SIGNAL	16	23
BACKGROUND ESTIMATE	5	6
ERROR ON SIGNAL	5	6
$\bar{\Lambda}$	0.6-1.0 GeV/c	1.0-1.5 GeV/c
SIGNAL	8	19
BACKGROUND ESTIMATE	0	8
ERROR ON SIGNAL	3	6
$\Lambda+\bar{\Lambda}$	0.6-1.0 GeV/c	1.0-1.5 GeV/c
SIGNAL	24	39
BACKGROUND ESTIMATE	5	10
ERROR ON SIGNAL	6	8

TABLE 9.2.1 $\Lambda,\bar{\Lambda}$ SIGNAL

9.2.2 Detection Efficiency

The efficiency for $\Lambda,\bar{\Lambda}$ detection was determined by generating Monte-Carlo events for $e^+e^- \rightarrow q\bar{q}, q\bar{q}g$ and simulating hits in the tracking chambers as well as decays,nuclear absorption and scattering. Also included were radiative effects. The detector simulation included a simulation of the TOF from the phototubes of the ITOF counters. The simulated events were subjected to the same chain of analysis programs as the real data.

Table 9.2.2 shows the result of an examination of 87,296 Monte-Carlo events. Of these 60,308 satisfied the hadronic event selection cuts and 66,308 events radiated less than 10% of the nominal beam energy of 17GeV.

	Λ		$\bar{\Lambda}$	
Λ momentum (GeV/c)	0.6-1.0	1.0-1.5	0.6-1.0	1.0-1.5
All generated, all events	870	1050	849	1009
All generated, events≧90%W	696	854	694	809
For decays $\Lambda \to p\pi^-$ or $\bar{\Lambda} \to \bar{p}\pi^+$				
Both tracks reconstructed	180	279	163	261
$\Lambda, \bar{\Lambda}$ identified	28	53	25	54
ε_1(%) $\Delta\varepsilon_1$	4.5 ±0.8	7.0 ±0.9	4.0 ±0.8	7.3 ±0.9

TABLE 9.2.2 $\Lambda, \bar{\Lambda}$ DETECTION EFFICIENCY

The detection efficiency for Λ particles in the selected hadronic events ε,was made up of the efficiency ε_1 determined from the Monte-Carlo simulation times a correction factor ε_2 for the efficiency of the TOF cut ($\varepsilon=\varepsilon_1.\varepsilon_2$).

The detection efficiency ε_1 was defined by $\varepsilon_1=n_1/n_2$ where n_1 was the number of reconstructed Λ particles and n_2 was the number of generated Λs in events which passed the hadronic event selection

cuts. This efficiency included correction for the unseen decay modes of the Λ (B.R. $\Lambda \to n\pi^0$ is 35.8±0.5%),the track reconstruction efficiency (for Λ momenta between 0.6 and 1.5 GeV/c both tracks were reconstructed with an efficiency of ~50%),and the probability that the tracks satisfied the selection criteria (~18%). Table 9.2.2 gives ε_1 for $\Lambda,\bar{\Lambda}$ in the two momentum intervals.

In addition ε_1 should include a correction,ε',for radiative effects and the difference between the acceptance of events with Λs to the acceptance for hadronic events in general. ε' was given by the ratio of the production rate of Λ particles in events selected as hadrons to that in events generated at the nominal centre of mass energy without radiative effects. We considered events generated with less than 10% of the centre of mass energy lost by radiative effects as being essentially generated at the nominal centre of mass energy. The correction factor ε' was defined by:

$$\varepsilon' = \frac{n_2/N_2}{n_0/N_0}$$

where n_2 was the number of Λs generated in N_2 events which passed the hadronic event selection cuts and n_0 was the number of Λs gen-

erated in N_0 events which after radiative effects, retained more than 90% of the nominal centre of mass energy in the hadronic system. ε' was found to be unity to within 1% and was therefore neglected.

The TOF simulation was checked by comparing the fractions of all tracks with flag1=0 (only 1 track in counter) and flag2=0 (good timing from both ends of counter) found for the real data and in the Monte-Carlo events . The Monte-Carlo produced more good tracks (65.2±0.1%) than the data (55.7±0.1%). It was therefore decided to determine the correction factor ε_2 by normalising to the previously measured Λ cross-section [30] in the momentum interval 1.0-1.5GeV/c. We did not therfore require a precise knowledge of the efficiency of the ITOF counters.

9.2.3 Determination of Cross-section

The differential cross-section $d\sigma/dp$ obtained for the reaction $e^+e^- \rightarrow \Lambda(\bar{\Lambda})+X$ at W>30GeV is given in Table 9.2.3. This was determined from the measured signal and the efficiency by:

$$d\sigma/dp = \sigma_{tot}/N_{events} \cdot \Delta n/\Delta p \cdot 1./\varepsilon$$

where Δn = # observed particles

Δp = momentum interval

N_{events} = # accepted hadronic events

σ_{tot} = total hadronic cross-section

= R 86.8/W^2 μb.

The correction factor,ε_2,was determined by the ratio of the previously measured cross-section to that obtained here in the momentum interval 1.0-1.5GeV/c. The corrected cross-section thus obtained for $\Lambda,\bar{\Lambda}$ momenta between 0.6 and 1.0GeV/c is given in Table 9.2.3.

The scaled cross-section $s/\beta\ d\sigma/dx$ ($s=W^2,\beta=p/E$ where p,E are the Λ momentum and energy, $x=2E/W$) was obtained from estimating the signal in mass plots weighted by $1/\beta$ and computing the efficiency for the two x intervals. The resulting cross-section for $0.075<x<0.090$ was corrected by normalising to the interval $0.090<x<0.110$,and is given in Table 9.2.3.

p (Λ,$\bar{\Lambda}$) (GeV/c)	0.6-1.0	1.0-1.5
Uncorrected dσ/dp (pbarn/GeV/c)	23.8±5.7	18.3±3.6
Previously measured dσ/dp (pbarn/GeV/c)	-	25.0±5.6
Correction factor	-	1.37±0.4
Corrected dσ/dp (pbarn/GeV/c)	32.6±12.3	-
x	0.075-0.090	0.090-0.110
Uncorrected s/β dσ/dx (nbarn.GeV^2)	1418±311	630±138
Previous measurement of s/β dσ/dx (nbarn.GeV^2)	-	818±190
Correction factor	-	1.30±0.42
Corrected s/β dσ/dx (nbarn.GeV^2)	1843±720	-

TABLE 9.2.3 Λ,$\bar{\Lambda}$ INCLUSIVE CROSS-SECTIONS

9.3 $e^+e^- \to \Xi^-, \bar{\Xi}^- + X$

9.3.1 Signal Isolation

For reconstruction of the Ξ^- we used the cascade decay

$$\Xi^- \to \Lambda\ \pi^-$$
$$\qquad\ \ \lfloor\!\!\rightarrow p\ \pi^-.$$

The antiparticles were selected through

$$\bar{\Xi}^- \to \bar{\Lambda}\ \pi^+$$
$$\qquad\ \ \lfloor\!\!\rightarrow \bar{p}\ \pi^+.$$

Unless specifically stated we shall refer to Ξ^-, $\bar{\Xi}^-$ and to $\Lambda,\bar{\Lambda}$ simply as Ξ^- and Λ in the following.

Λ candidates were selected with high efficiency by the standard cuts ((1)-(7) of §9.2.1) except that cuts (2),(4) and (5) were changed as follows:

- each pair had to have a momentum greater than 1.GeV/c
- all pairs had to intersect in the plane transverse to the beam (r-φ plane) between 5. and 45.cm from the interaction point
- the direction of the line joining the average interaction point (as determined from Bhabha scattering events) and the decay point had to agree with the direction of the Λ momentum vector within 10° in the r-φ plane.

In addition the following was required:

- pairs consisting of tracks with more hits in the tracking chambers in front of the decay point than could be considered accidental were rejected

- in the r-φ plane the distance of closest approach of the pion track (the lower momentum particle) to the interaction point had to be greater then 3mm if the decay point was less than 20cm away from the interaction point (the first tracking chamber had a radius of 18.7cm).

These cuts were chosen to provide a large Λ signal at the expense of a larger background than used for the Λ cross-section

measurement[30] so as to increase the final Ξ^- efficiency. This is possible as the background to the Ξ^- signal can be reduced by the cuts on the additional charged track presented below.

The resulting mass spectrum of $p\pi^-$ and $\bar{p}\pi^+$ combinations is shown in Fig 9.3.1. A clear signal of ~445 $\Lambda,\bar{\Lambda}$ are seen above a background of ~626. The r.m.s. Λ mass resolution is $\sigma \approx 4 MeV/c^2$.

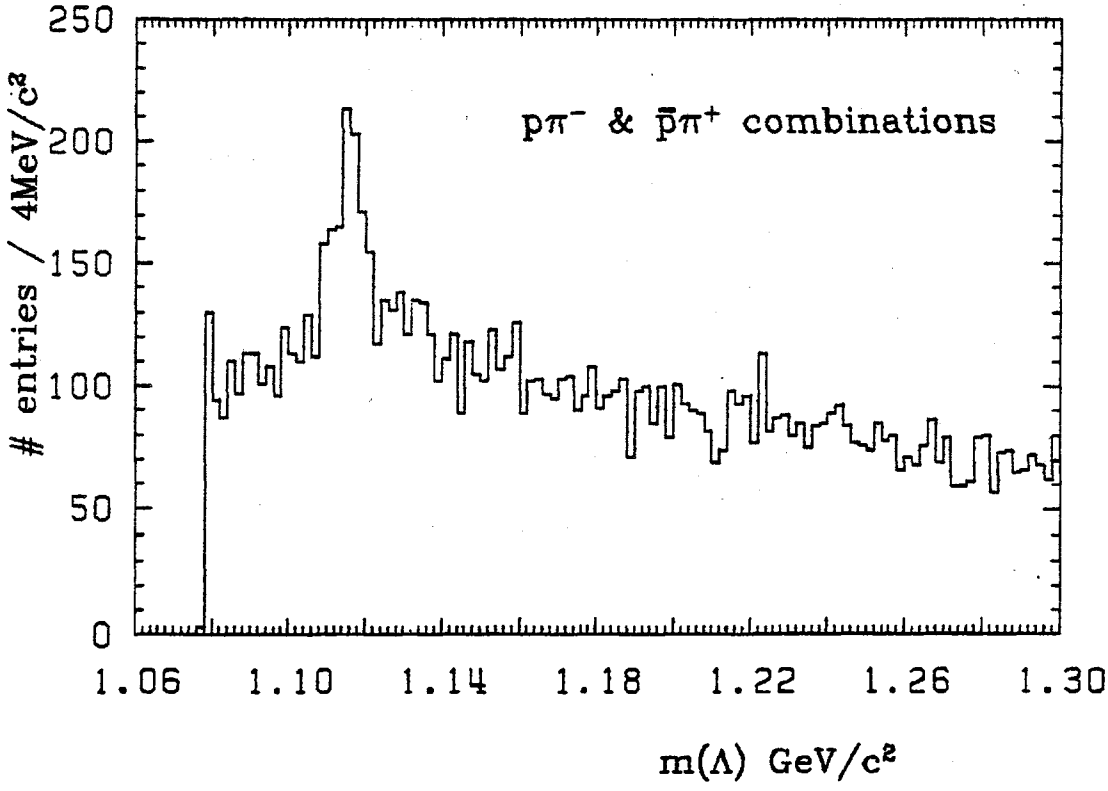

Figure 9.3.1

All particle combinations having an invariant mass within $\pm 0.006 GeV/c^2$ of the Λ mass ($1.116 GeV/c^2$) were then considered to be Λ candidates. For the further analysis their mass was fixed to the Λ mass.

To select Ξ^- we searched for an intersection of an additional charged track assumed to be a pion with the Λ. We required further that:

- the additional charged track satisfied $p_t > 0.1 GeV/c$ and $|\cos\vartheta| < 0.87$.
- the momentum of the $\Lambda\pi^-$ combination had to be greater than 1 GeV/c.
- the intersection of the additional charged track with the Λ should be both more than 1cm away from the interaction point in the r-φ plane and more than 1cm in front of the Λ decay point in the r-φ plane. The probability of a Ξ^- with the momentum of the Ξ^- candidate to decay after the reconstructed decay point had to be less than 80% by the requirement:

$$r_{vertex} > -p_t.(c\tau/m).\ln(0.8) \qquad (=0.83 p_t \quad p_t \text{ in} GeV/c)$$

where r_{vertex} was the distance between the interaction point and the decay point and τ,m are the lifetime and mass of the Ξ^-.

- the angle between the line joining the interaction point and the reconstructed decay point and the momentum vector of the $\Lambda\pi^-$ combination had to be smaller than 5°

The resulting $\Lambda\pi^-$ mass spectrum is shown in Fig 9.3.2. A narrow peak around the Ξ^- mass (1.312 GeV/c^2) is visible. No similar structure is seen in Fig 9.3.3 where the Λs are combined with tracks of the wrong charge. The width of the Ξ^- signal in Fig 9.3.2 is in agreement with the expected r.m.s. resolution of σ=8MeV/c^2 obtained from Monte-Carlo calculations. From Fig 9.3.2 we obtain 20 candidates (above a background of 15) with a mass 1.310GeV/c^2<M($\Lambda\pi$)<1.340GeV/c^2. Separating our sample of 20 Ξ^- candidates into baryons and antibaryons we find 16 Ξ^- and 4 $\bar{\Xi}^-$ above background ($\bar{\Xi}^-$ entries are shaded in Fig 9.3.2).

By making cuts on the χ^2/dof of a refit to the Λ tracks and a fit of the additional charged track with respect to the position of the Λ at the reconstructed Ξ^- decay point,a cleaner signal is observed (Fig 9.3.4 & Fig 9.3.5) of 13 Ξ^- above a background of 8 candidates.

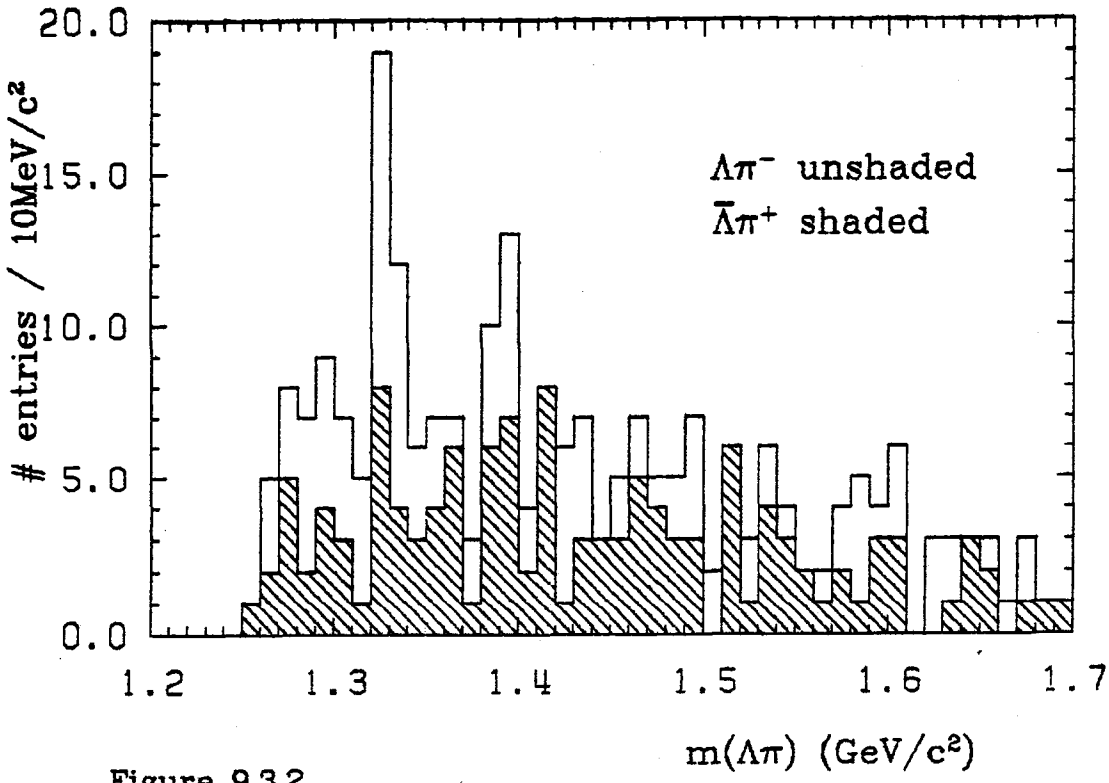

Figure 9.3.2

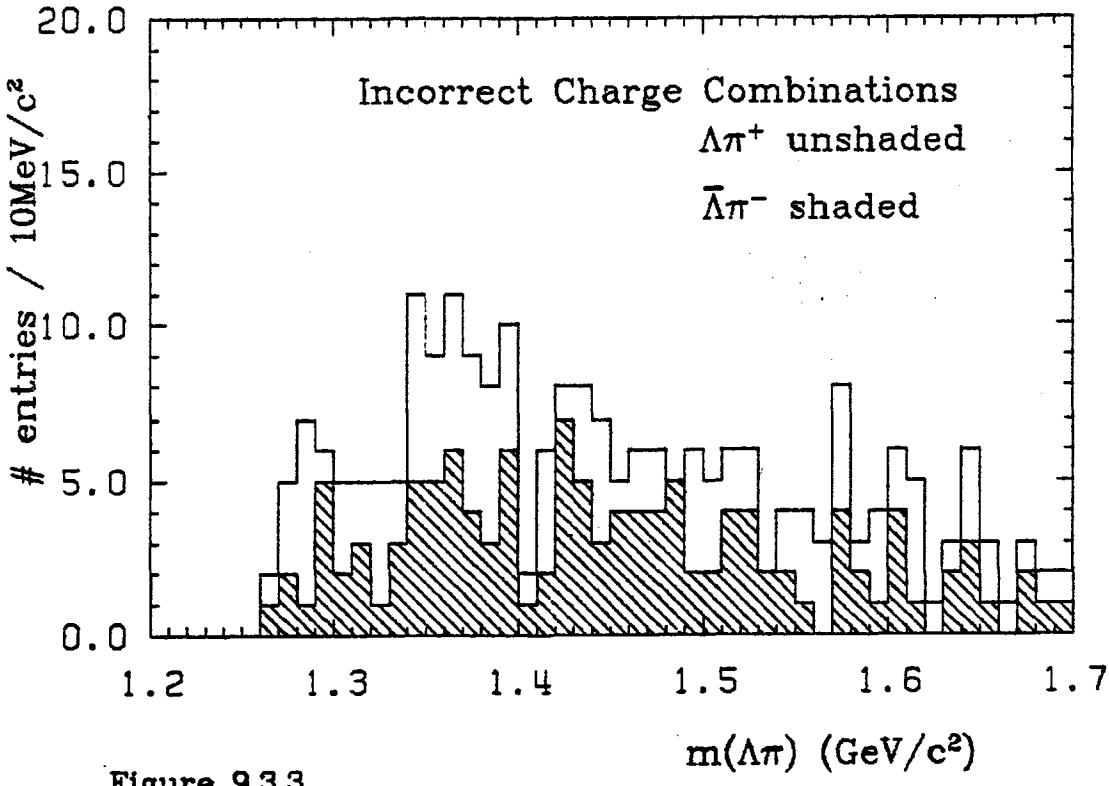

Figure 9.3.3

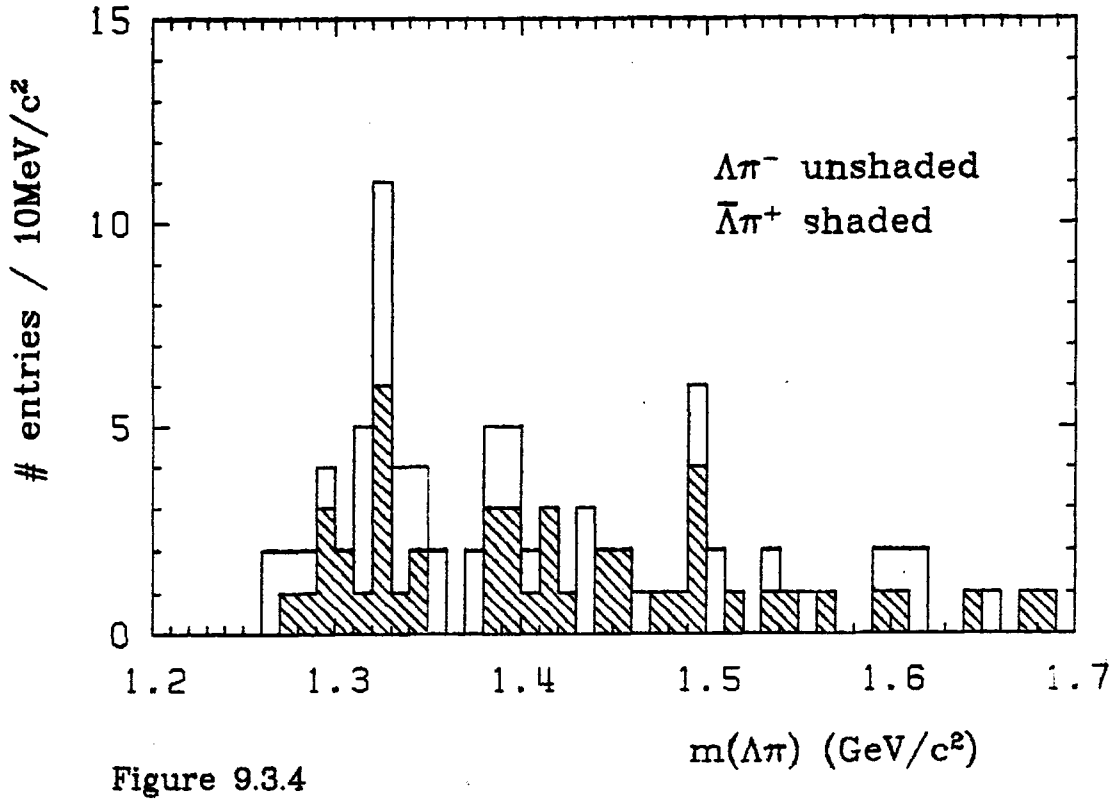

Figure 9.3.4

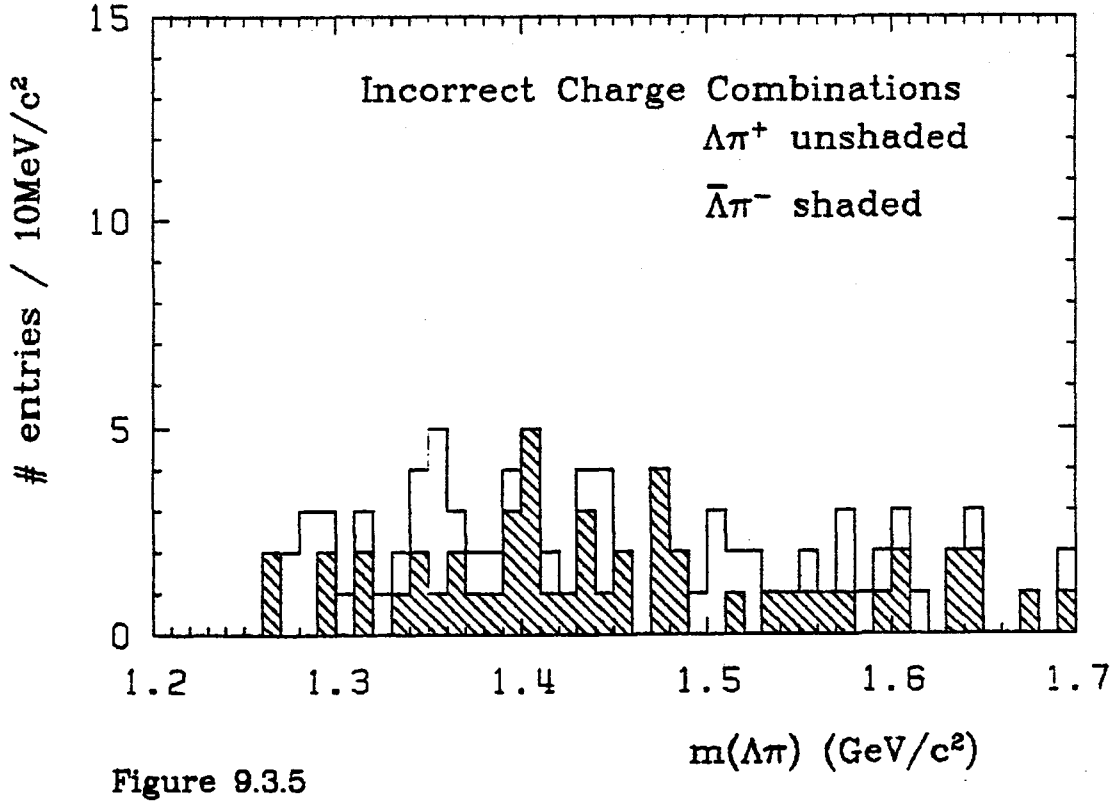

Figure 9.3.5

9.3.2 Detection Efficiency

The efficiency for Ξ^- detection was determined by generating Monte-Carlo events for $e^+e^- \rightarrow q\bar{q}, q\bar{q}g$ and simulating hits in the tracking chambers as well as decays,nuclear absorption and scattering. Also included are radiative effects. The simulated events were subjected to the same chain of analysis programs as the real data.

Table 9.3.1 shows the result of an examination of 2340 Monte-Carlo events which contained a generated Ξ^-. Of these 1582 satisfied the hadronic event selection cuts. 1929 events radiated <10% of the nominal beam energy of 17GeV.

The detection efficiency ε_1 was defined by $\varepsilon_1 = n_1/n_2$ where n_1 was the number of reconstructed Ξ^- particles and n_2 was the number of generated Ξ^-s in events which passed the hadronic event selection cuts. This efficiency included correction for the unseen decay modes of the Λ (B.R. $\Lambda \rightarrow n\pi^0$ is 35.8±0.5%),the track reconstruction efficiency (for Ξ^- momenta between 1.2 and 8.0 GeV/c the efficiency for reconstruction of the 3 tracks was ~24%),and the probability that the tracks satisfied the selection criteria (~29%).

The correction for radiative effects and for the dependence in event acceptance on Ξ^- production was considered as described in §9.2.2 for Λ production. Here also the correction factor was unity within its error for Ξ^- momenta between 1.2 and 8.0 GeV/c.

The overall detection efficiency ε_1 increased from 2% at 1.2GeV/c to 8% at 2.5GeV/c and decreased to 2.5% at 6GeV/c. ε was parametrised by the function $\varepsilon=a/p+b+cp+dp^2$ where p is the Ξ^- momentum in GeV/c and a,b,c,d are constants (a=-27.1,b=32.0,c=-6.1,d=0.32).

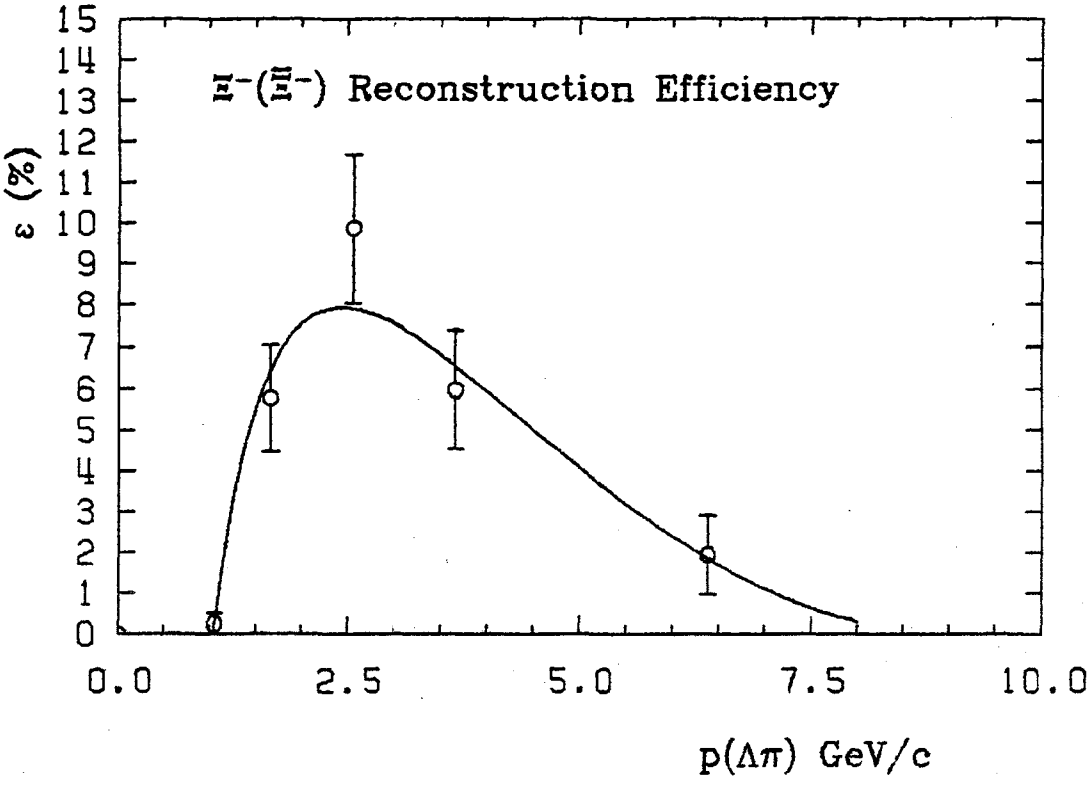

Figure 9.3.6

9.3.3 Inclusive Ξ^- Cross-section

The number of Ξ^- candidates was obtained by subtraction of the wrong charge combination from the correct charge combinations in the mass range $1.31 GeV/c^2 < M(\Xi^-) < 1.34 GeV/c^2$. The differential

cross-section $d\sigma/dp$ for the reaction $e^+e^- \rightarrow \Xi^-(\overline{\Xi^-})+X$ at W>30GeV was calculated by:

$$d\sigma/dp = \sigma_{tot}/N_{events} \cdot \Delta n/\Delta p \cdot 1./\varepsilon$$

as discussed above for the Λ cross-section. The resulting cross-section is given in Table 9.3.2 and shown, together with the measured $\Lambda,\overline{\Lambda}$ cross-section in Fig 9.3.7.

$\Xi^-,\overline{\Xi^-}$ Cross-Sections	
p (GeV/c)	$d\sigma/dp$ (pbarn/ GeV/c)
1.2-2.0	3.0±1.6
2.0-3.0	1.4±0.8
3.0-5.0	0.3±0.3
x	$s/\beta\ d\sigma/dx$ (nbarn.GeV^2)
0.10-0.14	106±51
0.14-0.19	33±21
0.19-0.30	6±6

TABLE 9.3.2 $\Xi^-,\overline{\Xi^-}$ CROSS-SECTIONS

The scaled cross-section $s/\beta\ d\sigma/dx$ was computed in a similar way,the efficiency being calculated for each candidate from the parametrisation of §9.3.2, and is shown in Fig 9.3.8.

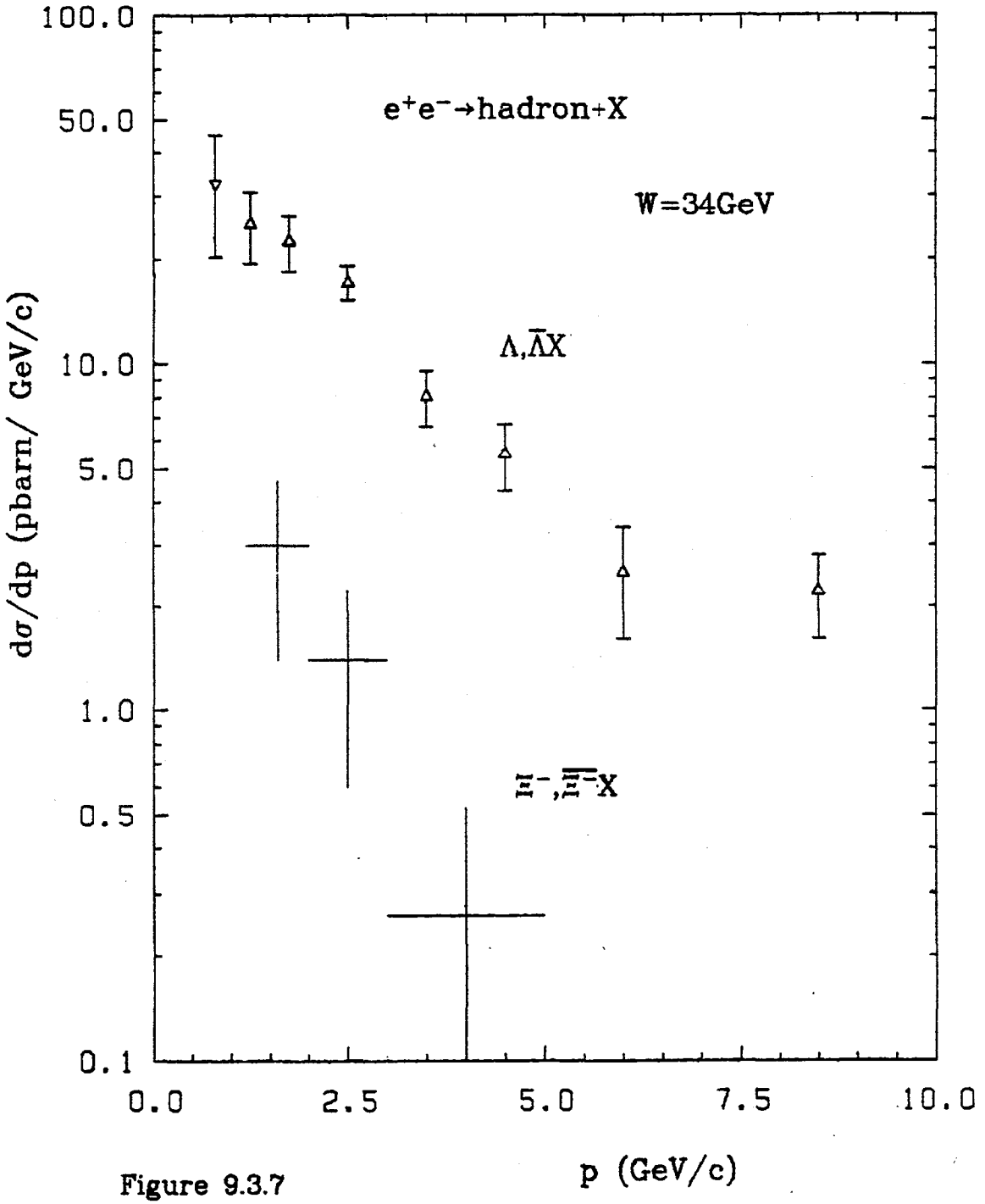
100.0
50.0
10.0
5.0
1.0
0.5
0.1
dσ/dp (pbarn/ GeV/c)
e⁺e⁻→hadron+X
W=34GeV
Λ,Λ̄X
Ξ⁻,Ξ̄⁻X
0.0
2.5
5.0
7.5
10.0
p (GeV/c)

Figure 9.3.7

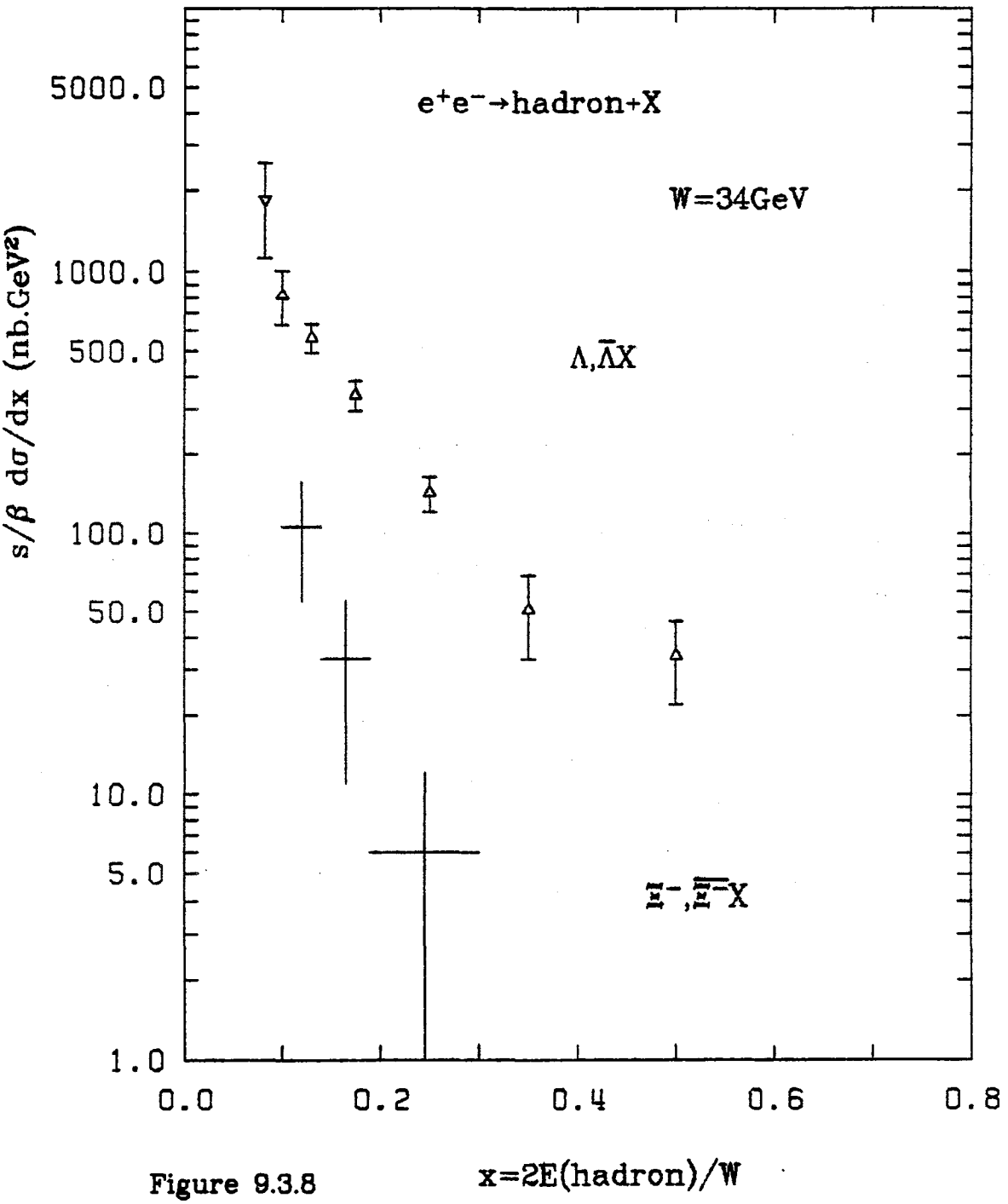
5000.0
1000.0
500.0
100.0
50.0
10.0
5.0
1.0
0.0
0.2
0.4
0.6
0.8
e+e−→hadron+X
W=34GeV
Λ,Λ̄X
Ξ−,Ξ̄−X
s/β dσ/dx (nb.GeV²)
x=2E(hadron)/W

Figure 9.3.8

9.3.4 Total Inclusive Ξ^- Cross-section

In order to obtain the total $\Xi^-,\overline{\Xi^-}$ yield, the cross-section measured in the Ξ^- momentum interval 1.2-5.0GeV/c was extrapolated to zero and to the maximum possible momentum using the shape of the momentum spectrum predicted by the Lund Monte-Carlo. The fraction of the Ξ^- yield outside the measured momentum interval was estimated to be 41%. The total yield of $\Xi^-,\overline{\Xi^-}$ per hadronic event at W=34.4GeV was found to be $0.026\pm0.008\pm0.009$. The systematic error stems mainly from uncertainties in estimates of the track finding efficiency and the efficiency for the cuts (~25%) and in the extrapolation to all momenta (~20%). Together with the measured $\Lambda,\bar{\Lambda}$ and $p,\bar{p}$ rates we obtain the ratios $\Xi^-,\overline{\Xi^-}/\Lambda,\bar{\Lambda}= 0.087\pm0.03\pm0.03$ and $\Xi^-,\overline{\Xi^-}/p,\bar{p}= 0.033\pm0.011\pm0.011$.

9.4 $e^+e^- \to \Sigma^*(1385)+X$

9.4.1 Signal Detection

For reconstruction of the Σ^* we used the cascade decays:

$$\Sigma^{*+} \to \Lambda\ \pi^+ \qquad\qquad \Sigma^{*-} \to \Lambda\ \pi^-$$
$$\quad\ \ | \qquad\qquad\qquad\quad\ \ |$$
$$\quad\ \ \to p\ \pi^- \qquad\qquad\quad\ \ \to p\ \pi^+$$

$$\overline{\Sigma^{*+}} \to \bar{\Lambda}\ \pi^- \qquad\qquad \overline{\Sigma^{*-}} \to \bar{\Lambda}\ \pi^+$$
$$\quad\ \ | \qquad\qquad\qquad\quad\ \ |$$
$$\quad\ \ \to \bar{p}\ \pi^+ \qquad\qquad\quad\ \ \to \bar{p}\ \pi^+.$$

These Σ^* decays have a branching ratio of 88±2%. The Σ^{*+},Σ^{*-} have masses of 1382.3±0.4MeV/c^2 and 1387.5±0.6MeV/c^2 respectively and widths of 35±2 and 40±2 MeV/c^2.

Unless specifically stated we shall refer to Σ^{*+},Σ^{*-} and their antiparticles simply as Σ^*.

Λ candidates were selected by the cuts of §9.3.1 as used for the Ξ^- analysis. In addition in the refit to two intersecting helices the χ^2/dof was required to be less than 3.0.

The resulting mass spectrum of $p\pi^-$ and $\bar{p}\pi^+$ combinations is shown in Fig 9.4.1. A clear signal of ~590 $\Lambda,\bar{\Lambda}$ are seen above a background of ~730.

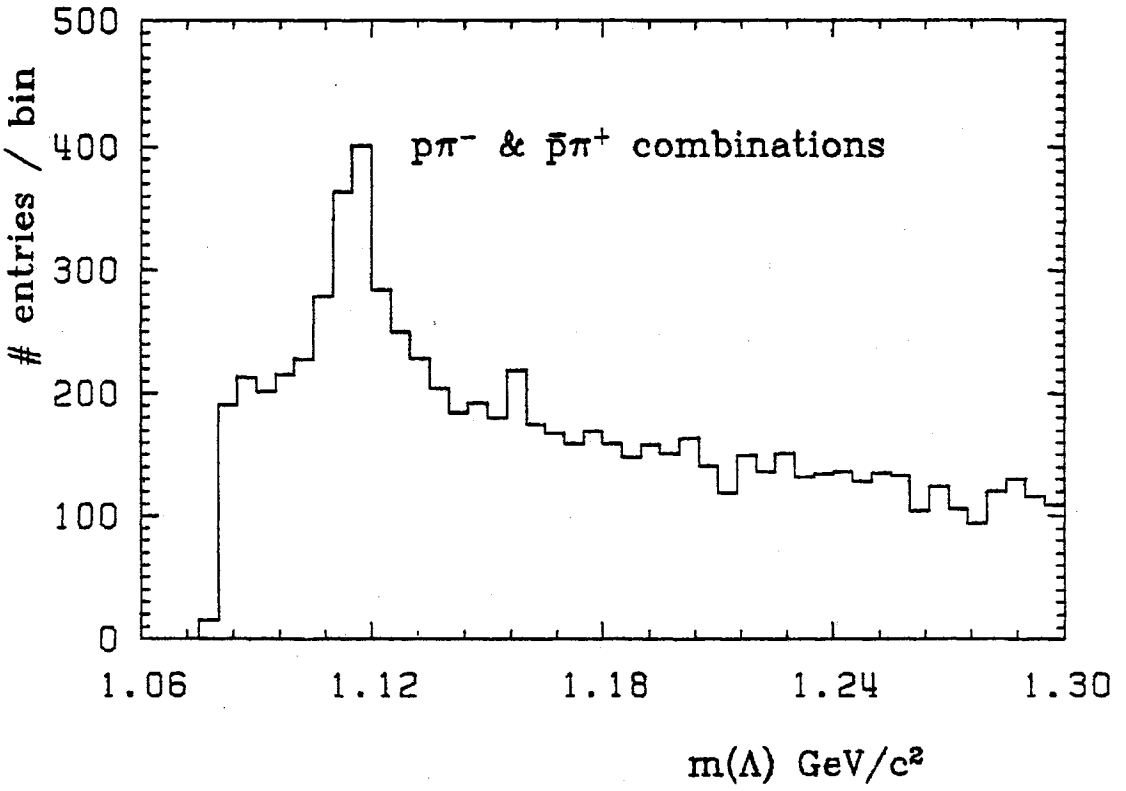

Figure 9.4.1

All particle combinations having an invariant mass within $\pm 0.010 GeV/c^2$ of the Λ mass ($1.116 GeV/c^2$) were then considered to be Λ candidates. For the further analysis their mass was fixed to the Λ mass.

To select Σ^*s we calculated the invariant mass for each combination of Λ candidate and additional charged track,considered as a pion. We required further that:

- the additional charged track satisfied p_t>0.1GeV/c and $|\cos\vartheta|$<0.87.
- the additional charged track passed within 1cm of the interaction point in r-φ and within 5cm of the interaction point in the beam direction.

to select tracks from the primary interaction.

The resulting $\Lambda\pi$ mass spectrum is shown in Fig 9.4.2. No structure is visible in the Σ^* mass region.

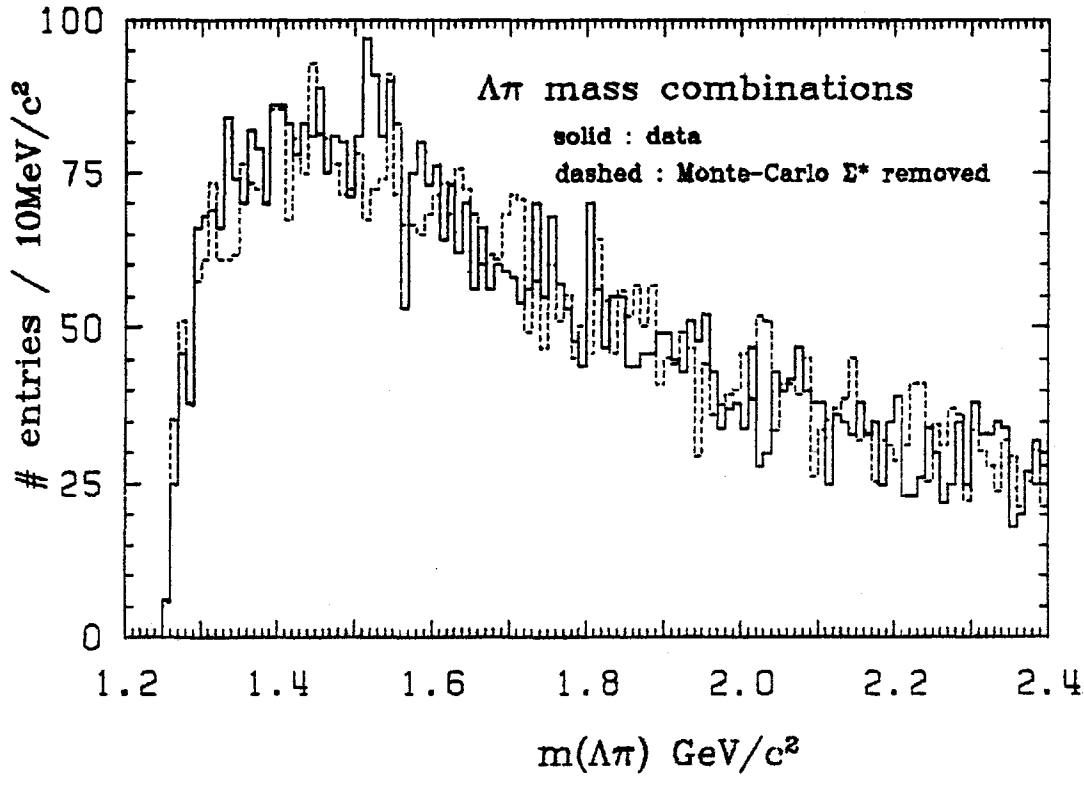

Figure 9.4.2

9.4.2 Detection Efficiency

The detection efficiency for Σ^* detection was determined by Monte-Carlo techniques as described in §9.3.2 for Ξ^- detection. Table 9.4.1 shows the result of an examination of Lund Monte-Carlo events in which a Σ^* was generated with the appropriate

Breit-Wigner mass distribution. 1567 of these events passed the hadronic event selection cuts and 1748 radiated less than 10% of the nominal beam energy of 17GeV.

Σ^* momentum (GeV/c)	0.0-1.0	1.0-8.0	>8.0
All generated, all events	323	1899	140
All generated, events≧90%W	265	1501	115
All generated, 'hadron' events	237	1357	93
For decays by the reconstructed chain			
Both tracks from Λ reconstructed	60	456	5
All 3 tracks reconstructed	42	349	4
Λ identified	0	95	5
$\Sigma^{\#}$ identified	0	84	5
ε_1(%)	0	6.2	5.0
$\Delta\varepsilon_1$(%)	-	0.6	2.2
ε_2	-	1.01	0.90

TABLE 9.4.1 Σ^* DETECTION EFFICIENCY

The average detection efficiency for Σ^* of momentum between 1.0 and 8.0 GeV/c was ε=6.2±0.6%. For the determination of the limit on the Σ^*/Λ ratio the efficiency for the detection of a Σ^* given that the Λ has been detected was computed (=77.8±2.9%).

9.4.3 Determination of Cross-section Limit

No Σ^* signal is evident in the data. Figure 9.4.2 compares the observed Λ-π mass spectrum with that predicted from Monte-Carlo events in which no Σ^* was generated. The χ^2 for comparison of these distributions was 105.4 for 114 degrees of freedom.

To determine the 90% confidence upper limit on the production cross-section of Σ^* particles the observed $\Lambda\pi$ mass spectrum (Fig 9.4.2) was fitted to a straight line in the Σ^* sidebands $1290<M(\Lambda\pi)<1350 GeV/c^2$ and $1420<M(\Lambda\pi)<1470 GeV/c^2$. This fit had a χ^2 of 4. for 9 d.o.f.. A non-relativistic Breit-Wigner (BW) function was added to the background predicted by the straight line so that a χ^2 of 11.0 for agreement with the observed $\Lambda\pi$ mass spectrum in the 'signal' region ($1350<M(\Lambda\pi)<1420 GeV/c^2$) was obtained ($\chi^2$=11. is

expected for 6 d.o.f. (7 bins and 1 parameter) at 90% confidence). The amplitude of the BW corresponded to a total of 108 entries. The straight line background and BW are shown in Fig 9.4.3.

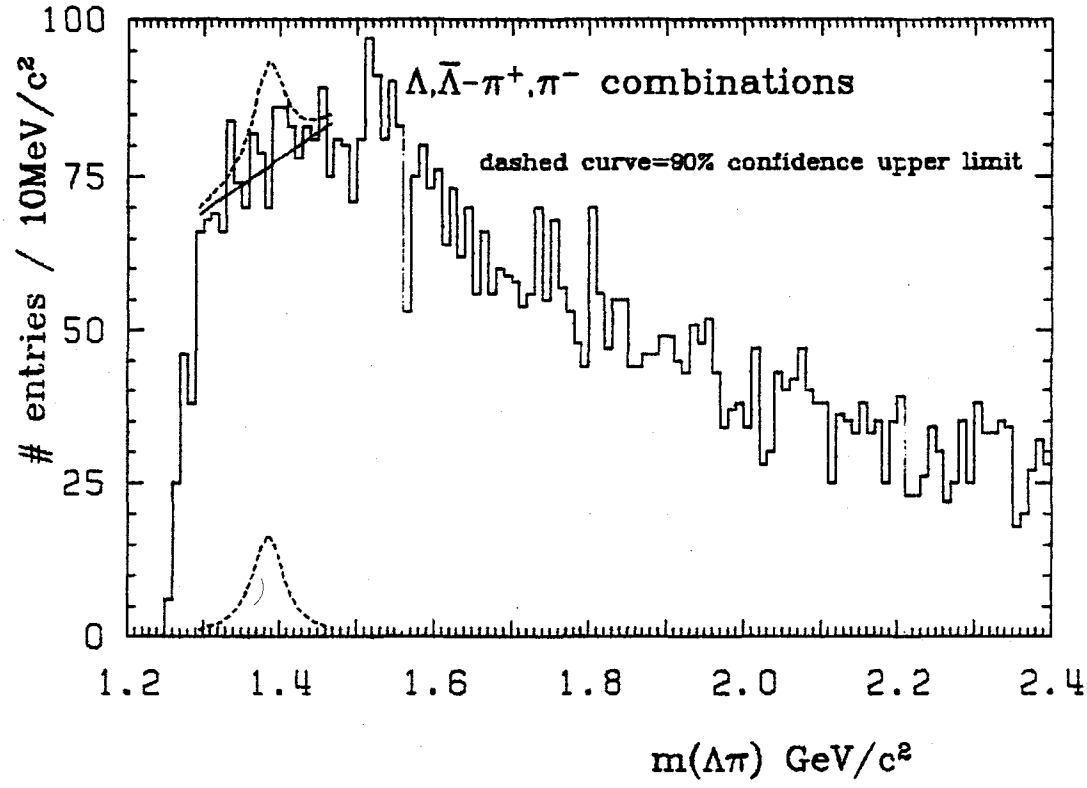

Figure 9.4.3

In order to obtain the 90% confidence level upper limit on the total number of Σ^*,the limit for the measured momentum interval 1.0-8.0GeV/c was extrapolated to zero and to the maximum possible momentum using the shape of the momentum spectrum pre-

dicted by the Lund Monte-Carlo program. The fraction,f,of Σ^* outside the measured momentum interval was estimated to be ~20%.

We computed the upper limit on the inclusive cross-section for charged Σ^* production from:

$$\sigma_{limit} = \frac{\sigma_{tot}}{N_{events}} \cdot \frac{n_{limit}}{\varepsilon} \cdot \frac{1}{(1-f)} .$$

An upper limit of 31pbarn was obtained. This corresponds to a limit of 0.105 charged Σ^* per event.

To compute the upper limit on the Σ^*/Λ ratio we evaluated:

$$\frac{n_{limit}}{\varepsilon_3} \cdot \frac{1}{(\#\ \Lambda \text{ observed})}$$

where ε_3 was the efficiency for reconstruction of a Σ^* given the Λ was reconstructed. The resulting upper limit on the ratio of charged Σ^* to $\Lambda,\bar{\Lambda}$ was 24%.

Together with the non-observation of Δ baryons[33], this limit implies that diquarks must be predominately produced in a spin 0 state. The Lund Monte Carlo, with a spin 1 diquark probability of 15% of the spin 0 diquark probability predicts a charged Σ^* to Λ ratio of ~11.5%.

APPENDIX A.

The co-ordinate system used defines the positron beam direction to be the positive z-axis, the y-axis to be vertically upwards and the x-axis then points to the centre of the PETRA ring (see fig. A.1). The (r-φ) plane is the plane containing the x and y axes. The following parameters are used as characteristics of a track: Q, p, p_T, ϑ, φ, p_x, p_y, p_z, d_0, z_0, R and C (see fig. A.2):

where	Q	is the charge of the track,
	p	is the momentum of the track,
	p_T	is its momentum transverse to the beam direction,
	ϑ	is polar angle of the track to the positive z-axis,
	φ	is angle of the track to the positive x-axis in the (r-φ) plane,
	p_x, p_y, p_z	are the components of the momentum parallel to the x, y and z axes respectively,
	d_0	is the distance of closest approach of the track to the interaction point in the (r-φ) plane and is positive if the track contains the origin, otherwise it is negative,
	z_0	is the distance of the track from the interaction point parallel to the z-axis at its point of closest approach in the (r-φ) plane,
	R	is the radius of curvature of the track,
and	C	is the curvature of the track = 1/R.

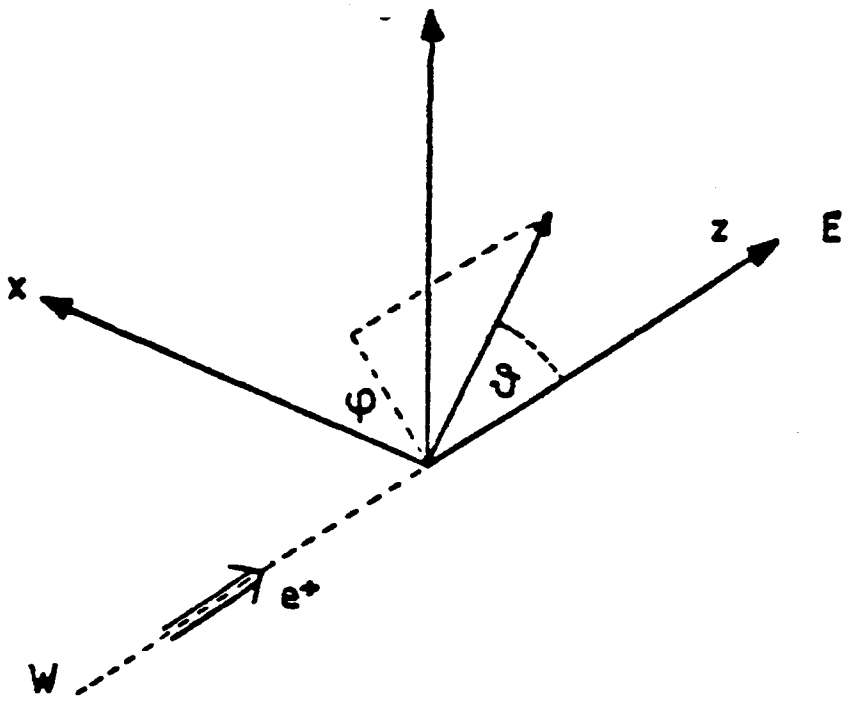

Figure A.1. Co-ordinate system used in analysis.

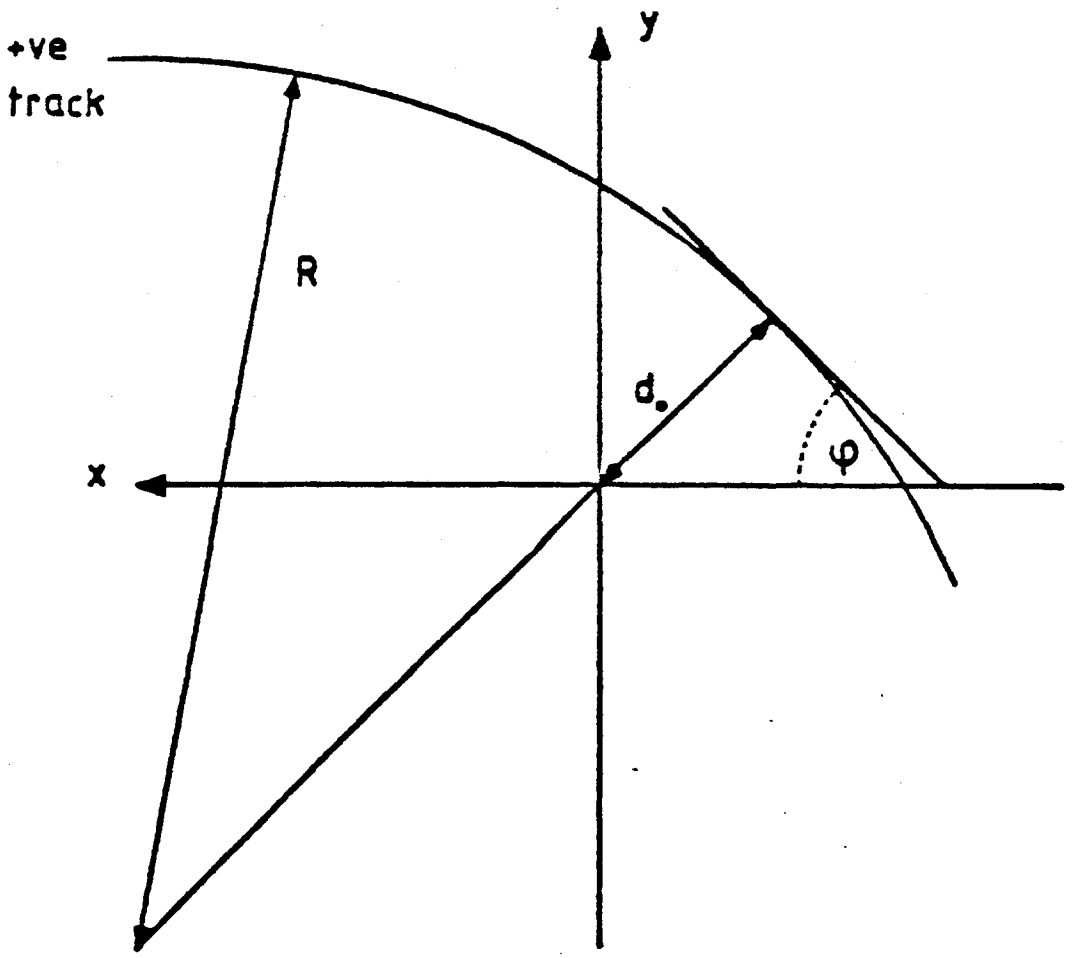

Figure A.2. Projection of a track onto the (r-φ) plane.

APPENDIX B.

List of Members of the TASSO Collaboration in April 1982.

R.Brandelik#, W.Braunschweig, K.Gather, F.J.Kirschfink,
K.Lübelsmeyer, H.-U.Martyn, G.Peise, J.Rimkus, H.G.Sander,
D.Schmitz, H.Siebke, D.Trines, W.Wallraff
I.Physikalisches Institut der RWTH Aachen, Germany $

H.Boerner##, H.M.Fischer, H.Hartmann, E.Hilger, W.Hillen, G.Knop,
L.Köpke, H.Kolanoski, R.Wedemeyer, N.Wermes, M.Wollstadt
Physikalisches Institut der Universität Bonn, Germany $

H.Burkhardt, S.Cooper, J.Franzke, D.Heyland, H.Hultschig, P.Joos,
W.Koch, U.Kötz*, H.Kowalski*, A.Ladage, B.Löhr, D.Lüke,
H.L.Lynch**, P.Mättig, K.H.Mess, D.Notz, J.Pyrlik, D.R.Quarrie***,
R.Riethmüller, W.Schütte, P.Söding, G.Wolf
Deutsches Elektronen-Synchrotron, DESY, Hamburg, Germany

R.Fohrmann, H.L.Krasemann, P.Leu, E.Lohrmann, D.Pandoulas, G.Poelz,
O.Römer###, P.Schmüser, B.H.Wiik
*II.Institut für Experimentalphysik der Universität Hamburg,
Germany* $

I.Al-Agil, R.Beuselinck, D.M.Binnie, A.J.Campbell, P.J.Dornan,
D.A.Garbutt, T.D.Jones, W.G.Jones, S.L.Lloyd, J.K.Sedgebeer
Department of Physics, Imperial College London, England $$

K.W.Bell, M.G.Bowler, I.C.Brock, R.J.Cashmore, R.Carnegie, P.E.L.Clarke,
R.Devenish, P.Grossmann, J.Illingworth, M.Ogg####, G.L.Salmon,
J.Thomas, T.R.Wyatt, C.Youngman
*Department of Nuclear Physics, Oxford University,
England* $$

B.Foster, J.C.Hart, J.Harvey, J.Proudfoot, D.H.Saxon, P.L.Woodworth
Rutherford Appleton Laboratory, Chilton, England $$

M.Holder
Gesamthochschule Siegen, Germany

E.Duchovni, Y.Eisenberg, U.Karshon, G.Mikenberg, D.Revel,
E.Ronat, A.Shapira
Weizmann Institute, Rehovot, Israel $$$

T.Barklow, T.Meyer#####, G.Rudolph, E.Wicklund, Sau Lan Wu, G.Zobernig
Department of Physics, University of Wisconsin, Madison, Wisconsin, USA $$$$

---

* On leave at CERN, Geneva, Switzerland
** On leave at UC Santa Barbara, CA, USA
*** On leave from Rutherford Appleton Laboratory, Chilton, England

\# Now at IST, Darmstadt, Germany
\## Now at KEK, Oho-Machi, Japan
\### Now at SCS, Hamburg, Germany
Now at Cornell University, Ithaca, NY, USA
Now at Texas A + M University, Texas, USA

$ Supported by the Deutsches Bundesministerium für Forschung und Technologie
$$ Supported by the UK Science and Engineering Research Council
$$$ Supported by the Minerva Gesellschaft für Forschung mbH
$$$$ Supported by the US Department of Energy contract WY-76-C-02-0881

REFERENCES.

1. G. WOLF DESY 81/086 (1981) 36
2. G. WOLF DESY 81/086 (1981) 57
3. TASSO COLLABORATION,M. ALTHOFF ET AL, DESY 82/070(1982)
4. TASSO COLLABORATION,R. BRANDELIK ET AL, DESY 82/046(1982)
5. G. WOLF, JOURNAL DE PHYSIQUE 43 (1982) 525
6. T. MEYER, Z. PHYS. C12 (1982) 77;

   P.HOYER ET AL, NUCL. PHYS. B161 (1978)34.
7. H. BOERNER ET AL, DESY 80/27(1980)
8. K. BELL ET AL, NUCL. INSTR. & METH. 179 (1981) 27
9. D.R. QUARRIE, RL-81-048 (1981).
10. TASSO COLLABORATION, R.BRANDELIK ET AL, PHYS. LETT. 113b (1082) 499.
11. G. CHARPAK ET AL, NUCL. INST. & METH. 167(1979) 455;

    I. EHDO ET AL, HIROSHIMA UNI., JAPAN;

    A. BRESKIN ET AL, NUCL. INST. & METH. 143 (1977) 29;

    G. CHARPAK ET AL, NUCL. INST. & METH. 148 (1978) 471;

    G. FISCHER ET AL, NUCL. INST. & METH. 100 (1972) 515;

    E. GATTI ET AL, NUCL. INST. & METH. 163 (1979) 83;
12. S. JAROWSLAVSKI, NUCL. INSTR. & METH. 176 (1980) 263.
13. BOUCLIER ET AL., NUCL. INSTR. & METH. 88 (1970) 149.
14. TASSO COLLABORATION, Z. PHYS C 16 (1982) 13.

15. TASSO COLLABORATION, PHYSICS LETT. 121B (1983).

16. D. LÜEKE, TASSO NOTE 173.

17. D.G. CASSEL AND H. KOWALSKI, DESY 80/107 (1980).

18. A.V. AHO, J.E. HOPCROFT, J.D. ULLMAN ;The design and analysis of computer algorithms, ADDISON- WESLEY, READING, MASS.

19. H. KOWALSKI, DESY 80/72 (1980).

20. TASSO COLLABORATION, upgrade to proposal 190.

21. B.D. HYAMS, SLAC-250 (1982) 51;

A. BROSS, SLAC-250 (1982) 56.

22. R. L. GLÜCKSTERN, NUCL. INSTR. & METH. 24 (1963) 381.

23. B. FOSTER, RL-82-034.

24. TASSO COLLABORATION, PHYS. LETT. 92b (1980) 199.

25. G. KALMUS, RAL, XXI INTERNATIONAL CONF., PARIS, JULY 1982.

26. TASSO COLLABORATION, DESY 83/010.

27. NIJENHUIS AND WILF, COMBINATORIAL ALGORITHMS, ACADEMIC PRESS (1978).

28. D.H. SAXON, TASSO NOTE 260.

29. F.J.KIRSCHFINK AND E.VOGEL, TASSO NOTE 265

30. J.K. SEDGBEER, PhD Thesis, University of London.

31. B. ANDERSON ET AL, PHYS. LETT. 94B (1980) 211; NUCL. PHYS. B197 (1982) 45;

32. B. FOSTER AND S.L. LLOYD, SIMPLE WRITE-UP ,UNPUBLISHED.

33. D.H.SAXON AND P. WOODWORTH, TASSO NOTE 252